

Title	リチウムイオン二次電池用BIAN由来高容量アノード
Author(s)	MANTRIPRAGADA, BHARAT SRIMITRA
Citation	
Issue Date	2022-09
Type	Thesis or Dissertation
Text version	ETD
URL	<a href="http://hdl.handle.net/10119/18148">http://hdl.handle.net/10119/18148</a>
Rights	
Description	Supervisor :松見 紀佳, 先端科学技術研究科, 博士

# **BIAN derived high-capacity anodes in lithium-ion secondary batteries**

**Mantripragada Bharat Srimitra**

Japan Advanced Institute of Science and Technology

# **Doctoral Dissertation**

## **BIAN derived high-capacity anodes in lithium-ion secondary batteries**

**Mantripragada Bharat Srimitra**

Supervisor: Noriyoshi Matsumi

Graduate School of Advanced Science and Technology

Japan Advanced Institute of Science and Technology

Materials Science

September 2022

# **BIAN derived high-capacity anodes in lithium-ion secondary batteries**

## **Chapter 1:**

Energy is the key factor that governs technological progress. So far fossil fuels have been highest supplier of energy to satiate our day-to-day needs. However, the adverse ecological effects and the lack of renewability led to the exploration of various other sustainable energy sources. In this context, lithium-ion secondary batteries are attractive devices in terms of power and energy densities. Anode is a crucial component of lithium-ion batteries. In this thesis, the synthesis and electrochemical application of BIAN based polymers and N-doped carbon derived from BIAN based polymers in lithium-ion batteries are presented.

## **Chapter 2:**

Organic polymers are materials with strong covalent bonds and possess the possibility of crosslinking between the organic moieties with different geometries. Organic polymers offer a distinct advantage of integrating multiple redox sites, tunable porosity, and relatively high surface area. In this chapter, the synthesis and anodic applications of imine and azo functionalized BIAN-Bismarck brown based conjugated organic polymer (BBP) are presented.

## **Chapter 3:**

The charge storage properties of organic polymers can be enhanced by increasing the density of redox active groups. In this chapter, the synthesis and applications of Bis-imino-acenaphthoquinone (BIAN)-melamine based organic polymer (PBM) as an anode material in lithium-ion battery is presented.

## **Chapter 4:**

Increasing the density of redox active sites by introducing hetero atoms and reducing the lithium diffusion length by generating porosity are enticing strategies to increase the fast-charging ability of anodes. In this chapter, synthesis, and application of N-doped carbon (Py PBM) derived from BIAN-melamine organic polymer as single source of carbon and nitrogen, as anodic active material was presented.

**Keywords:** Organic anode, n-type conjugated polymers, fast charging, BIAN, N-doped carbon.

# Table of Contents

<b>1.Introduction.....</b>	<b>1</b>
1.1Abstract.....	1
1.2 General introduction to energy sources.....	2
1.3 Electrochemical energy storage.....	3
1.3.1 Fuel cells.....	3
1.3.2 Super capacitors.....	5
1.3.3 Batteries.....	7
1.4 Lithium-ion battery.....	12
1.4.1 Working mechanism of a lithium-ion battery.....	13
1.4.2 Cathode.....	14
1.4.3 Electrolyte.....	19
1.4.4 Anode.....	22
1.4.5 Binder materials.....	28
1.5 Electrochemical techniques used in characterization of lithium-ion batteries.....	29
1.5.1 Cyclic voltammetry.....	29
1.5.2 Electrochemical Impedance spectroscopy (EIS) .....	30
1.5.3 Galvanostatic charge-discharge study (GCD) .....	33
1.6 Design principles of a lithium-ion battery.....	34
1.7 Strategy employed in this thesis towards the design of lithium-ion battery anode.....	37
1.8 Objective and scope of this thesis.....	38
References.....	40

## **Chapter 2. BIAN-Bismarck brown organic polymer as efficient anode materials for lithium-ion batteries..... 43**

2.1 Abstract.....	43
2.2 Introduction.....	44
2.3 Experimental section.....	45

2.3.1 Materials.....	45
2.3.2 Electrochemical studies. ....	46
2.4 Characterization.....	47
2.4.1 Infra-red spectroscopy.....	48
2.4.2 EDX. ....	49
2.4.3 XPS.....	50
2.4.4 TGA.....	51
2.4.5 XRD.....	52
2.5 Electrochemical studies.....	53
2.5.1 Cyclic voltammetry.....	53
2.5.2 Potentiostatic impedance spectroscopy.....	53
2.5.3 Dynamic electrochemical impedance spectroscopy.....	54
2.5.4 Galvanostatic charge discharge studies.....	56
2.5.5 Kinetic studies.....	59
2.6 XPS after cycling.....	62
2.7 Conclusion.....	64
References.....	65

**Chapter 3. BIAN based organic polymer as high performing anode for lithium-ion batteries.....68**

3.1 Abstract.....	68
3.2 Introduction.....	69
3.3 Experimental section.....	71
3.3.1 Materials.....	71
3.3.2 Electrochemical studies.....	72
3.4 Synthesis of PBM.....	73
3.5 Characterization.....	73
3.5.1 Infra-red spectroscopy.....	74
3.5.2 X-ray photo electron spectroscopy .....	74

3.5.3 TGA. ....	75
3.5.4 XRD. ....	76
3.5.5 BET studies. ....	77
3.5.6 TEM. ....	78
3.6 Electrochemical studies.....	79
3.6.1 Cyclic voltammetry.....	79
3.6.2 PEIS. ....	80
3.6.3 Charge-discharge studies. ....	80
3.6.4 Kinetic studies.....	82
3.6.5 Theoretical studies.....	85
3.7 Postmortem studies.....	86
3.8 Conclusion.....	89
References.....	91

**Chapter 4. Pyrolyzed BIAN-Melamine organic polymer as high performing anode in lithium-ion batteries. .... 95**

4.1 Abstract.....	95
4.2 Introduction.....	96
4.3 Materials and methods.....	98
4.3.1 Materials.....	98
4.3.2 Electrochemical studies.....	98
4.3.3 Synthesis of PBM.....	99
4.3.4 Synthesis of Py PBM600 and Py PBM800.....	99
4.4 Characterization.....	100
4.4.1 Elemental dispersive x-ray spectroscopy.....	100
4.4.2 X-ray photo electron spectroscopy .....	101
4.4.3 Thermogravimetric analysis.....	102
4.4.4 X-ray diffraction.....	103

4.4.5 TEM images.....	104
4.5 Electrochemical characterization.....	106
4.5.1 Cyclic voltammetry.....	106
4.5.2 Potentiostatic impedance spectroscopy.....	107
4.5.3 Galvanostatic charge-discharge studies.....	107
4.5.4 DEIS.....	110
4.5.5 Kinetic studies.....	113
4.5.6 Full-cell studies.....	116
4.5 XPS after cycling.....	118
4.6 Conclusion.....	121
References.....	122

**5. Conclusion.....123**

Chapter 1.....	123
Chapter 2.....	124
Chapter 3.....	124
Chapter 4.....	125
Future scope.....	125



## Preface

The importance of efficient energy storage systems is becoming more and more evident with the increase in day-to-day energy requirements. Hence, electrochemical energy storage devices are the most sought-after devices throughout the globe. In this context, the success witnessed by lithium-ion batteries in the field of portable electronics show a glimpse of its possible extended applications in future. Globally, much research effort is directed towards obtaining an economical and high performing lithium-ion batteries. In this field, organic polymers have been majorly restricted to the application in electrolytes and as binder materials. The magnanimity of organic molecules is relatively underutilized in lithium-ion batteries. This thesis mainly focuses on the application of BIAN based organic molecules as organic anodes in lithium-ion batteries. The electron rich nature of BIAN moiety has been exploited in formation of inorganic complexes for catalysis and the polymers of BIAN have been reported by my colleagues, in the past. Organic chemistry, as believed by chemists is the basis of all life forms on this globe and possibly elsewhere. Motivated by the wide scope of organic molecules, the author, with the guidance of *Prof. Noriyoshi Matsumi* at Graduate School of Advanced Science and Technology, Japan Advanced Institute of Science and Technology started researching the application of BIAN based materials in applications with the hope of making a battery with organic anode. In this thesis, titled, **Design of BIAN derived organic polymers and their derivatives as efficient anode materials in Lithium-ion batteries**, the author has presented his humble endeavors towards developing a BIAN based organic anode for lithium-ion battery. Although the aim is to study the direct application of organic anodic materials, an indirect application through synthesizing N-doped carbon from organic polymers is also presented in significant detail.

Mantripragada Bharat Srimitra

Graduate School of Advanced Science and Technology

Japan Advanced Institute of Science and Technology

May 2022.

## Acknowledgement

This work titled, **Design of BIAN derived organic polymers and their derivatives as efficient anode materials in Lithium-ion batteries**, has been conducted under the supervision of *Prof. Noriyoshi Matsumi* at Graduate School of Advanced Science and Technology, Japan Advanced Institute of Science and Technology. I am immensely grateful to my supervisor *Prof. Noriyoshi Matsumi* for the constant support, guidance and the motivation throughout this work. I also extend my heartfelt gratitude to senior lecturer Rajashekar Badam for the valuable inputs, characterization expertise and scientific insights he has provided during the course of this work without which this work would have been incomplete.

I am thankful to the review members, Prof. Yoichi Tominaga, Prof. Yuki Nagao, Prof. Toshiaki Taniike and Prof. Yoshifumi Oshima for sparing their valuable time to evaluate this thesis.

I am also extremely thankful to Prof. Toshiaki Taniike for allowing me to perform my minor research under his guidance. The inputs provided by him helped me improve my skills in theoretical studies.

I extend my thankfulness to technical specialist Koichi Higashimine, Dr. Kai Kan, Technical specialist Akio Miyazato and the staff of Center for Nano Materials and Technology (CNMT), Japan Advanced Institute of Science and Technology, for their valuable technical support without which the thesis would have been incomplete.

I am infinitely indebted to my parents, family, members of Matsumi lab, friends who stood by me in my personal and professional life and provided great emotional strength towards completion of this work.

I dedicate this work to the universal spirit running through the fabric of this universe.

Mantripragada Bharat Srimitra

Graduate School of Advanced Science and Technology

Japan Advanced Institute of Science and Technology

May 2022.

## **1. Introduction**

### **1.1 Abstract**

Generation of sustainable energy and energy storage stand as the key challenges today. Though there has been a high reliance on fossil fuel-based energy materials, the non-renewability of resources and environmental issues related to fossil fuels warrant extensive utilization of these resources. Hence, the quest for energy has to be directed towards eco-friendly renewable resources. In this context, the inconsistency of the availability of renewable resources imply development of efficient energy storage devices. Owing to various benefits like high energy density, fast charging ability, low memory effect etc., lithium-ion batteries are popularized in portable electronic devices. This chapter provides a brief review on various energy storage devices like capacitors, fuel cells, primary batteries, and secondary batteries. Further, a brief discussion on the cathode, anode, and electrolyte components along with the design considerations and the design of materials reported in this thesis are presented.

## 1.2 General introduction to energy sources

Post 18<sup>th</sup> century, the world has witnessed a vast change in the technological and industrial advancements. Energy was the key factor that drove the process of change from an agrarian and handicraft-based economy to industry dominated economy. The industrial and technological advancements that were brought from that period changed the lifestyle of human civilization. Large scale industrial advancements implied large scale energy requirements for various processes involved in the industries. To satisfy such huge energy requirements, fossil fuels were found to be most effective, as they are easily available, abundant, and efficient in terms of energy. Fossil fuels are essentially organic matter that was buried deep in the earth and thereby subjected to high pressure and temperature for long period of time. Fossil fuel can broadly be categorized into three:

- i) Coal
- ii) Petroleum
- iii) Natural gas

Coal is generated when dead plant matter is exposed to huge amounts of heat and pressure. During industrial revolution, coal was the primary source of energy to generate heat required in the industry and to facilitate transport as it is easily available within few meters under the earth and the supply is abundant. Furthermore, after the invention of electricity, the large-scale production of electricity is also conducted using the thermal energy obtained from coal. In the year 2020, coal supplied about 25% of world's primary energy and about 30% of world's electricity. With the increase in technological innovation, drilling and oil mining techniques were introduced. With these techniques, petroleum and natural gas became available. Petroleum products are currently widely used in automobiles and other transport modes. Natural gas, apart from being used in automobile industry, is also an important fuel used for cooking purposes in household. With these benefits, fossil fuel-based energy resources have been primary sources of energy. However, the benefits of utilizing fossil fuels come with an enormous cost of environmental destruction. Post industrial revolution, global CO<sub>2</sub> emissions rose drastically threatening the balance of eco-system. Besides this, due to the extensive usage, the resources of fossil are depleting at a faster rate. Hence, it is essential to shift from fossil fuels to ecofriendly renewable resources. Though various kinds of renewable energy resources are available in nature, unlike the fossil fuel-based sources, the

availability of such renewable resources is always not consistent. Hence, the aspect of energy storage becomes more crucial.

### **1.3 Electrochemical energy storage**

Electrochemical energy storage is the storage of electrical energy in the form of chemical energy. It is one of the key developments of 21<sup>st</sup> century and offers the promise of sustainability. Currently, electrochemical energy storage devices emerged as the promising alternatives to the fossil fuel-based energy resources. Compared to fossil fuels, these devices have the advantages of eco friendliness, better energy density etc.,<sup>1</sup> In this context, much research is being directed towards developing better electrochemical storage techniques. Currently, automobile companies like Tesla, Nissan, Mercedes have already launched completely battery powered cars. Hence, in few years, the replacement of fossil fuel-based vehicles by electrochemical energy powered vehicles seems inevitable. However, more improvements are necessary in terms of longevity, widening the range of applications etc., Electrochemical energy storage systems can broadly be classified into three types:

- i) Fuel cells
- ii) Super capacitors
- iii) Batteries

#### **1.3.1 Fuel cells**

A fuel cell is an electrochemical cell that generates electricity by transforming hydrogen-based fuel and oxygen through a series of redox processes generating water<sup>2</sup>. The distinct advantage of a fuel cell is, as long as the outer supply of hydrogen fuel is maintained, electricity can be generated continuously. This property makes fuel cells a promising contender to fossil fuel systems. Along with this, fuel cells also offer the benefits of minimal or no CO<sub>2</sub> emissions<sup>3</sup>, higher efficiency<sup>4</sup>, better scalability.

The components of fuel cell are an anode, cathode and an ion conducting membrane enabling the movement of proton. Figure 1 shows the schematic representation of a fuel cell. In a typical fuel cell, hydrogen supplied to the anode, it gets oxidized, and electron is released<sup>5</sup>. The electron thus released in the anode migrate towards anode through an external circuit, completing the circuit. The electrons released from anode reduce the oxygen at the cathode forming oxygen anion. The

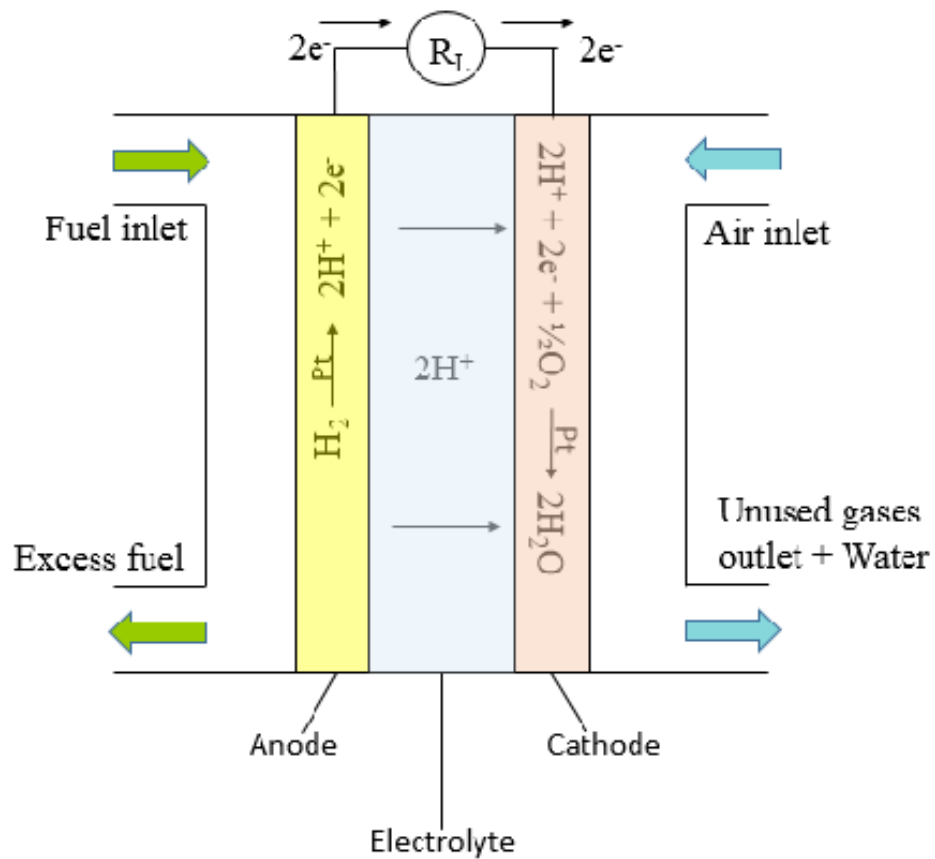


*Figure 1-Schematic representation of fuel cell (Ref:5)*

positively charged hydrogen diffuses through the electrolyte and reacts with the negatively charged oxygen forming water<sup>6</sup>.

Unlike heat engine, fuel cell is not bound by the limitation of maximum carnot efficiency. The efficiency of a fuel cell is given by the ratio of Gibbs free energy ( $\Delta G^0$ ) and enthalpy or heat energy of the fuel ( $\Delta H^0$ ). Depending on the type of fuel cell used, fuel cells are broadly classified into six types<sup>7</sup>:

- i) Direct methanol fuel cell
- ii) Polymer electrolyte membrane fuel cell
- iii) Alkaline fuel cell
- iv) Phosphoric acid fuel cell
- v) Molten carbonate fuel cell
- vi) Solid oxide fuel cell

Figure 2 summarizes the operation of six types of fuel cells.

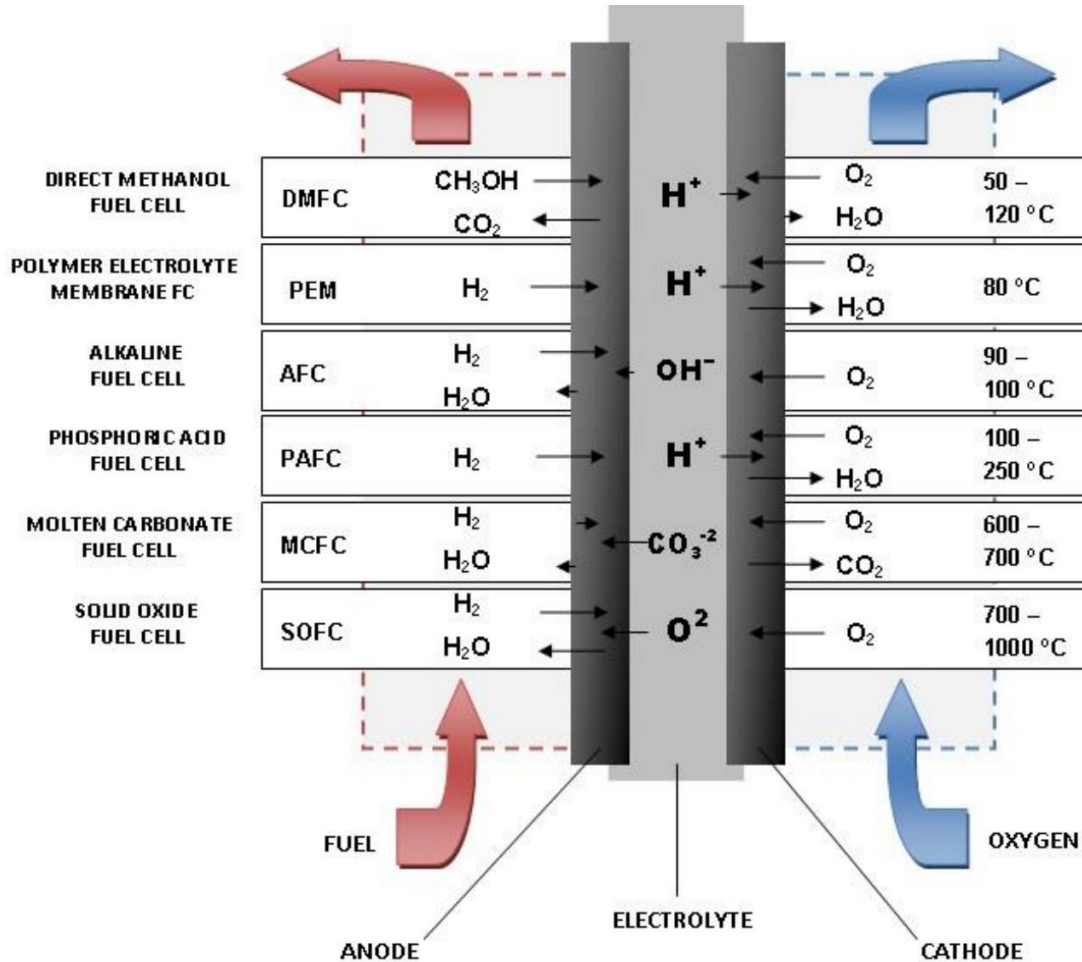


Figure 2-various types of fuel cells and their operation conditions (Ref:7)

### 1.3.2 Super capacitors

Electrochemical capacitors also known as super capacitors or ultra-capacitor is a device to store and release energy. Supercapacitors store electricity in a static state enabling extremely fast charging and discharging. Like conventional capacitors, supercapacitors too have two electrodes separated by an electrolyte. Typically, copper or aluminum coated with active material with high surface area are used as electrodes. Based on the type of active material, the charge storage mechanism differs. Based on the type of electrode and mechanism of charge storage, super capacitors are classified into three categories<sup>8</sup>:

- i) Electric double layer capacitors
- ii) Hybrid capacitors
- iii) Pseudo capacitors

### **1.3.2a Electric double layer capacitors**

In an electric double layer capacitors are supercapacitors in which charge storage mechanism follows Helmholtz double layer formation. According to Helmholtz model, the electrode surface depending on the excess presence or deficiency of electrons has a charge density. The surface charge density of the electrode is balanced by a redistribution of ions with equal and oppositely charged ions at a certain distance of separation<sup>9</sup>.

### **1.3.2b Pseudo capacitors**

The charge storage in pseudo capacitors is based on redox reactions and a certain amount of energy transfer occurs between electrolyte and electrode occurring during the charge-discharge process. In these devices, charge storage doesn't occur by the formation of a dielectric layer. Compared to the surface dependent electric double layer capacitors, the charge discharge time is longer in case of pseudo capacitors due to the occurrence of a charge transfer reaction<sup>10</sup>.

### **1.3.2c Hybrid capacitors**

Hybrid capacitors are a hybrid of electric double layer capacitors and pseudo capacitors. A negative electrode made of pseudo capacitive material and positive electrode is typically made of activated carbon. At the negative electrode, faradaic charge transfer process occurs and at the positive electrode, the charge storage occurs through the mechanism described for electric double layer capacitors<sup>11</sup>.

The electrode materials used in these devices are listed in Table 1



### 1.3.3 Batteries

Batteries are storage devices that store electrical energy in the form of chemical energy and convert chemical energy back to electrical energy while discharging. The first ever known battery was invented by Alessandro Volta in 1800 called as the Voltaic pile. This battery consists of copper

*Table 1-Electrode materials used for different types of supercapacitors*

Type of capacitor	Electrode material
<b>EDLC</b>	<ul style="list-style-type: none"> <li>• Activated carbon</li> <li>• Carbon aerogels</li> <li>• Carbon fibers</li> <li>• Carbon nanotubes</li> </ul>
<b>Pseudo supercapacitor</b>	<ul style="list-style-type: none"> <li>• Metal oxides</li> <li>• Conducting polymers</li> </ul>
<b>Hybrid supercapacitor</b> <ul style="list-style-type: none"> <li>• Asymmetric</li> <li>• Composite</li> <li>• Battery type</li> </ul>	<ul style="list-style-type: none"> <li>• Carbon materials - Conducting polymers,</li> <li>• Carbon materials – metal oxides.</li> </ul>

and zinc as electrodes sandwiching brine-based electrolyte<sup>12</sup>. Followed by Alessandro Volta, John Fredric Daniell, invented a battery consisting of a copper container filled with copper sulphate solution and zinc immersed in sulfuric acid<sup>13</sup>. This cell was considered to be the first one of practical importance. Figure 3 illustrates the working of a Daniell cell<sup>14</sup>.

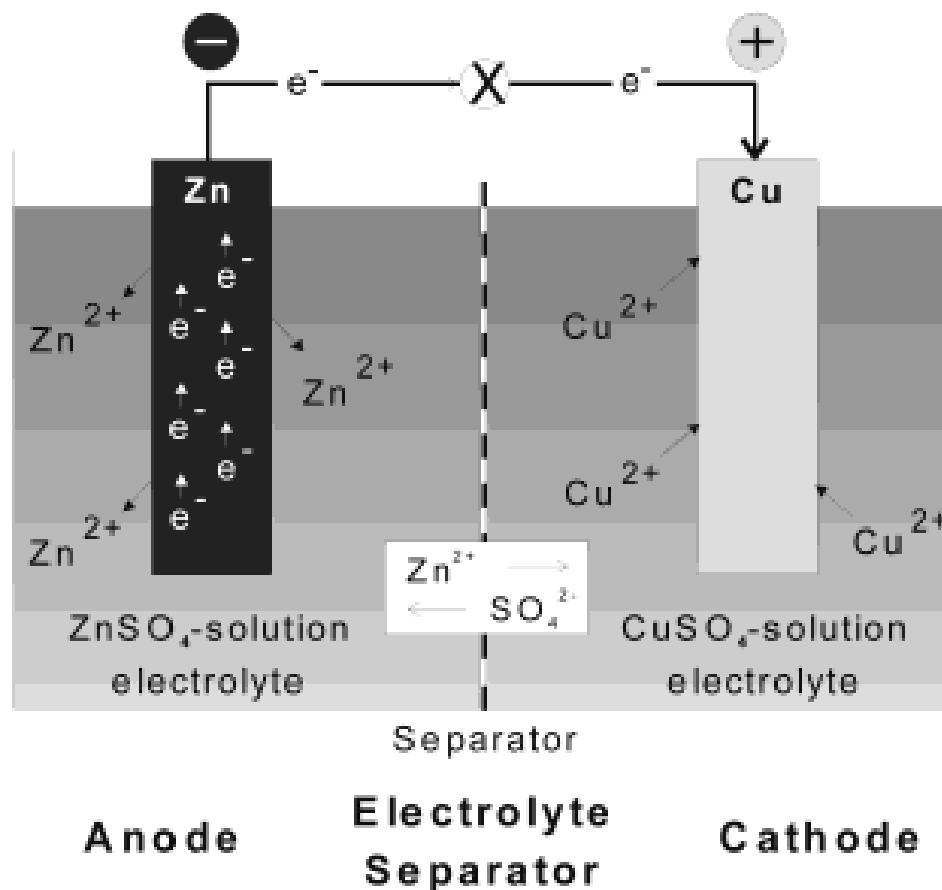


Figure 3-Schematic representation of a Daniell cell (Ref:14)

However, in these cells, after the zinc metal atoms get oxidized to zinc ions and electrons are released, the cell can no longer supply electricity. This implies that such batteries can only be used once. Such batteries that generate electricity by irreversible chemical reactions are known as primary batteries. Based on such chemical processes, many primary batteries like leclanche cell, which consists of an electrolyte paste instead of liquid electrolyte are popular. Though, these batteries have a wide range of applications in portable devices, it is important to note that the non-reusability of these materials leads to generation of toxic chemical waste in high amounts. In this regard, secondary batteries offer the benefit of reusability<sup>15</sup>.

### 1.3.3a Secondary batteries

Secondary batteries are batteries in which electrical energy is stored in the form of chemical energy and chemical energy is converted to electrical energy upon discharging. The additional benefit in these systems is that the chemical reactions involved are reversible in nature i.e., these batteries

can be reused after discharging. Hence, in the context of efficient utilization of materials and eco friendliness, secondary batteries offer a sustainable means of energy storage<sup>16</sup>.

Various secondary batteries (examples are listed in Table 2) were developed to meet the energy requirements. However, due to practical reasons, only a few of them saw the phase of commercialization. The following sections give a brief overview on few of the commercialized batteries.

*Table 2-List of primary and secondary batteries*

Primary batteries	Secondary batteries
<ul style="list-style-type: none"> <li>• Alkaline battery (zinc manganese oxide, carbon)</li> <li>• Aluminum–air battery</li> <li>• Atomic battery</li> <li>• Beta voltaic device</li> <li>• Chromic acid cell (Poggendorff cell)</li> <li>• Clark cell</li> <li>• Daniell cell</li> <li>• Dry cell</li> <li>• Galvanic cell</li> <li>• Grove cell</li> <li>• Leclanché cell</li> </ul>	<ul style="list-style-type: none"> <li>• Aluminum-ion battery</li> <li>• Calcium battery</li> <li>• Flow battery</li> <li>• Lead–acid battery</li> <li>• Lithium-ion battery</li> <li>• Lithium–sulfur battery</li> <li>• Lithium–titanate battery (LTO)</li> <li>• Thin-film lithium-ion battery</li> <li>• Lithium–ceramic battery</li> <li>• Rechargeable lithium–metal battery</li> <li>• Magnesium-ion battery</li> <li>• Metal–air electrochemical cells</li> </ul>

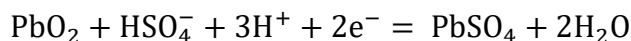
### **1.3.3a-i Lead acid battery**

Lead acid battery is a rechargeable battery consisting of pure lead as a cathode and lead oxide as anode and sulfuric acid as electrolyte. Among the various available batteries, lead acid batteries are most developed ones. They are widely used in applications requiring high current such as lighting, uninterrupted power supply systems etc., During discharge, both the electrodes become lead sulfate. The reaction during discharge is as follows<sup>17</sup>:

At anode:



At cathode:



Total reaction:



In the charged state, there is a potential difference between pure lead and the lead oxide electrodes which leads to the cell potential. During discharge, electrons are released from the cathode to anode through external circuit along with the exothermic reaction of  $\text{H}^+$  and  $\text{OH}^-$  to generate water. During the charging, reverse process occurs i.e., water splitting takes place. Figure 4 shows the schematic representation of charging and discharging of lead-acid batteries.

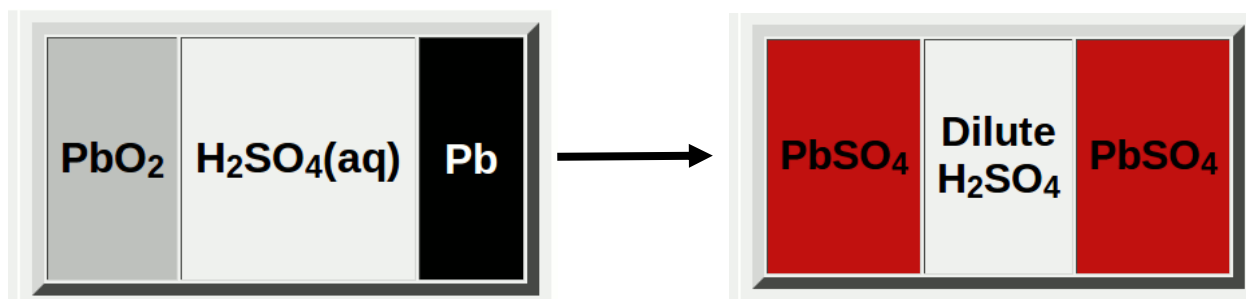


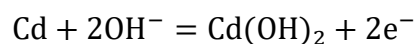
Figure 4-Charged and discharged state of lead acid batteries (black is charged and red is discharged) (Ref: 17)

The merits of lead-acid batteries include cheap manufacturing costs, high current capability, abuse tolerance and it is also tolerant to overcharging to certain extent. However, it is important to note that the charging and discharging takes place as a result of reaction between lead and sulfonate ions, in which one of the reactants is in solid state. Hence, when charging or discharging occurs, charge storage or removal will occur at the interface of the electrode and electrolyte and spreads diffusively throughout the volume of the electrode. So, the achievable capacity, largely depends on the time of charge or discharge. Since the kinetics involved are of second order, fast charging capability is difficult in the case of lead acid batteries. Furthermore, the charge discharge process involves water splitting and release of hydrogen gas, the risk of explosion is high in the case of these batteries<sup>17</sup>. Also, the utilization of lead-based electrodes poses a greater environmental problem during the disposal.

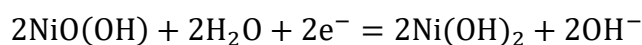
### 1.3.3a-ii Nickel cadmium batteries

Nickel-cadmium batteries are secondary batteries that use nickel oxide hydroxide and cadmium as electrodes and aqueous KOH as electrolyte<sup>18</sup>(schematic diagram is shown in Figure 5). The reaction during charging is as follows<sup>19,20</sup>:

At cadmium electrode:



At nickel oxide electrode:



Total reaction:

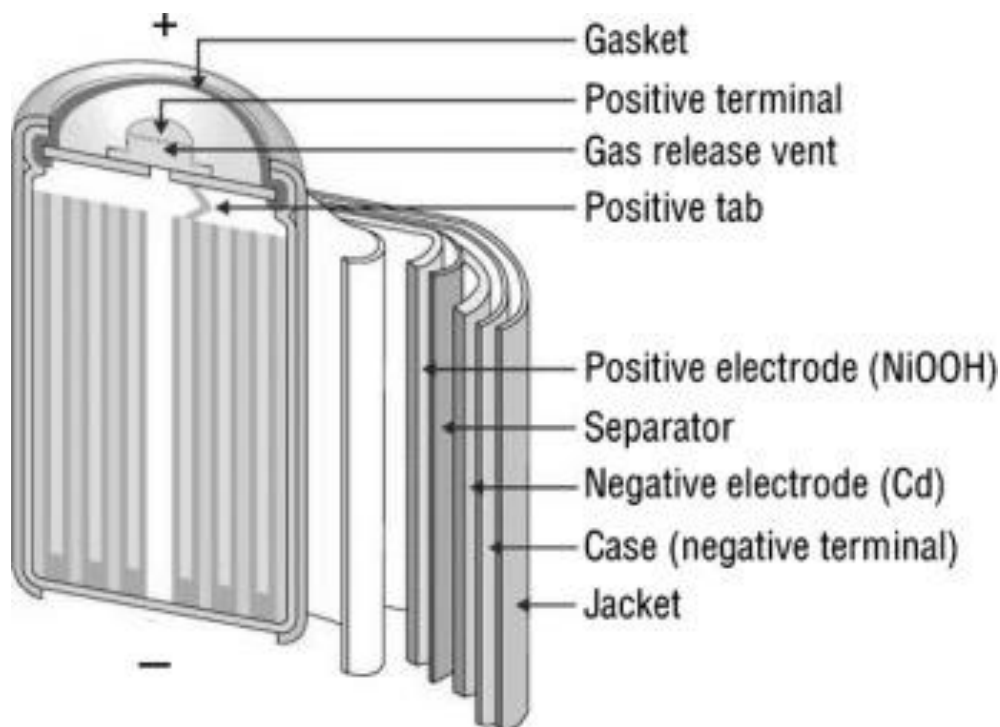
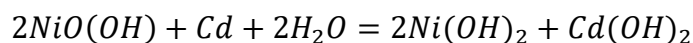
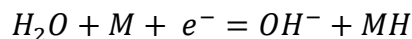


Figure 5-schematic representation of Ni-Cd battery (Ref: 21)

The advantages of these batteries include low maintenance, ability to maintain constant operating potential to a large number of cycles. However, utilization of cadmium metal as the anode raises serious concerns as it is a toxic heavy metal<sup>21</sup>. European union has banned the commercial usage of these batteries. To negotiate this problem, cadmium is replaced with a hydrogen absorbing alloy

and a variation of Ni-Cd battery called Nickel-metal hydride battery was introduced with NiOOH as positive electrode<sup>22</sup>. These batteries can have up to three times higher capacity than Ni-Cd batteries. The chemistry involved is largely similar to that of Ni-Cd battery<sup>23</sup>.

The reaction at negative electrode is:



The reaction at positive electrode is:



Here M is an intermetallic compound. The reaction proceeds from right to left during charge and opposite during discharge.

### **1.3.3a-iii Metal-ion batteries**

Alkali metal ion batteries ( $Li^+$ ,  $Na^+$ ,  $K^+$ ) are batteries that work based on the movement of alkali metal ions. Typically, an alkali metal ion battery consists of an anode, cathode, ion conducting electrolyte and an electrically insulating and ion conducting separator<sup>24</sup>. By the virtue of smaller size, the energy density is higher in case of lithium-ion batteries than in the case of sodium or potassium ion batteries. Furthermore, due to the smaller size of lithium ion, the kinetics are much faster in this case than in sodium and potassium ion batteries<sup>25</sup>. With these benefits, lithium-ion batteries are under immense research considerations for over 40 years till now.

## **1.4 Lithium-ion battery**

Lithium-ion battery is a battery that works based on intercalation and deintercalation of lithium ions. Lithium-ion batteries are considered to be the most promising technology to be used as the source of energy. This is due to the properties of lithium-ion battery like high volumetric power density, better ease of diffusion, supports wide range of host-guest chemistry. Because of these benefits, lithium-ion batteries are widely applied in portable electronic devices like mobile phones, wrist watches etc., Apart from these applications, lithium-ion batteries are also being explored for the potential application in electric vehicles. Electric vehicles powered completely by lithium-ion batteries are also introduced in the automobile market. However, research is yet to be matured on reducing the cost of lithium-ion battery production for electric vehicles and to reduce the weight of the battery without compromising on the power/energy density of the battery. Furthermore,

intense research is being conducted to optimize various other factors like SEI formation, solid state electrolyte etc., The various factors involved in lithium-ion battery fabrication are described in the following section.

### 1.4.1 Working mechanism of a lithium-ion battery

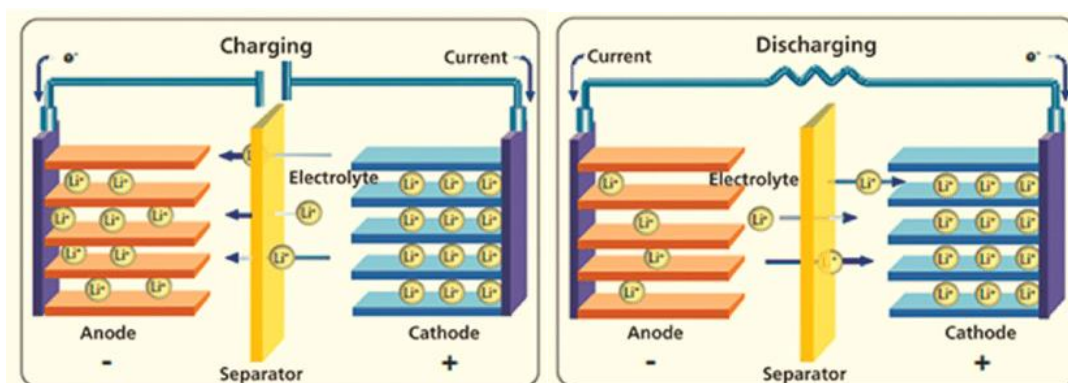
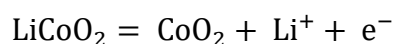


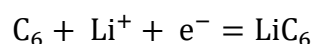
Figure 6-Mecahnism of charging and discharging of a lithium-ion battery (Ref: 29)

Figure 6 shows the illustration of charge-discharge process in a lithium-ion battery. In discharged state of a lithium-ion battery, lithium is stored in the cathode in the form of lithium transition metal oxide. When a potential is applied, lithium ions in the cathode migrate towards the anode, where they get intercalated or alloyed based on the nature of the active material. In general, graphite is the widely used anodic active material in lithium-ion battery. The mechanism of the charging when graphite is used as anode and  $\text{LiCoO}_2$  is used as cathode can be explained using the following equations<sup>26,27,28</sup>:

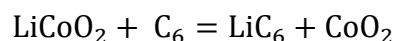
At cathode:



At anode:



Full reaction:



In case of discharge, reverse reaction (right to left takes place) i.e., lithium gets de-intercalated from graphite and migrates towards cathode through the ion conducting electrolyte accompanied

by the migration of electrons externally from anode to cathode across a load. The detailed discussion cathode, anode and electrolyte in a lithium-ion battery is presented in the following sections<sup>26</sup>.

### 1.4.2 Cathode

The first generation of lithium-ion batteries were fabricated using lithium metal as anode. Theoretically lithium anode can deliver a high reversible capacity of 3860 mAh/g<sup>29</sup>. Hence, much importance was given towards developing a suitable cathode material. Nearly, all the elements in the periodic table were researched upon to prepare prospective cathode materials. Based on the geometry of the materials, cathodic materials researched so far can be classified into the following categories<sup>30</sup>:

- a) Layered oxides
- b) Spinel oxides
- c) Polyanion oxides

#### 1.4.2a Layered oxides

In the context of cathodes, one might recall the cathode used in nickel cadmium battery i.e., NiOOH, in which proton can be reversible inserted and de-inserted. Replacement of proton in

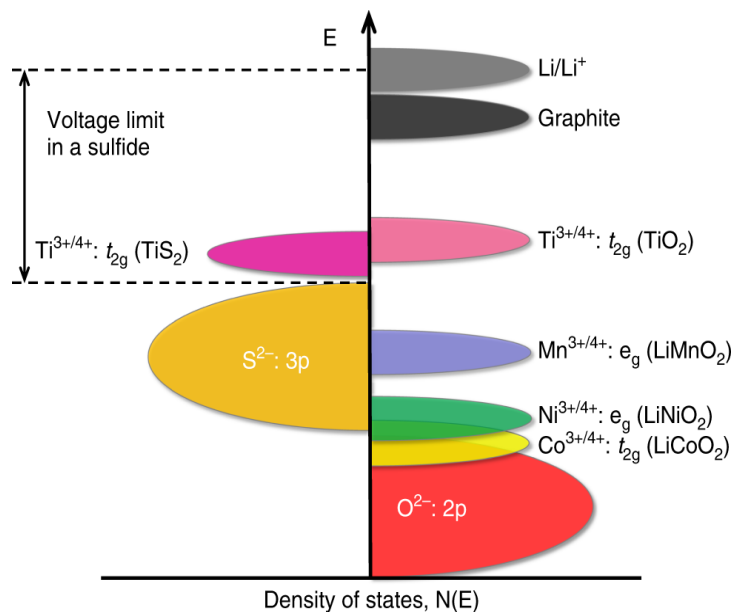


*Figure 7-Schematic representation of density of states of various cathodes (Ref:31)*

NiOOH with LiNiO<sub>2</sub> and analogous oxides of Mn and Co i.e., LiMnO<sub>2</sub>, LiCoO<sub>2</sub>. Though materials like Li<sub>x</sub>TiS<sub>2</sub> were investigated for cathodic applications, comparatively lower electronic



conductivity of sulfides than oxides, make oxides a better choice. Besides electrical conductivity, one more important factor that limits the application of sulfide materials is the fact that, higher  $V_{oc}$  can be achieved using oxides than sulfides. This can be explained using an illustrative example of spinel  $\text{LiMnO}_2$  cathode (where in 1:1  $\text{Mn}^{4+}$ :  $\text{Mn}^{3+}$  ions are octahedrally placed) in aqueous electrolyte provided by Goodenough et al. The valence band of sulfide anion is energetically higher than  $\text{Mn}^{4+}/\text{Mn}^{3+}$  redox couple i.e., the fermi energy of the total material is higher than the standard potential of the  $\text{Mn}^{4+}/\text{Mn}^{3+}$  redox couple and it also lies above the HOMO of the aqueous electrolyte. This restricts the realization higher operating potentials. In the case of oxides, the valence band of oxides is energetically lower than the  $\text{Mn}^{4+}/\text{Mn}^{3+}$  redox couple i.e., the fermi energy of the total material is equal to the standard potential of the  $\text{Mn}^{4+}/\text{Mn}^{3+}$  redox couple. Hence, it is possible to place the  $\text{Mn}^{4+}/\text{Mn}^{3+}$  redox couple above the HOMO of electrolyte in case of oxides<sup>30</sup>. Figure 7 shows the comparison of the energies of the various cathode materials. From Figure 7, it is also evident that the standard potential of  $\text{Li}/\text{Li}^+$  is much higher than the cathodic materials. Also, in comparison between various cathode materials,  $\text{Co}^{4+}/\text{Co}^{3+}$  couple seems to have lowest standard potential that enables higher working potentials.  $\text{LiCoO}_2$  also offers good structural stability along with good electrical and ion conducting properties. Furthermore, it was observed that the operating voltage of  $\text{LiCoO}_2$  can be greater than 4 V<sup>31</sup>. Perhaps,  $\text{LiCoO}_2$  happens to be the first successful material that enabled lithium free anode, since the cathode has innate lithium ions. Motivated by the success of  $\text{LiCoO}_2$ , various other layered oxides with Sc, Ti, V, Cr, Mn, Fe, Co, Ni, Cu metal ions were prepared (general structure of layered oxides is shown in Figure 8). Even among these layered oxides,  $\text{LiCoO}_2$  was found to be better in terms of ease of synthesis, low polarization etc.,<sup>32</sup> However, it is important to note that despite the various benefits like high electrical conductivity and good lithium-ion conduction of  $\text{LiCoO}_2$ , the high cost of cobalt and low chemical stability led to exploration of various other cathodic materials<sup>33</sup>. The low chemical stability of  $\text{LiCoO}_2$  arises from the fact that the standard potentials of cobalt ions and oxygen ions overlap as shown in Figure 7 suggesting that the redox process of the cobalt during charge-discharge process also effects the redox activity of oxygen anions leading to chemical instability of the cathode. To overcome these drawbacks,  $\text{LiNi}_{1-y-z}\text{Mn}_y\text{Co}_z\text{O}_2$  (LiNMC) type cathode materials with multiple metal ions was developed. Cobalt based oxides have high electrical conductivity and structural stability whereas manganese-based oxides have low electrical conductivity and structural stability<sup>34</sup>. The low structural stability of manganese oxides arises from

the lower octahedral site stabilization energy that allows Mn ions to migrate from octahedral sites in the metal plane to the octahedral sites in lithium plane leading to a change in geometry from

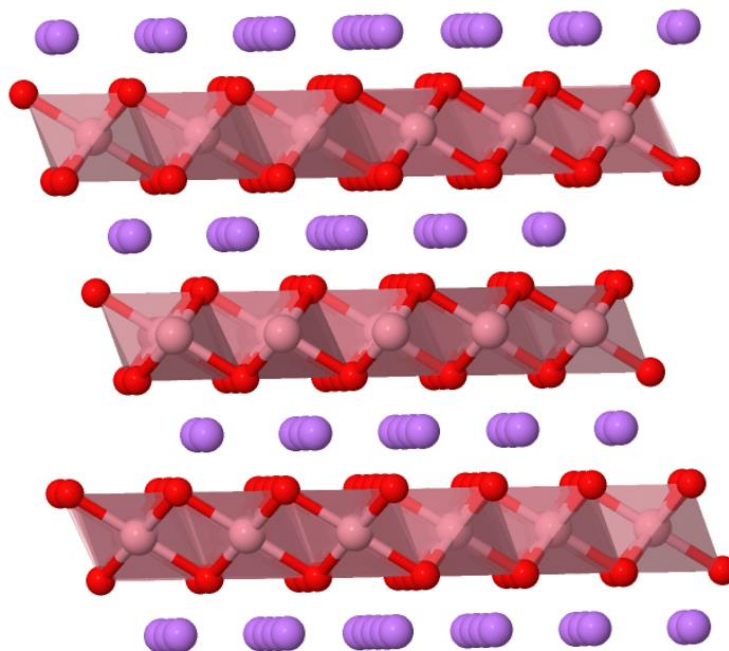


*Figure 8-Illustration of layered oxides. (Pink color indicates transition metals: Co, Mn, Ni; red indicates oxygen and violet indicates lithium) (Source: Chem Tube 3D)*

layered to spinel geometry. Nickel oxides have intermediate properties to these two materials. Also, the standard potential of  $\text{Ni}^{4+}/\text{Ni}^{3+}$  is intermediate to both  $\text{Mn}^{4+}/\text{Mn}^{3+}$  and  $\text{Co}^{4+}/\text{Co}^{3+}$  and the octahedral site stabilization energy of nickel oxides is intermediate to that of manganese and cobalt. Hence, efforts are directed towards increasing the Ni content in  $\text{LiNi}_{1-y-z}\text{Mn}_y\text{Co}_z\text{O}_2$  (LiNMC) type cathode<sup>35</sup>.

### 1.4.2b Spinel oxides:

Followed by layered oxides as mentioned above, research efforts were directed towards developing low cobalt containing, spinel oxides. Goodenough et al., have demonstrated spinel  $\text{LiMn}_2\text{O}_4$ , in which magnesium ions occupy octahedral sites and lithium ions occupy tetrahedral sites of the spinel network. This arrangement of the  $\text{LiMn}_2\text{O}_4$  allows three-dimensional diffusion pathway for lithium ions<sup>36</sup> (Structure of  $\text{LiMn}_2\text{O}_4$  is shown in Figure 9). The key advantage that  $\text{LiMn}_2\text{O}_4$  has over  $\text{LiCoO}_2$  is that the cost of production is much lesser in the case of  $\text{LiMn}_2\text{O}_4$ <sup>37</sup>. Further,

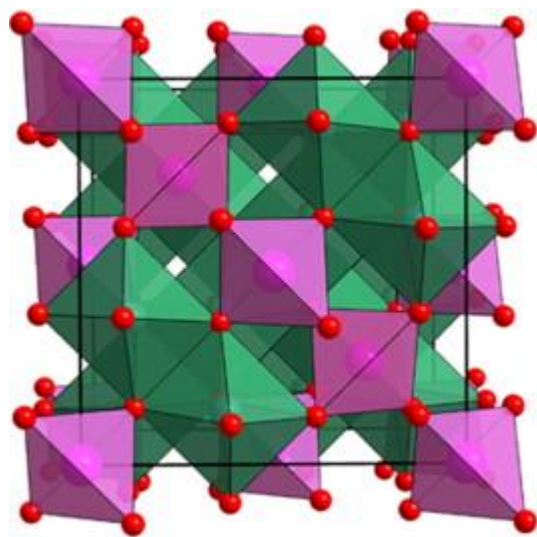


Figure 9-Illustration of  $\text{LiMn}_2\text{O}_4$  spinel oxide (Ref:38)

$\text{LiMn}_2\text{O}_4$  also possess better structural stability and high electrical conductivity and hence gives the scope for fast charging and discharging property. However, one key disadvantage with these materials is the dissolution of Mn in electrolyte if the electrolyte has trace number of protons (i.e., if the electrolyte is slightly acidic). The dissolution of Mn, besides disturbing the integrity of the cathode, causes migration of Mn towards anode which poisons graphite and leads to poor cycle life. The spinel oxides are known only with Ti, V and Mn<sup>38,39</sup>.  $\text{LiTi}_2\text{O}_4$  has very low operating voltage (~1.5 V) which limits the practical application.  $\text{LiV}_2\text{O}_4$  undergoes huge structural changes and has a low operating voltage of ~3 V. Hence,  $\text{LiV}_2\text{O}_4$  too doesn't support practical application<sup>40</sup>.

#### 1.4.2c Polyanion oxides:

Manthiram et al., investigated the function of polyanion oxides. Polyanion oxides are compounds with more than one anion present in the oxide.  $\text{Fe}_2(\text{MoO}_4)_3$ ,  $\text{Fe}_2(\text{WO}_4)_3$  type oxides were synthesized and were found to undergo lithium insertion either chemically or electrochemically yielding  $\text{Li}_2\text{Fe}_2(\text{MoO}_4)_3$  or  $\text{Li}_2\text{Fe}_2(\text{WO}_4)_3$ <sup>41</sup>. The advantage of employing such  $\text{Fe}_2(\text{XO}_4)_3$  type oxides where X can be Mo, W or S is, the octahedral  $\text{FeO}_6$  share the corner of octahedron with the tetrahedral  $\text{XO}_4$  leading to a extended -O-Fe-O-X-O-Fe-O- linkage. The strong covalency of bond between X and O weakens the covalent bond strength between Fe and O through inductive effect compared to the simple  $\text{Fe}_2\text{O}_3$ , leading to the lowering of  $\text{Fe}^{2+}/\text{Fe}^{3+}$  redox energy and thus increases the operating voltage<sup>42</sup>. It was observed that the operating voltage in case of  $\text{Fe}_2(\text{MoO}_4)_3$ , (the discharge potential) was around 3 V which is 0.5 V higher than  $\text{Fe}_2\text{O}_3$ . Exploration of molybdate,

sulphate and phosphate-based polyanion oxides yielded  $\text{LiFePO}_4$  as effective cathode material<sup>39</sup>. On similar lines, polyanion oxides were also found to be effective cathodes in sodium ion batteries too<sup>43</sup>.

### 1.4.3 Electrolyte:

Electrolyte in a lithium-ion battery is a lithium conducting and electron insulating material that facilitates lithium movement from cathode to anode and vice versa. The following are the desirable properties for a lithium-ion battery electrolyte<sup>44</sup>:

1. High lithium-ion conductivity
2. Thermal and chemical stability
3. Must support higher potential window
4. Nontoxicity and cost effectiveness
5. Low reactivity with cathode and anode

The electrolytes used for lithium-ion batteries or under scrutiny for possible applications in lithium-ion batteries can broadly be classified into the following categories<sup>45</sup>:

- a) Non aqueous electrolytes
- b) Aqueous electrolytes
- c) Ionic liquid electrolytes
- d) Polymer electrolytes

#### 1.4.3a Non aqueous electrolyte

Non aqueous electrolyte consists of a lithium salt dissolved in organic solvent or a mixture of organic solvents. Alkyl carbonates are commonly used solvents as electrolyte solvents. Linear alkyl esters like dimethyl carbonate (DMC), diethyl carbonate (DEC) are low viscous solvents with relatively lower permittivity arising from the higher degrees of freedom in the linear chains. On the other hand, cyclic esters like ethylene carbonate, propylene carbonate have high permittivity but are highly viscous (Figure 10 shows the structure of cyclic and linear cyclic esters). Hence, generally a combination of cyclic esters and linear esters are used in lithium-ion batteries<sup>46</sup>. Besides solvent, lithium salts with monovalent anions are preferred as electrolytes because of the higher degree of dissociation and better mobility. To support better mobility and dissociation, anions with moderate size are preferred. Thus, salts like  $\text{LiClO}_4$ ,  $\text{LiPF}_6$ ,  $\text{LiAsF}_6$ ,  $\text{LiBF}_4$  were

considered as suitable electrolytes. Lately, anions like trifluoromethanesulfonyl imide (TFSI), fluoromethanesulfonyl imide (FSI) are also being researched upon as electrolytes owing to better dissociation of salts, high solubility and possess a wide potential window<sup>47</sup>.

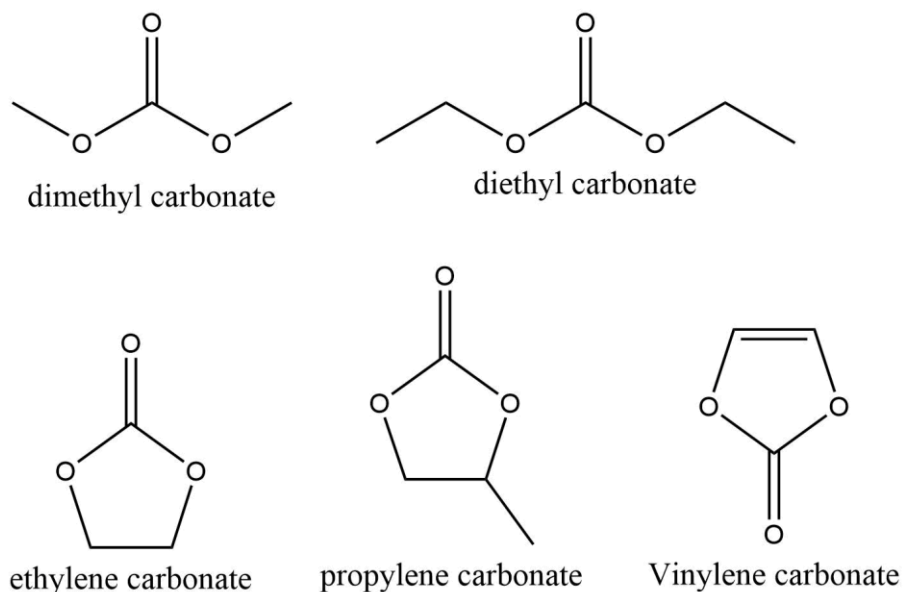


Figure 10-structure of linear and cyclic esters used as solvents in lithium-ion battery electrolyte

### 1.4.3b Aqueous electrolytes

The issue of flammability offsets the benefits mentioned in the previous section about organic electrolytes. Hence, using aqueous electrolytes with better ionic conductivity and transference number are most enticing materials for battery applications<sup>48</sup>. Dahn et al., demonstrated the first aqueous electrolyte for lithium-ion battery using  $\text{LiNO}_3$ . However, the cyclability was observed to be very poor owing to the low potential window of water ( $<1.23$  V). Since then, much research is being carried out towards developing aqueous electrolytes. Recently, a new water in salt type electrolyte was reported. This is obtained by preparing a very high concentration (molarity  $> 20$  m) Lithium bis(trifluoromethanesulfonyl)imide solution in water. These electrolytes can extend the potential window up to  $3.0$  V<sup>49</sup>.

### 1.4.3c Ionic liquid electrolytes

Ionic liquid electrolytes consist of a lithium salt dissolved in ionic liquids. The key advantage of using ionic liquid-based electrolytes is, they are non-volatile and non-flammable liquids. Hence, they are much safer compared to the organic solvents. Figure 11 shows the structures of various anions and cations of ionic liquids. They also exhibit good chemical stability and high solubility

of organic and inorganic compounds<sup>50</sup>. However, these materials also have high viscosities and hence low ionic conductivity. The cost of ionic liquids is also much higher than organic solvents.

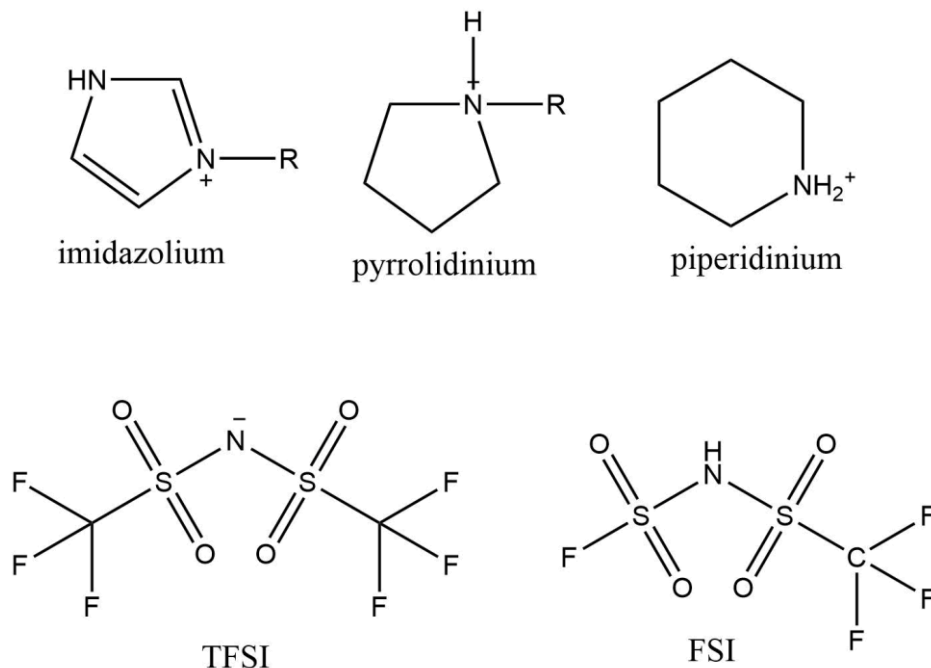


Figure 11-Structures of various anions and cations of ionic liquids

Ionic liquids have a variety of anions and cations. The commonly used anions are  $\text{PF}_6^-$ ,  $\text{BF}_4^-$ , TFSI<sup>-</sup>, FSI<sup>-</sup> and the cations used are imidazolium, phosphonium, quaternary ammonium, pyrrolidinium, piperidinium etc.,<sup>51</sup>

#### 1.4.3d Polymer electrolytes

Polymer electrolytes can be classified into:

- i. Solid polymer electrolyte.
- ii. Gel polymer electrolyte.

##### 1.4.3d-i Solid polymer electrolyte

Solid polymer electrolyte is an electrolyte consisting of a polymer and a lithium salt. Commonly poly (ethylene oxide) is the polymer used for solid polymer electrolyte application. Poly (ethylene oxide) conducts lithium ions when complexed with lithium ion. Solid polymer electrolytes such as poly (ethylene oxide) have high structural stability, can avoid lithium dendrite formation and are nonflammable. However, the ionic conductivity of these materials was observed to be very poor. To negotiate this problem, various lithium salts like LiTFSI, LiFSI,  $\text{LiClO}_4$  were added to

the electrolyte mixture<sup>45</sup>. Even after such addition, the ionic conductivity obtained was in the order of  $10^{-4}$  S/cm. Research efforts are directed towards improving the ionic conductivity of solid polymer electrolytes. In this regard, Archer et al., found that the addition of ceramic particles like  $\text{SiO}_2$ ,  $\text{Al}_2\text{O}_3$ ,  $\text{Fe}_3\text{O}_4$ ,  $\text{TiO}_2$  to polymer electrolytes can increase the ionic conductivity and improve the mechanical stability<sup>45</sup>.

#### **1.4.3d-ii Gel polymer electrolyte**

Gel polymer electrolyte consists of a polymer dissolved and lithium salt dissolved in a solvent (typically ionic liquid). Poly (vinylene difluoride) (PVDF) is the most commonly used polymer in gel polymer electrolyte. PVDF based gel polymer electrolytes are stable in anodic conditions due to the strongly electron withdrawing C-F functional group present in PVDF. Gel polymer electrolytes are also nonvolatile, stable till high temperatures and are nonflammable. However, poor mechanical strength and low interfacial stability towards lithium metal are the key drawbacks of gel polymer electrolyte<sup>52</sup>. Poly (methyl methacrylate) is also used as an additive in gel polymer electrolyte with PVDF. The addition of PMMA was found to improve the pore size, porosity, and electrolyte uptake of the PVDF containing electrolyte and thus the ionic conductivity of the electrolyte is improved<sup>53</sup>. Poly(acrylonitrile) is also used for gel polymer electrolyte. It offers good mechanical strength, heat resistance, chemical stability, and non-flammability. However, the interface stability is poor.

The advantages and disadvantages of each class of electrolyte is discussed briefly. The choice of electrolyte largely depends on the required application of the lithium-ion battery and the electrode active material choice in the battery.

#### **1.4.4 Anode**

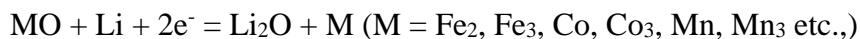
During the initial phase of lithium-ion battery development, lithium metal was used as anode. Lithium metal anode can deliver a high theoretical capacity of 3860 mAh/g, which is the highest among known anode materials at room temperature. However, the interaction between lithium metal and the known organic polar aprotic solvents produces a dense surface film leading to the formation of insufficient surface passivation layer. Hence, during the charge discharge process, lithium dendrites form over the lithium metal anode leading to short circuit of the cell. Owing to this draw back, lithium-ion battery with lithium anode has not seen the phase of commercialization<sup>35</sup>. The prospect of highly beneficial applications of lithium-ion battery led

researchers to experiment on various anodic materials. Broadly, the anodic materials used currently in lithium-ion battery can be classified as following<sup>54</sup>:

- a) Conversion type anodes.
- b) Alloy type anodes.
- c) Intercalation type anodes.

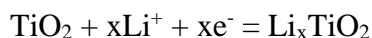
#### 1.4.4a Conversion type anodes

Transition metal oxides like Fe<sub>2</sub>O<sub>3</sub>, Fe<sub>3</sub>O<sub>4</sub>, CoO, Co<sub>3</sub>O<sub>4</sub>, TiO<sub>2</sub> etc., have a high theoretical capacity of 500 – 1000 mAh/g. The cyclic performance of these materials was also observed to be good. Fe<sub>2</sub>O<sub>3</sub> (hematite), Fe<sub>3</sub>O<sub>4</sub> (magnetite) have a theoretical capacities of 1007 mAh/g and 926 mAh/g respectively and hence are widely used as anodic materials. CoO, Co<sub>3</sub>O<sub>4</sub> have a theoretical capacity of 716 mAh/g and 890 mAh/g respectively. The general mechanism of lithium storage for these oxides is as follows:



Analogous transition metal sulfides like MoS<sub>2</sub>, FeS<sub>2</sub>, CoS<sub>2</sub>, SnS also displayed good lithium storage properties. These materials too have higher theoretical capacities. Among the transition metal sulfides, MoS<sub>2</sub> displays interesting lithium storage properties yielding capacities in the range of 800-1000 mAh/g.

Apart from the metal oxides and metal chalcogenides discussed above which exhibit conversion type mechanism, TiO<sub>2</sub> displays insertion type mechanism of lithium storage. The theoretical capacity of TiO<sub>2</sub> (~330 mAh/g) is lower than other transition metal oxides. But the structural stability improves after lithium-ion insertion. TiO<sub>2</sub> also exhibits minimum volume change during the charge-discharge process (~3%). Furthermore, TiO<sub>2</sub> based materials also support fast charging. The redox reaction can be expressed as follows:



In spite of these benefits, transition metal oxides suffer with the disadvantages of poor electrical conductivity, higher cost of production, electrode powdering due to large volume change in cases of iron and cobalt oxides and electrolyte decomposition because there is no formation of surface



passivation layer in this case. Hence research is now being directed towards optimizing the performance of transition metal oxides by overcoming the problems listed above.

#### 1.4.4b Alloy type anodes

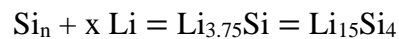
Alloy type anodes are metals or metalloids that can form alloy with lithium. The commonly used metals or metalloids for alloying anodes are Si, Sn, Ge. Sn is a metal and undergoes addition reaction. The reaction mechanism can be explained as follows:



The theoretical capacity of Sn anode is 993.4 mAh/g. From the above equation, it can be understood that Sn undergoes huge volume expansion during lithiation and delithiation. This will cause deformation of electrode material, decomposition of electrolyte. Hence, despite of the high theoretical capacity, Sn based anodes are yet to be completely optimized.

##### 1.4.4b-i Silicon

Silicon has a theoretical specific capacity of 3650 mAh/g at room temperature and 4200 mAh/g at higher temperatures. Among the known anode materials except lithium metal, silicon has the highest theoretical capacity. The lithiation process of silicon anode can be described as follows:



During lithiation, crystalline Si gradually converts into amorphous  $\text{Li}_{3.75}\text{Si}$  and then to crystalline  $\text{Li}_{15}\text{Si}_4$ . Reverse of this process happens during delithiation. As one can anticipate, the lithiation and delithiation process involves a huge volume change<sup>55</sup> (~320%) (Figure 12). During the first intercalation of silicon, an interphase between crystalline silicon and amorphous silicon is formed. As the crystalline  $\text{Li}_{15}\text{Si}_4$  component increases, it causes stress on the amorphous  $\text{Li}_{3.75}\text{Si}$  component. This stress keeps accumulating and slows down the lithium insertion process. This

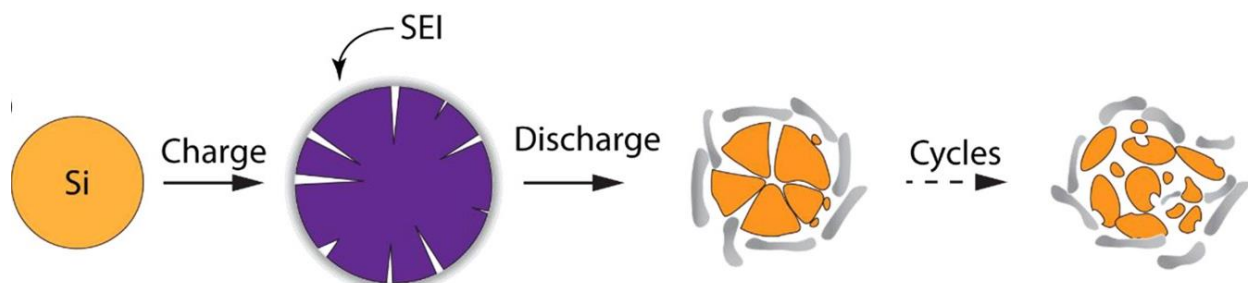


Figure 12-Volume expansion in silicon (Ref: 56)

behavior is observed only in the first lithiation because, after first cycle Si-Si bond break and causes cracks or fractures in the silicon particle making the material amorphous in nature. This behavior makes the application of silicon anode very difficult as during the cracking or fracture of silicon particle leads to exposure of new electrode surfaces to electrolytes causing the formation of new SEI layer. As this process takes place repeatedly, much electrolyte is consumed in the formation of SEI, and it is accompanied by huge irreversible capacity loss due to consumption of lithium in SEI formation. To negotiate this issue various strategies for designing the morphology of the active material, synthesizing a suitable polymeric binder etc., are being experimented upon.

#### **1.4.4b-ii Germanium**

Ge belongs to the same group as silicon and exhibit similar lithium storage properties. Though Ge is a semiconductor, the conductivity of Ge is better than silicon. Ge exhibits similar volume expansion behavior as silicon. Being a rare metal, utilizing Ge as anode involved high cost.

#### **1.4.4c Carbon based materials**

Carbon based anodes especially, graphite are the most successful anode materials in lithium-ion battery. Most of the commercially available lithium-ion batteries consist of graphite anode (Figure 13b). The attempts to use graphite as anode started in 1976. However, graphite caused decomposition of the commonly used electrolyte solvent at time (propylene carbonate). Touzain et al., have first demonstrated the successful utilization of graphite anode in lithium-ion battery using a solid-state electrolyte<sup>54</sup>. Meanwhile Akira Yoshino demonstrated carbonaceous material derived from petroleum coke as anode material for lithium-ion battery<sup>56</sup>. They could also commercialize the first commercial lithium-ion battery. In 1990 Dahn et al., have demonstrated the first successful intercalation and deintercalation of lithium ions in graphite using ethylene carbonate liquid electrolyte<sup>57</sup>. No decomposition of ethylene carbonate was observed because of the formation of stable solid electrolyte interphase (SEI) on the surface of graphite. Subsequently, a mixture of ethylene carbonate and dimethyl carbonate was employed as electrolyte solvent mixture. The general charge storage in graphite anode was shown to be  $\text{LiC}_6$  i.e., one lithium per six  $\text{sp}^2$  carbon atoms<sup>26</sup>. Thus, the theoretical capacity of graphite anode is 372 mAh/g, which is considered to be less for high energy applications and graphite anode undergoes anodic polarization during fast charging process which limits its application in devices requiring fast charging. Despite of this disadvantage, graphite continues to be the leading anode material in

lithium-ion battery. To improve the specific capacity of the anode material, various morphological changes were brought out. In this regard, various one dimensional, two dimensional and three-dimensional carbon materials were prepared. Carbon nano tubes (single wall and multi wall) (Figure 13c) are well known allotropes of carbon<sup>58</sup>. CNTs were used as anodic materials owing to the high conductivity and large surface area. The charge storage in CNT anodes was found to be  $\text{LiC}_2$ . Zhao et.al., have demonstrated a lithium storage capacity of 1116 mAh/g. Though CNTs exhibit high lithium storage, it also suffers with irreversible capacity loss and thus leads to lower coulombic efficiency<sup>59</sup>. Graphene based materials (two dimensional) were also investigated for the anodic applications. The high surface area of over  $2630 \text{ m}^2/\text{g}$ , relatively high conductivity and good mechanical properties are some of the advantages in utilizing graphene-based anodes (Figure 13a). The charge storage in graphene is  $\text{LiC}_3$  i.e., one lithium ion per three  $\text{sp}^2$  carbons. The high surface area of graphene causes agglomeration between graphene layers and thus reduce the effective surface area leading to the reduction in capacity<sup>60</sup>. Apart from these three-dimensional structures with varying porosity are also being experimented as anodic materials (Figure 13d). Various works on utilizing hollow carbon nano spheres<sup>61</sup>, porous carbonaceous materials<sup>62</sup>, heteroatom doped carbonaceous materials were reported<sup>63</sup>. Such morphological changes lead to

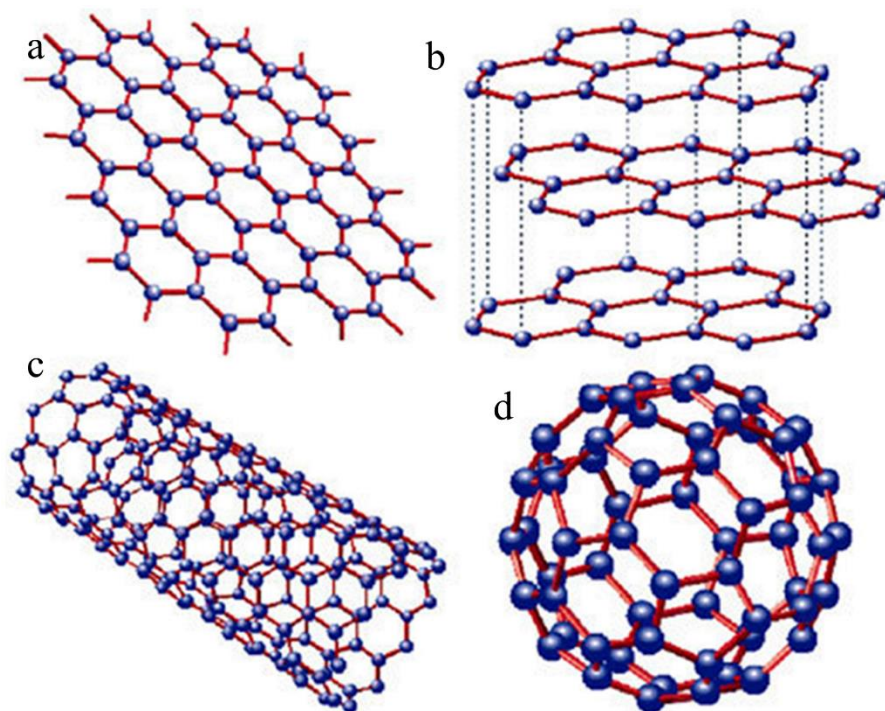


Figure 13-Structrures of various allotropes of carbon (Ref: 59)

overcoming the disadvantages of low specific capacity and incapability of fast charging in graphitic material. Research is still under progress to optimize a suitable carbonaceous structure for anodic applications supporting fast charging and which offers a higher reversible capacity. In this context, various works on utilizing organic molecules as anodic materials were reported, which store lithium ions partly by intercalation mechanism and partly by surface controlled pseudocapacitive mechanism. Ruoff et al., have demonstrated a triazine based active material for anodic applications. The triazine framework exhibited a high reversible capacity of 1200 mAh/g at 300 mA/g current density<sup>64</sup>. Wang et al., demonstrated a COF coated CNT as anodic material in lithium-ion battery. The COF-CNT composite delivered a reversible capacity of 1021 mAh/g at 100 mA/g current density<sup>65</sup>. Zhao et al., have demonstrated a different strategy of doping nitrogen in carbonaceous material. The N-doped carbon delivered a very high reversible capacity of 1253 mAh/g<sup>66</sup>. These reports show the wide range of possibilities towards improving the performance of intercalation type materials. This thesis too partially focuses on the optimization of carbonaceous materials for lithium-ion battery anode applications. Details of which will be discussed in subsequent chapters.

#### 1.4.5 Binder materials:

Binders are materials that provide mechanical support to the electrode material by providing adhesion between the current collector and the active material. Besides this, a binder is also

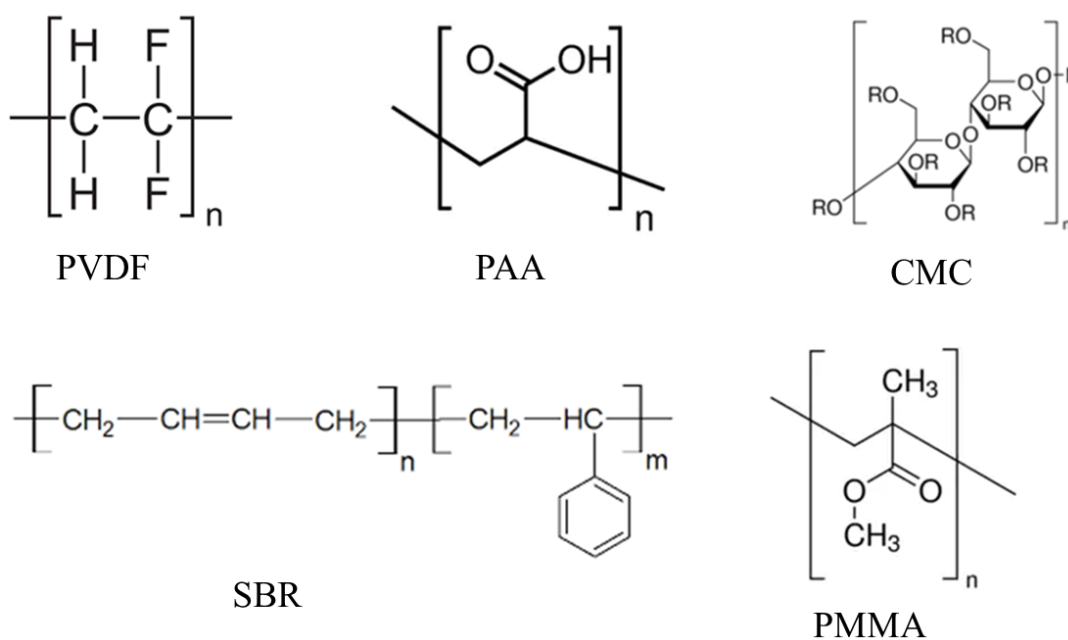


Figure 14-Structures of various binders used in lithium-ion batteries

expected to maintain good adhesion among the active material itself. Generally, polymers like poly (vinylene difluoride) (PVDF)<sup>67</sup>, poly (acrylic acid) (PAA), carboxy methyl cellulose (CMC), styrene-butadiene rubber (SBR), poly (methyl methacrylate) (PMMA) etc., are commonly used binders<sup>67,68,69,70,71</sup> (Figure 14). Each of the above-mentioned binders have their advantages and disadvantages. The choice of binder largely depends on the type of active material chosen. However, it is important to note that all the above-mentioned binders are non-conducting in nature. Hence, much research is being conducted towards developing a conducting binder. Though, the electron conduction of binder is not mandatory, it is hypothesized that a conducting polymer would have a low lying LUMO and hence restricts excessive reduction of electrolyte on the electrode surface leading to a thinner SEI<sup>72</sup>. However, special attention must be given to the flexibility of the polymer, as rigid polymers are found to have insufficient binding abilities in case of materials like silicon and tin. Solubility is also an important factor for a prospective polymer to be used as a binder. The polymer should have sufficient solubility in commonly used organic solvents<sup>73</sup>.

## **1.5 Electrochemical techniques used in characterization of lithium-ion batteries:**

In this section a brief introduction to the basic electrochemical techniques i.e., cyclic voltammetry, impedance spectroscopy and galvanostatic charge-discharge study used in the context of lithium-ion batteries would be presented.

### **1.5.1 Cyclic voltammetry**

Electrochemistry deals with the study of flow of electrons leading to chemical changes and vice versa. Cyclic voltammetry is an electrochemical technique that reflects a current response due to

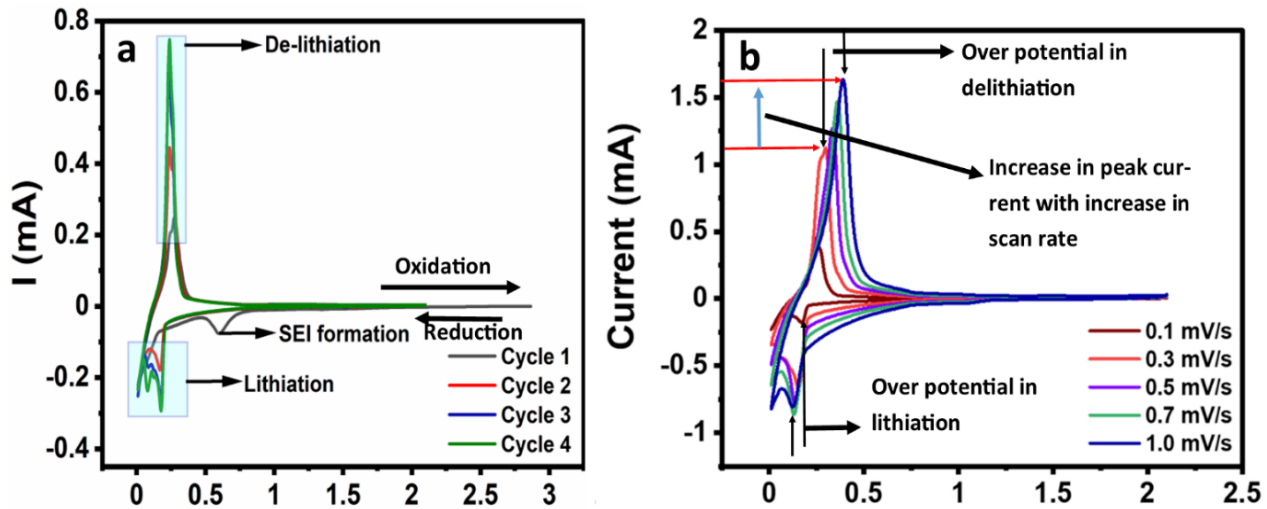


Figure 15-a) Cyclic voltammogram indicating the SEI formation, lithiation and delithiation of graphite anode b) Cyclic voltammograms at different scan rates indicating overpotential and scan rate dependence of peak current (Ref: 76)

a redox process arising from a cyclic potential sweep between two potential points<sup>74</sup>. In a lithium-ion battery, redox processes involved are lithiation and delithiation of anode and cathode, For example, lithiation/delithiation of graphite leads (accompanied by flow of electrons) occurs at a certain potential (~0.2-0.4 V). Cyclic voltammetry helps in determining the exact potential at which lithiation or delithiation occurs. Figure 15 a and b show illustrative example of cyclic voltammogram of lithium-ion anodic half-cell with graphite anode<sup>75</sup>.

In Figure 15a, the peaks in the reduction half at 0.2 V and 0.02 V correspond to the formation of  $\text{LiC}_{12}$  and  $\text{LiC}_6$  respectively. In the oxidation half, peaks at 0.25-0.4 V correspond to the delithiation of anode. An important factor to be considered in cyclic voltammetry is the scan rate. Scan rate refers to the potential sweep per unit time<sup>75</sup>. Figure 15b depicts the cyclic voltammogram at various scan rates. Faster scan rates cause polarization in the anode and leads to the deviation of anode from ideal behavior i.e., the potential at which the redox reaction has to take place would shift to a higher potential. This difference between the potential at which the redox reaction should take place ideally and the potential at which the reaction took place is called the overpotential. High overpotential is not desired as it causes lower voltage efficiency. Further, the intensity of peak current is proportional to the scan rate. The relation between peak current and scan rate is given by Randles-Sevcik equation<sup>1</sup>:

$$i = 2.69 * 10^5 n^{1.5} D^{0.5} A C \nu^{0.5} \dots \dots \dots \textcircled{7}$$

Where,  $i$  is peak current,  $n$  is number of electrons or ions transferred,  $D$  is diffusion coefficient,  $A$  is area of the electrode,  $C$  is concentration of electrolyte and  $\nu$  is scan rate. The lithium-ion diffusion coefficient of a material can be evaluated using this equation. Considering these merits of cyclic voltammetry, it is used for the initial redox characterization of anodic materials in this thesis.

### 1.5.2 Electrochemical Impedance spectroscopy (EIS)

Impedance is the ability of a circuit to resist the flow of current in an alternating current flow. Unlike resistance, impedance considers the factors like inductance and capacitance. The popular ohms law is valid only in the case of an ideal resistor. However, in a complex circuit, ohms law doesn't stand good<sup>76</sup>. In an impedance measurement, AC potential is applied which is a function of frequency. Depending on the various electrochemical processes occurring at different frequencies, current response is measured. The ratio of potential and current response gives the impedance value at the particular frequency or in a frequency range.

The potential as a function of frequency can be described as<sup>77</sup>:

$$V = V_o e^{i\omega t} \dots\dots\dots (8)$$

Where,  $V$  is time dependent potential,  $\omega$  is frequency,  $t$  is time and  $i$  is imaginary number.

Current response is given by:

$$I = I_o e^{i\omega t - \Phi} \dots\dots\dots (9)$$

Where,  $I$  is current and  $\Phi$  is phase difference (if present) between current and potential.

Therefore, the impedance can be described as:

$$Z = \frac{V}{I} = \frac{V_0 e^{i\omega t}}{I_0 e^{i\omega t}} \dots\dots\dots (10)$$

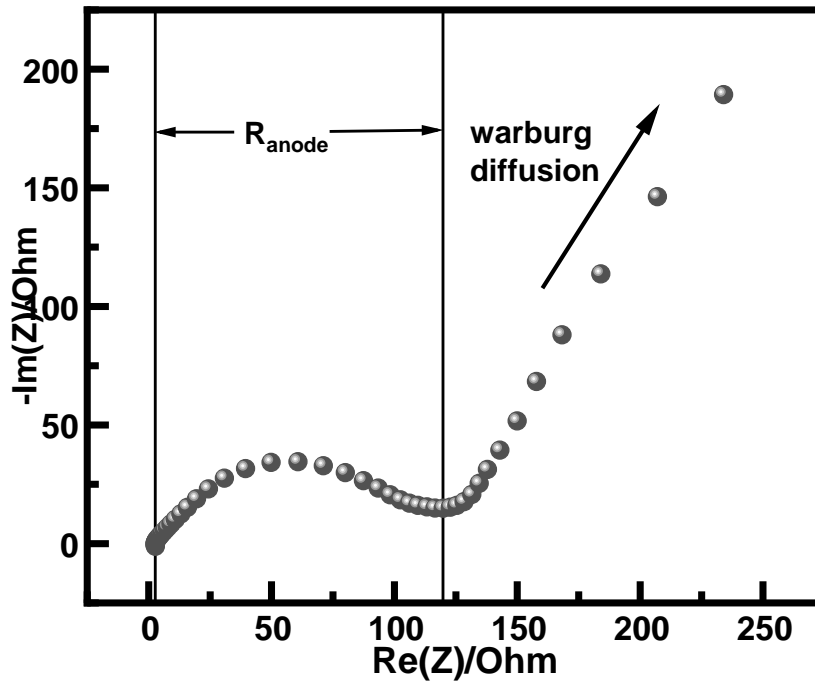


Figure 16-Illustrative example of an EIS spectrum

$$\Rightarrow Z = Z_0 [\cos(\omega t) + i \sin(\omega t)] \dots\dots\dots (11)$$

$$\Rightarrow Z = Z' + Z'' \dots\dots\dots (12)$$

Where,  $Z'$  ( $= Z_0 \cos(\omega t)$ ) is real impedance and  $Z''$  ( $= Z_0 i \sin(\omega t)$ ) is imaginary impedance.

In the context of lithium-ion batteries, impedance measurement is important because, it aids the determination of resistance due to the electrolyte, resistance at the electrode-electrolyte interface, charge-transfer process, Warburg factor etc., Unlike ideal ohmic resistors, capacitance and inductance are frequency dependent. The impedance contribution from capacitor is inversely proportional to frequency and the impedance contribution from inductance is directly proportional to frequency. Figure 16 shows a typical impedance spectrum of an anodic half-cell.

Depending on the constituents of lithium-ion battery, various combinations of the following elements are possible<sup>78</sup>:



Table 3-Description of standard circuit elements

Element	Description
Resistor (R)	Can arise from the electrolyte solution, charge transfer
Capacitor (C)	Can be due to the double layer formed at electrode-electrolyte interface, due to high surface area of the active material. Impedance contribution = $(i\omega C)^{-1}$
Inductance (L)	Inductive effects during the diffusion of lithium-ions. Impedance contribution = $i\omega L$
Constant phase element (Q)	Describes non ideal capacitor (if the surface is irregular or the electrode-electrolyte surface is irregular, or the current distribution is non uniform). Impedance contribution = $(i\omega C)^{-\alpha}$ , $0.5 \leq \alpha \leq 1$
Warburg impedance (W)	$W = \frac{1}{\sqrt{\omega}}(1 - i)\sigma$ ; where $\sigma$ is Warburg factor. Warburg impedance arises from the diffusion of oxidized or reduced species.

By constructing a circuit with appropriate combination of the above-mentioned circuit elements, the impedance from each electrochemical process can be estimated. Furthermore, the Warburg-impedance can be used to estimate the lithium-ion diffusion from the following formula:

$$\sigma = \frac{RT}{n^2 F^2 A \sqrt{2D}} \left( \frac{1}{C_o} + \frac{1}{C_r} \right) \dots \dots \dots (13)$$

Where, R is universal gas constant, T is temperature, n is number of electrons transferred, F is faraday's constant, A is the surface area of electrode, D is diffusion coefficient,  $C_o$  is concentration of oxidized species and  $C_r$  is concentration of reduced species. In this thesis, impedance spectroscopy was employed to understand the impedance from basic process like charge transfer, solid-electrolyte interface formation.

### 1.5.3 Galvanostatic charge-discharge study (GCD)

Galvanostatic charge-discharge refers to the cycling of cell between two fixed potential points at a constant current. When current is applied to an electrochemical system, due to the influx of

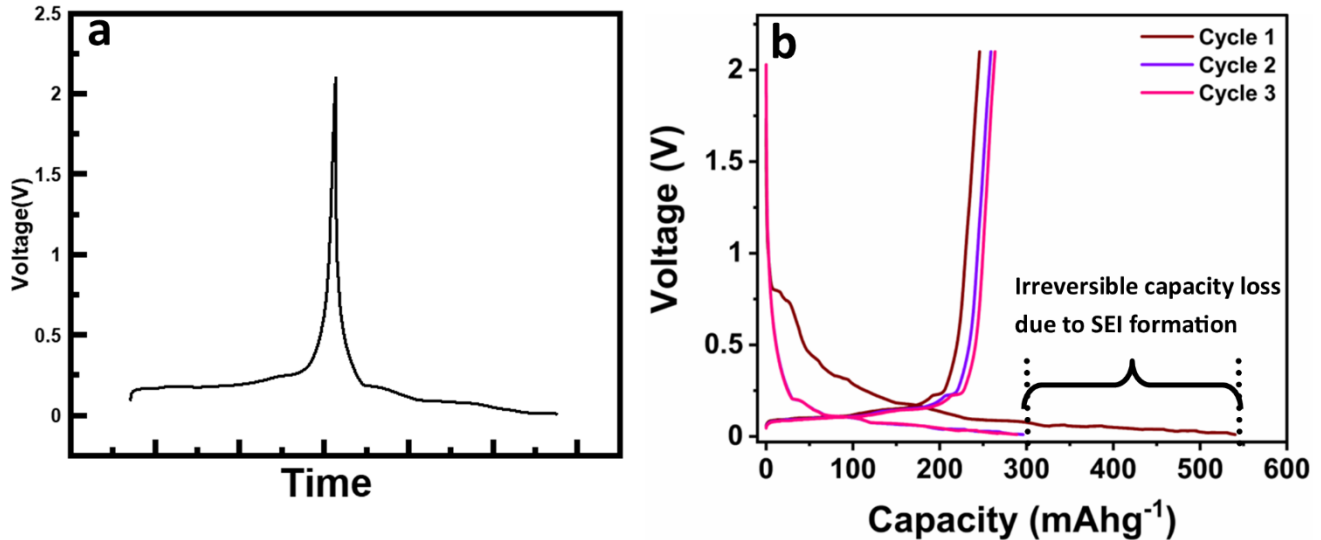


Figure 17-a) typical potential vs time plot of a lithium-ion anodic half-cell with graphite anode b) Potential vs capacity plot of lithium-ion anodic half-cell with graphite anode (Ref: 76)

electrons electrochemical reactions take place<sup>72</sup>. In the context of lithium-ion batteries, lithiation and delithiation occur depending on the direction of current. In this study, the time taken by the lithium-ion battery to reach completely discharged state (i.e., upper/lower potential limit) from completely charged state (i.e., upper/lower potential limit) at a constant current is measured. The product of current and time gives the lithiation/delithiation capacity of the material. The typical potential vs time plot and potential vs capacity plot of a lithium-ion battery with graphite anode is shown in the Figure 17 a and b. The specific capacity of a material can be calculated by dividing the capacity with the mass of the material. The coulombic efficiency of the material can also be calculated from the data obtained in GCD using the following formula:

$$\text{coulombic efficiency (\%)} = \frac{\text{delithiation capacity}}{\text{lithiation capacity}} * 100 \dots\dots\dots(14)$$

### 1.6 Design principles of a lithium-ion battery<sup>79</sup>

A typical lithium-ion battery consists of an anode that supports intercalation of lithium ions and a cathode typically lithium transition metal oxides, which is also the source of lithium ions in the battery. The redox reactions at anode occur at lower potentials than in cathode. In general, the

requirement for a battery is to deliver good power density and energy density. The power density and energy density of a lithium-ion battery are given by the following equations:

$$P = \frac{\text{Current} * \text{voltage}}{\text{mass of the cell}} \dots \textcircled{1}$$

$$E = \frac{\text{voltage} * \text{capacity}}{\text{mass of the cell}} \dots \textcircled{2}$$

Where, P is power density and E is energy density. In both the formulae, voltage is a key component which impacts the overall power or energy density.

$$\text{Voltage} = V_{oc} - IR_b \dots \textcircled{3}$$

The chemical potentials of both the anode and cathode are different, which gives rise to the natural potential difference between the electrodes termed as open circuit voltage or open circuit potential. The difference between chemical potential of anode  $\mu_A$  and the chemical potential of cathode  $\mu_C$ ,  $\mu_A - \mu_C$  (< 5V) is the constraint that limits the maximum open circuit voltage.

$$V_{OC} = \frac{(\mu_A - \mu_C)}{-nF} < 5V \dots \textcircled{4}$$

Further, the  $V_{OC}$  is also limited by the thermodynamic stability of the anode, cathode, and the electrolyte i.e., the chemical potential of the anode, which is the HOMO of the anode, must lie below the LUMO of the liquid electrolyte to avoid electron transfer from HOMO of the anode to the LUMO of electrolyte leading to reduction of electrolyte. Similarly, the chemical potential of the oxidant, which is also the LUMO of cathode, must lie above the HOMO of the electrolyte to avoid oxidation of electrolyte (comparison of HOMO-LUMO energy levels of anode, cathode and electrolyte are shown in Figure 18). Hence, the open circuit potential is also dependent on the band gap of the electrolyte i.e.,

$$\mu_A - \mu_C \leq E_{el} \dots \textcircled{5}$$

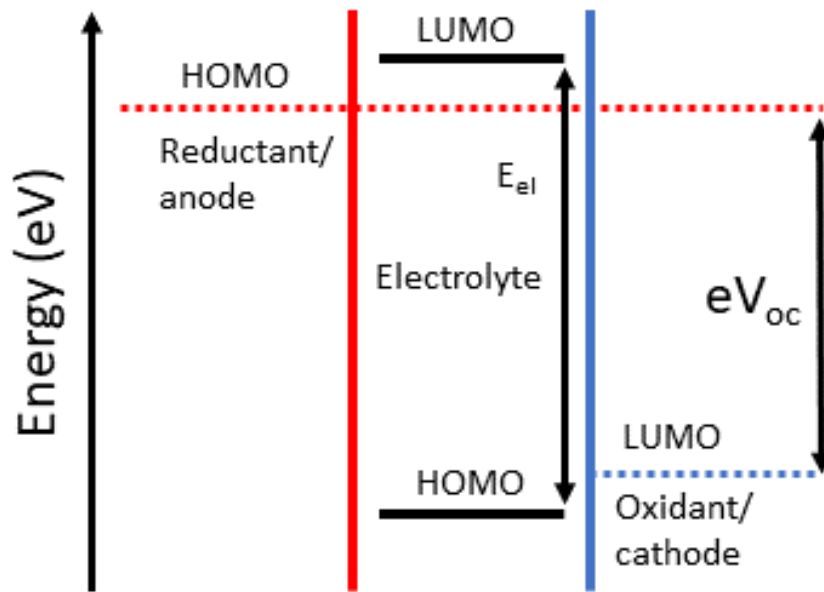


Figure 18-Energies of electrolyte window  $E_{el}$  and the anode HOMO and LUMO of cathode (Ref: 31)

The conditions mentioned in equations 4 and 5 dictate the value of  $V_{oc}$ . Further to achieve high power and energy densities, as mentioned in formulae 1, 2 and 3, another important factor is the battery resistance ( $R_b$ ). Battery resistance is dependent on multiple factors like the resistance of electrolyte ( $R_{el}$ ), resistance of anode ( $R_a$ ), resistance of cathode ( $R_c$ ). Briefly, battery resistance can be equated to the sum of the individual resistances as follows:

$$R_b = R_{el} + R_a + R_c \dots \dots \dots \textcircled{6}$$

From equation 6, it is clear that, to increase the power output of a lithium-ion battery, it is important to decrease the resistance of the individual components. Hence, for an efficient design of lithium-ion battery materials, the fermi energies (or the HOMO-LUMO energy levels) of the electrodes and the HOMO-LUMO energy levels of liquid electrolyte are the key factors to be considered.

Apart from these considerations, electrode fabrication requires intricate care in processing. The general process of slurry preparation involves mixing of active material, conducting carbon (if required) and a polymeric binder material using a suitable solvent. The process of mixing usually involves stirring the mixture of solvent and electrode mixture till a consistent dispersion is obtained or ball milling the mixture. Various factors in the process of slurry preparation effect the

performance of the electrode. The following is the discussion on each of the potential factors to be taken into consideration during the slurry preparation:

1) Particle size:

Particle size has a significant effect on the performance of lithium-ion battery. Krewer et al., found that a very small particle size (< 5 nm) leads to high-capacity loss due to the higher surface areas leading to higher SEI growth. Whereas the using a large particle ( $\mu\text{M}$ ) poor cyclability and significant loss of capacity occurs due to the ion transport problem. Further, micro cracking takes place after repeated cycling, which leads to more capacity loss and higher over potentials. Hence, choosing the appropriate particle size is important for slurry preparation<sup>80</sup>.

2) Particle dispersibility:

A uniform slurry preparation requires better particle dispersion. Zhou et al., demonstrated the effect of particle dispersion on the performance of the battery. It was found that a well dispersed active material particles deliver a better capacity even at higher charge/discharge currents. Whereas in the case of non-uniformly dispersed slurry, aggregation of particles leads the particles to be inactive especially at high charge-discharge currents<sup>81</sup>.

3) Viscosity of slurry:

Viscosity of the slurry has a larger impact on the electrode preparation. Low viscous slurry leads to improper coating of active material, conducting carbon and binder onto the surface of copper (or aluminum) and can lead to particle agglomeration. Whereas if the slurry viscosity is too high, effective mixing of each component of the electrode cannot be efficient. Hence, based on the type of active material, conducting carbon and binder, a slurry viscosity which enables better mixing of each component and facilitating uniform coating on the surface of current collector is desired<sup>82</sup>.

4) Binder solubility:

The solubility of binder in the solvent used for preparation of slurry is a prerequisite for efficient electrode fabrication. Commonly used active materials like graphite, silicon,  $\text{LiTiO}_2$  etc., are insoluble in commonly used organic solvents or water. Hence for a better interaction between the active material, current collector and conducting carbon it is essential for the binder to coat the active particles which requires solubility of binder<sup>83</sup>.

## 5) Electrode drying process:

After coating the slurry onto the copper foil, the electrode is dried under vacuum at a certain temperature to remove the solvent from electrode. Schabel et al., demonstrated that the electrode thickness also has to be considered during the drying process. In case of thicker electrodes (mass loading  $> 4 \text{ mg/cm}^2$ ), drying at lower temperatures lead to capillary transport of binder towards the surface of the electrode leading to poor adhesion between current collector and electrode material. Hence, in such cases drying at higher temperatures is beneficial<sup>84</sup>.

Apart from these factors, to achieve a better performance, the molecular structure is crucial. Jiang et al., demonstrated the effect of molecular structure and morphology on the performance of lithium-ion battery. Comparison was made between polythiophene and porous poly (3,3' bithiophene). Porous poly (3,3' bithiophene) delivered a reversible capacity of 663 mAh/g at 500 mA/g current density for over 1000 cycles whereas, polythiophene delivered a reversible capacity of 100 mAh/g at 500 mA/g current density<sup>85</sup>. This study indicates the importance of the morphology of the anode active material in terms of lithium-ion storage property. Matsumi et al. have reported a heavily nitrogen-doped carbon material (Py PBI) as an anode in lithium-ion batteries exhibiting much better capacity. In this work, the presence of nitrogen was found to enhance the fast-charging ability of the anode, but the maximum achievable capacity was found to be 400 mAh/g at a current density of 40 mA/g, which is much lower than the capacity obtained using PBM as an anode<sup>75</sup>. In a different study, Matsumi et al. reported a BIAN-Para phenylene (BP)-based binder system with excellent binder properties for the graphite anode. The BP polymer performance as an anode was also evaluated in the study. The anode with the BP polymer with two nitrogen atoms per repeating unit and a linear, nonporous morphology delivered a negligible capacity and was found to be unsuitable as an anode in lithium-ion batteries<sup>72</sup>. Hence, it can be observed that the lithium storage property depends on the content of nitrogen in the active material and the morphology of the anode.

These studies indicate the importance of careful design of active materials in terms of the structure and heteroatom content leading to better lithium-ion storage property.

## 1.7 Strategy employed in this thesis towards the design of lithium-ion battery anode

The scope of this thesis is concentrated on the anodic active material design. As mentioned in the equation 14, the resistance of individual components is of crucial importance. In an anode, resistance can arise from, the internal resistance of the active material and the electrode-electrolyte interface (SEI). The resistance of any material is given by<sup>24</sup>:

$$R = \rho \frac{l}{A} \dots \dots \dots (15)$$

Where,  $\rho$  is resistivity,  $l$  is length of the resistor and  $A$  is area of the resistor. From equation 15, it is clear that the area of the resistor is inversely proportional to the resistance. Hence, the interfacial resistance, when the  $\rho$  and  $l$  are constant is given by:

$$R_{in} \sim \frac{\text{Total area of the electrode}}{\text{interfacial area of the electrode}} \dots \dots \dots (16)$$

Equations 15 and 16 indicate that, to obtain lower resistance of electrode, the electrode material must possess high surface area. Higher surface area can be obtained by tuning the morphology of the material. Further, the characteristic time of diffusion ( $\tau$ ) is given by:

$$\tau = \frac{L^2}{D} \dots \dots \dots (17)$$

Where,  $L$  is length of diffusion and  $D$  is diffusion coefficient. According to equation 17, the time of diffusion is proportional to the diffusion length. Hence, the time of charge can be decreased by decreasing the length of diffusion. Hence, developing porous anode materials can aid in reducing the anode resistance as well as decreasing the time of diffusion. Another implication of equation 17 is, as the diffusive nature of charge storage decreases and the surface contribution increases, the time of diffusion can be decreased while maintaining a relatively high capacity. Therefore, the surface charge storage ability of the anode has to be developed. Since, lithium ion is electropositive, employing heteroatoms like nitrogen in the anode can improve the lithium-ion storage ability of the anode<sup>86,87</sup>. Matsumi et al., have demonstrated the improvement in time of charging by utilizing highly nitrogen doped carbon material as anode. With a high nitrogen content of ~14%, they could achieve an extreme fast charging (<15 minutes) anodic half-cell<sup>75</sup>. In this

context, the strategy to develop a fast-charging anode with better capacity, two important properties are chosen in this thesis namely, porosity and polarity.

## 1.8 Objective and scope of this thesis

Organic moieties offer the unique benefits of the ability of tailor the structure and introduce various heteroatoms in the form of functional groups<sup>88,89</sup> (Figure 19). Hence, in this study, Bis imino acenaphthene (BIAN) based organic polymers were chosen as anodic active materials and also as precursor materials for the synthesis of nitrogen doped carbon, which is also employed as anodic material in lithium-ion batteries.

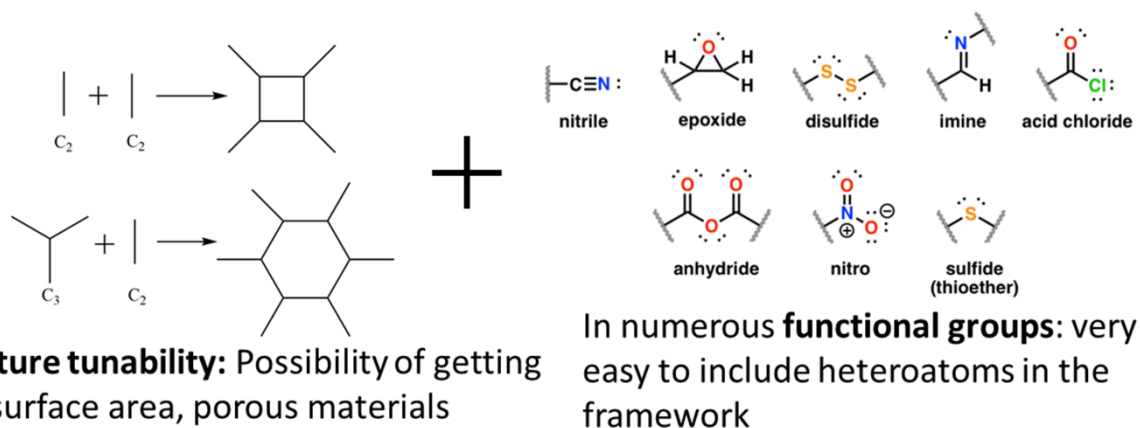


Figure 19-Schematic representation of benefits of organic materials in anode applications

Matsumi et al. reported a Bis-imino acenaphthene (BIAN) based electroactive polymer as a metal free catalyst. A composite of the polymer with graphene oxide showed even better electro catalytic activity. Such performance was attributed to the presence of two different types of electrophilic carbon atoms linked to nitrogen<sup>90</sup>. The same group also reported utilization of BIAN-Fluorene copolymer<sup>73</sup> and BIAN-Para phenylene copolymer as efficient polymeric binders for graphitic anode material<sup>72</sup>. However, the synthesis and application of BIAN based organic polymer in lithium-ion storage has not been reported yet. With this motivation, the charge storage properties of BIAN based organic polymers were studied in this thesis.

Chapter 2 presents the synthesis of BIAN-Bismarck brown based organic copolymer (BBP), synthesis of N-doped carbon (Py BBP) from BBP as single source of carbon and nitrogen was presented. The as synthesized polymer and N-doped carbon displayed better performance in terms of charge storage, cyclability and rate performance.



Chapter 3 presents the synthesis, characterization, and electrochemical charge storage properties of BIAN-melamine organic copolymer (PBM). Melamine moiety being a nitrogen rich material and a triamine, enables the synthesis of a nitrogen rich, polymer. The as synthesized PBM, exhibited high lithium storage capacity and better coulombic efficiency. The detailed analysis of the electrochemical performance is also presented in chapter 2.

Chapter 4 presents the synthesis of N-doped carbon from PBM (Py PBM), the characterization of the material and electrochemical properties of N-doped carbon in detail. Further the temperature effect on the synthesis of N-doped carbon was also presented. The as synthesized carbon material delivered good reversible capacity at higher currents and also exhibited fast charging ability.

In Chapter 5, the summary of physical and electrochemical properties of PBM, Py PBM, BBP, Py BBP were presented along with the structure-activity relation in all the cases.

## **References**

- 1 V. Augustyn, P. Simon and B. Dunn, *Energy Environ. Sci.*, 2014, **7**, 1597–1614.
- 2 M. D. Bhatt, G. Lee and J. S. Lee, *J. Phys. Chem. C*, 2016, **120**, 26435–26441.
- 3 D. Grumelli, B. Wurster, S. Stepanow and K. Kern, *Nat. Commun.*, 2013, **4**, 1–6.
- 4 X. Wang, Z. Li, Y. Qu, T. Yuan, W. Wang, Y. Wu and Y. Li, *Chem*, 2019, **5**, 1486–1511.
- 5 M. Winter and R. J. Brodd, *Chem. Rev.*, 2004, **104**, 4245–4269.
- 6 J. K. Nørskov, J. Rossmeisl, A. Logadottir, L. Lindqvist, J. R. Kitchin, T. Bligaard and H. Jónsson, *J. Phys. Chem. B*, 2004, **108**, 17886–17892.
- 7 A. L. Zhu, D. P. Wilkinson, X. Zhang, Y. Xing, A. G. Rozhin and S. A. Kulinich, *J. Energy Storage*, 2016, **8**, 35–50.
- 8 L. Kong, L. Su, S. Hao, W. Yang, G. Shao and X. Qin, *Electrochim. Acta*, , DOI:10.1016/j.electacta.2020.136303.
- 9 Poonam, K. Sharma, A. Arora and S. K. Tripathi, *J. Energy Storage*, 2019, **21**, 801–825.
- 10 G. Lota, K. Lota and E. Frackowiak, *Electrochem. commun.*, 2007, **9**, 1828–1832.

- 
- 11 R. Kahwaji, , DOI:10.13140/RG.2.2.14032.35846.
  - 12 A. Sulcius, A. Lopez and C. Trujillo, *J. Sci. Educ. Int. Biling.*, 2016, 112–116.
  - 13 G. F. Martins, *J. Chem. Educ.*, 1990, **67**, 482.
  - 14 X. Dong, Y. Wang and Y. Xia, *Sci. Rep.*, 2014, **4**, 1–6.
  - 15 G. Jenson, G. Singh, J. K. Bhama and A. Ratner, *Energies*, 2020, **13**, 1–15.
  - 16 C. Xu, Y. Chen, S. Shi, J. Li, F. Kang and D. Su, *Sci. Rep.*, 2015, **5**, 1–8.
  - 17 J. Yang, C. Hu, H. Wang, K. Yang, J. B. Liu and H. Yan, *Int. J. Energy Res.*, 2017, **41**, 336–352.
  - 18 T. Sasaki, Y. Ukyo and P. Novák, *Nat. Mater.*, 2013, **12**, 569–575.
  - 19 P. Sirisinudomkit, P. Iamprasertkun, A. Krittayavathananon, T. Pettong, P. Dittanet and M. Sawangphruk, *Sci. Rep.*, 2017, **7**, 1–9.
  - 20 L. M. Rodrigues, C. Montez, R. Moraes, P. Portugal and F. Vasques, *Sensors (Switzerland)*, , DOI:10.3390/s17020422.
  - 21 A. Green, *Power Eng. J.*, 1999, **13**, 117–121.
  - 22 E. Blumbergs, V. Serga, E. Platacis, M. Maiorov and A. Shishkin, *Metals (Basel)*, 2021, **11**, 1–14.
  - 23 T. Meng, K. H. Young, D. F. Wong and J. Nei, *Batteries*, 2017, **3**, 1–13.
  - 24 D. Deng, *Energy Sci. Eng.*, 2015, **3**, 385–418.
  - 25 K. Kubota and S. Komaba, *J. Electrochem. Soc.*, 2015, **162**, A2538–A2550.
  - 26 J. Asenbauer, T. Eisenmann, M. Kuenzel, A. Kazzazi, Z. Chen and D. Bresser, *Sustain. Energy Fuels*, 2020, **4**, 5387–5416.
  - 27 A. S. Hameed, A. Katogi, K. Kubota and S. Komaba, *Adv. Energy Mater.*, 2019, **9**, 4–11.
  - 28 N. Chawla, N. Bharti and S. Singh, *Batteries*, , DOI:10.3390/batteries5010019.
  - 29 T. Wang, Y. Li, J. Zhang, K. Yan, P. Jaumaux, J. Yang, C. Wang, D. Shanmukaraj, B. Sun,

- 
- M. Armand, Y. Cui and G. Wang, *Nat. Commun.*, 2020, **11**, 1–9.
- 30 A. Manthiram, *Nat. Commun.*, 2020, **11**, 1–9.
- 31 M. Nishizawa, S. Yamamura, T. Itoh and I. Uchida, *Chem. Commun.*, 1998, 1631–1632.
- 32 J. B. Goodenough, *Prog. Solid State Chem.*, 1971, **5**, 145–399.
- 33 S. Venkatraman and A. Manthiram, *Chem. Mater.*, 2003, **15**, 5003–5009.
- 34 S. Venkatraman, Y. Shin and A. Manthiram, *Electrochem. Solid-State Lett.*, 2003, **6**, 6–10.
- 35 M. H. Braga, N. S. Grundish, A. J. Murchison and J. B. Goodenough, *Energy Environ. Sci.*, 2017, **10**, 331–336.
- 36 M. M. Thackeray, W. I. F. David, P. G. Bruce and J. B. Goodenough, *Mater. Res. Bull.*, 1983, **18**, 461–472.
- 37 Z. Tianran, L. Daixin, Z. Tao and C. Jun, *Prog. Nat. Sci. Mater. Int.*, 2013, **23**, 256–272.
- 38 M. M. Thackeray, *J. Electrochem. Soc.*, 1995, **142**, 2558–2563.
- 39 W. Choi and A. Manthiram, *J. Electrochem. Soc.*, 2006, **153**, A1760.
- 40 J. Chable, C. Baur, J. H. Chang, S. Wenzel, J. M. García-Lastra and T. Vegge, *J. Phys. Chem. C*, DOI:10.1021/acs.jpcc.9b11235.
- 41 A. Manthiram and J. B. Goodenough, *J. Solid State Chem.*, 1987, **71**, 349–360.
- 42 A. Manthiram and J. B. Goodenough, *J. Power Sources*, 1989, **26**, 403–408.
- 43 C. Masquelier and L. Croguennec, *Chem. Rev.*, 2013, **113**, 6552–6591.
- 44 Z. Wen, C. Shen and Y. Lu, *Chempluschem*, 2015, **80**, 270–287.
- 45 Q. Li, J. Chen, L. Fan, X. Kong and Y. Lu, *Green Energy Environ.*, 2016, **1**, 18–42.
- 46 K. Xu, *Chem. Rev.*, 2004, **104**, 4303–4417.
- 47 L. Hu, Z. Zhang and K. Amine, *J. Power Sources*, 2013, **236**, 175–180.

- 
- 48 Y. Wang, J. Yi and Y. Xia, *Adv. Energy Mater.*, 2012, **2**, 830–840.
- 49 W. Li, J. R. Dahn and J. H. Root, *Mater. Res. Soc. Symp. - Proc.*, 1995, **369**, 69–80.
- 50 M. Ishikawa, T. Sugimoto, M. Kikuta, E. Ishiko and M. Kono, *J. Power Sources*, 2006, **162**, 658–662.
- 51 R. Vedarajan, K. Matsui, E. Tamaru, J. Dhankhar, T. Takekawa and N. Matsumi, *Electrochem. commun.*, 2017, **81**, 132–135.
- 52 J. Jie, Y. Liu, L. Cong, B. Zhang, W. Lu, X. Zhang, J. Liu, H. Xie and L. Sun, *J. Energy Chem.*, 2020, **49**, 80–88.
- 53 X. Liu, X. Xin, L. Shen, Z. Gu, J. Wu and X. Yao, *ACS Appl. Energy Mater.*, 2021, **4**, 3975–3982.
- 54 H. Cheng, J. G. Shapter, Y. Li and G. Gao, *J. Energy Chem.*, 2021, **57**, 451–468.
- 55 S. Zhang, *npj Comput. Mater.*, 2017, **3**, 1–10.
- 56 A. Yoshino, *Angew. Chemie - Int. Ed.*, 2012, **51**, 5798–5800.
- 57 A. M. Wilson and J. R. Dahn, *J. Electrochem. Soc.*, 1995, **142**, 326–332.
- 58 A. A. Iqbal, N. Sakib, A. K. M. P. Iqbal and D. M. Nuruzzaman, *Materialia*, , DOI:10.1016/j.mtla.2020.100815.
- 59 M. Zhao, Y. Xia and L. Mei, *Phys. Rev. B - Condens. Matter Mater. Phys.*, 2005, **71**, 1–6.
- 60 P. Lian, X. Zhu, S. Liang, Z. Li, W. Yang and H. Wang, *Electrochim. Acta*, 2010, **55**, 3909–3914.
- 61 P. U. Nzereogu, A. D. Omah, F. I. Ezema, E. I. Iwuoha and A. C. Nwanya, *Appl. Surf. Sci. Adv.*, 2022, **9**, 100233.
- 62 H. Yamamoto, S. Muratsubaki, K. Kubota, M. Fukunishi, H. Watanabe, J. Kim and S. Komaba, *J. Mater. Chem. A*, 2018, **6**, 16844–16848.
- 63 X. Liu, J. Zhang, S. Guo and N. Pinna, *J. Mater. Chem. A*, 2016, **4**, 1423–1431.

- 
- 64 O. Buyukcakir, J. Ryu, S. H. Joo, J. Kang, R. Yuksel, J. Lee, Y. Jiang, S. Choi, S. H. Lee, S. K. Kwak, S. Park and R. S. Ruoff, *Adv. Funct. Mater.*, 2020, **30**, 1–11.
- 65 Z. Lei, Q. Yang, Y. Xu, S. Guo, W. Sun, H. Liu, L. P. Lv, Y. Zhang and Y. Wang, *Nat. Commun.*, 2018, **9**, 1–13.
- 66 S. Huang, Z. Li, B. Wang, J. Zhang, Z. Peng, R. Qi, J. Wang and Y. Zhao, *Adv. Funct. Mater.*, 2018, **28**, 1–10.
- 67 M. T. Jeena, J. I. Lee, S. H. Kim, C. Kim, J. Y. Kim, S. Park and J. H. Ryu, *ACS Appl. Mater. Interfaces*, 2014, **6**, 18001–18007.
- 68 Y. Pan, S. Ge, Z. Rashid, S. Gao, A. Erwin, V. Tsukruk, K. D. Vogiatzis, A. P. Sokolov, H. Yang and P. F. Cao, *ACS Appl. Energy Mater.*, 2020, **3**, 3387–3396.
- 69 T. W. Kwon, J. W. Choi and A. Coskun, *Chem. Soc. Rev.*, 2018, **47**, 2145–2164.
- 70 T. P. Jayakumar, R. Badam and N. Matsumi, *ACS Appl. Energy Mater.*, 2020, **3**, 3337–3346.
- 71 V. Ponnuchamy and E. S. Esakkimuthu, *Appl. Surf. Sci.*, 2022, **573**, 151461.
- 72 A. Gupta, R. Badam, A. Nag, T. Kaneko and N. Matsumi, *ACS Appl. Energy Mater.*, 2021, **4**, 2231–2240.
- 73 S. G. Patnaik, R. Vedarajan and N. Matsumi, *J. Mater. Chem. A*, 2017, **5**, 17909–17919.
- 74 N. Elgrishi, K. J. Rountree, B. D. McCarthy, E. S. Rountree, T. T. Eisenhart and J. L. Dempsey, *J. Chem. Educ.*, 2018, **95**, 197–206.
- 75 K. S. Patnaik, R. Badam, Y. Peng, K. Higashimine, T. Kaneko and N. Matsumi, *Chem. Commun.*, 2021, **57**, 13704–13707.
- 76 M. Gaberšček, *Nat. Commun.*, 2021, **12**, 19–22.
- 77 P. Kurzweil and M. Shamonin, *Batteries*, 2018, **4**, 1–13.
- 78 A. Habekost, *World J. Chem. Educ.*, 2020, **9**, 14–21.
- 79 L. Ion, *Kodansha 8*, 1998.
-

- 
- 80 L. Bläubaum, F. Röder, C. Nowak, H. S. Chan, A. Kwade and U. Krewer, *ChemElectroChem*, 2020, **7**, 4755–4766.
- 81 C. Jiang, M. Ichihara, I. Honma and H. Zhou, *Electrochim. Acta*, 2007, **52**, 6470–6475.
- 82 A. Cushing, T. Zheng, K. Higa and G. Liu, *Polymers (Basel)*, 2021, **13**, 1–8.
- 83 T. Zheng, T. Zhang, M. S. de la Fuente and G. Liu, *Eur. Polym. J.*, 2019, **114**, 265–270.
- 84 J. Kumberg, M. Müller, R. Diehm, S. Spiegel, C. Wachsmann, W. Bauer, P. Scharfer and W. Schabel, *Energy Technol.*, , DOI:10.1002/ente.201900722.
- 85 C. Zhang, Y. He, P. Mu, X. Wang, Q. He, Y. Chen, J. Zeng, F. Wang, Y. Xu and J. X. Jiang, *Adv. Funct. Mater.*, 2018, **28**, 1–9.
- 86 D. Yan, Y. Wu, R. Kitaura and K. Awaga, *J. Mater. Chem. A*, 2019, **7**, 26829–26837.
- 87 G. Fang, Z. Wu, J. Zhou, C. Zhu, X. Cao, T. Lin, Y. Chen, C. Wang, A. Pan and S. Liang, *Adv. Energy Mater.*, 2018, **8**, 1–10.
- 88 B. S. Mantripragada, R. Badam and N. Matsumi, *ECS Meet. Abstr.*, 2021, **MA2021-01**, 104–104.
- 89 B. S. Mantripragada, R. Badam and N. Matsumi, *ACS Appl. Energy Mater.*, 2022, **5**, 6903–3912.
- 90 S. G. Patnaik, R. Vedarajan and N. Matsumi, *ACS Appl. Energy Mater.*, 2018, **1**, 1183–1190.

## **Chapter 2. BIAN-Bismarck brown based organic polymer as efficient anode materials for lithium-ion batteries**

### **2.1 Abstract**

Lithium-ion batteries are regarded as promising alternatives to fossil fuel-based energy. The extensive application of lithium-ion batteries requires development of better anodes. In this context, organic polymers are materials with strong covalent bonds and crosslinking between the organic moieties with different geometries. Organic polymers offer a distinct advantage of integrating multiple redox sites, tunable porosity, and relatively high surface area. These properties of organic polymers can be beneficial from the perspective of electrochemical energy storage because, due to tunable structure, the lithium-ion diffusion length is reduced, and the availability of active sites can also be increased due to the presence of heteroatoms like nitrogen. In this work, the synthesis and anodic applications of imine and azo functionalized BIAN-Bismarck brown based conjugated organic polymer (BBP) is presented. The anodic half-cells with BBP delivered a capacity of 500 mAh/g at 400 mA/g after 1500 cycles. The charge storage mechanism was investigated in detail.

## 2.2 Introduction

In the current scenario of fossil fuel depletion and the environmental hazards associated with the utilization of fossil fuels, a great amount of research attention is being directed towards utilization of renewable energy resources<sup>1,2</sup>. In this context, lithium-ion batteries (LIB) emerged as the promising energy storage devices<sup>3,4</sup>. The evolution of anodes in LIB from petroleum coke to silicon have seen a drastic increase in the maximum achievable specific capacity<sup>5,6,7,8</sup>. However, most of the inorganic anodes that are currently under use have drawbacks like limited specific capacity or low cyclability etc., due to the lack of structural flexibility<sup>9,10,11</sup>. Organic materials on the other hand provide a unique opportunity to tailor the structure of the anode material. Furthermore, the functional groups with precisely known redox activity can be introduced using the plethora of low cost and easy reactive mechanisms<sup>12,13,14,15</sup>. Typical inorganic materials require intense and cost ineffective reactive processes for any chemical or structural modifications. This unique advantage of organic materials makes their utilisation as anodes in rechargeable batteries very enthralling. In this context, organic molecules with various functional groups were investigated as the anodes in lithium-ion batteries. However, many of the small organic molecules suffer with the problem of dissolution in typically used polar organic electrolyte solution in rechargeable batteries<sup>16,17,18</sup>. Hence to overcome this problem of dissolution, a possible approach is to utilise organic polymers with redox active groups as anodic active materials. Organic polymers can broadly be classified into p-type, n-type based on the possibility of reducing or oxidising the polymer. By partially doping the polymer, it is possible to reduce the polymer (n-type) i.e., introduce electrons which requires a lower LUMO level. Similarly, it is possible to oxidise the polymer (p-type) i.e., introduce cations or remove electrons<sup>19,20</sup>. By the virtue of accepting electrons when doped, n-type polymers exhibit better electron transport properties, and the electron rich nature of these polymers also supports lithium storage<sup>21,22</sup>. In this regard, various strategies like introducing functional groups containing electronegative elements (nitrogen, oxygen sulphur etc.) like imine, azo, carbonyl etc., were brought out to reduce the LUMO energy level and obtain a n-type conjugated polymer. Inclusion of heteroatoms also improves the lithium storing ability through pseudocapacitive mechanism arising due to the polarity difference between electronegative heteroatoms and the positively charged lithium ion<sup>23,24,25</sup>. Besides the



advantage of the pseudocapacitive properties of organic materials, the geometry of organic polymers can be tailored by choosing reactants with suitable geometry<sup>26,12,27</sup>. In this context, Zhang et al., have demonstrated a hexaamino benzene-based imine functional covalent organic framework. The hexaamino benzene-based COF delivered a reversible capacity of 1255 mAh/g at 1000 mA/g after 1100 cycles<sup>28</sup>. Wang et al., reported a similar imine functional COF-CNT composite which delivered a reversible capacity of 1536 mAh/g after 500 cycles at 100 mA/g current density<sup>16</sup>. Ruoff et al., reported a covalent triazine framework (CTF). The CTF delivered a reversible capacity of 1190 mAh/g at 300 mA/g current density<sup>29</sup>. Dai et al., reported, super lithiation performance of CTF<sup>30</sup>. A lithiation capacity of 1626 mAh/g was obtained and the reversible capacity was 740 mAh/g. However, it is important to note that the synthesis of COF and CTF requires stringent synthetic procedures. Zhang et al., reported a synthesis of porous polymer that delivers a reversible capacity of 550 mAh/g after 100 cycles<sup>31</sup>. In this work, synthesis, and electrochemical application of an azo, imine dual functional, nitrogen rich, BIAN-Bismarck brown-based n-type conjugated organic polymer (BBP) are reported as anodic active material in lithium-ion batteries. The inclusion of imino and azo groups lowers the LUMO energy level and contributes to a pseudocapacitive charge storage property. The geometry of Bismarck brown supports in crosslinking of the polymer and thus create porosity. Anodic half-cell fabricated using BBP anode delivered a reversible capacity of 550 mAh/g at 400 mA/g current density after 1500 cycles.

## 2.3 Experimental section

### 2.3.1 Materials

Acenaphthoquinone, Bismarck brown Y, 1,4 dioxane, mesitylene and N-methyl pyrrolidone (NMP) were purchased from Tokyo chemical industries, Ltd. and were used without further purification. 1.0 M LiPF<sub>6</sub> (50/50) ethylene carbonate/diethyl carbonate (EC/DEC) electrolyte and PVDF binder (molecular weight: 540,000) were purchased from Sigma-Aldrich. Battery-grade acetylene black was purchased from Denka Japan Private Co., Ltd. Copper foil of thickness of 20 μm was purchased from the Nilaco corporation.

**Fourier transform-infrared spectrometer measurements.** The FT-IR spectra were recorded using a PerkinElmer 100 FT-IR spectrometer. The spectra were averaged over 50 scans with a resolution of 2 cm<sup>-1</sup>.

**X-ray photo electron spectroscopy.** X-ray photoelectron spectroscopy (XPS) measurements were conducted on a Fisons instruments S-probe TM 2803 instrument.

**Thermogravimetric analysis.** TGA was recorded using Hitachi STA7200 thermal analysis system at a heating rate of 10°C/min and a nitrogen flow rate of 200 ml/min.

**X-ray diffraction.** Powder XRD studies were conducted on Smart Lab X-Ray Diffractometer, Rigaku with Cu K $\alpha$  radiation ( $\lambda = 0.154$  nm, over the  $2\theta$  range of 2°–45° with a step size of 0.02°).

**Elemental dispersive X-ray scattering.** EDX spectra were recorded in TM3030plus at 15 kV.

**Theoretical studies.** The theoretical calculations were based on density functional theory in the dmol<sup>3</sup> module of the material studio. The Gibbs free energy was applied to determine the most stable lithiated state.  $\Delta G$  is evaluated using the following equation:

$$\Delta G = E_{Li-polymer} - E_{polymer}$$

Where  $E_{Li-cof}$  is the energy of lithiated PBM and  $E_{cof}$  is the energy of PBM in unlithiated state.

### 2.3.2 Electrochemical studies.

#### 2.3.2a Electrode preparation and cell fabrication

BBP, PVDF and acetylene black were taken in 80%, 10% and 10% weight percentages respectively and the slurry was prepared in NMP using kakuhunter ball mill. The homogenous slurry thus obtained was coated on a copper foil using a doctor blade (coating thickness: 0.1 mm). The electrode was dried under vacuum at 80°C for about 12 hours and was calendared to 0.06 mm thickness at 80°C. Disks of 17 mm diameter were punched from the calendared electrode sheet. 2025 type coin cells were fabricated in an argon filled glove box ( $O_2, H_2O < 0.5$  ppm) using BBP electrode as anode, lithium metal foil as counter electrode, polypropylene separator (25  $\mu$ m, celgard) and 1.0 M LiPF<sub>6</sub> (50/50) ethylene carbonate/diethyl carbonate (EC/DEC) as electrolyte. The cells were rested for about 8 hours before measurements.

#### 2.3.2b Electrochemical measurements.

All electrochemical measurements were performed in the potential range of 5 mV to 3.0 mV (vs Li/Li+) at 25°C. Cyclic voltammetry was performed in biologic VSP workstation at 0.1, 0.2, 0.4, 0.6, 0.8 and 1.0 mV/s scan rates. Potentiostatic electrochemical impedance spectroscopy was performed in a frequency range of 10 MHz to 0.1 Hz. Galvanostatic charge-discharge measurements were conducted in biologic battery cycling system at various current densities.

### 2.3.2c Synthesis

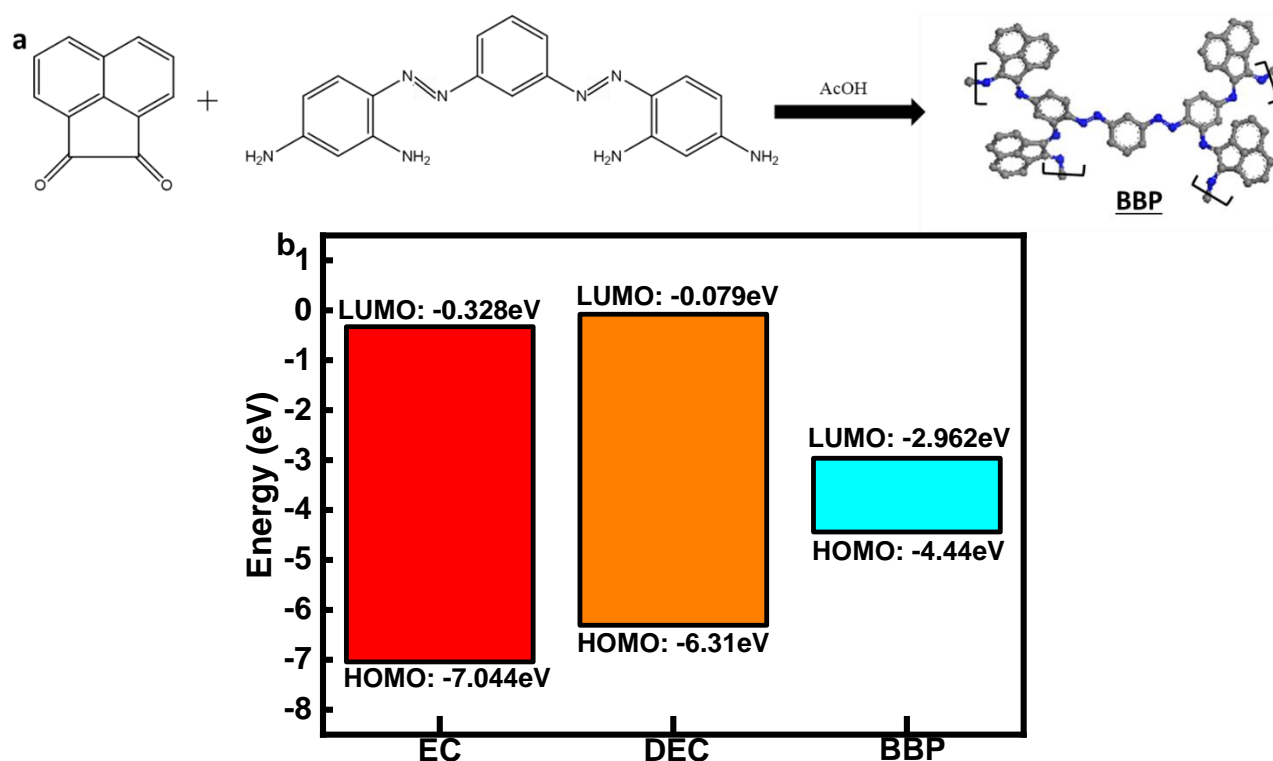


Figure 1-a) Synthetic scheme of BBP polymer b) Comparison of HOMO-LUMO energy levels of EC, DEC and BBP.

15 mM of acenaphthoquinone, 10 mM of Bismarck brown and 30 mM of acetic acid were taken in about 60 ml 1,4-dioxane. This mixture was refluxed at 110 °C for about 48 hours. The product was obtained by solvent evaporation. Figure 1a shows the synthetic scheme of BBP.

### 2.4 Characterization

BBP organic polymer was conducted using various characterization techniques. The HOMO-LUMO energy levels were evaluated by DFT studies using dmol<sup>3</sup> module of material studio (Figure 1b). The LUMO of PBM lies well below the LUMO of commonly used EC-DEC based electrolyte. This indicates that the material is more prone to undergo electrochemical reduction than electrolyte during the initial cycles of charge discharge of lithium-ion battery<sup>32</sup>.

## 2.4.1 Infra-red spectroscopy

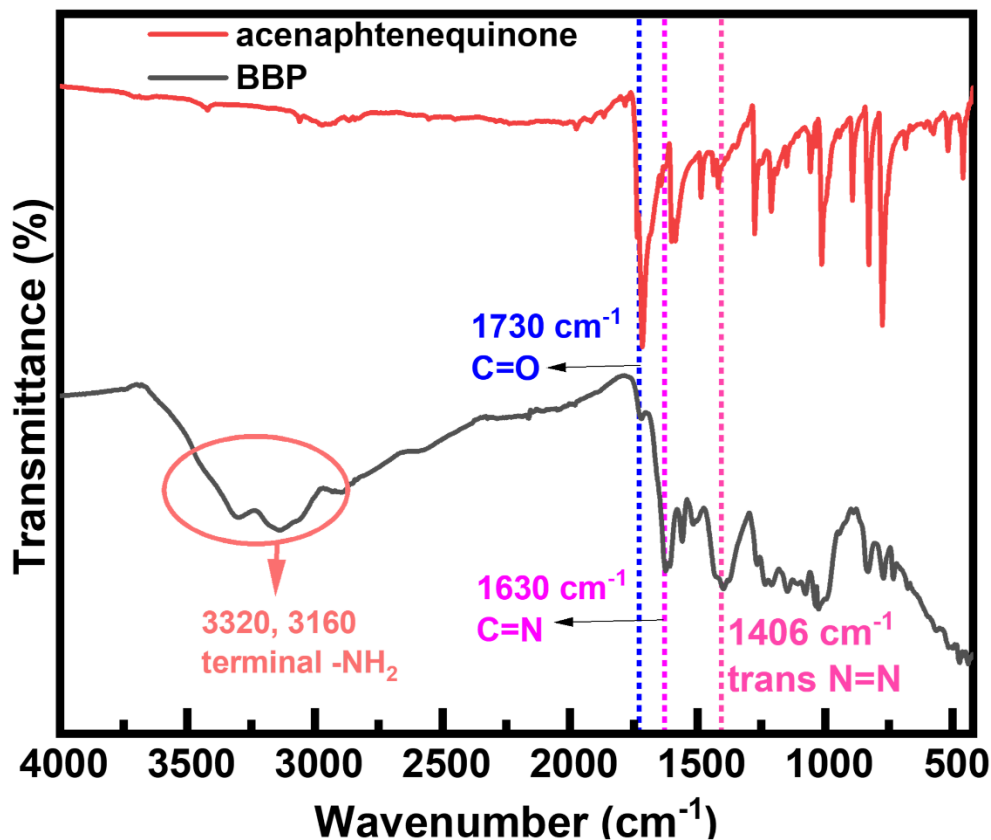


Figure 2-IR spectra of BBP and acenaphthenequinone

The IR spectrum (shown in Figure 2) of acenaphthoquinone shows a peak at 1710 cm<sup>-1</sup> corresponding to ketone (C=O) functional group, a peak at 1520 cm<sup>-1</sup> corresponding to C=C stretching. The IR spectrum of BBP shows a peak at 1630 cm<sup>-1</sup> corresponding to C=N, a peak at 1540 cm<sup>-1</sup> corresponding to C-N stretch, two minor peaks at 3320 cm<sup>-1</sup> and 3160 cm<sup>-1</sup> correspond to the unreacted or terminal amine groups. The peak at 1730 cm<sup>-1</sup> corresponding to ketone was observed to diminish in the product molecule and corresponding peak at 1630 cm<sup>-1</sup> was observed<sup>33</sup>. This indicates the successful conversion of ketone to imine during the polycondensation reaction. Further, the peak corresponding to trans N=N stretch was observed at 1406 cm<sup>-1</sup> in the product molecule<sup>34</sup>.

## 2.4.2 EDX.

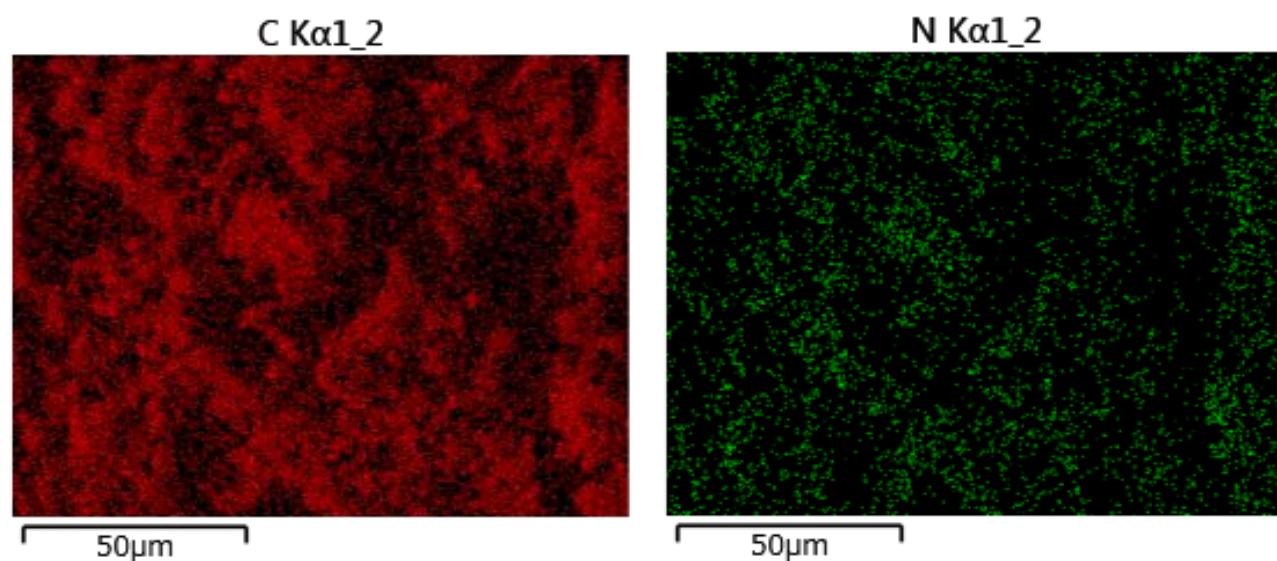


Figure 3-Elemental mapping of BBP

Table 1-Elemental composition of BBP

Element	Atom%	Weight%
Carbon	61.4	56.4
Nitrogen	24.4	26.2
Oxygen	14.2	17.4

Figure 3 shows the elemental mapping of BBP. The mapping of nitrogen shows its uniform distribution along with carbon. Further, the atomic percentage (shown in Table 1) of carbon was detected to be 61% corresponding to a weight percent of 56 and an atomic percentage of nitrogen was detected to be 24% corresponding to a weight percent of 26.

## 2.4.3 XPS

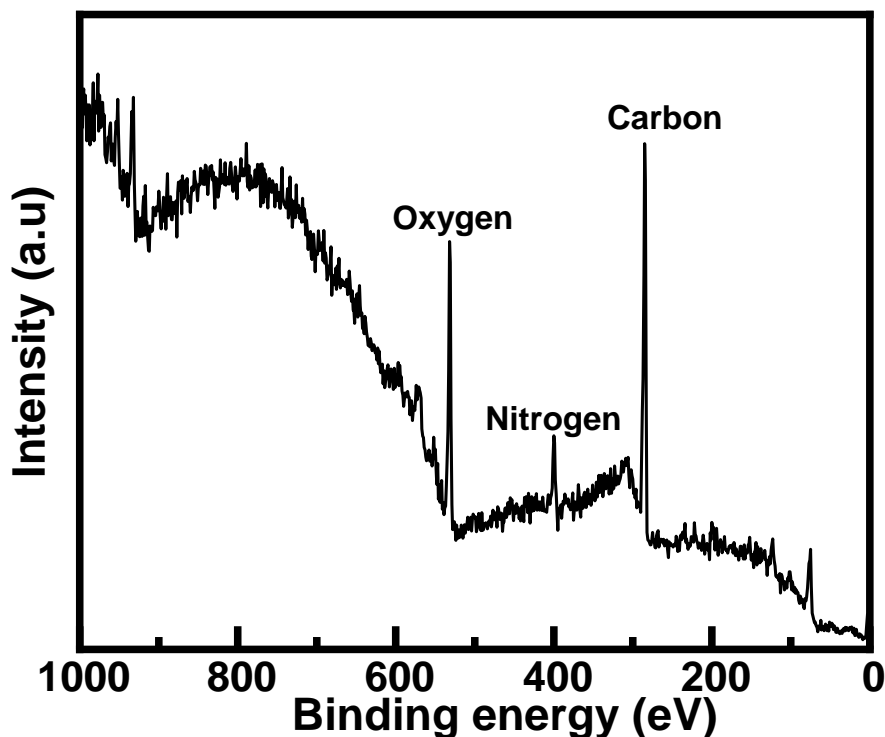


Figure 4-XPS wide scan spectrum of BBP

X-ray photo-electron spectroscopy was conducted to study the elemental and functional group composition of BBP. Figure 4 shows wide scan XPS spectrum of BBP. The XPS survey spectrum shows three peaks at 284 eV, 400 eV and 530 eV corresponding to carbon, nitrogen and oxygen elements respectively. The following formula was used to calculate the atomic percentages:

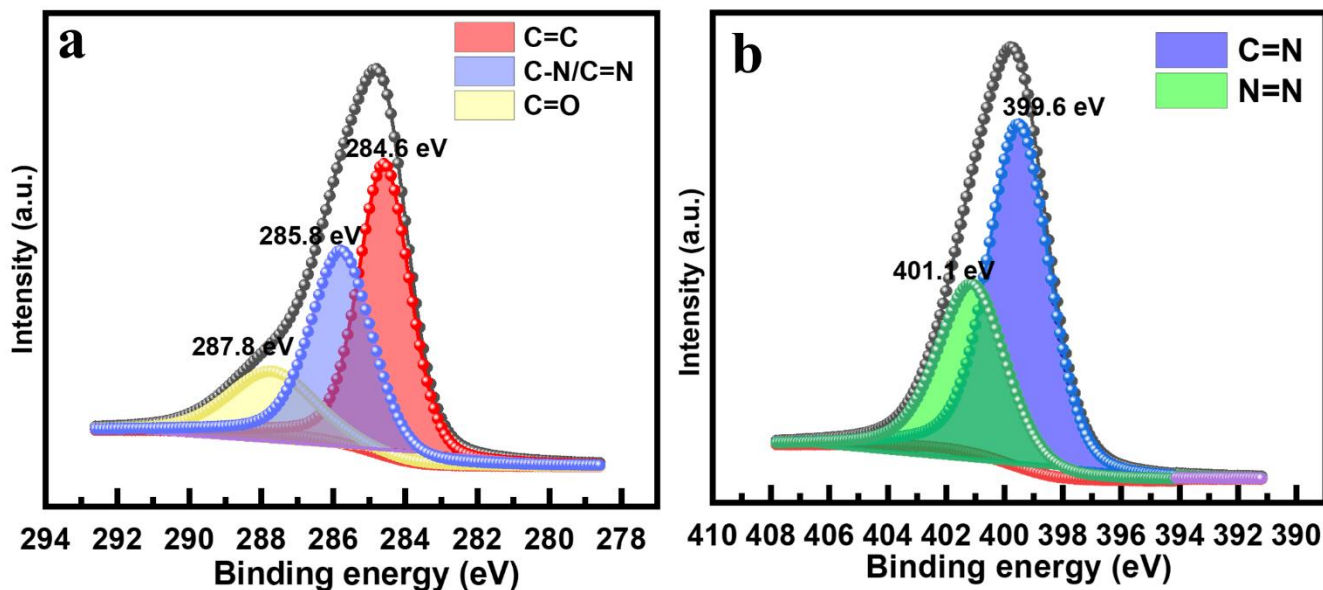


Figure 5-a) Deconvoluted C 1s XPS spectrum b) Deconvoluted N 1s XPS spectrum

$$\text{Atomic percentage} = \frac{\frac{\text{area of the peak}}{\text{sensitivity factor}}}{\sum \frac{\text{area}}{\text{sensitivity factor}}} \times 100 \dots\dots\dots \textcircled{1}$$

From the above formula<sup>35</sup>, the atomic percentage of carbon was found to be 86 and the atomic percentage of nitrogen was found to be 14. The deconvoluted C 1s spectrum (Figure 5a) indicates peaks at 284.6 eV, 285.8 eV and 287.8 eV corresponding to C=C, C=N and C=O functional groups<sup>36</sup>. The deconvoluted N 1s spectrum (Figure 5b) indicates peaks at 399.6 eV and 401.1 eV corresponding to C=N and N=N functional groups in BBP. IR spectrum also revealed a similar functional group composition<sup>34</sup>.

#### 2.4.4 TGA

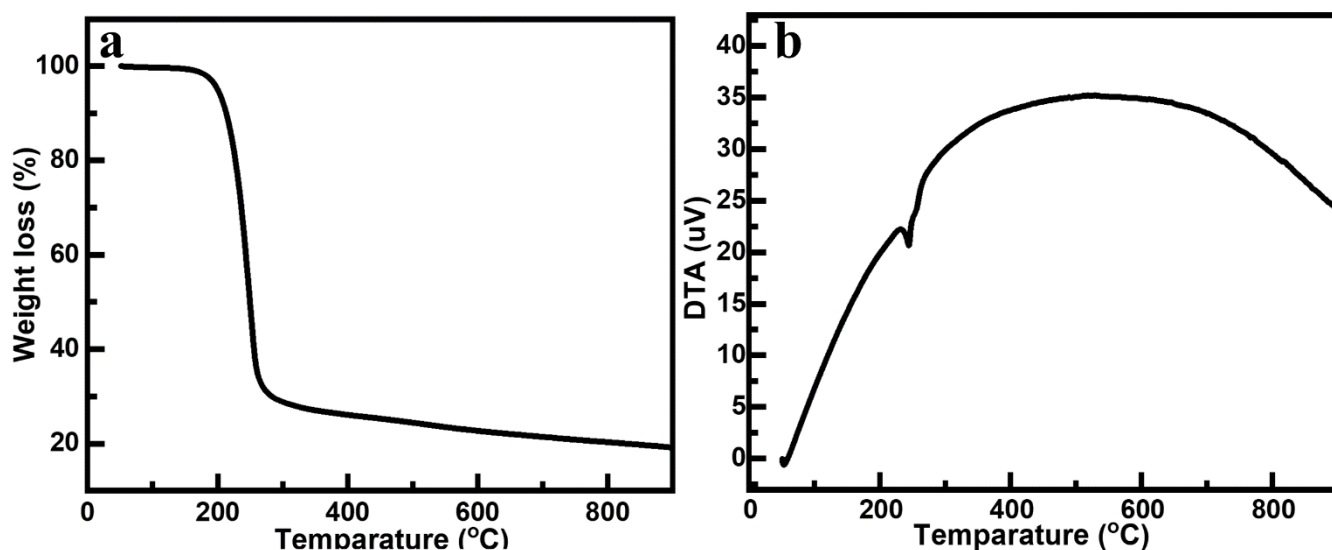


Figure 6-a) TGA of BBP in air b) DTA of BBP in air

The TGA studies are conducted in the temperature range of 50-800 °C in air flow of 200 ml/min. Figure 6a depicts the TGA profile of BBP in air, which show a loss of (~)3% in the region of 50-200 °C corresponding to the loss of adsorbed gases or moisture. A weight loss of 73 % due to edge groups and degradation of framework was observed from 200-300 °C. Further, DTA (Figure 6b) indicates the change in the phase of molecule after 300 °C. An exothermic peak was observed at 210 °C indicating the degradation of the BBP. After 300 °C, a broad plateau was observed suggesting the phase change of the material from organic polymer to carbonaceous material<sup>31</sup>.

### 2.4.5 Mass Spectra (MALDI-TOF)

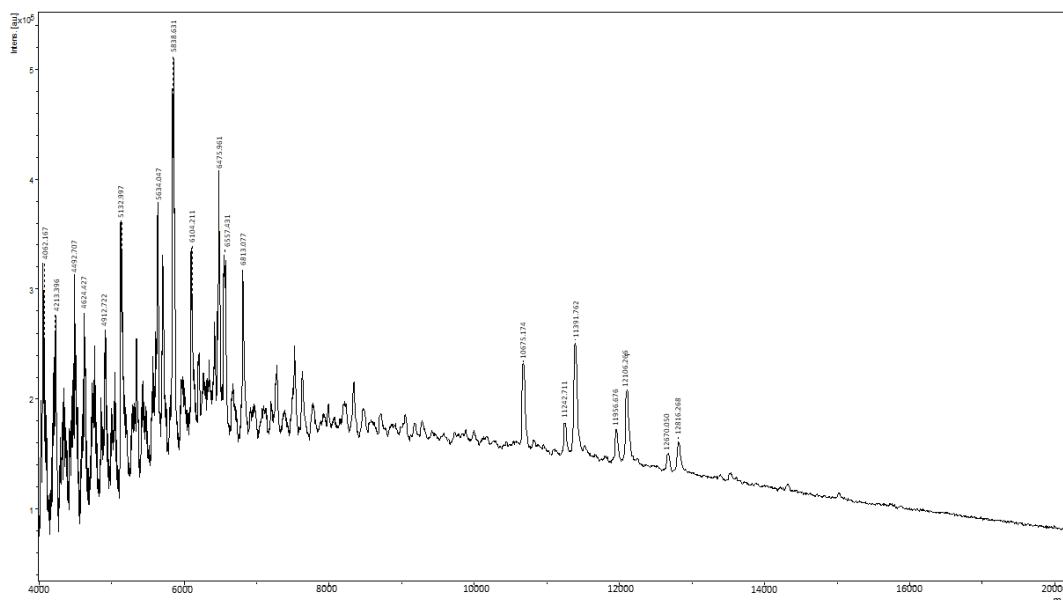


Figure 7-MALDI-TOF of BBP

MALDI-TOF study has been conducted to understand the molecular weight of BBP (Figure 7). The polymer showed molecular weight in the range of 4 kDa- 7kDa.

### 2.4.6 NMR

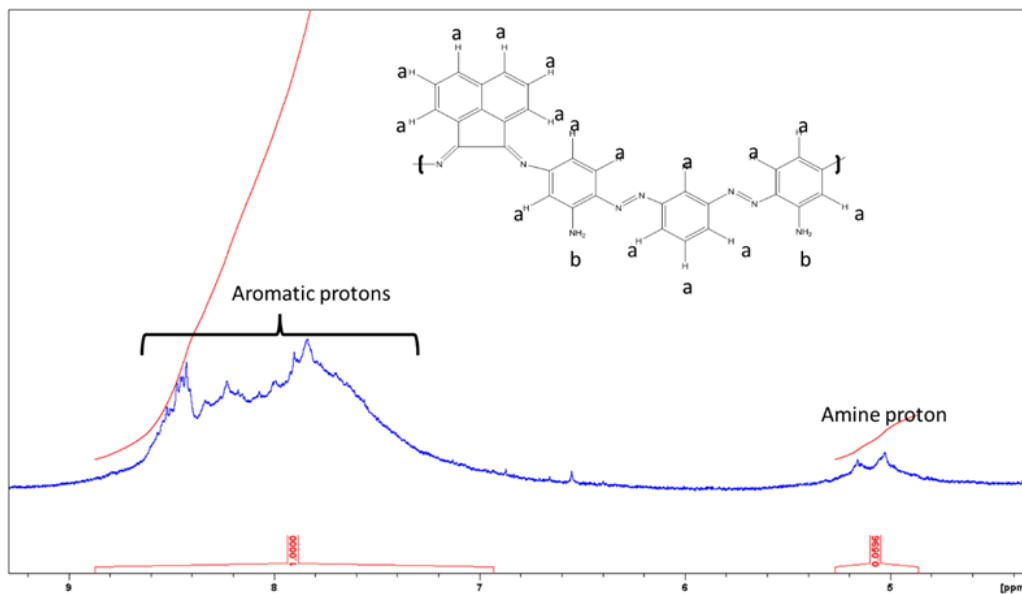


Figure 8-<sup>1</sup>H NMR of BBP

<sup>1</sup>H NMR was conducted to understand the structure of polymer. The NMR result (Figure 8) is as follows: <sup>1</sup>H NMR (dimethyl sulfoxide (DMSO) <sub>d</sub><sub>6</sub>, 400 MHz)  $\delta$ 7.6- $\delta$ 8.6,  $\delta$ 5.1.



## 2.4.7 XRD

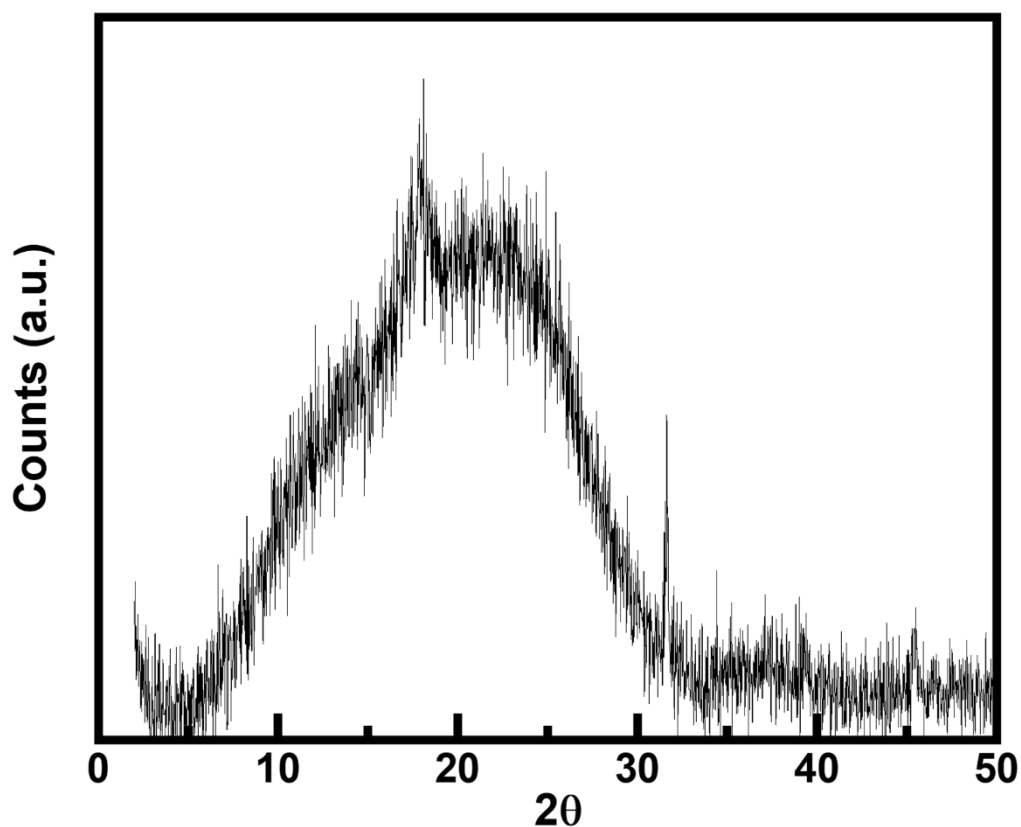


Figure 9-X-ray diffractogram of BBP

Figure 9 shows X-ray diffractogram of BBP. The X-ray diffractogram of BBP shows a broad peak with the peak centered at  $22^\circ$ . Broad peak suggests amorphous nature of BBP<sup>37</sup>. The amorphous nature suggests better movement of lithium ions and availability of more redox sites. Further amorphous nature also indicates that the lithium-ion storage is largely surface controlled. The effect of morphology on electrochemical properties will be discussed later in the light of electrochemical studies.

## 2.5 Electrochemical studies

### 2.5.1 Cyclic voltammetry

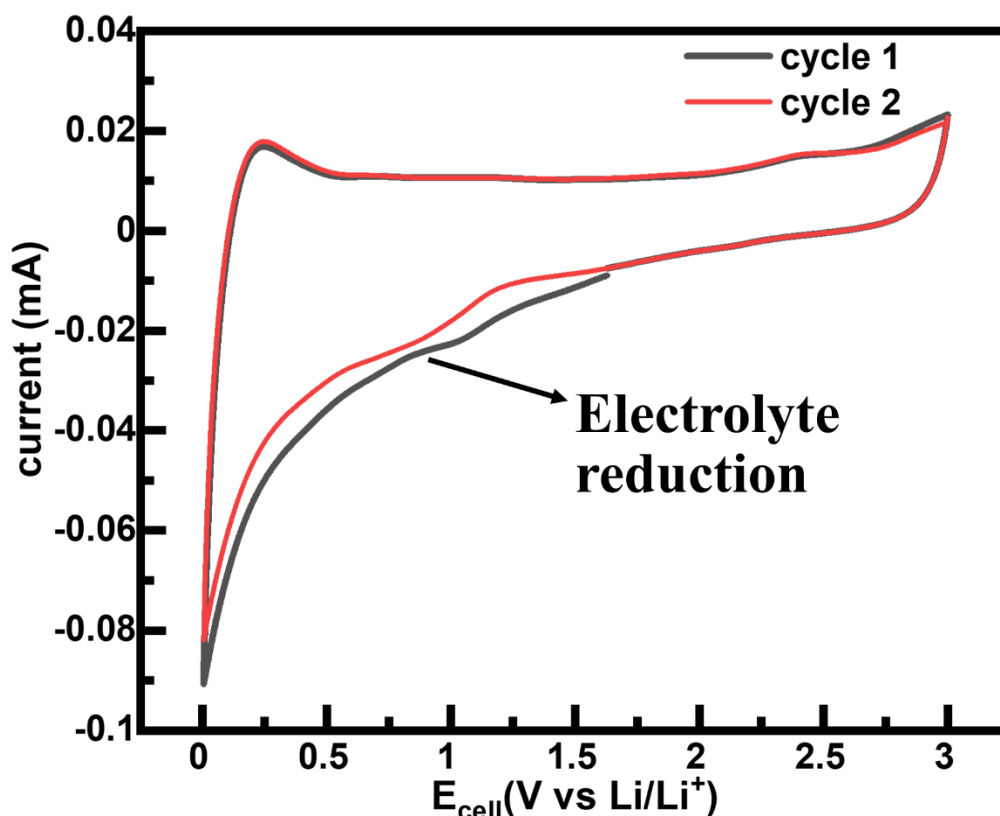


Figure 10-Cyclic voltammogram at 0.1 mV/s of anodic half-cell with BBP as anode

Figure 10 shows the cyclic voltammogram of anodic half-cell with BBP as anode at a scan rate of 0.1 mV/s in the potential range of 5 mV to 3.0 V. The CV shows a broader reduction peak in the first cycle corresponding to the reduction of electrolyte. A peak at 1 V was observed in reduction half which corresponds to the lithiation of C=N. Further, there are no detectable redox peaks after 1 V and between 1 V and 3 V, CV was observed to resemble a rectangle. Hence, the current contribution between 1 V and 3 V can be attributed to the double layer capacitance<sup>38</sup>.

### 2.5.2 Potentiostatic impedance spectroscopy

Figure 11 shows the PEIS of anodic half-cell with BBP as anode. The internal resistance of the anode was found to be 553 ohms before cyclic voltammetry. After cyclic voltammetry the internal resistance of the anode was found to be 81 ohms. The decrease in the internal resistance after CV indicates the formation of robust SEI layer that facilitates the lithium diffusion into the electrode galleries<sup>39,40</sup>.

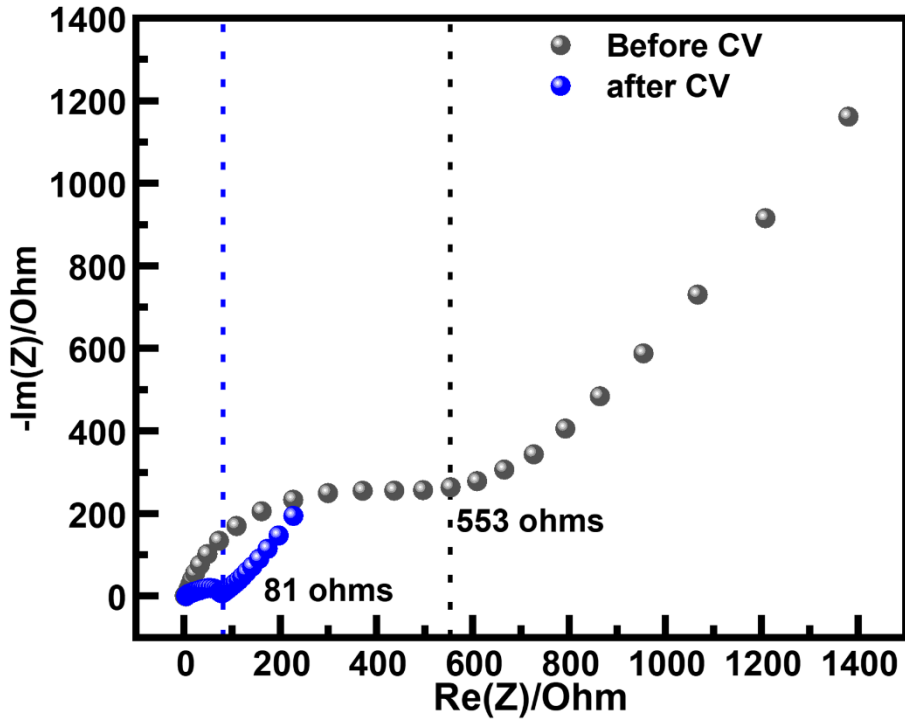


Figure 11-PEIS of anodic half-cell with BBP as anode

### 2.5.3 Dynamic electrochemical impedance spectroscopy

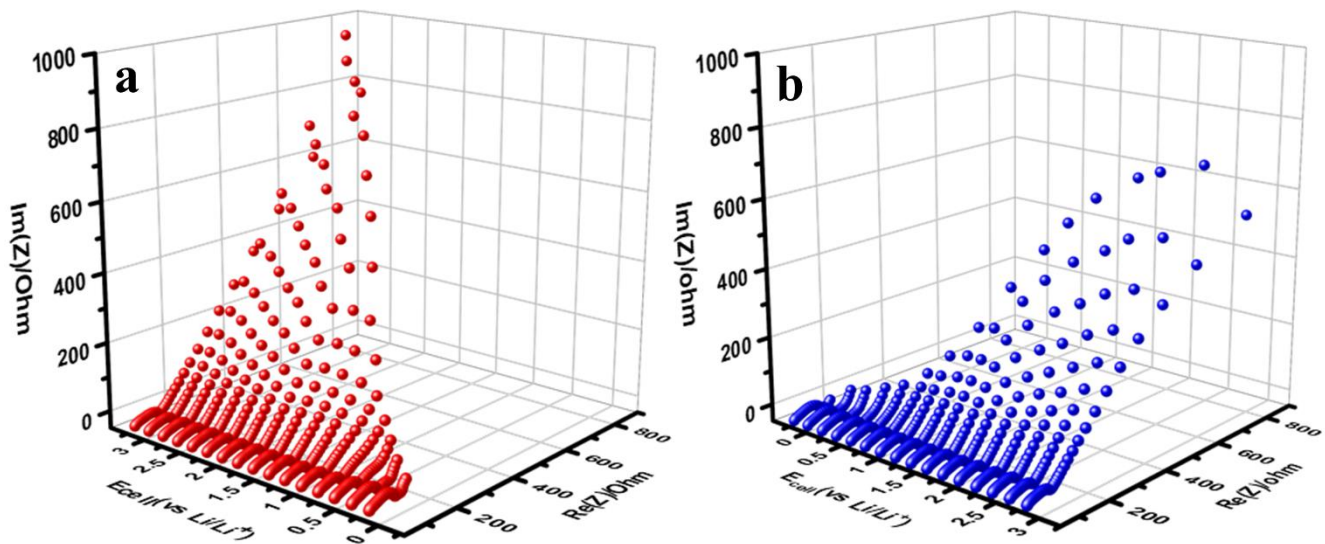


Figure 12-DEIS of anodic half-cell with BBP as anode a) in the lithiation half b) in the delithiation half

Dynamic electrochemical impedance spectroscopy has been performed to understand the impedance at each potential step. Figure 12a shows DEIS in the lithiation half in the potential

range of 3 V to 0.005 V with a potential step of 20 mV. It can be observed that the internal resistance decreases with potential in general and the resistance due to Warburg diffusion component also decreases with voltage. Figure 12b shows DEIS in delithiation half in the potential range of 0.005 V to 3 V with a potential step of 20 mV. Similar trend as in lithiation half was observed. The following circuit was used to obtain the various contributing components to the

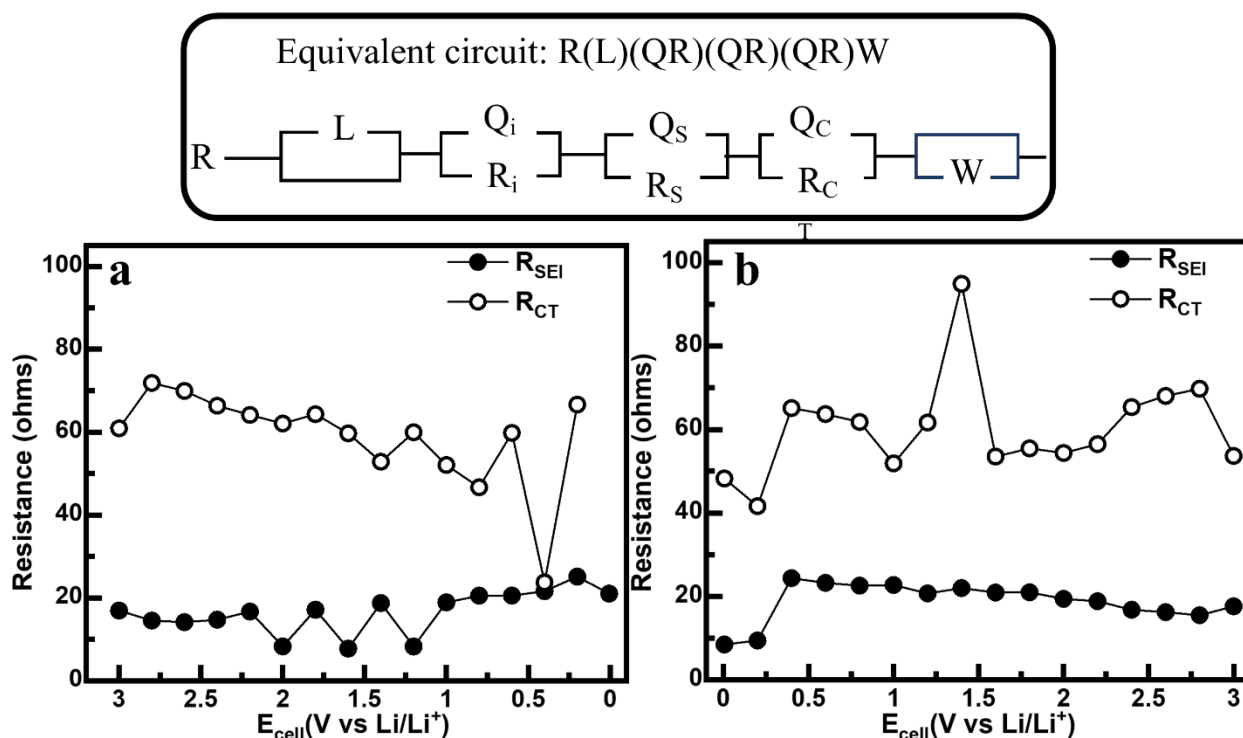


Figure 13-a) charge transfer resistance and SEI resistance in the lithiation half b) charge transfer resistance and SEI resistance in the delithiation half

impedance and the charge-transfer resistance and resistance from SEI were obtained (Figure 13 a and b).

The charge transfer resistance was observed to be in the range of 60-90 ohms in both lithiation and delithiation cases. In the lithiation half, lowest charge transfer resistance was observed between 0.5 V and 0.2 V, indicating easier charge transfer in this potential range. In the delithiation half too, the lowest charge transfer resistance was observed between 0.2 V and 0.5 V. In both the cases of lithiation and delithiation, the charge transfer resistance after 1 V was observed to be relatively high. Further, the SEI resistance was observed to be in the range of 15-25 ohms in both the cases. Lower SEI resistance validates the initial hypothesis about n-type polymers i.e., Due to the lower energy of LUMO in the polymer, excessive reduction of electrolyte on the surface of anode is

restricted and thus leads to the formation of a thinner SEI layer<sup>21</sup>. As resistance is proportional to the length of the resistor, thinner SEI leads to lower SEI resistance. Thus, the lower SEI resistance observed in BBP anodic half-cell confirms the formation of a thinner SEI layer.

#### 2.5.4 Galvanostatic charge discharge studies

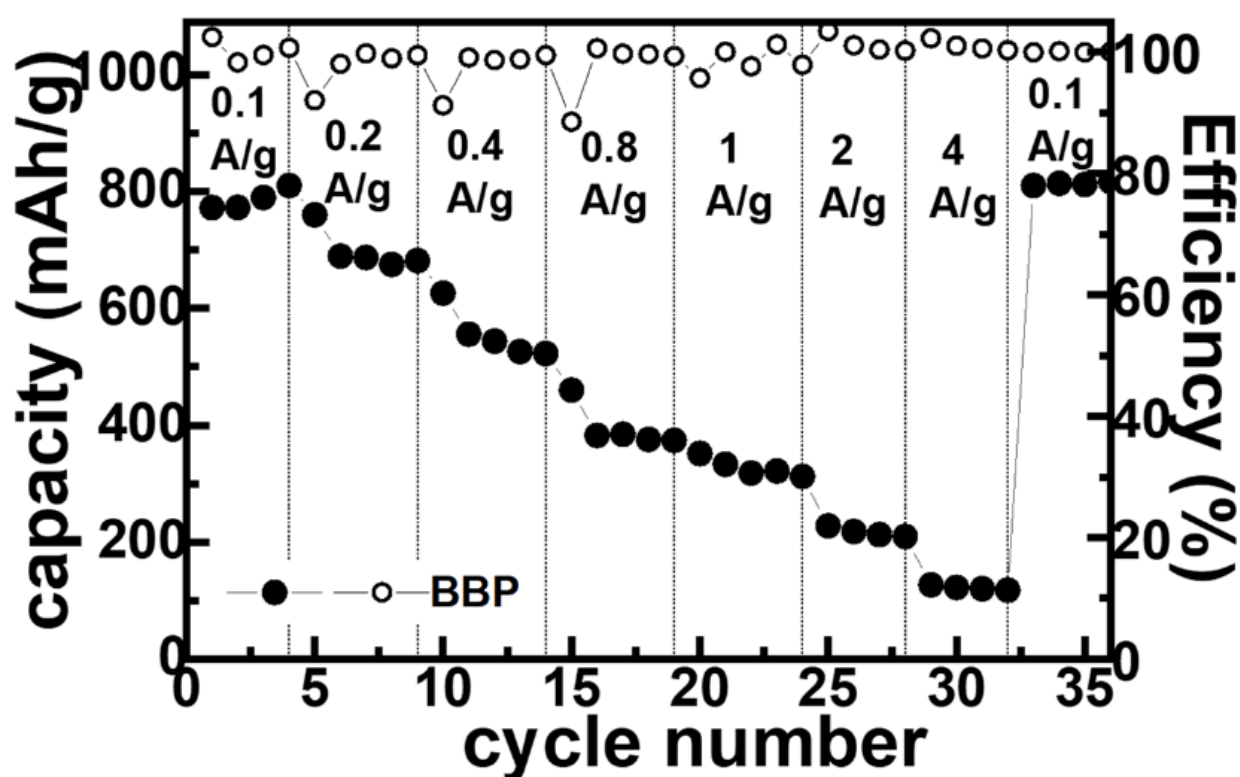


Figure 14-Rate studies of anodic half-cell with BBP as anode.

Table 2-Summary of rate performance of anodic half-cell with BBP as anode

Current density (mA/g)	Capacity (mAh/g)
100	800
200	700
400	550
800	400
1000	350
2000	200
4000	100

Figure 14 shows rate studies of anodic half-cell with BBP as anode active material. The anodic half-cell with BBP anode delivered a reversible capacity of 800 mAh/g at 100 mA/g, 700 mAh/g at 200 mA/g, 550 mAh/g at 400 mA/g, 400 mAh/g at 800 mA/g, 350 mAh/g at 1000 mA/g, 200 mAh/g at 2000 mA/g and 100 mAh/g at 4000 mA/g current densities. Followed by rate studies, long cycling studies were conducted at 400 mA/g current density. Figure 15 a shows the cycle number vs capacity and coulombic efficiency plot of anodic half-cell with BBP as anode. Figure 15 b shows the potential vs capacity plot of anodic half-cell with BBP anode. The discharge capacity was found to be 550 mAh/g after 1500 cycles at 400 mA/g current density with a coulombic efficiency of 99.8%. The potential vs capacity plot shows a nearly linear delithiation profile, which is an indication of minimum redox activity taking place during delithiation. In materials like graphite a plateau can be observed in potential vs capacity plots (chapter 1, section 1.5.3) corresponding to intercalation/deintercalation of Li. However, straight line indicates that there is no chemical reaction taking place during the process. Hence, it can be concluded that the BBP anode does not undergo intercalation, alloying or insertion type reactions that are known in anodes so far. Figure 15 c shows the dQ/dV plot of anodic half-cell with BBP anode at cycles 1, 1000 and 1500 at a current density of 400 mA/g. dQ/dV plot of first cycle shows an almost rectangular plot. At 1000, 1500 cycles, the dQ/dV plot was observed to be broadened indicating higher capacity contribution<sup>41</sup>. The dQ/dV plots also were observed to be rectangular except for the peaks at in the lower voltage regions corresponding to the lithiation of C=C, C=N and N=N.

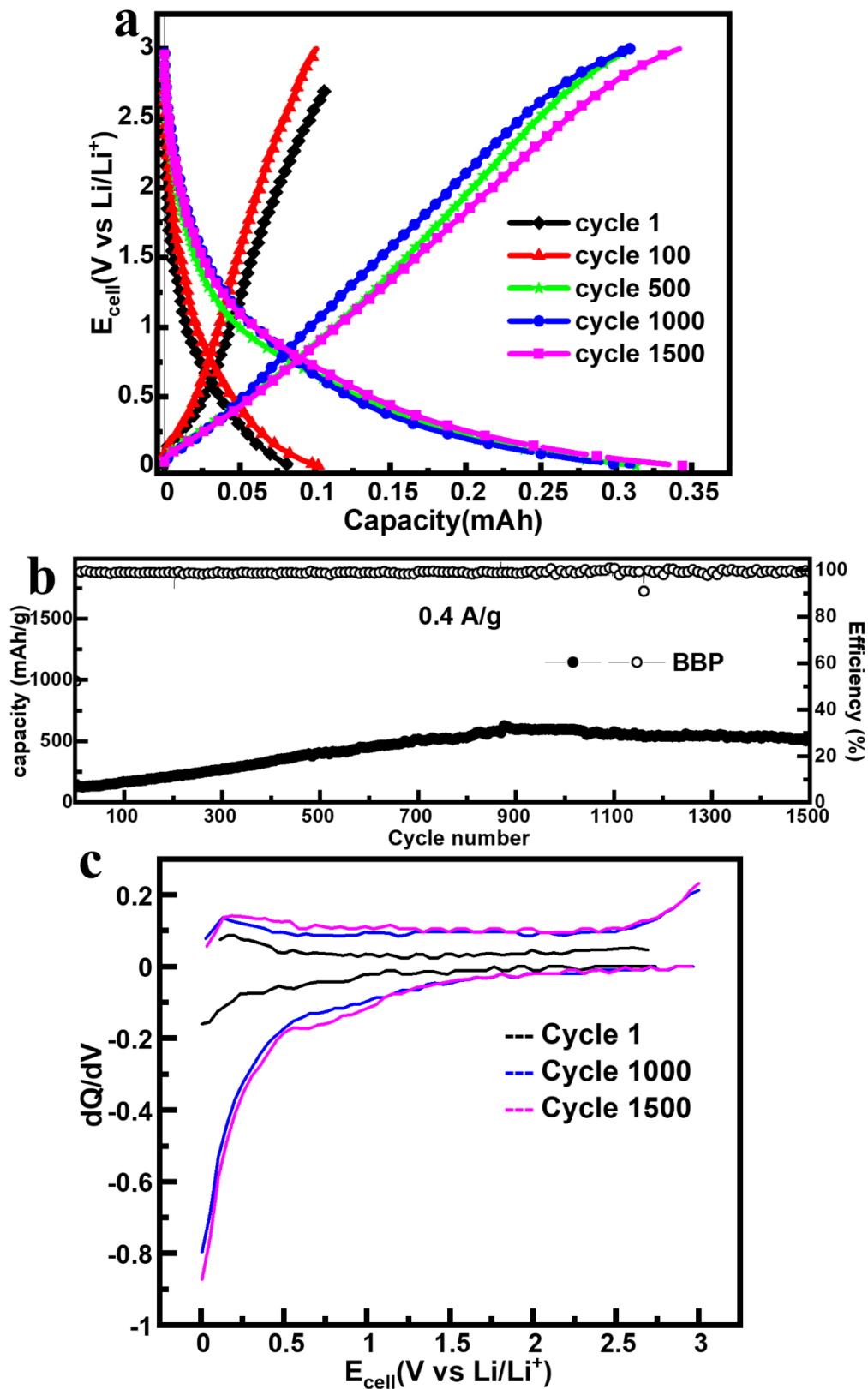


Figure 15-a) Potential vs capacity plot of BBP anodic half-cell b) cycle number vs capacity plot of BBP anodic half-cell c)  $dQ/dV$  plot of BBP anodic half-cell at 1, 1000 and 1500 cycles

## 2.5.5 Kinetic studies

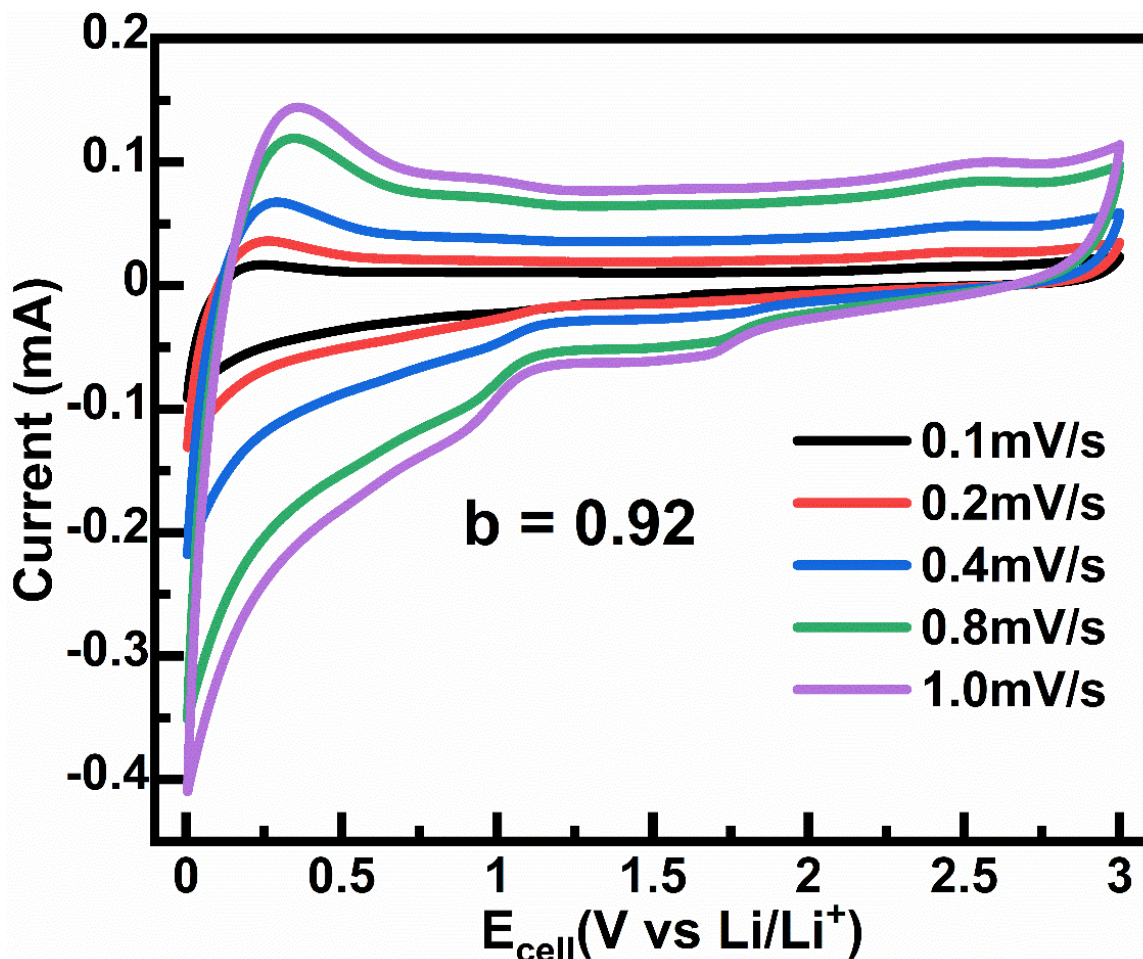


Figure 16-Cyclic voltammograms of BBP based anodic half-cell at various scan rates.

Figure 16 shows cyclic voltammograms of BBP based anodic half-cell at various scan rates. As discussed earlier in the section on cyclic voltammogram, the CV at lower scan rates was observed to exhibit capacitive behavior. At higher scan rates, a peak at 1.6 V is observed in the reduction half corresponding to the lithiation of N=N moiety. BBP based anodic half-cell shows low delithiation overpotential till 0.4 mV/s after which it increases by 0.1 V, which suggests that BBP anode shows higher delithiation overpotential at higher rates. Using the peak current values obtained in the cyclic voltammograms, diffusion coefficient was calculated using Randles-Sevcik equation<sup>42</sup>:

$$i = 2.69 * 10^5 n^{1.5} D^{0.5} A C \nu^{0.5} \dots\dots\dots \textcircled{2}$$

Where,  $i$  is peak current,  $n$  is number of electrons or ions transferred,  $D$  is diffusion coefficient,  $A$  is area of the electrode,  $C$  is concentration of electrolyte and  $\nu$  is scan rate.



Linear fit of peak current and square root of scan rate was plotted (Figure 14) and the diffusion coefficient was evaluated to be  $1.5 \times 10^{-3} \text{ cm}^2/\text{s}$ . The following equation was used to evaluate the contribution of capacitive and diffusive behaviors<sup>24,43</sup>:

$$i = i_{cap} + i_{diff} \dots \dots \dots \textcircled{3}$$

Where  $i_{cap}$  and  $i_{diff}$  are capacitive and diffusive currents.

$$i = k_{cap}v + k_{diff}v^{0.5} \dots \dots \dots \textcircled{4}$$

Where  $k_{cap}$  and  $k_{diff}$  are proportionality constant for capacitance and diffusion respectively. Rearranging equation 4, following equation was obtained:

$$\frac{i}{v^{0.5}} = k_{diff} + k_{cap}v^{0.5} \dots \dots \dots \textcircled{5}$$

Equation 5 was used to calculate the contribution of capacitive and diffusive behaviors by plotting linear fit of  $i/v^{0.5}$  vs  $v^{0.5}$ (Figure 17 a). The slope and intercept values obtained were used to calculate capacitive and diffusive behaviors as shown in equation 4. Figures 17 b shows the contribution of capacitance and diffusive contributions in BBP based anodic half-cell. BBP anodic half-cell predominantly exhibits a capacitive behavior.

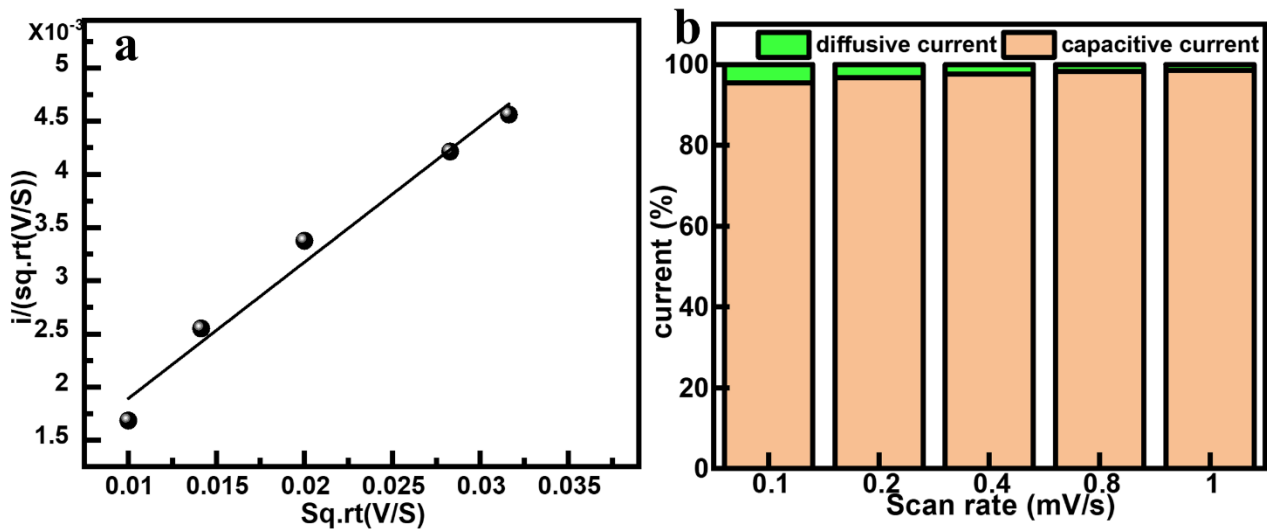


Figure 17-a) Linear fit of  $i/v^{0.5}$  vs  $v^{0.5}$  b) capacitive and diffusive current contributions

As seen in equations 3 and 4, the peak current and scan rate relation can be generalized into a power law<sup>44</sup>:

$$i = kv^b \dots \dots \dots \textcircled{6}$$

Where  $i$  is peak current,  $\nu$  is scan rate and  $b$  is exponent of scan rate. The current response obtained from a cell during cyclic voltammetry is largely dependent on the scan rate applied and the mechanism of charge storage. If the charge mechanism is diffusive, the increase in scan rate does not directly correlate to increase in current. In diffusive controlled materials, it is observed that the  $b$  value is 0.5. In surface-controlled charge storage, the increase in scan rate directly correlated to the increase in current. Hence, the  $b$  value was observed to be 1.0. Equation 6 was employed to determine the  $b$  value by plotting linear fit between  $\log i$  and  $\log \nu$  (Figure 18). The slope obtained i.e.,  $b$  (exponent) value was found to be 0.92 in case of BBP anodic half-cell. This suggests that BBP is tending towards a capacitive behavior.

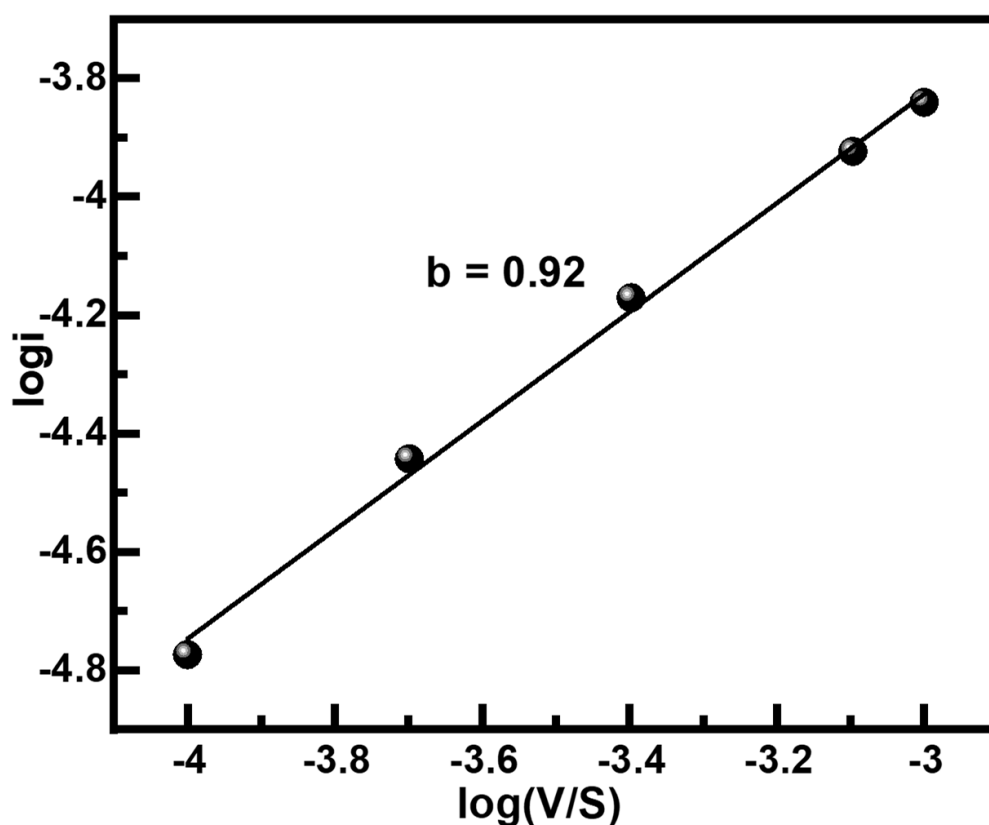


Figure 18-Linear fit of  $\log(V/s)$  vs  $\log i$

### 2.5.6 Theoretical studies

To understand the gradual activation of the BBP anode, molecular models were constructed using material studio software. The lithium storage can happen as per one lithium ion per each C=C, C=N and two lithium ions per N=N. Based on this understanding, the changes in the structure during lithiation (shown in Figure 19) is as follows:

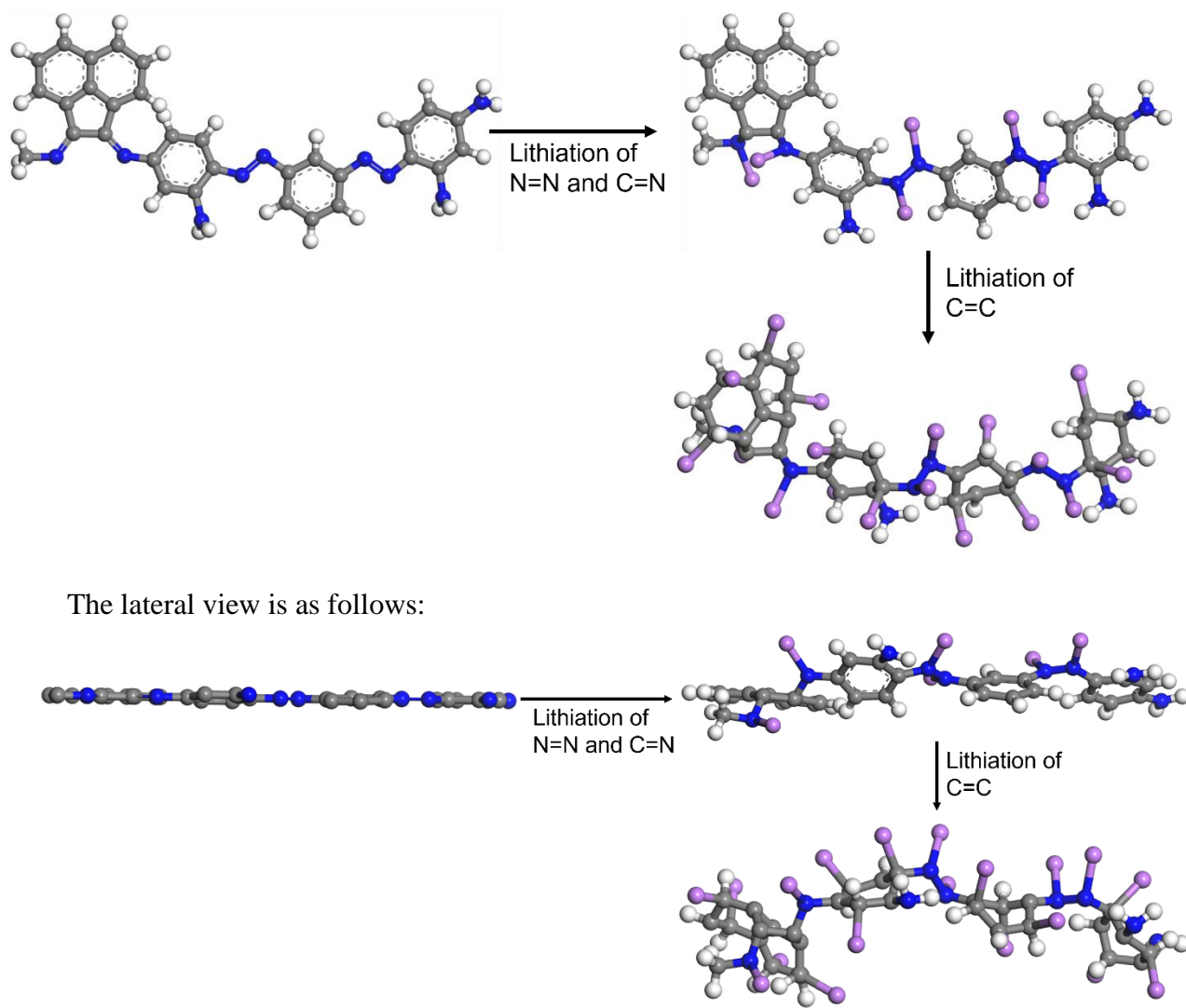


Figure 19-Lithiation scheme of BBP.

After complete lithiation of anode, the morphology of the polymer changes leading to increase in the interlayer spacing and exposure of new redox active sites. This exposure of new active sites leads to the increase in capacity over number of cycles. The cross section FESEM images (shown in Figure 20) of the pristine electrode and cycled electrodes in lithiated state after 1500 cycles are shown in Figure. As expected from the molecular models, The lithiated electrode shows an increased thickness than the pristine electrode indicating the exposure of newer active sites during the cycling

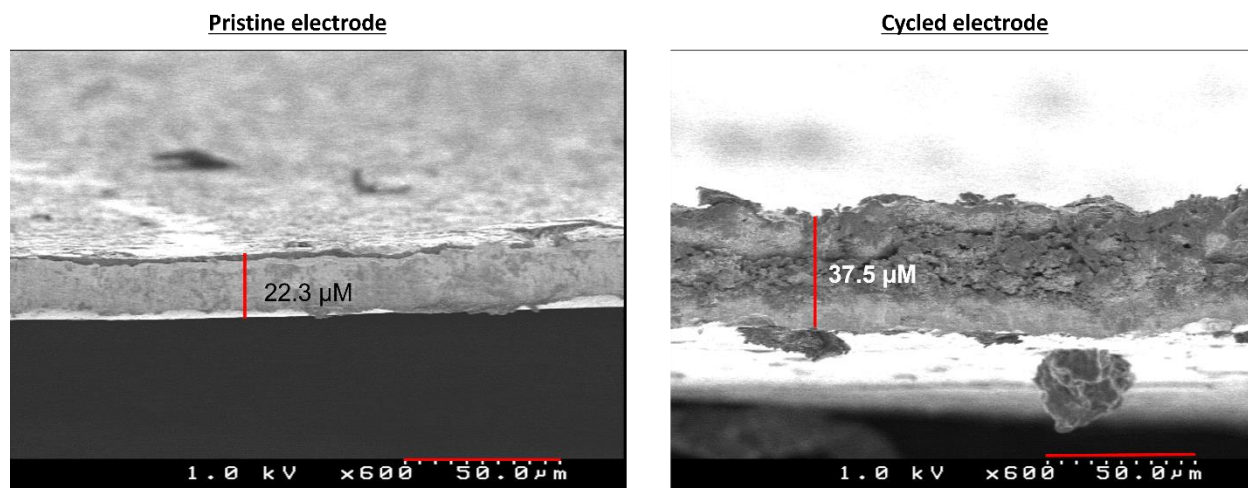


Figure 21-FESEM images of pristine and cycled BBP electrodes

## 2.6 XPS after cycling

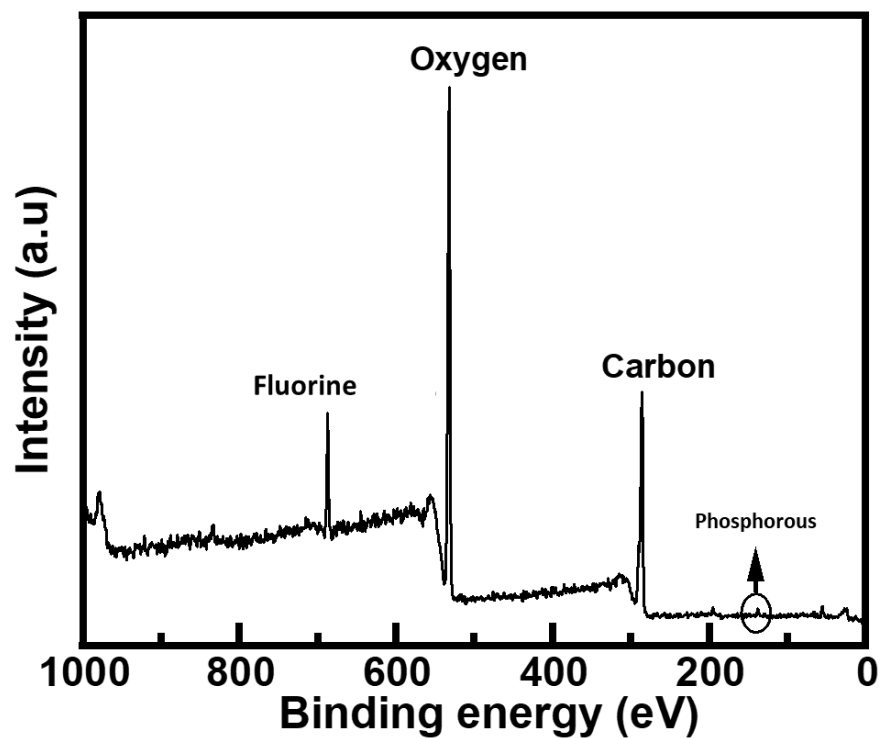


Figure 20-XPS survey spectrum of BBP cycled electrode.

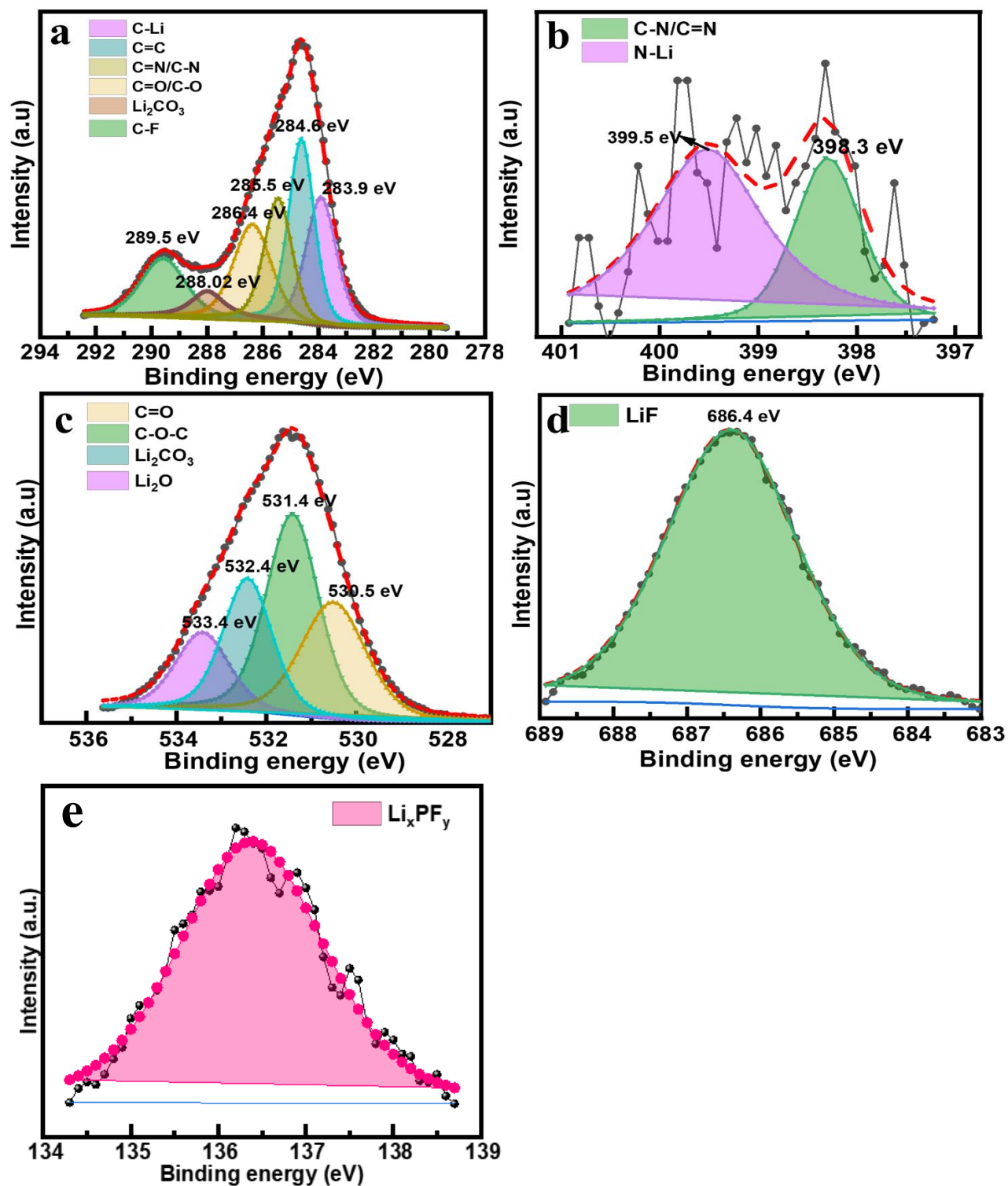


Figure 22-a) C 1s spectra of cycled BBP anode b) N 1s spectra of cycled BBP anode c) O 1s spectra of cycled BBP anode d) F 1s spectra of cycled BBP anode e) P 1s spectra of cycled BBP anode

The cycled anodic half-cell (at 400 mA/g for 1500 cycles) was disassembled in an argon filled glove box ( $O_2$ ,  $H_2O < 0.5\text{ppm}$ ) and the BBP electrode was collected and dried. Figure 21 shows XPS survey spectrum of BBP cycled anode. The survey spectrum shows peaks at 136 eV, 284 eV, 530 eV and 670 eV corresponding to fluorine, carbon, oxygen, and phosphorus elements. Figure 18 shows C 1s, N 1s, O 1s and F 1s XPS spectra of cycled BBP anode. The penetration depth of X-rays in XPS is  $\sim 5$  nm. The fact that nitrogen is detected in XPS indicates that the thickness of SEI formed is  $< 5$  nm. The C 1s spectra (Figure 22a) of cycled BBP anode showed peaks at 283.9 eV, 284.6 eV, 285.5 eV, 286.4 eV, 288.02 eV and 289.5 eV corresponding to C-Li, C=C, C=N/C-N, C=O, C-O-C and  $Li_2CO_3$  respectively<sup>45</sup>. The N 1s spectra (Figure 22b) of cycled BBP anode shows peaks at 398.3 eV and 399.5 eV corresponding to N-Li and C=N respectively<sup>16</sup>. The O 1s spectra (Figure 22c) of cycled BBP anode shows peaks at 530.5 eV, 531.4 eV, 532.4 eV and 533.4 eV corresponding to C=O, C-O-C,  $Li_2CO_3$  and  $Li_2O$ <sup>35</sup>. The F 1s spectra (Figure 22d) of cycled BBP shows a peak at 686.4 eV corresponding to  $LiF$ <sup>35</sup> and the P 1s spectra (Figure 22e) of cycled BBP electrode shows a peak at 136.4 eV. The XPS results suggest that  $Li_2CO_3$ ,  $Li_2O$  and  $LiF$  are the components of SEI in case of cycled BBP electrode<sup>46,47,48,49</sup>.

## 2.7 Conclusion

The synthesis of n-type BIAN-Bismarck brown organic polymer (BBP) was demonstrated. The anodic half-cells fabricated using BBP active material demonstrated good rate performance in galvanostatic charge discharge studies. The anodic half-cell fabricated using BBP anode delivered 550 mAh/g after 1500 cycles at 400 mA/g current density. The effect of using n-type polymer was reflected in lower SEI resistance as observed in DEIS. Owing to the amorphous nature of the polymer and presence of imine, azo groups, the charge transfer resistance was also observed to be lower. Furthermore, the mechanism of charge storage was observed to be capacitive in nature. The diffusive contribution was observed to be minimum at all scan rates. The relatively high capacity and better electrochemical activity makes this a prospective anodic material<sup>50,51</sup>.

## References

- 1 Y. Sui, C. Liu, R. C. Masse, Z. G. Neale, M. Atif, M. AlSalhi and G. Cao, *Energy Storage Mater.*, 2020, **25**, 1–32.
- 2 Y. Pan, S. Ge, Z. Rashid, S. Gao, A. Erwin, V. Tsukruk, K. D. Vogiatzis, A. P. Sokolov,

- 
- H. Yang and P. F. Cao, *ACS Appl. Energy Mater.*, 2020, **3**, 3387–3396.
- 3 B. Boz, T. Dev, A. Salvadori and J. L. Schaefer, *J. Electrochem. Soc.*, 2021, **168**, 090501.
- 4 A. Manthiram, *Nat. Commun.*, 2020, **11**, 1–9.
- 5 D. Deng, *Energy Sci. Eng.*, 2015, **3**, 385–418.
- 6 J. Asenbauer, T. Eisenmann, M. Kuenzel, A. Kazzazi, Z. Chen and D. Bresser, *Sustain. Energy Fuels*, 2020, **4**, 5387–5416.
- 7 P. U. Nzereogu, A. D. Omah, F. I. Ezema, E. I. Iwuoha and A. C. Nwanya, *Appl. Surf. Sci. Adv.*, 2022, **9**, 100233.
- 8 M. S. Balogun, Y. Luo, W. Qiu, P. Liu and Y. Tong, *Carbon N. Y.*, 2016, **98**, 162–178.
- 9 A. Tornheim, R. Sahore, M. He, J. R. Croy and Z. Zhang, *J. Electrochem. Soc.*, 2018, **165**, A3360–A3368.
- 10 H. Zhu, J. Yin, X. Zhao, C. Wang and X. Yang, *Chem. Commun.*, 2015, **51**, 14708–14711.
- 11 Y. Yang, W. Yuan, W. Kang, Y. Ye, Y. Yuan, Z. Qiu, C. Wang, X. Zhang, Y. Ke and Y. Tang, *Nanoscale*, 2020, **12**, 7461–7484.
- 12 K. Geng, T. He, R. Liu, S. Dalapati, K. T. Tan, Z. Li, S. Tao, Y. Gong, Q. Jiang and D. Jiang, *Chem. Rev.*, 2020, **120**, 8814–8933.
- 13 H. Chen, Y. Zhang, C. Xu, M. Cao, H. Dou and X. Zhang, *Chem. - A Eur. J.*, 2019, **25**, 15472–15476.
- 14 S. M. Zeng, X. X. Huang, Y. J. Ma and L. J. Zhi, *Xinxing Tan Cailiao/New Carbon Mater.*, 2021, **36**, 1–18.
- 15 W. Wang, V. S. Kale, Z. Cao, S. Kandambeth, W. Zhang, J. Ming, P. T. Parvatkar, E. Abou-Hamad, O. Shekhah, L. Cavallo, M. Eddaoudi and H. N. Alshareef, *ACS Energy Lett.*, 2020, **5**, 2256–2264.
- 16 Z. Lei, Q. Yang, Y. Xu, S. Guo, W. Sun, H. Liu, L. P. Lv, Y. Zhang and Y. Wang, *Nat. Commun.*, 2018, **9**, 1–13.
-

- 
- 17 S. Goriparti, E. Miele, F. De Angelis, E. Di Fabrizio, R. Proietti Zaccaria and C. Capiglia, *J. Power Sources*, 2014, **257**, 421–443.
  - 18 H. Cheng, J. G. Shapter, Y. Li and G. Gao, *J. Energy Chem.*, 2021, **57**, 451–468.
  - 19 A. Shafiee, M. M. Salleh and M. Yahaya, *Sains Malaysiana*, 2011, **40**, 173–176.
  - 20 X. K. Kong and Q. W. Chen, *Phys. Chem. Chem. Phys.*, 2013, **15**, 12982–12987.
  - 21 A. Gupta, R. Badam, A. Nag, T. Kaneko and N. Matsumi, *ACS Appl. Energy Mater.*, 2021, **4**, 2231–2240.
  - 22 S. G. Patnaik, R. Vedarajan and N. Matsumi, *J. Mater. Chem. A*, 2017, **5**, 17909–17919.
  - 23 Y. Jiang and J. Liu, *Energy Environ. Mater.*, 2019, **2**, 30–37.
  - 24 V. Augustyn, P. Simon and B. Dunn, *Energy Environ. Sci.*, 2014, **7**, 1597–1614.
  - 25 Y. Gao, J. Zhang, N. Li, X. Han, X. Luo, K. Xie, B. Wei and Z. Xia, *J. Mater. Chem. A*, 2020, **8**, 7756–7764.
  - 26 D. Rodríguez-San-Miguel, C. Montoro and F. Zamora, *Chem. Soc. Rev.*, 2020, **49**, 2291–2302.
  - 27 J. Li, X. Jing, Q. Li, S. Li, X. Gao, X. Feng and B. Wang, *Chem. Soc. Rev.*, 2020, **49**, 3565–3604.
  - 28 H. Zhao, D. Luo, H. Xu, W. He, B. Ding, H. Dou and X. Zhang, *J. Mater. Sci.*, , DOI:10.1007/s10853-022-07115-w.
  - 29 O. Buyukcakir, J. Ryu, S. H. Joo, J. Kang, R. Yuksel, J. Lee, Y. Jiang, S. Choi, S. H. Lee, S. K. Kwak, S. Park and R. S. Ruoff, *Adv. Funct. Mater.*, 2020, **30**, 1–11.
  - 30 F. Jiang, Y. Wang, T. Qiu, Y. Zhang, W. Zhu, C. Yang, J. Huang, Z. Fang and G. Dai, *ACS Appl. Mater. Interfaces*, 2021, **13**, 48818–48827.
  - 31 X. Liu, J. Zhang, S. Guo and N. Pinna, *J. Mater. Chem. A*, 2016, **4**, 1423–1431.
  - 32 T. P. Jayakumar, R. Badam and N. Matsumi, *ACS Appl. Energy Mater.*, 2020, **3**, 3337–3346.



- 
- 33 S. G. Patnaik, R. Vedarajan and N. Matsumi, *ACS Appl. Energy Mater.*, 2018, **1**, 1183–1190.
- 34 Y. Xu, Z. Li, F. Zhang, X. Zhuang, Z. Zeng and J. Wei, *RSC Adv.*, 2016, **6**, 30048–30055.
- 35 K. S. Patnaik, R. Badam, Y. Peng, K. Higashimine, T. Kaneko and N. Matsumi, *Chem. Commun.*, 2021, **57**, 13704–13707.
- 36 X. Xue, J. Luo, L. Kong, J. Zhao, Y. Zhang, H. Du, S. Chen and Y. Xie, *RSC Adv.*, 2021, **11**, 10688–10698.
- 37 Z. Chen, A. Jaworski, J. Chen, T. M. Budnyak, I. Szewczyk, A. Rokicińska, R. Dronskowski, N. Hedin, P. Kuśtrowski and A. Slabon, *Dalt. Trans.*, 2021, **50**, 6857–6866.
- 38 M. H. Braga, N. S. Grundish, A. J. Murchison and J. B. Goodenough, *Energy Environ. Sci.*, 2017, **10**, 331–336.
- 39 A. Habekost, *World J. Chem. Educ.*, 2020, **9**, 14–21.
- 40 F. Linsenmann, D. Pritzl and H. A. Gasteiger, *J. Electrochem. Soc.*, 2021, **168**, 010506.
- 41 I. Bloom, A. N. Jansen, D. P. Abraham, J. Knuth, S. A. Jones, V. S. Battaglia and G. L. Henriksen, *J. Power Sources*, 2005, **139**, 295–303.
- 42 S. Huang, Z. Li, B. Wang, J. Zhang, Z. Peng, R. Qi, J. Wang and Y. Zhao, *Adv. Funct. Mater.*, 2018, **28**, 1–10.
- 43 E. Kazyak, K. H. Chen, Y. Chen, T. H. Cho and N. P. Dasgupta, *Adv. Energy Mater.*, 2022, **12**, 1–12.
- 44 S. Haldar, K. Roy, S. Nandi, D. Chakraborty, D. Puthusseri, Y. Gawli, S. Ogale and R. Vaidhyanathan, *Adv. Energy Mater.*, 2018, **8**, 1–11.
- 45 K. Duan, J. Ning, L. Zhou, W. Xu, C. Feng, T. Yang, S. Wang and J. Liu, *Chem. Commun.*, 2020, **56**, 8420–8423.
- 46 Z. Zhao, W. Chen, S. Impeng, M. Li, R. Wang, Y. Liu, L. Zhang, L. Dong, J. Unruangsri, C. Peng, C. Wang, S. Namuangruk, S. Y. Lee, Y. Wang, H. Lu and J. Guo, *J. Mater. Chem. A*, 2020, **8**, 3459–3467.
-

- 47 E. Peled and S. Menkin, *J. Electrochem. Soc.*, 2017, **164**, A1703–A1719.
- 48 N. L. Hamidah, F. M. Wang and G. Nugroho, *Surf. Interface Anal.*, 2019, **51**, 345–352.
- 49 M. B. Pinson and M. Z. Bazant, *J. Electrochem. Soc.*, 2013, **160**, A243–A250.
- 50 B. S. Mantripragada, R. Badam and N. Matsumi, *ACS Appl. Energy Mater.*, 2022, **5**, 6903–6912.
- 51 B. S. Mantripragada, R. Badam and N. Matsumi, *ECS Meet. Abstr.*, 2021, **MA2021-01**, 104–104.

## **Chapter 3. BIAN based organic polymer as high performing anode for lithium-ion batteries.**

### **3.1 Abstract**

Lithium-ion batteries are heralded as the potential candidates for the large-scale energy storage applications. Low specific capacity or poor cyclability of commonly used anodes limit the extensive application of lithium-ion batteries. In this context, organic molecules can offer a potential solution to extend the scope of lithium-ion battery application. In this chapter, the synthesis and electrochemical properties of a nitrogen rich, n-type organic polymer bearing BIAN and melamine moieties (PBM) were demonstrated. The PBM exhibits a porosity of 1.5 nm and displays excellent electrochemical performance in terms of its rate capability, cycling behavior and capacity. The anodic half-cell of PBM active material delivers specific capacities of 850 mAh/g at 400 mA/g, 740 mAh/g at 750 mA/g and 300 mAh/g at 1000 mA/g current densities with an excellent cyclability over 3000, 2000 and 1100 cycles respectively at each current density. Thus, this material exhibits a promising candidacy as anodic material in lithium-ion batteries.

## 3.2 Introduction

Post industrial revolution, the energy requirements of the world have increased exponentially. In the last three centuries, fossil fuel-based energy has been the key sources of energy. However, limited availability of resources, rising prices of fossil fuels, and the associated environmental concerns<sup>1</sup> implicate change in the direction of our energy quest towards sustainable resources. Energy storage stands as the key bottle neck in tapping the intermittent energy from renewable sources. In the latter half of 20<sup>th</sup> century, rechargeable lithium-ion batteries have been developed. With higher energy density, higher operating voltages, limited self-discharging and low memory effect, these batteries were proved to be very efficient.<sup>2,3,4</sup> However, low theoretical capacity and power density of commercially used graphite anode limits its applications in high energy and power density applications.<sup>5,5</sup> Hence, to increase the scope of the application of lithium-ion batteries, it is imperative to develop the anodes that can deliver higher specific capacity. Though graphene based anodic materials exhibited 3-4 times higher capacity than graphite, expensive synthetic processes limit the commercialisation<sup>7</sup>. In this regard, Dey et al. found that lithium can electrochemically alloy with metals like Sn, Pb, Al, Au, Pt, Zn, Cd, Ag and Mg.<sup>6</sup> In 1990's Dahn et al., reported the utilization of Si based composites as anodic materials in lithium-ion batteries.<sup>7</sup> However, the charge storage in these systems is based on alloy / de-alloy mechanism.<sup>8,9,10,11,12</sup> This mechanism leads to a huge volume expansion in lithiation followed by contraction during delithiation.<sup>13,14</sup> This causes the loss of conductivity and unstable SEI generation. Hence, much effort is being directed towards optimizing the morphology of active material<sup>15,16,17,18,19</sup> and towards developing polymeric materials<sup>20,21,22,23,3</sup> which can negotiate volume change. The lack of electrical conductivity and expansion of the anode limits the application of metal-chalcogen type anodes (ex. MoS<sub>2</sub> etc.,) which work on replacement type reaction mechanism.<sup>24,25</sup>

The volume expansion problem in anodic active materials like silicon which undergo alloy / de-alloy mechanism has proven to be very challenging and the known diffusion-based anodes suffer with low power density. In the traditional anodes like graphite, one of the key factors that limit the capacity, and the power density is the long diffusion length<sup>26</sup> and the lack of redox active groups.<sup>27</sup>

Hence the modification of the morphology of the material to obtain a short diffusion length can improve the capacity and cyclability.<sup>28,29</sup> Further, the non-polar nature of the anodes does not support the exploitation of positive charge and small size of lithium ions. Hence, introducing polarity in the active material can improve the performance of the anode because of pseudo-

capacitance.<sup>30</sup> Thus, a suitable alliance of shorter diffusion length and pseudo-capacitance can be an alluring prospective. In this regard, organic materials have not been given their due attention. Organic molecules provide a unique opportunity to tailor the polarity by various functional groups<sup>31</sup> and therefore exploit the positive charge and the relatively smaller size of lithium ion by introducing the aspect of pseudo capacitance. Further, it is known that by extension of  $\pi$ -conjugation length, inclusion of electron-deficient groups, the LUMO of material can be lowered by combining these two approaches to obtain n-type conducting materials. The porosity of these materials can be tuned by choosing reactants with appropriate geometry.<sup>32,33</sup> Apart from porosity, the polarity of the material can be tailored as per the need by choosing appropriate reactants. This aspect opens a wide possibility of bringing down the limitations of lithium-ion battery anodes because of diffusion and alloy / de-alloy. Hence, the alliance of diffusion and pseudo-capacitance can effectively be brought out with these materials. Heng et al., demonstrated organic anodic active materials derived by the reaction of 2,4,6-triaminopyrimidine with 1,4-phthalaldehyde and 1,3,5-triformylbenzene<sup>34</sup> respectively. The anodic half-cells with the two active materials delivered a reversible discharge capacity of up to 401.3 and 379.1 mAh/g. Yang et al. synthesized an anodic active material based on polyporphyrin (TThPP) linked by 4-thiophenophenyl synthesized through an in-situ chemical oxidative polymerization on the surface of copper foil. The polyporphyrin based material delivered reversible capacity up to 666 mAh/g<sup>35</sup>. Halder et al. synthesized a triazole-triformyl phloroglucinol based active material which delivered 720 mAh/g<sup>36</sup>. Although, such materials demonstrated a high capacity and coulombic efficiency, high cost of the starting materials hinder the commercialization of these materials.

In this work, a low cost, easy to synthesize, nitrogen rich organic polymer as a potential candidate for lithium-ion battery anodes was demonstrated. As discussed earlier, nitrogen leads to pseudo-capacitance<sup>37,38</sup> and layered structure with microporosity of this polymer, which leads to shorter diffusion distance. Besides, due to the presence of electron rich BIAN moiety and many imino groups, the LUMO of obtained material is lower resulting in a n-type conjugated polymer. The mechanism of charge storage was observed to be 50% diffusion based and 50% capacitance based. Furthermore, the anodic half-cell delivers a high capacity of 740 mAh/g and was stable for 2000 cycles with a coulombic efficiency of above 99%. A 14-electron redox process during the intercalation and deintercalation was supported by computational studies through dmol<sup>3</sup>.

### 3.3 Experimental section

#### 3.3.1 Materials

Acenaphthoquinone, melamine, 1,4 dioxane, mesitylene and N-methyl pyrrolidone (NMP) were purchased from Tokyo chemical industries, Ltd. and were used without further purification. 1.0 M LiPF<sub>6</sub> (50/50) ethylene carbonate/diethyl carbonate (EC/DEC) electrolyte and PVDF binder (molecular weight: 540,000) were purchased from Sigma-Aldrich. Battery-grade acetylene black was purchased from Denka Japan Private Co., Ltd. Copper foil of thickness of 20 μm was purchased from the Nilaco corporation.

**Fourier transform-infrared spectrometer measurements.** The FT-IR spectra were recorded using a PerkinElmer 100 FT-IR spectrometer. The spectra were averaged over 50 scans with a resolution of 2 cm<sup>-1</sup>.

**NMR measurements:** <sup>1</sup>H NMR spectra were recorded with a Bruker AVANCE II 400 MHz spectrometer. In the spectra, the respective chemical shifts are depicted in ppm according to the protons of the deuterated solvent used as an internal standard.

**X-ray photo electron spectroscopy.** X-ray photoelectron spectroscopy (XPS) measurements were conducted on a Fisons instruments S-probe TM 2803 instrument.

**Field emission scanning electron microscopy (FESEM).** A Hitachi S-4500 field emission scanning electron microscopy (FESEM) instrument was used to obtain the scanning electron microscopy (SEM) images of respective anodes before and after fabrication at 1.0 kV voltage.

**BET measurements.** The surface area and pore size distributions were measured on BELSORP mini, accelerated surface area and porosity analyzer.

**Transmission electron microscopy.** TEM images were acquired by JOEL H7100.

**Thermogravimetric analysis.** TGA was recorded using Hitachi STA7200 thermal analysis system at a heating rate of 10°C/min and a nitrogen flow rate of 200 ml/min.

**X-ray diffraction.** Powder XRD studies were conducted on Smart Lab X-Ray Diffractometer, Rigaku with Cu Kα radiation ( $\lambda = 0.154$  nm, over the 2θ range of 2°–45° with a step size of 0.02°).

**Elemental dispersive X-ray scattering.** EDX spectra were recorded in TM3030plus at 15 kV.

**Theoretical studies.** The theoretical calculations were based on density functional theory in the dmol<sup>3</sup> module of the material studio. The Gibbs free energy was applied to determine the most stable lithiated state.  $\Delta G$  is evaluated using the following equation:

$$\Delta G = E_{Li-polymer} - E_{polymer}$$

Where  $E_{Li-cof}$  is the energy of lithiated PBM and  $E_{cof}$  is the energy of PBM in unlithiated state.

### 3.3.2 Electrochemical studies.

#### 3.3.2a Electrode preparation and cell fabrication:

PBM, PVDF and acetylene black were taken in 60%, 20% and 20% weight percentages respectively and the slurry was prepared in NMP using kakuhunter ball mill. The homogenous slurry thus obtained was coated on a copper foil using a doctor blade (coating thickness: 0.1 mm). The electrode was dried under vacuum at 80°C for about 12 hours and was calendared to 0.06 mm thickness at 80°C. Disks of 17 mm diameter were punched from the calendared electrode sheet. 2025 type coin cells were fabricated in an argon filled glove box ( $O_2, H_2O < 0.5$  ppm) using PBM electrode as anode, lithium metal foil as counter electrode, polypropylene separator (25  $\mu$ m, celgard) and 1.0 M  $LiPF_6$  (50/50) ethylene carbonate/diethyl carbonate (EC/DEC) as electrolyte. The cells were rested for about 8 hours before measurements.

#### 3.3.2b Electrochemical measurements.

All electrochemical measurements were performed in the potential range of 5 mV to 3.0 mV (vs  $Li/Li^+$ ) at 25°C. Cyclic voltammetry was performed in biologic VSP workstation at 0.1, 0.2, 0.4, 0.6, 0.8 and 1.0 mV/s scan rates. Potentiostatic electrochemical impedance spectroscopy was performed in a frequency range of 10 MHz to 0.1 Hz. Galvanostatic charge-discharge measurements were conducted in biologic battery cycling system at various current densities.

### 3.4 Synthesis of PBM

Acenaphthoquinone (546 mg, 3 mmol) and melamine (252 mg, 2 mmol) were dispersed in about 5 ml of 1:1 1,4 dioxane and mesitylene. 0.4 ml of acetic acid was added to the suspension. The mixture was then refluxed at 105 °C for about 72 hours. A dark yellow precipitate was obtained after the reaction. The precipitate obtained was washed with copious amount of THF and DMF, dried at 80°C under vacuum for about 12 hours. The yield obtained was about 74 %.  $^1\text{H}$  NMR (DMSO  $d_6$ , 400 MHz)  $\delta$  8.45 (dd,  $J = 8.3, 0.7$  Hz, 2H),  $\delta$  8.05 (dd,  $J = 6.8, 0.7$  Hz, 2H) and  $\delta$  7.92 (t,  $J = 6.9$  Hz, 2H)

### 3.5 Characterization

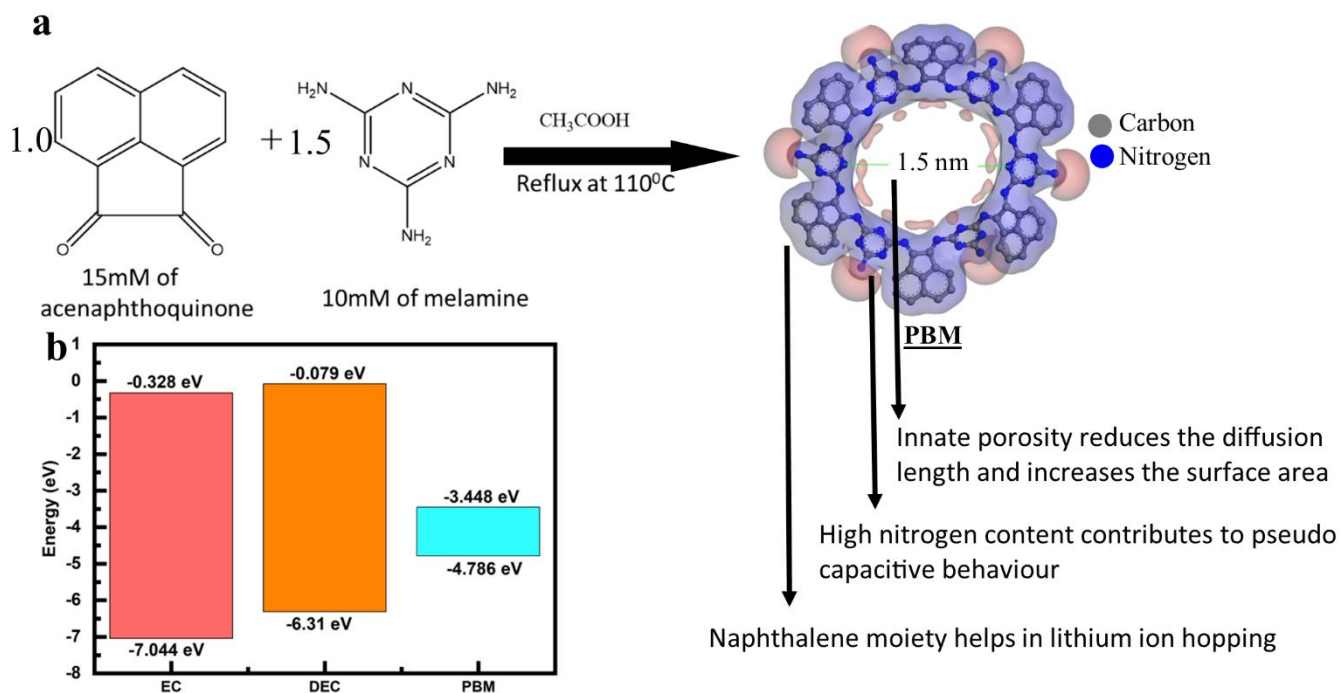


Figure 1-a) synthetic scheme of PBM b) HOMO-LUMO energy levels of EC, DEC and PBM

The characterization of PBM was conducted by various techniques. The HOMO-LUMO energy levels were evaluated by DFT studies using  $\text{dmol}^3$  module of material studio (Figure 1b). The LUMO of PBM lies well below the LUMO of commonly used EC-DEC based electrolyte. This indicates that the material is more prone to undergo electrochemical reduction than electrolyte<sup>39</sup> during the initial cycles of charge-discharge of Li ion battery. Further, it was also observed from the calculations that the LUMO is in the proximity of nitrogen (Indicated with red in the Figure 1a), which suggests that the imine bonds are the possible sites for lithium storage.



### 3.5.1 Infra-red spectroscopy

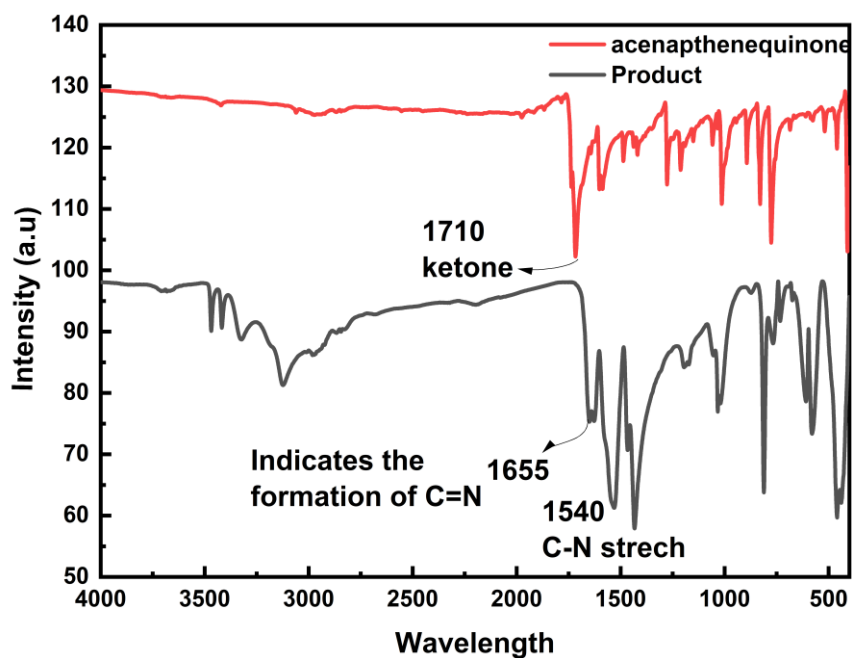


Figure 2-IR spectra of PBM

The IR spectrum (shown in Figure 2) of acenaphthoquinone shows a peak at  $1710\text{ cm}^{-1}$  corresponding to ketone ( $\text{C}=\text{O}$ ) functional group, a peak at  $1520\text{ cm}^{-1}$  corresponding to  $\text{C}=\text{C}$  stretching. The IR spectrum of PBM shows a peak at  $1655\text{ cm}^{-1}$  corresponding to  $\text{C}=\text{N}$ , a peak at  $1540\text{ cm}^{-1}$  corresponding to  $\text{C}-\text{N}$  stretch, two minor peaks at  $3200\text{ cm}^{-1}$  and  $3300\text{ cm}^{-1}$  correspond to the unreacted or terminal amine groups. The peak at  $1710\text{ cm}^{-1}$  corresponding to ketone was observed to diminish in the product molecule and corresponding peak at  $1655\text{ cm}^{-1}$  was observed. This indicates the successful conversion of ketone to imine during the polycondensation reaction. Further, the peak corresponding to  $\text{C}=\text{C}$  stretch observed at  $1520\text{ cm}^{-1}$  in the reactant shifted to  $1490\text{ cm}^{-1}$  in PBM due to extensive conjugation.

### 3.5.2 X-ray photo electron spectroscopy

Detailed elemental analysis was performed by X-ray photoelectron spectroscopy (XPS) (Figure 3). XPS survey spectra showed in Figure 3a indicated the presence of carbon, nitrogen, and oxygen atoms in the PBM moiety at their respective binding energies. The peak corresponding to  $\text{C}\ 1\text{s}$  was deconvoluted (Figure 3a), to obtain three peaks at  $284.7$ ,  $285.6$  and  $287.8\text{ eV}$  corresponding to  $\text{C}=\text{C}$ ,  $\text{C}=\text{N}/\text{C}-\text{N}$  and  $\text{C}=\text{O}$  respectively.<sup>40</sup> Figure 3b shows the deconvoluted  $\text{N}\ 1\text{s}$  spectra of consisting two peaks at  $399.1$  and  $400.5\text{ eV}$  corresponding to  $\text{C}=\text{N}$  and  $\text{C}-\text{N}^{41}$  functional groups

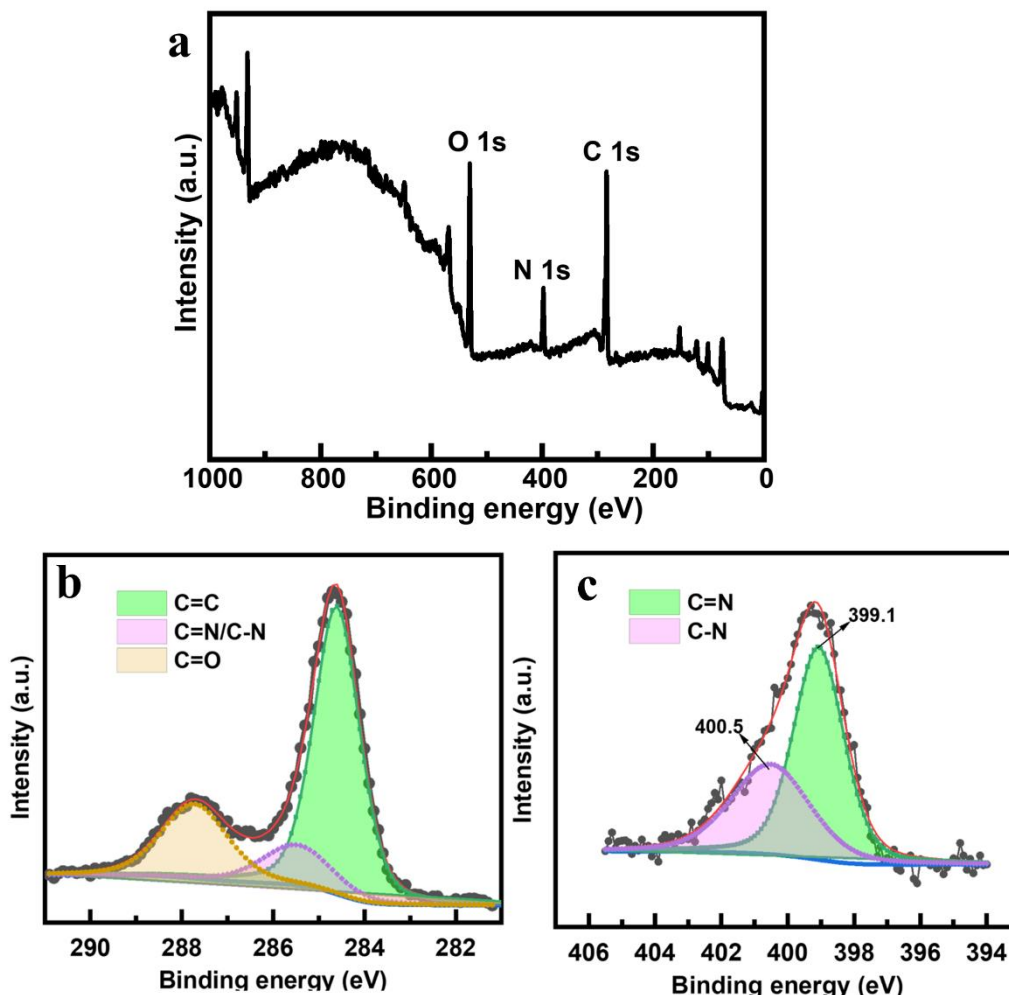


Figure 3-a) XPS Survey spectrum of PBM b) deconvoluted C 1s spectrum of PBM c) deconvoluted N 1s spectrum of PBM

present in the PBM. IR spectra has revealed a similar functional group composition i.e., the formation of imine bond ( $1655\text{ cm}^{-1}$  in IR, 399.1 eV in XPS) is confirmed in these studies.

### 3.5.3 TGA

The TGA studies are conducted in the temperature range of 50-800 °C in air flow of 200 ml/min. Figure 4a depicts the TGA profile of PBM in air, which show a loss of 2% in the region of 50-200 °C corresponding to the loss of adsorbed gases or moisture. A weight loss of 81 % due to edge groups and degradation of framework was observed from 200-300 °C. Further, DTA (Figure 4b) indicates the change in the phase of molecule after 300 °C. An exothermic peak was observed at 200 °C indicating the degradation of the PBM. After 300 °C, a broad plateau was observed suggesting the phase change of the material from organic polymer to carbonaceous material.

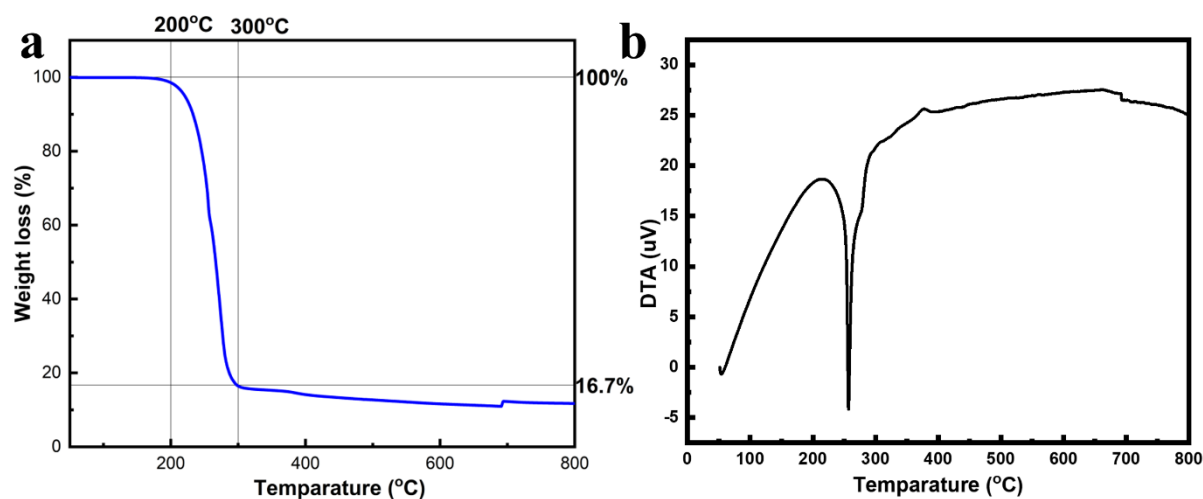


Figure 4-a) TGA of PBM in air b) DTA of PBM in air

### 3.5.4 XRD

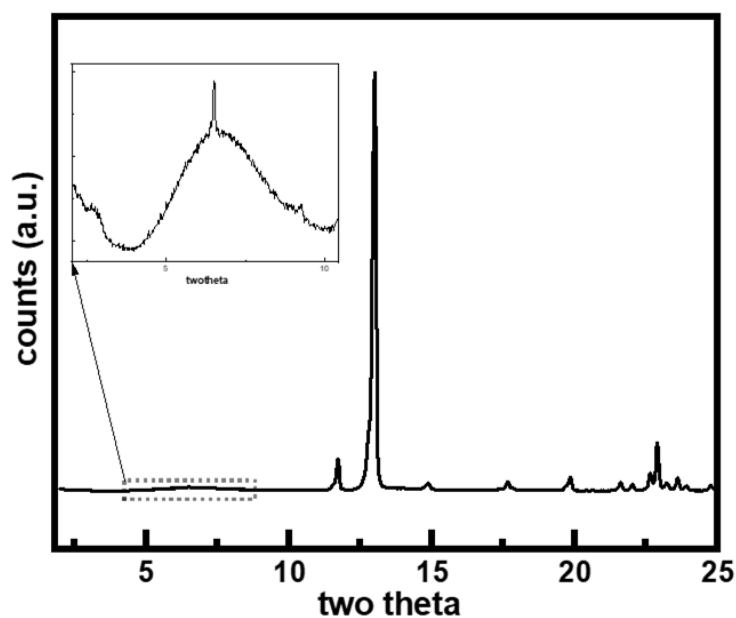


Figure 5-XRD pattern of PBM

The X-ray diffraction (XRD) studies of PBM were conducted to understand the morphology of PBM. Powder XRD pattern shown in Figure 5 shows a sharp peak at  $13.02^\circ$  corresponding to (110) plane which suggests AB type stacking of the layers of PBM. Further, a peak at  $6^\circ$  was observed corresponding to the pore diameter of 1.5 nm in the structure. A sharp peak at  $22.9^\circ$  was observed corresponding to (002) reflections, suggesting 0.39 nm of interlayer spacing between the

conjugated layers of PBM. The interlayer spacing of 0.39 nm supports better diffusion of lithium ions between the layers of PBM. Nitrogen adsorption and desorption studies were conducted to estimate the surface area and porosity of the PBM.

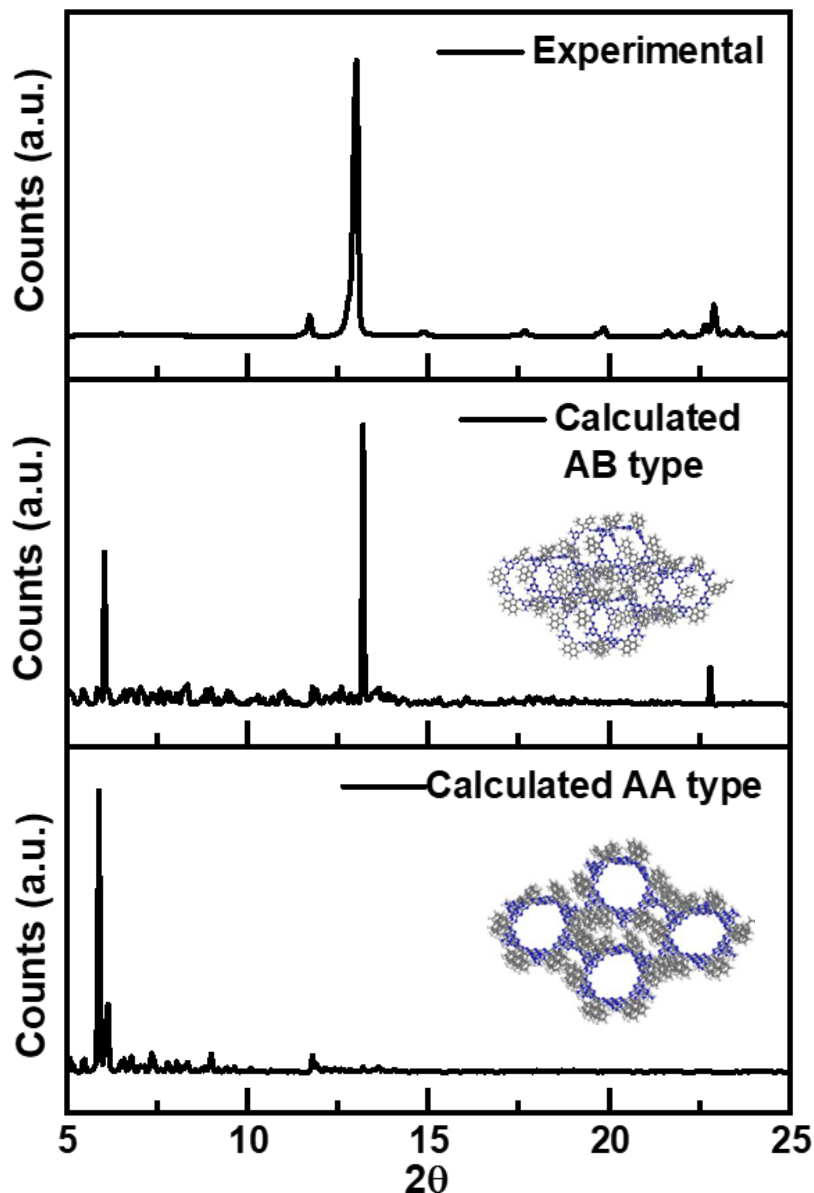


Figure 6- Comparison of XRD experimental and simulated data.

Theoretically XRD was simulated in AA and AB stacking models (Figure 6) using reflex module of material studio, the crystal parameters are as follows:  $a = 36.5$ ,  $b = 32$ ,  $c = 4.0$  for AA model and  $a = 38.0$ ,  $b = 32$  and  $c = 4.3$  for AB model and  $\alpha = \beta = 90^\circ$  and  $\gamma = 120^\circ$ . The peak at  $\sim 13^\circ$  was seen in case of AB stacking but not in AA stacking, which proves the AB type arrangement of the layers of PBM.

## 3.5.5 BET studies

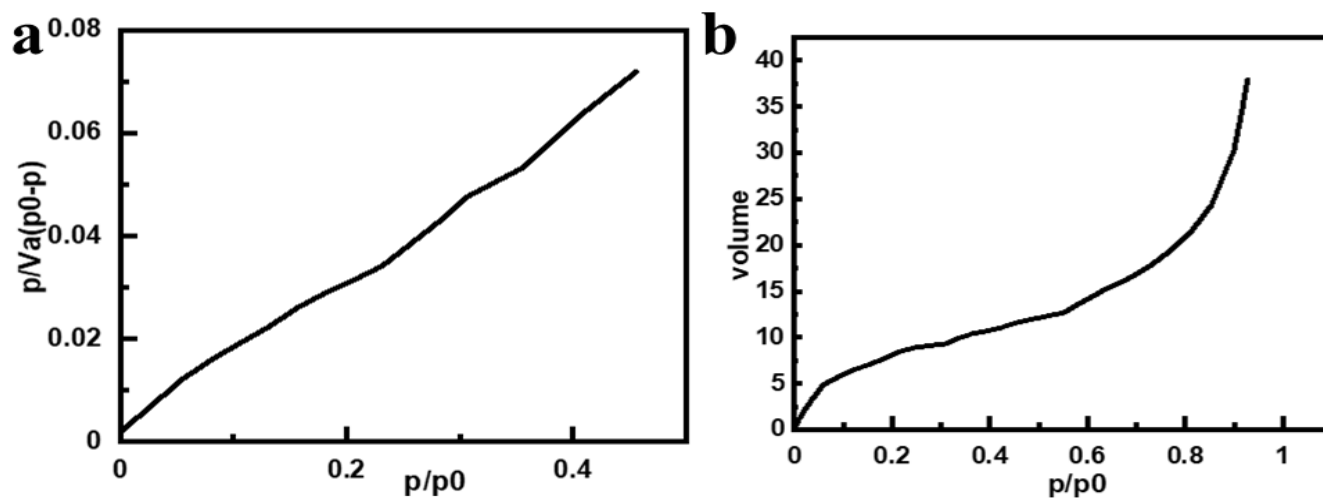
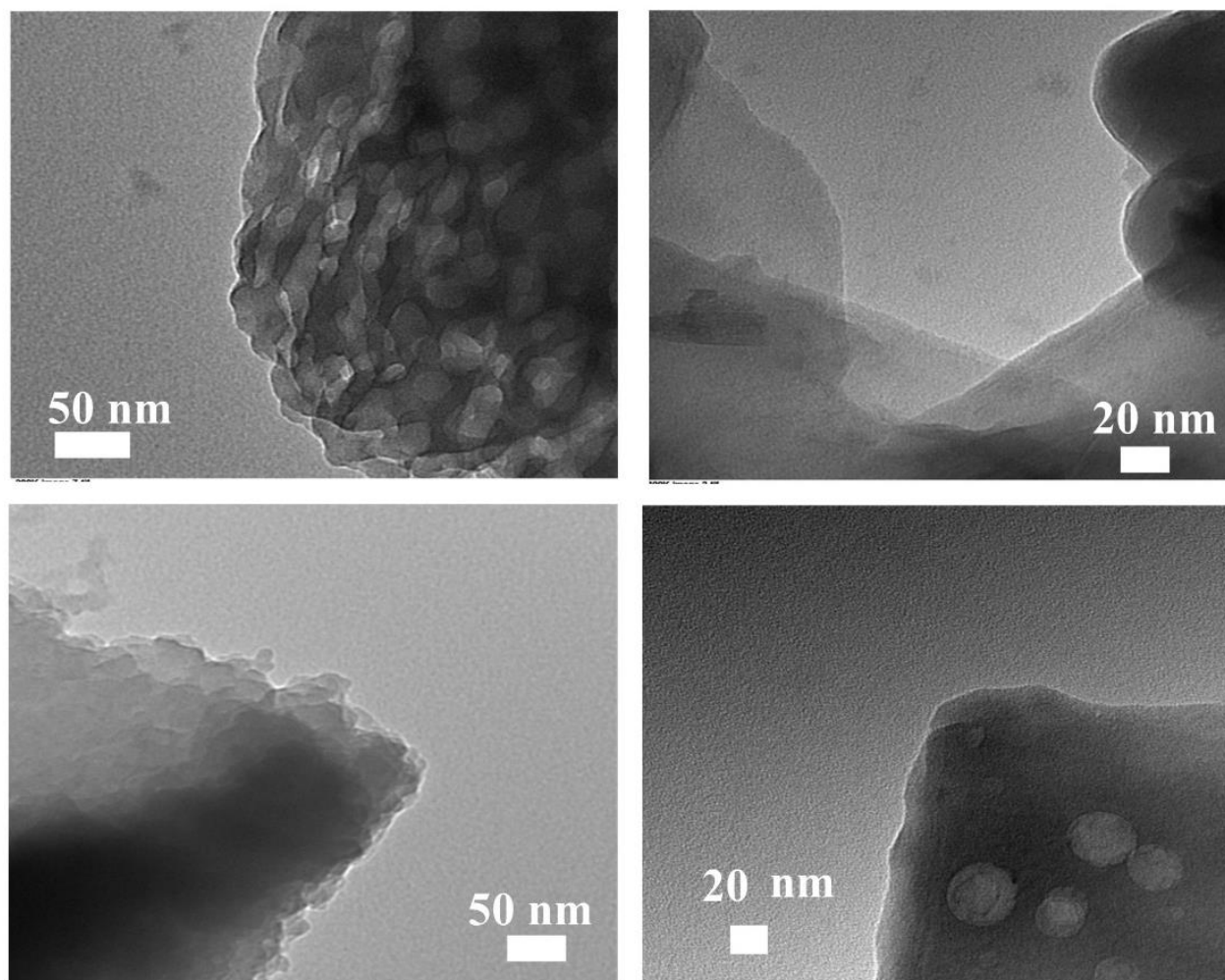


Figure 7-a) BET plot b) MP plot

The surface area was evaluated using BET plot (Figure 7a) methods and PBM was found to be having a surface area of  $\sim 32 \text{ m}^2/\text{g}$  by both the methods and the adsorption-desorption data was analyzed using MP plot (Figure 7b) to estimate the pore diameter. The average pore diameter of 1.7 nm was observed. The porosity value obtained through MP plot and XRD are in close agreement. The structure of PBM was theoretically optimized using  $\text{dmol}^3$  module of Material Studio software. The optimized structure (Figure 1) revealed a pore diameter of 1.5 nm and both the XRD and BET studies support the proposed model and theoretical outcome.

### 3.5.6 TEM

Figure 8 shows the TEM micrographs which reveal a 2-dimensional sheet like overlapped layered arrangement of the PBM. Due to extensive  $\pi - \pi$  stacking, the morphology of the material is expected to be layered, similar to graphite but with an increased interlayer spacing due to the conformation of organic moieties, the TEM micrographs in support with XRD studies confirm such a morphology.



*Figure 8-TEM images of BMCOF*

## 3.5.7 NMR

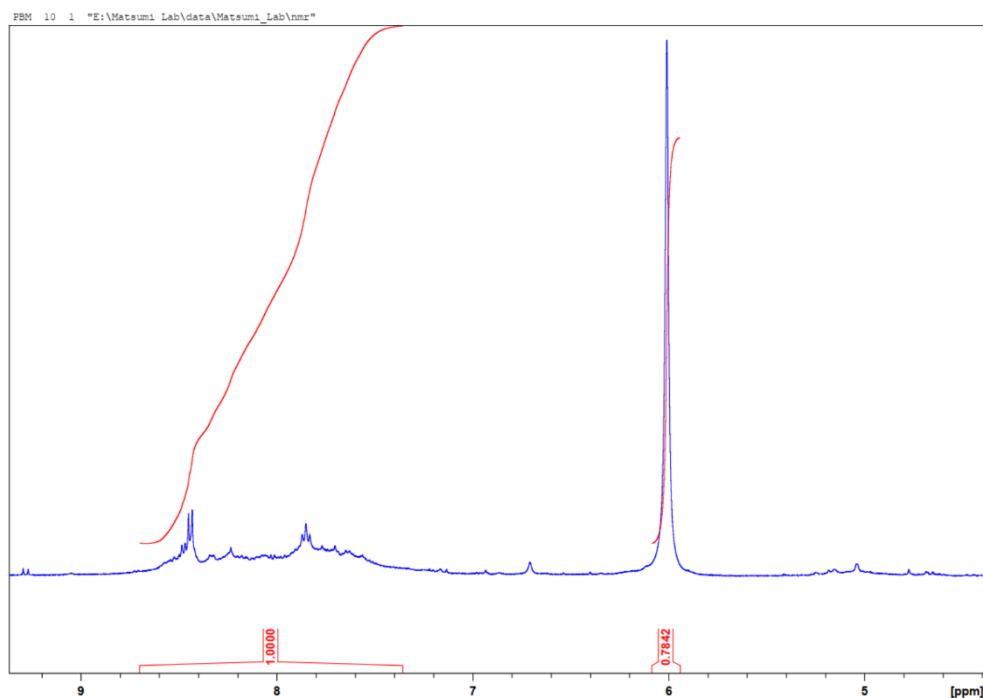


Figure 9- $^1\text{H}$  NMR of PBM

$^1\text{H}$  NMR was conducted to understand the structure of polymer. The NMR result (Figure 9) is as follows:  $^1\text{H}$  NMR (dimethyl sulfoxide (DMSO)  $d_6$ , 400 MHz)  $\delta$ 7.6- $\delta$ 8.6,  $\delta$ 5.9.

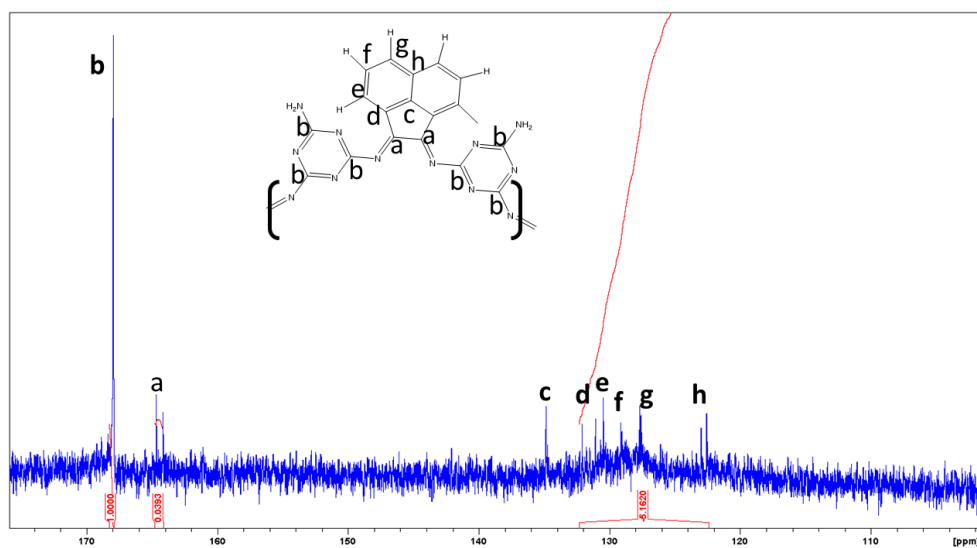
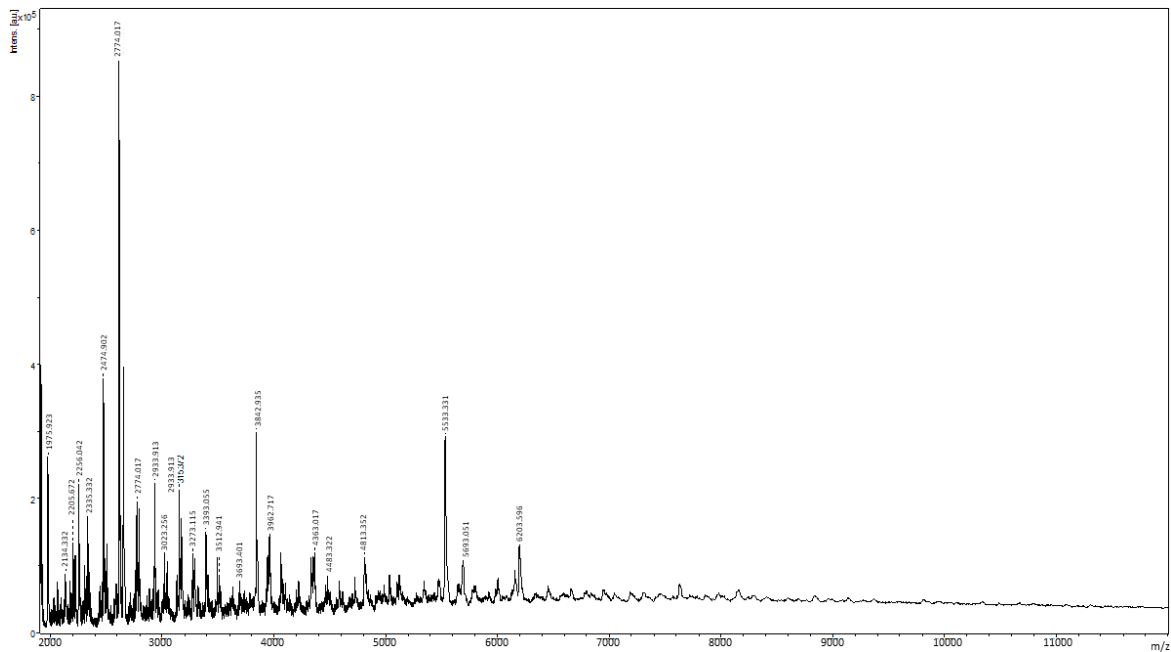


Figure 10- $^{13}\text{C}$  NMR of PBM

$^{13}\text{C}$  NMR (dimethyl sulfoxide (DMSO)  $d_6$ , 400 MHz)  $\delta$ 168,  $\delta$ 164,  $\delta$ 136,  $\delta$ 132,  $\delta$ 130,  $\delta$ 128,  $\delta$ 126,  $\delta$ 122 (Figure 10).

### 3.5.8 Mass Spectra (MALDI-TOF):



*Figure 11-MALDI-TOF of PBM*

MALDI-TOF technique was used to understand the molecular weight of PBM (Figure 11), the molecular weight was found to be 2 kDa – 6 kDa.



## 3.6 Electrochemical studies

### 3.6.1 Cyclic voltammetry

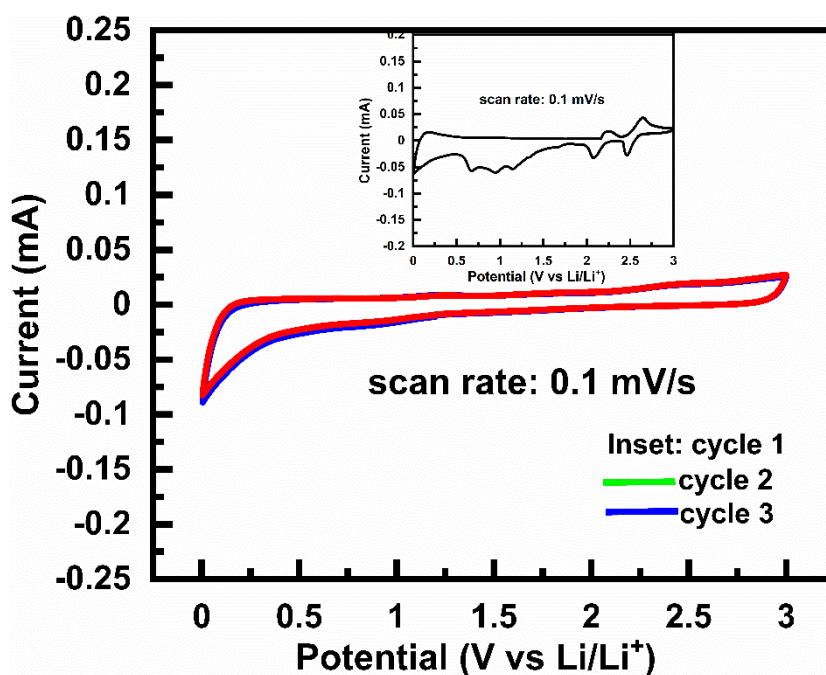


Figure 12-Cyclic voltammogram at 0.1 mV/s

Figure 12 shows the cyclic voltammogram of anodic half-cell fabricated using PBM electrode in the potential window of 5 mV to 3 V (vs Li/Li<sup>+</sup>) at a scan rates of 0.1 mV/s. In the first cycle of cyclic voltammetry (inset Figure 12), peaks at 2.4 V, 2.1 V, 0.9 V were observed in the reduction half. The peaks at 2.4 V, 2.1 V were not observed in subsequent cycles which indicate that the peaks correspond to irreversible redox reactions of PBM and the peak at 0.9 V corresponds to the lithiation of the anode and the peak at 1.15 V, which was not observed in the subsequent cycles suggested electrolyte reduction. In the oxidation half, peaks were observed at 0.1, 2.4 and 2.6 V. The peaks at 2.4 V and 2.6 V are due to irreversible oxidation of PBM, which was not observed in subsequent cycles. The peak at 0.1 V can be ascribed to delithiation of the anode.

### 3.6.2 PEIS

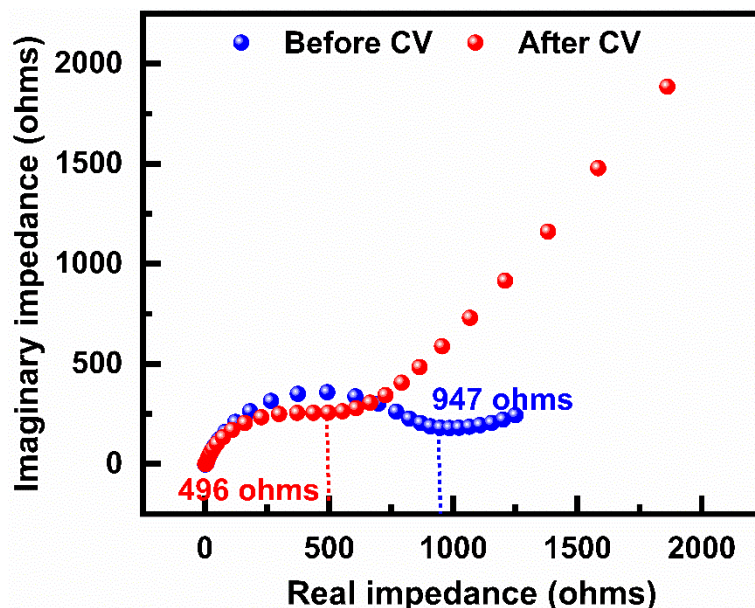


Figure 13-PEIS before and after CV

Electrochemical impedance spectroscopy (EIS) was performed on PBM based half-cells at OCP before and after the CV studies. Figure 13 shows the Nyquist plots revealing a decrease in internal resistance of the cell after cyclic voltammetry. This can be attributed to the ease of lithium diffusion due to the formation of robust SEI layer.

### 3.6.3 Charge-discharge studies

Galvanostatic charge-discharge studies were performed in the potential range of 0.01 – 3.0 V vs Li/Li<sup>+</sup> at various current densities to evaluate the specific capacity and cyclability of the anodic half-cells. At 400 mA/g current density, a high specific capacity of 850 mAh/g was observed with an average coulombic efficiency of 99% (Figures 14a and 14c) for over 3000 cycles. Figure 14a and 14b show the  $E_{\text{cell}}$  (vs Li/Li<sup>+</sup>) vs capacity plots and specific capacity vs cycle number plots at 750 mA/g current density. From the  $E_{\text{cell}}$  vs capacity curve shown in the Figure 14b, it can be observed that in the first cycle of charge-discharge the

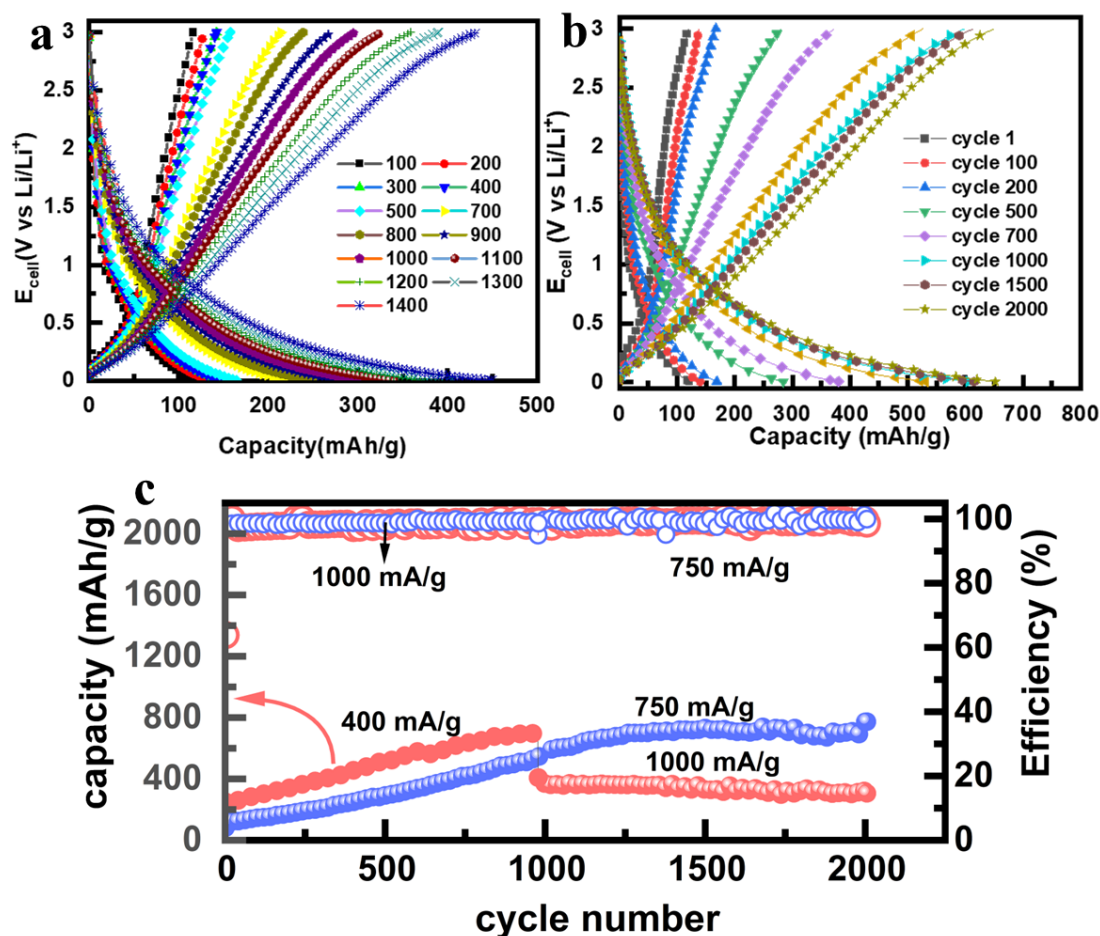


Figure 14- a) potential vs capacity curves at 400 mA/g b) potential vs capacity at 750 mA/g c) charge-discharge studies at 400 mA/g, 750 mA/g, and 1000 mA/g.

specific capacity obtained was 120 mAh/g. In the lithiation profile, a sudden change in the slope of the curve can be observed at 1.0 V. The delithiation profile is seen to be a near linear curve till 2.8 V and at 2.8 V, there is a change in the slope of the curve. This type of charge-discharge profiles is generally observed in the case of anodes with pseudocapacitive behaviour. Further, it can also be observed that both the lithiation and delithiation curves shift away from the origin, as number of cycles increase. The specific capacity at 750 mA/g was found to be 740 mAh/g with an excellent cyclability for 2000 cycles and a coulombic efficiency of 99.2% (Figure 14c). Figure 10c shows the long cycle performance of PBM at 1000 mA/g. The anodic half-cell was cycled at 400 mA/g for about 700 cycles to obtain the peak capacity. Followed by the cycling at 400 mA/g, the current was increased to 1000 mA/g. At 1000 mA/g an initial capacity of 400 mAh/g was observed with a coulombic efficiency of 100% and a capacity retention of 80% after 1100 cycles (Figure 14c). The

dQ/dV plots corresponding to the 1<sup>st</sup> and 1000<sup>th</sup> charge-discharge cycles performed at 750 mA/g current density are shown in Figure 15. dQ/dV vs voltage profile show a visible increment in the peak height during the charge-discharge process and the peak during lithiation shifted towards the lower potential in 1000<sup>th</sup> cycle indicating a lower delithiation overpotential. The gradual increase in capacity coupled with the observations in dQ/dV vs voltage plots indicate that the ease of lithium intercalation increases with cycling. This

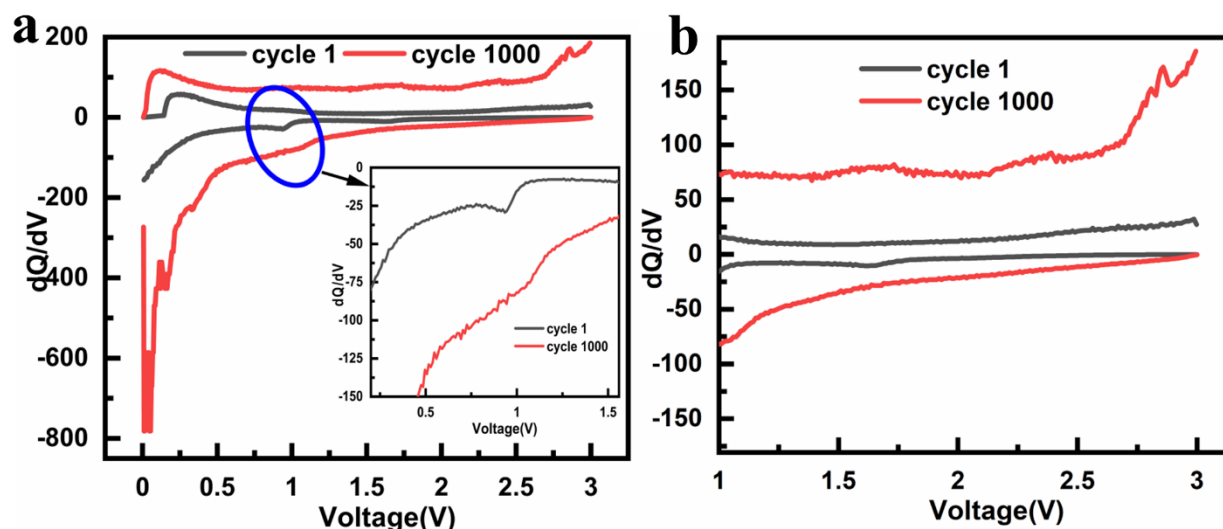


Figure 15-a) dQ/dV plot at 750 mA/g b) dQ/dV plot from 1 V to 3 V at 750 mA/g

behaviour is a result of increase of the interlayer spacing of PBM layers as the lithium penetrate between the layers of PBM. Furthermore, it was observed that the double layer region from 1 V to 3 V broadened (Figure 15b) with cycling indicating higher surface charge storage that can be ascribed to increased surface area due to expansion of electrode during the charge-discharge cycles.

### 3.6.4 Kinetic studies

To understand whether the charge storage mechanism in PBM is dominated by bulk diffusion or surface redox (pseudocapacitive) processes, CV was performed at various scan rates and power law<sup>42</sup> (shown in equation 1) was employed,

$$i = a\nu^b \quad (1)$$

where,  $i$  is peak current,  $\mathcal{V}$  is scan rate,  $b$  is the exponent of scan rate and  $a$  is the proportionality constant. Figure 16 shows the cyclic voltammograms at 0.2 mV/s, 0.4 mV/s, 0.6 mV/s, 0.8 mV/s and 1.0 mV/s. Figure 17 shows the linear  $\log i$  vs  $\log \mathcal{V}$  plot. The  $b$  (exponent)

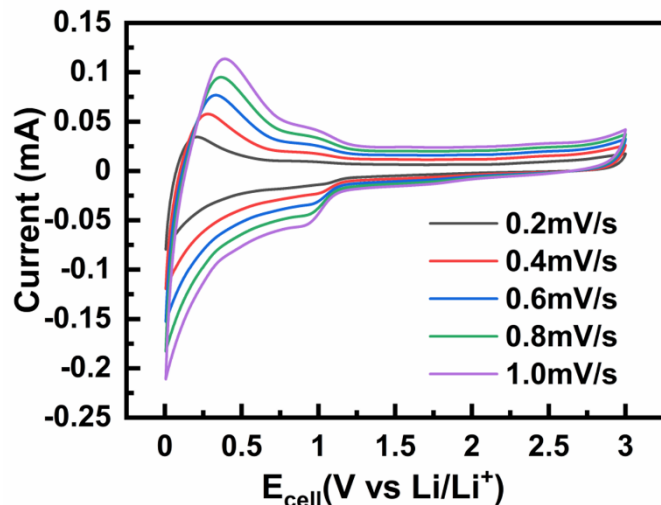


Figure 16-Cyclic voltammograms at different scan rates

value was evaluated from the slope of  $\log i$  vs  $\log \mathcal{V}$  plot to be 0.81. The cathodic peak current in cyclic voltammogram corresponds to the delithiation of anode in half-cells. In case bulk-controlled charge storage mechanism as observed in graphite, due to limited surface area and less interlayer spacing, lithium-ion movement is hindered. Hence increase of scan rate does not directly correspond to increase in peak current. It was observed that in such materials the current response is dependent on the square root ( $b = 0.5$ ) of the voltage scan rate. In case of surface-controlled

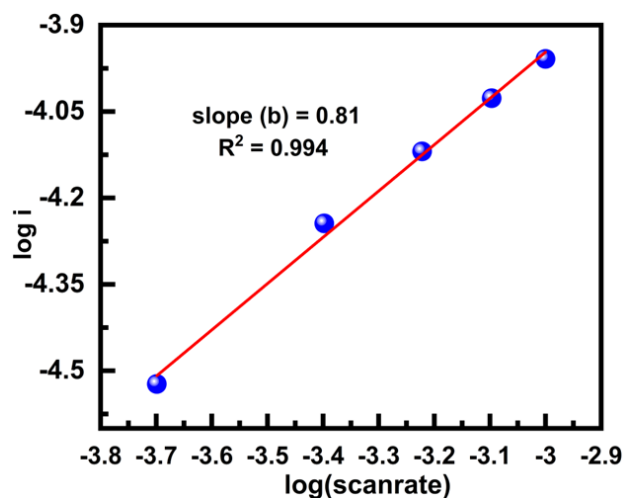


Figure 17-  $\log i$  vs  $\log \mathcal{V}$  plot

charge storage process, the current response is directly proportional to the voltage scan rate ( $b = 1$ )<sup>43</sup>. The  $b$  value of 0.81 represents a mixed charge storage mechanism including both diffusion and a dominant capacitance-based surface process.

Further to quantitatively determine the charge storage contribution from the diffusion and pseudocapacitive processes, equation 2 was employed. The current response ( $i$ ) at a certain potential is a combination of response from capacitive process ( $k_c\vartheta$ ) and diffusion-controlled process ( $k_d\vartheta^{0.5}$ ).

$$i = k_c\vartheta + k_d\vartheta^{0.5} \quad (2)$$

Here,  $i$  is peak current,  $k_c$  and  $k_d$  are the proportionality constants for capacitance and diffusion respectively and  $\vartheta$  is scan rate. The values for  $k_d$  and  $k_c$  were evaluated by

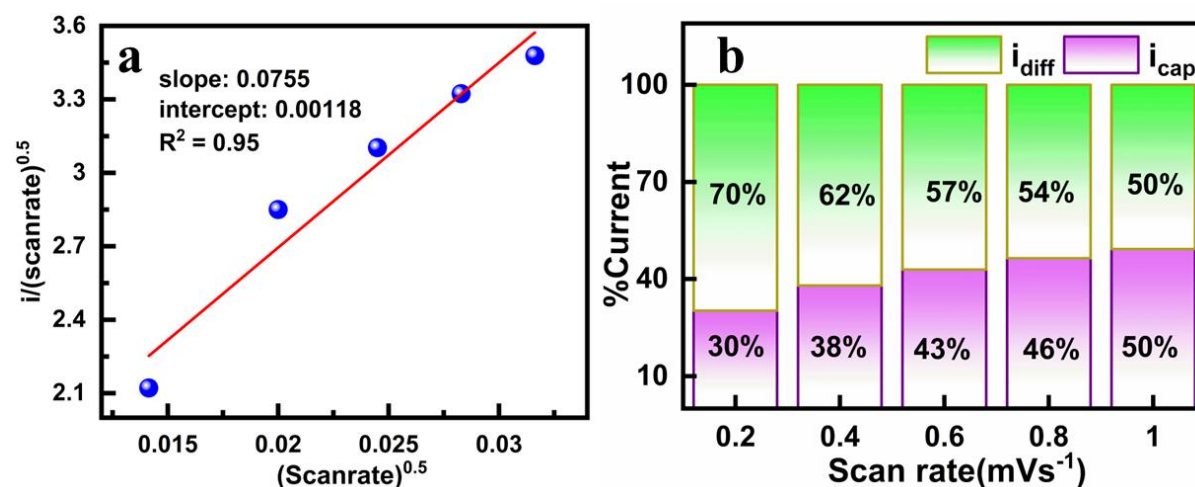


Figure 18- Linear fit of  $i/90.5$  vs  $90.5$  plot b) distribution of current contribution from capacitance and diffusion at various scan rates

plotting  $i/\vartheta^{0.5}$  vs  $\vartheta^{0.5}$  plot (Figure 18a). Figure 18b shows the distribution of current contribution from capacitance and diffusion at various scan rates. It was observed that the contribution from pseudo-capacitance-based surface processes increases with the scan rate. The contribution of capacitance at lower scan rate of 0.1 mV/s was observed to be 30 % and as scan rate was increased gradually to 1.0 mV/s, the capacitance contribution was observed to be 50 %. The relatively high specific capacities and excellent cyclability demonstrate the applicability of PBM as an anode in lithium-ion battery.

### 3.6.5 Theoretical studies

DFT based theoretical studies were performed to understand the lithium storage mechanism (Figure 19). Two possible lithiation stages were considered per monomer unit of PBM. The first stage is the lithiation of C=N and the second stage is the lithiation of C=C, in which lithium storage is as follows: one lithium per each C=N and one lithium per C=C. Theoretically, the  $\Delta G$  value of the PBM monomer was found to be -381 eV after the lithiation of the imine moieties present in the linkage, further, the lithiation of each melamine moiety with 3 lithium ions i.e., a total of 6 lithium ions for a monomer of PBM. The  $\Delta G$  of the PBM in which all the imine groups are lithiated is -1252 eV. This step is followed by lithiation of C=C in naphthalene moiety with 6 lithium ions. The  $\Delta G$  of PBM monomer in which all possible lithium storage sites are lithiated was found to be -2050 eV. The PBM molecule was observed to have least free energy i.e., most stable state after all the possible lithium storage sites got lithiated. Based on these observations, the maximum

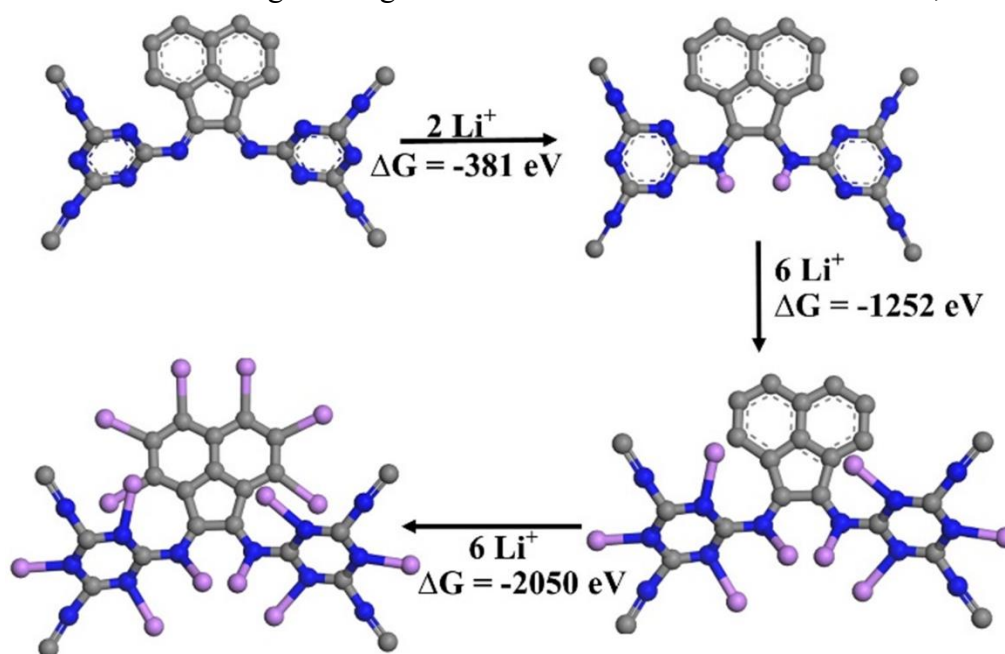


Figure 19- Lithiation scheme of PBM

achievable capacity (theoretical capacity) was calculated to be 1068.5 mAh/g. The capacity contribution from the lithium storage in both the aforementioned steps of lithiation was calculated. Figure 16 shows the lithiation profile of PBM anodic half-cell at 1st, 1000th, 1500th and 2000th cycles at 750 mA/g current density. The capacity contribution from each step is indicated in the lithiation profiles given in Figure 20. The capacity contribution from the lithiation of imine group

was found to be 78.2 mAh/g, 342 mAh/g, 399 mAh/g and 421.8 mAh/g in the 1st, 1000th cycle, 1500th and 2000th cycles respectively. The contribution from the lithiation of naphthalene was found to be 58.8 mAh/g, 258 mAh/g, 301 mAh/g and 318 mAh/g in the 1st, 1000th cycle, 1500th and 2000th cycles respectively. Furthermore, the capacity vs voltage plots show a distinct change in the slope of the curve at 0.9 V which validates initial hypothesis of the two step lithiation.  $dQ/dV$  vs voltage plots also indicate the increase in peak height as well as broadening of the double layer region from 1.0 V to 3.0 V, which suggest the increase in ease of lithium diffusion with cycles. This can be due to the exposure of new active sites for lithium storage due to increase in the interlayer spacing of PBM layers as lithium ions penetrate the layers of PBM. This expansion of PBM leads to the gradual activation of the anode.

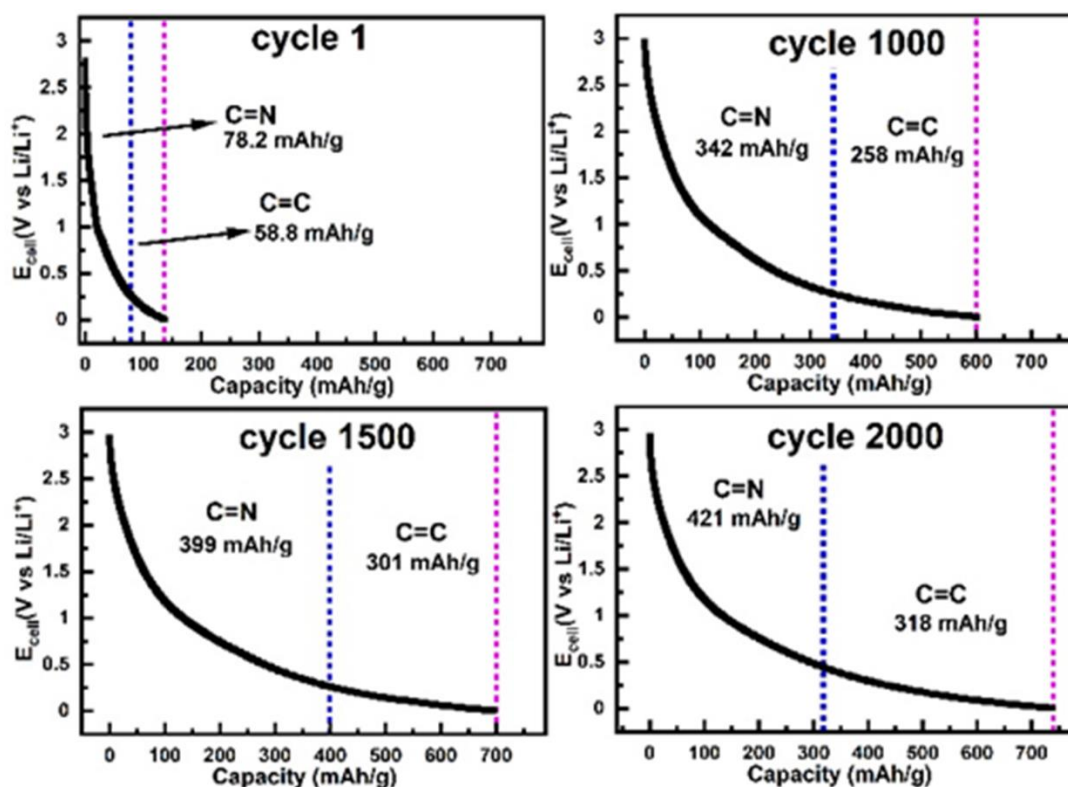


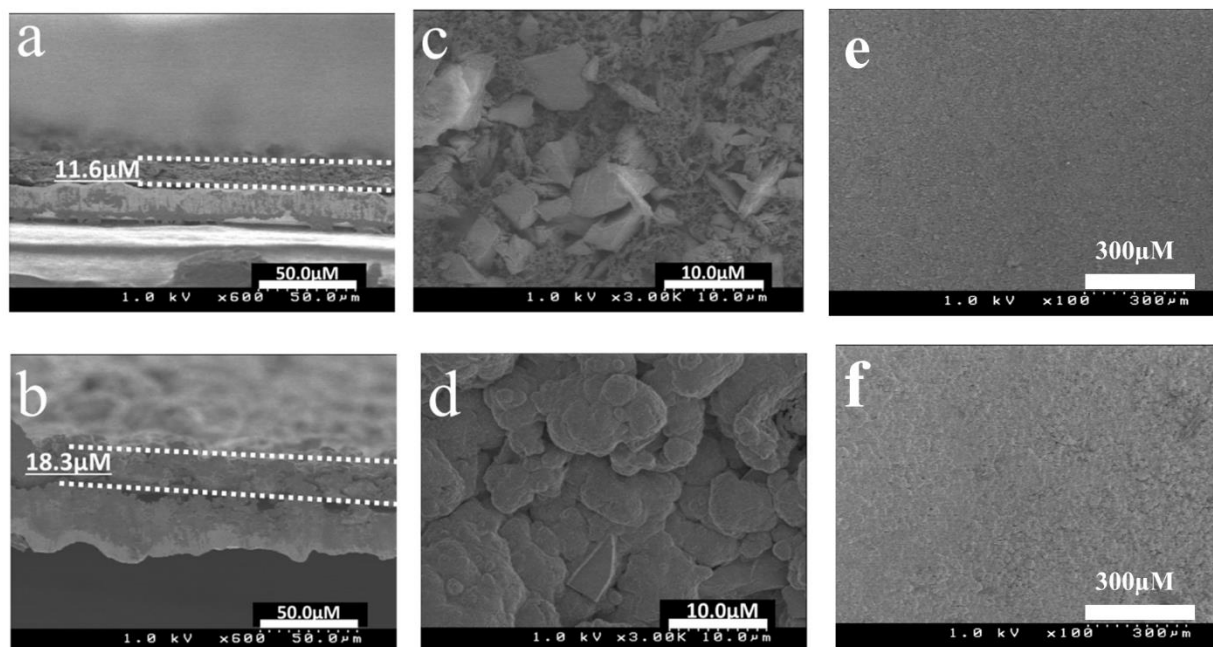
Figure 20- Lithiation scheme of PBM anodic half-cell at cycles 1, 1000, 1500 and 2000

### 3.7 Postmortem studies

The electrode cycled for 2000 charge-discharge cycles at 750 mA/g was dis-assembled in argon filled glove box ( $O_2 < 0.5$  ppm and  $H_2O < 0.5$  ppm) and washed with fresh EC:DEC carefully before drying to measure FESEM and XPS. FESEM study (Figure 21 a-f) was conducted on the cycled



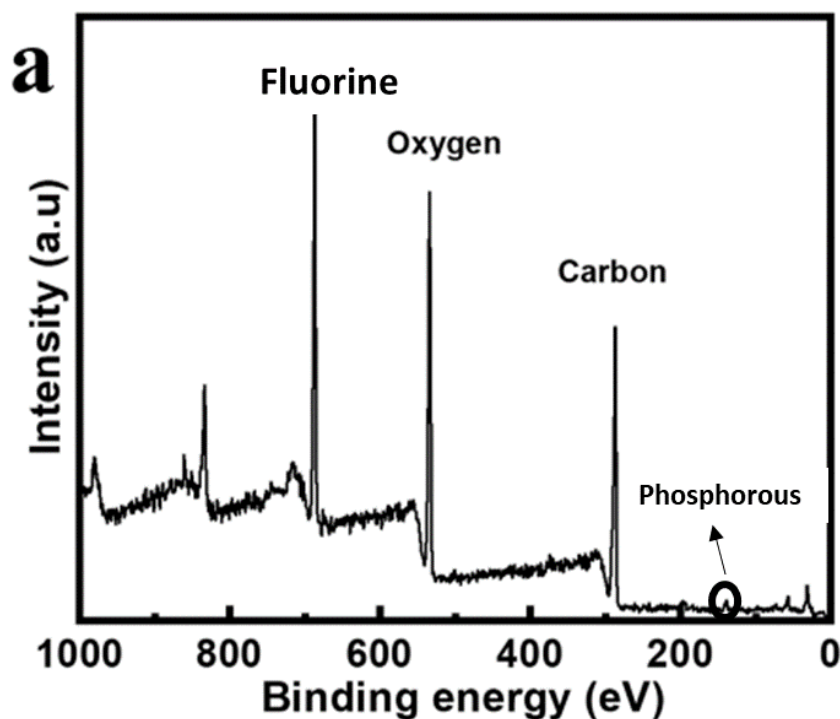
electrode to understand the changes in the morphology of electrode after cycling. Figure 21a, b shows the FESEM cross-section images of the pristine and the electrode cycled for 2000 cycles



*Figure 21- FESEM cross-section images of PBM electrode a)before cycling b)after cycling; FESEM images of PBM electrode c,e)before cycling d,f)after cycling*

respectively. The cross-section images show a thickness of 11.6  $\mu\text{m}$  and 18.3  $\mu\text{m}$  for pristine and cycled electrode respectively. Figure 21 c and d show the lateral FESEM images of PBM electrode before and after cycling for 2000 cycles. In the FESEM image of pristine electrode (Figure 21 c) crystalline particles with distinct boundaries can be observed whereas in the FESEM image of the cycled electrode (Figure 21 d), such clear distinction between particles cannot be observed which is due to the change in the particle morphology after SEI formation. Further, expansion of the PBM electrode also altered the morphology of the particle. This fact is supported by the increase in the thickness of the electrode by 6.7  $\mu\text{m}$ , corresponding to 157.8 % volume change as observed in FESEM cross section images (Figure 21 a shows the FESEM cross-section image before cycling, Figure 21 b shows the FESEM cross-section image after cycling). The volume increase that was observed in FESEM images suggested the change in morphology of PBM electrode substantiating the exposure of new active sites for lithium storage, which led to a gradual increase in the specific capacity. Interestingly, due to the presence of about 20 wt% binder in the electrode, even after such expansion of the electrode material, no significant cracks on the surface were detected (Figure 21 f).

XPS analysis has been performed on the cycled electrode in lithiated state, to understand the chemical composition after charge-discharge studies (Figure 22 a-e). Figure 22a shows the survey spectrum of cycled PBM anode. The survey spectrum shows presence of fluorine, carbon oxygen and phosphorus. The deconvoluted C 1s spectra (Figure 22b) showed peak at 284.0 eV corresponding to the C-Li group, peaks at 284.6 eV, 285.3eV, 286.2eV corresponding to C=C, C=N and C-N which are functional groups in PBM and peaks at 287.1 eV, 288.1 eV, 289.0 eV, 290.3 eV corresponding to C=O, C-O-C,  $\text{Li}_2\text{CO}_3$  and C-F groups which are components of SEI<sup>44</sup>. The deconvoluted N 1s spectra (Figure 22c) shows two peaks at 398.6 eV and 401.0 eV corresponding to the C=N and N-Li groups<sup>45</sup>. Since the detection depth of XPS is approximately 5 nm, the detection of nitrogen indicates that the SEI layer is thinner than 5 nm so that it enabled the detection of nitrogen. The formation of a thinner SEI layer also reiterates the resistance of the material towards reducing the electrolyte and better kinetics. The deconvoluted O 1s spectra of cycled PBM electrode (Figure 22d) shows four peaks at 533.1 eV, 534.2 eV, 535.3 eV and 536.6 eV corresponding to C=O, C-O-C,  $\text{Li}_2\text{CO}_3$  and  $\text{Li}_2\text{O}$  respectively. The deconvoluted F 1s spectra of cycled PBM electrode (Figure 22e) show peaks at 684.7 eV, 685.6 eV and 686.8 eV corresponding to LiF,  $\text{Li}_x\text{PF}_y$  and C-F respectively.



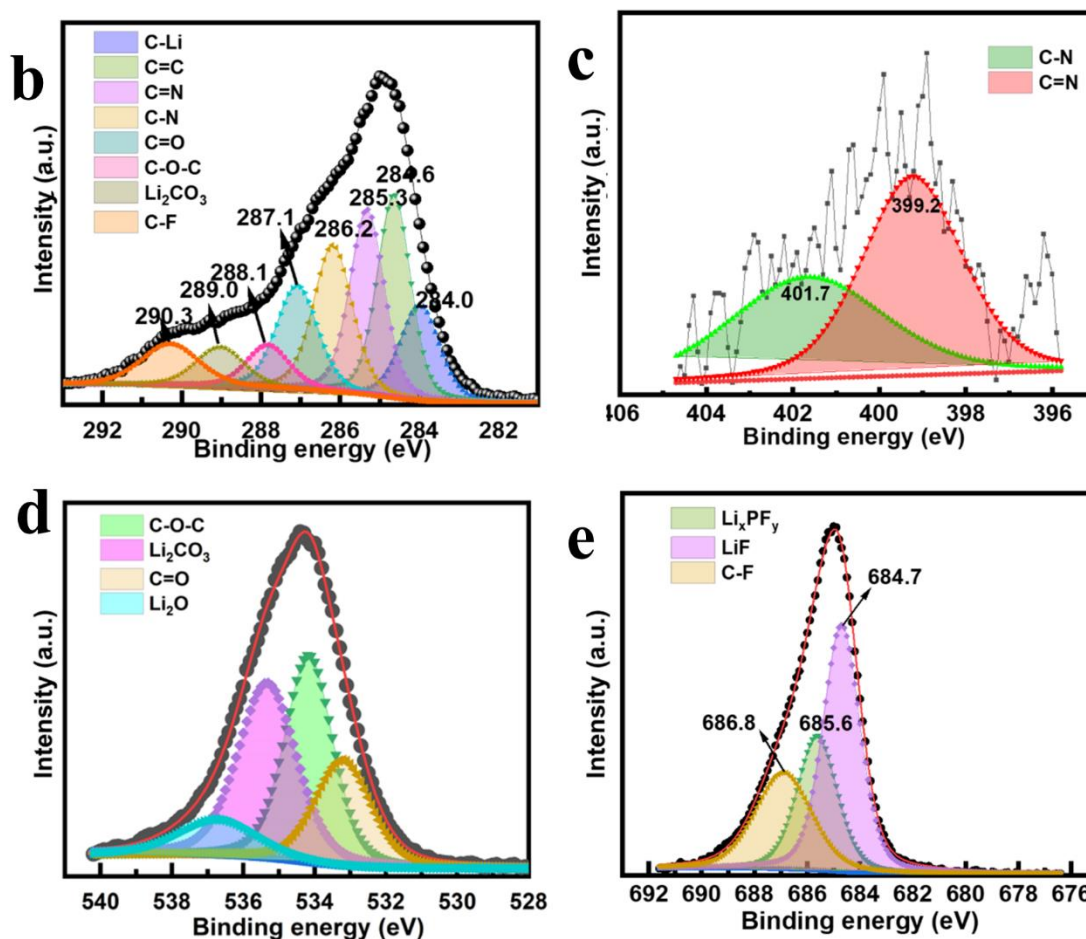


Figure 22- a) XPS Survey spectrum of PBM cycled electrode b) deconvoluted C 1s spectrum of PBM cycled electrode c) deconvoluted N 1s spectrum of PBM cycled electrode c) deconvoluted O 1s spectrum of PBM cycled electrode d) deconvoluted F 1s spectrum of PBM cycled electrode

### 3.8 Conclusion

As discussed in the earlier sections, the nitrogen rich PBM, exhibited both diffusive and capacitive charge storage properties. An excellent electrochemical performance with high reversible capacities at various current densities was demonstrated. Table 1 shows the comparison of PBM with some of the earlier reports. Comparatively, this material delivers a better electrochemical performance in terms of specific capacity at high current density and cyclability. In most of the works shown in Table 1, the nitrogen content is limited to the imine or azo linkage

of monomers<sup>46,47</sup>, hence due to the lower nitrogen content, the specific capacity and the cyclability was observed to be poor.

*Table 1- Comparison with earlier works.*

Material	Current density (mA/g)	Capacity (mAh/g)	Coulombic efficiency %	Cycles
JUC-526 <sup>48</sup>	200	441.2	100	500
ISERP-CON <sup>36</sup>	100	720	100	1000
Cz-COF1 <sup>46</sup>	200	300	59	400
Cz-COF2 <sup>49</sup>	400	50	-	-
E-CIN-1/CNT <sup>49</sup>	100	538	91	1000
<b>BMCOF</b>	<b>750</b>	<b>740</b>	<b>99</b>	<b>2000</b>

The high nitrogen content in the structure of PBM enabled the deliverance of high specific capacity. Further, most of the reported organic materials that are utilized as anodes have benzene moiety in the structure. It was observed that naphthalene can more efficiently assist lithium hopping than benzene<sup>50</sup>. Hence, by including naphthalene moiety in the structure of PBM, the lithium hopping in the anode was increased which eases the lithium diffusion in anode. Considering these merits of the PBM, it is a highly attractive and promising candidate for the anode application in lithium-ion battery. In conclusion, a high performing n-type organic anode material was developed to meet the energy requirements. In this work, the synthesis and characterization of the PBM was demonstrated. The PBM based anodic half-cell exhibited good reversible capacity. This opens the possibilities of utilizing this material for a wide range of applications as a novel class of anodic material. The PBM anodic half-cell exhibits a reversible capacity of 740 mAh/g at 750 mA/g and 300 mAh/g at 1000 mA/g for 2000 and 1000 cycles, respectively. The charge storage mechanism was evaluated computationally. The viability of Li<sup>+</sup> storage arises from the presence of high nitrogen content and the porosity of organic polymer. The high capacity and stable electrochemical activity make this a prospective anodic material<sup>51,52</sup>.

---

## References

- 1 J. Asenbauer, T. Eisenmann, M. Kuenzel, A. Kazzazi, Z. Chen and D. Bresser, *Sustain. Energy Fuels*, 2020, **4**, 5387–5416.
- 2 T. Sasaki, Y. Ukyo and P. Novák, *Nat. Mater.*, 2013, **12**, 569–575.
- 3 Y. Pan, S. Ge, Z. Rashid, S. Gao, A. Erwin, V. Tsukruk, K. D. Vogiatzis, A. P. Sokolov, H. Yang and P. F. Cao, *ACS Appl. Energy Mater.*, 2020, **3**, 3387–3396.
- 4 L. Ion, *Kodansjha* 8, 1998.
- 5 D. Deng, *Energy Sci. Eng.*, 2015, **3**, 385–418.
- 6 A. N. Dey, *J. Electrochem. Soc.*, 1971, **118**, 1547.
- 7 A. M. Wilson and J. R. Dahn, *J. Electrochem. Soc.*, 1995, **142**, 326–332.
- 8 T. Zheng, T. Zhang, M. S. de la Fuente and G. Liu, *Eur. Polym. J.*, 2019, **114**, 265–270.
- 9 Y. Jin, B. Zhu, Z. Lu, N. Liu and J. Zhu, *Adv. Energy Mater.*, 2017, **7**, 1–17.
- 10 F. Huisken, B. Kohn, R. Alexandrescu, S. Cojocar, A. Crunteanu, G. Ledoux and C. Reynaud, *J. Nanoparticle Res.*, 1999, **1**, 293–303.
- 11 T. W. Kwon, J. W. Choi and A. Coskun, *Chem. Soc. Rev.*, 2018, **47**, 2145–2164.
- 12 J. Wu, Y. Cao, H. Zhao, J. Mao and Z. Guo, *Carbon Energy*, 2019, **1**, 57–76.
- 13 B. Jerliu, E. Hüger, L. Dörrer, B. K. Seidlhofer, R. Steitz, V. Oberst, U. Geckle, M. Bruns and H. Schmidt, *J. Phys. Chem. C*, 2014, **118**, 9395–9399.
- 14 D. J. Pereira, J. W. Weidner and T. R. Garrick, *J. Electrochem. Soc.*, 2019, **166**, A1251–A1256.
- 15 G. Sandu, M. Coulombier, V. Kumar, H. G. Kassa, I. Avram, R. Ye, A. Stopin, D. Bonifazi, J. F. Gohy, P. Leclère, X. Gonze, T. Pardoën, A. Vlad and S. Melinte, *Sci. Rep.*, 2018, **8**, 1–11.
- 16 N. Liu, L. Hu, M. T. McDowell, A. Jackson and Y. Cui, *ACS Nano*, 2011, **5**, 6487–6493.
- 17 Y. Yao, M. T. McDowell, I. Ryu, H. Wu, N. Liu, L. Hu, W. D. Nix and Y. Cui, *Nano*

- Lett.*, 2011, **11**, 2949–2954.
- 18 M. Haro, P. Kumar, J. Zhao, P. Koutsogiannis, A. J. Porkovich, Z. Ziadi, T. Bouloumis, V. Singh, E. J. Juarez-Perez, E. Toulkeridou, K. Nordlund, F. Djurabekova, M. Sowwan and P. Grammatikopoulos, *Commun. Mater.*, 2021, **2**, 1–10.
- 19 S. Y. Lai, J. P. Mæhlen, T. J. Preston, M. O. Skare, M. U. Nagell, A. Ulvestad, D. Lemordant and A. Y. Koposov, *Nanoscale Adv.*, 2020, **2**, 5335–5342.
- 20 M. T. Jeena, J. I. Lee, S. H. Kim, C. Kim, J. Y. Kim, S. Park and J. H. Ryu, *ACS Appl. Mater. Interfaces*, 2014, **6**, 18001–18007.
- 21 X. Wang, S. Liu, Y. Zhang, H. Wang, A. A. Aboalhassan, G. Li, G. Xu, C. Xue, J. Yu, J. Yan and B. Ding, *ACS Appl. Mater. Interfaces*, 2020, **12**, 38132–38139.
- 22 S. Gao, F. Sun, A. Brady, Y. Pan, A. Erwin, D. Yang, V. Tsukruk, A. G. Stack, T. Saito, H. Yang and P. F. Cao, *Nano Energy*, 2020, **73**, 104804.
- 23 L. Yu, J. Liu, S. He, C. Huang, L. Gan, Z. Gong and M. Long, *J. Phys. Chem. Solids*, 2019, **135**, 109113.
- 24 X. Yan, Z. Wang, M. He, Z. Hou, T. Xia, G. Liu and X. Chen, *Energy Technol.*, 2015, **3**, 801–814.
- 25 L. Ling, Y. Bai, Z. Wang, Q. Ni, G. Chen, Z. Zhou and C. Wu, *ACS Appl. Mater. Interfaces*, 2018, **10**, 5560–5568.
- 26 S. Goriparti, E. Miele, F. De Angelis, E. Di Fabrizio, R. Proietti Zaccaria and C. Capiglia, *J. Power Sources*, 2014, **257**, 421–443.
- 27 J. J. Samuel, V. K. Karrothu, R. K. Canjeevaram Balasubramanyam, A. A. Mohapatra, C. Gangadharappa, V. R. Kankanallu, S. Patil and N. P. B. Aetukuri, *J. Phys. Chem. C*, 2021, **125**, 4449–4457.
- 28 Q. Zhang, W. Cai, Y. X. Yao, G. L. Zhu, C. Yan, L. L. Jiang, C. He and J. Q. Huang, *Chem. Soc. Rev.*, 2020, **49**, 3806–3833.
- 29 S. Wang, Q. Wang, P. Shao, Y. Han, X. Gao, L. Ma, S. Yuan, X. Ma, J. Zhou, X. Feng and B. Wang, *J. Am. Chem. Soc.*, 2017, **139**, 4258–4261.

- 
- 30 G. Fang, Z. Wu, J. Zhou, C. Zhu, X. Cao, T. Lin, Y. Chen, C. Wang, A. Pan and S. Liang, *Adv. Energy Mater.*, 2018, **8**, 1–10.
- 31 M. E. Bhosale, S. Chae, J. M. Kim and J. Y. Choi, *J. Mater. Chem. A*, 2018, **6**, 19885–19911.
- 32 K. Geng, T. He, R. Liu, S. Dalapati, K. T. Tan, Z. Li, S. Tao, Y. Gong, Q. Jiang and D. Jiang, *Chem. Rev.*, 2020, **120**, 8814–8933.
- 33 X. Feng, X. Ding and D. Jiang, *Chem. Soc. Rev.*, 2012, **41**, 6010–6022.
- 34 H. Chen, Y. Zhang, C. Xu, M. Cao, H. Dou and X. Zhang, *Chem. - A Eur. J.*, 2019, **25**, 15472–15476.
- 35 H. Yang, S. Zhang, L. Han, Z. Zhang, Z. Xue, J. Gao, Y. Li, C. Huang, Y. Yi, H. Liu and Y. Li, *ACS Appl. Mater. Interfaces*, 2016, **8**, 5366–5375.
- 36 S. Haldar, K. Roy, S. Nandi, D. Chakraborty, D. Puthusseri, Y. Gawli, S. Ogale and R. Vaidhyanathan, *Adv. Energy Mater.*, 2018, **8**, 1–11.
- 37 D. Rodríguez-San-Miguel, C. Montoro and F. Zamora, *Chem. Soc. Rev.*, 2020, **49**, 2291–2302.
- 38 J. Li, X. Jing, Q. Li, S. Li, X. Gao, X. Feng and B. Wang, *Chem. Soc. Rev.*, 2020, **49**, 3565–3604.
- 39 S. G. Patnaik, R. Vedarajan and N. Matsumi, *J. Mater. Chem. A*, 2017, **5**, 17909–17919.
- 40 K. Duan, J. Ning, L. Zhou, W. Xu, C. Feng, T. Yang, S. Wang and J. Liu, *Chem. Commun.*, 2020, **56**, 8420–8423.
- 41 M. Ayiania, M. Smith, A. J. R. Hensley, L. Scudiero, J. S. McEwen and M. Garcia-Perez, *Carbon N. Y.*, 2020, **162**, 528–544.
- 42 V. Augustyn, P. Simon and B. Dunn, *Energy Environ. Sci.*, 2014, **7**, 1597–1614.
- 43 Y. Mu, M. Han, J. Li, J. Liang and J. Yu, *Carbon N. Y.*, 2021, **173**, 477–484.
- 44 N. L. Hamidah, F. M. Wang and G. Nugroho, *Surf. Interface Anal.*, 2019, **51**, 345–352.

- 
- 45 A. Gupta, R. Badam, A. Nag, T. Kaneko and N. Matsumi, *ACS Appl. Energy Mater.*, 2021, **4**, 2231–2240.
- 46 C. Li, L. Liu, J. Kang, Y. Xiao, Y. Feng, F. F. Cao and H. Zhang, *Energy Storage Mater.*, 2020, **31**, 115–134.
- 47 L. Bai, Q. Gao and Y. Zhao, *J. Mater. Chem. A*, 2016, **4**, 14106–14110.
- 48 G. Yang, J. Zhao, L. Cui, S. Song, S. Zhang, L. Yu and P. Zhang, *RSC Adv.*, 2017, **7**, 7944–7953.
- 49 O. Buyukcakir, J. Ryu, S. H. Joo, J. Kang, R. Yuksel, J. Lee, Y. Jiang, S. Choi, S. H. Lee, S. K. Kwak, S. Park and R. S. Ruoff, *Adv. Funct. Mater.*, 2020, **30**, 1–11.
- 50 Y. F. Wang, T. Qin, J. Huang, K. Yang and Z. R. Li, *J. Phys. Chem. C*, 2019, **123**, 24248–24254.
- 51 B. S. Mantripragada, R. Badam and N. Matsumi, *ACS Appl. Energy Mater.*, 2022, **5**, 6903–3912.
- 52 B. S. Mantripragada, R. Badam and N. Matsumi, *ECS Meet. Abstr.*, 2021, **MA2021-01**, 104–104.



---

## **Chapter 4. Pyrolyzed BIAN-Melamine based organic polymer as high performing anode in lithium-ion batteries.**

### **4.1 Abstract**

Energy storage is the key technological challenge that we are facing currently. Lithium-ion batteries are devices that are considered as promising alternatives for energy requirements. However, certain drawbacks like limited theoretical capacity, low fast charging ability etc., limit the extensive application of lithium-ion batteries. In this context, synthesis, and application of N-doped carbon (Py PBM) derived from BIAN-Melamine based organic polymer as single source of carbon and nitrogen, as anodic active material was presented. The effect of varying synthetic temperature (Py PBM600 at 600°C and Py PBM800° at 800°C) was also illustrated using various techniques. The as prepared Py PBM600 and Py PBM800 demonstrated superior electrochemical properties. Anodic half-cell prepared with Py BMCOF 600 as active material delivers a reversible specific capacity of 250 mAh/g at 1000 mA/g, 140 mAh/g at 2000 mA/g and 90 mAh/g at 4000 mA/g for over 1000 cycles at each current density. Anodic half-cell prepared with Py BMCOF 800 as active material delivers a reversible specific capacity of 250 mAh/g at 1000 mA/g, 105 mAh/g at 2000 mA/g and 70 mAh/g at 4000 mA/g for over 1000 cycles at each current density. The commercial competence of the materials is also studied by preparing full cells using Py PBM600 and Py PBM800 as anodes which delivered 1.1 mAh and 1.6 mAh respectively.

## 4.2 Introduction

Carbon, fourth most abundant element in the universe and fifteenth most abundant element in the earth's crust is unique in terms of its ability to catenate through covalent bond. Due to this feature of catenation, various allotropes of carbon in  $sp^3$  hybridized form, like diamond and allotropes in  $sp^2$  hybridized form, like graphite, fullerenes etc., are available in nature. The  $sp^2$  hybridized allotropes of carbon have attracted the attention of many material researchers all over the globe because, the  $sp^2$  carbon chain exhibits electron conduction property due to the lateral overlap of p-orbital. Further, in materials like graphite and derivatives of graphite, wherein the  $\pi$ -electron density is concentrated on a cyclic structure of carbon, cations like  $Li^+$ ,  $Na^+$ ,  $K^+$  etc., are observed to intercalate between the layers. This property has been widely exploited in metal ion ( $Li^+$ ,  $Na^+$ ,  $K^+$ ) batteries<sup>1,2</sup>. Though in terms of abundance sodium and potassium provide a better advantage<sup>3</sup>, smaller ionic radius of lithium ion and relatively simpler chemistry makes lithium ions an easier choice for batteries. Further, the low atomic weight of lithium also leads to a larger energy density than sodium and potassium. In lithium-ion battery, graphite anode can deliver a theoretical reversible capacity of 372 mAh/g<sup>4,5</sup>. However, realization of its theoretical capacity at faster charge-discharge conditions is found to be impossible<sup>6</sup>. At higher current densities, graphite was found to undergo anodic polarization owing limitations in ion transport and redox kinetics. The ion diffusion length ( $\tau$ ) in an electrode is given by  $\tau = L^2/D$ . Where, L is the diffusion length and D is the coefficient of diffusion<sup>7</sup>. Hence, by decreasing the diffusion length, it is possible to obtain faster ion transport kinetics. In this context, Lee et al., performed acid and base etching of graphite to increase the porosity of graphite, and the modified anode delivered a reversible capacity of 300 mAh/g at 100 mA/g current density<sup>8</sup>. In a different study, Neil Dasgupta et al., demonstrated a graphite-hard carbon hybrid anode that delivered a stable 1.0 Ah reversible capacity in full cell configuration<sup>6</sup>. Apart from the morphological adjustments, another alluring approach is to improve the redox properties of the anode by including elements that can act as anchoring sites for lithium ions, improve the electrical conductivity of the anode<sup>9</sup>. In this context, nitrogen atom is an interesting choice to be doped into carbon framework due to its, atomic radius (0.77 Å) which is close to that of carbon (0.74 Å) but has higher electronegativity (3.04) than carbon (2.55)<sup>10</sup>. Further, the lone pair of electrons present in unhybridized p-orbital of nitrogen boosts the electrical conductivity of the overall  $\pi$ -network. The polarity induced in the anode due to the inclusion of nitrogen leads to a non-faradaic interaction between the anode and lithium ion<sup>11</sup>. In this context,

Xia et al., have demonstrated a catalyst free synthesis of nitrogen-doped graphene by thermal annealing of graphite oxide with melamine. The results show an incorporation of 10.1 atomic percentage of nitrogen<sup>12</sup>. In a different study, Fu et al., have demonstrated the synthesis of nitrogen doped graphene with high nitrogen level through a one-step hydrothermal reaction of graphene oxide with urea for energy storage<sup>13</sup>. The results demonstrated a nitrogen atomic percentage of 10.13%. In N-doped carbon it is found that nitrogen can be present in four forms i.e., i) pyridinic ii) pyrrolic iii) graphitic iv) N-oxide<sup>14</sup>. However, all the  $sp^2$  nitrogen does not contribute to the  $\pi$ -conjugation, depending on the in plane or out of plane p orbital electrons. Chen et.al have shown using DFT calculations that pyridinic nitrogen is more beneficial for lithium-ion storage<sup>15</sup>. Though, synthesis of N-doped carbon from pyrolysis of carbon with a nitrogen source like urea or melamine is an interesting strategy and delivers a high nitrogen content, the type of nitrogen obtained after pyrolysis cannot be controlled in different ways of synthesis<sup>16</sup>. Matsumi et al., have shown polybenzimidazole can be single source of nitrogen and carbon for the synthesis of N-doped carbon. The results show a high nitrogen content of 17% and have shown an extremely fast charging lithium-ion battery performance<sup>7</sup>. In this work, BIAN-melamine organic polymer (PBM) as a single source of nitrogen and carbon to synthesize N-doped carbon is demonstrated. The synthesis was carried out at two different temperatures, i.e., 600°C (Py PBM 600) and 800°C (Py PBM 800). The as synthesized Py PBM 600 and Py PBM 800 were found to contain 14 and 10 atomic percentages of nitrogen. Furthermore, the as synthesized carbon materials delivered a high reversible capacity of 90 mAh/g and 86 mAh/g at 4 A/g current density. To understand the commercial competence of these materials, full cell studies were carried out and the results were found to be quite enticing.

## 4.3 Materials and methods

### 4.3.1 Materials

Acenaphthoquinone, melamine, 1,4 dioxane, mesitylene and N-methyl pyrrolidone (NMP) were purchased from Tokyo chemical industries, Ltd. and were used without further purification. 1.0 M LiPF<sub>6</sub> (50/50) ethylene carbonate/diethyl carbonate (EC/DEC) electrolyte and PVDF binder (molecular weight: 540,000) were purchased from Sigma-Aldrich. Battery-grade acetylene black was purchased from Denka Japan Private Co., Ltd. Copper foil of thickness of 20 μm was purchased from the Nilaco corporation.

**X-ray photo electron spectroscopy.** X-ray photoelectron spectroscopy (XPS) measurements were conducted on a Fisons instruments S-probe TM 2803 instrument.

**Transmission electron microscopy.** TEM images were acquired by scanning transmission electron microscope, JEM-ARM200F from JEOL Ltd at an acceleration voltage of 200 kV.

**Thermogravimetric analysis.** TGA was recorded using Hitachi STA7200 thermal analysis system at a heating rate of 10°C/min and a nitrogen flow rate of 200 ml/min.

**X-ray diffraction.** Powder XRD studies were conducted on Smart Lab X-Ray Diffractometer, Rigaku with Cu K $\alpha$  radiation ( $\lambda = 0.154$  nm, over the  $2\theta$  range of 2°–45° with a step size of 0.02°).

**Elemental dispersive X-ray scattering.** EDX spectra were recorded in TM3030plus at 15 kV.

### 4.3.2 Electrochemical studies

#### 4.3.2a Electrode preparation and cell fabrication

Py PBM600/Py PBM800, PVDF and acetylene black were taken in 80%, 10% and 10% weight percentages respectively and the slurry was prepared in NMP using kakuhunter ball mill. The homogenous slurry thus obtained was coated on a copper foil using a doctor blade (coating thickness: 0.1 mm). The electrode was dried under vacuum at 80°C for about 12 hours and was calendared to 0.06 mm thickness at 80°C. Disks of 17 mm diameter were punched from the calendared electrode sheet. 2025 type coin cells were fabricated in an argon filled glove box (O<sub>2</sub>, H<sub>2</sub>O < 0.5 ppm) using PBM electrode as anode, lithium metal foil as counter electrode, polypropylene separator (25 μm, celgard) and 1.0 M LiPF<sub>6</sub> (50/50) ethylene carbonate/diethyl carbonate (EC/DEC) as electrolyte. The cells were rested for about 8 hours before measurements.

**Electrochemical measurements.** All electrochemical measurements were performed in the potential range of 10 mV to 2.1 mV (vs Li/Li+) at 25°C. Cyclic voltammetry was performed in

biologic VSP workstation at 0.1, 0.2, 0.4, 0.6, 0.8 and 1.0 mV/s scan rates. Potentiostatic electrochemical impedance spectroscopy was performed in a frequency range of 10 MHz to 0.1 Hz. Galvanostatic charge-discharge measurements were conducted in biologic battery cycling system at various current densities.

### 4.3.3 Synthesis of PBM

Acenaphthoquinone (546 mg, 3 mmol) and melamine (252 mg, 2 mmol) were dispersed in about 5 ml of 1:1(v/v) 1,4 dioxane and mesitylene. 0.4 ml of acetic acid was added to the suspension. The mixture was then refluxed for 72 hours. A dark yellow precipitate was obtained after the reaction. The precipitate obtained was washed with copious amount of THF and DMF, dried at 80°C under vacuum for 12 hours. The yield obtained was 74 %.  $^1\text{H NMR}$  (DMSO  $d_6$ , 400 MHz)  $\delta$  8.45 (dd,  $J = 8.3, 0.7$  Hz, 2H),  $\delta$  8.05 (dd,  $J = 6.8, 0.7$  Hz, 2H) and  $\delta$  7.92 (t,  $J = 6.9$  Hz, 2H)

### 4.3.4 Synthesis of Py PBM600 and Py PBM800

BIAN-melamine organic polymer (PBM) was synthesized according to the procedure as described in chapter 3. Figure 1 shows the schematic representation of synthesis of Py PBM600 and Py PBM800. Py PBM 600 and Py PBM 800 were synthesized by pyrolyzing PBM at 600°C and 800°C respectively. The pyrolyzed samples were ultrasonicated in deionized water to remove any amorphous carbon or carbonate impurities in the samples. The ultrasonication was followed by drying at 80°C under vacuum for 12 hours to remove water. The samples thus obtained were ground finely using a mortar and pestle.

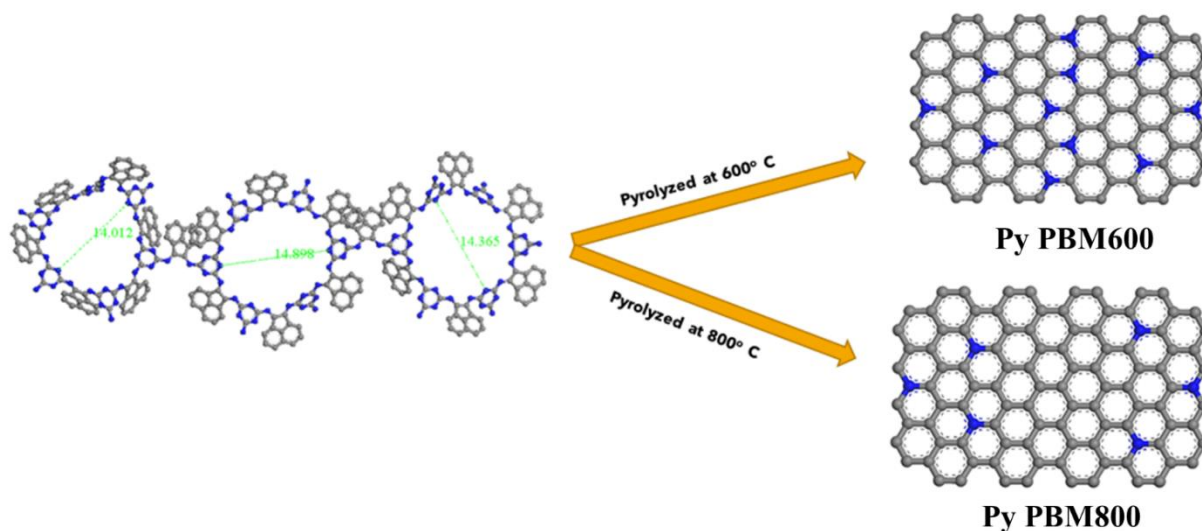


Figure 1-synthetic scheme of Py PBM 600 and Py PBM 600

## 4.4 Characterization

Py PBM 600 and Py PBM 800 were characterized using various characterization techniques.

### 4.4.1 Elemental dispersive X-ray spectroscopy

*Table 1-Elemental composition of Py PBM600*

Element	Atom%	Weight%
C	78.82	75.32
N	14.35	15.99
O	6.83	8.69

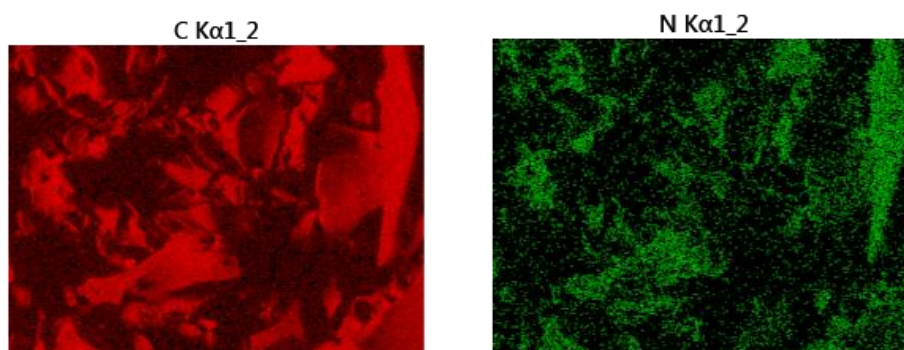


*Figure 2-EDX mapping of py PBM600*

Figure 2 shows the elemental mapping of Py PBM600. The nitrogen content was found to be uniform throughout the sample. The atomic percentage (Table 1) of Py PBM600 was found to be 78.82% corresponding to a weight percentage of 75.32 and a high nitrogen atomic percentage of 14.35% corresponding to a weight percent of 15.99%. Further, 6.8 atom percentage of oxygen was detected due to the adsorbed CO<sub>2</sub> on the sample corresponding to a weight percentage of 8.69%.

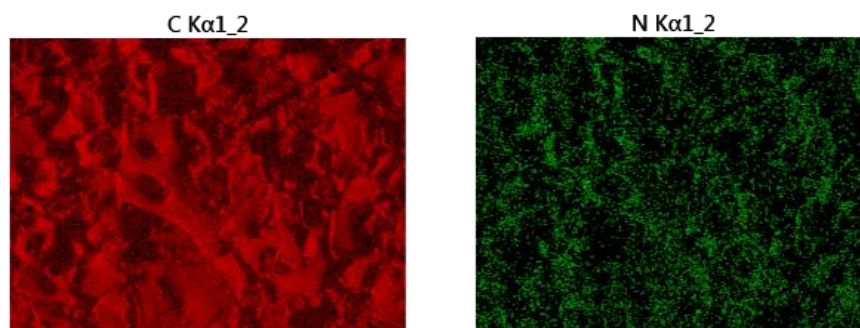


*Figure 3- EDX mapping of py PBM 800*

Table 2- Elemental composition of Py PBM800

Element	Atom%	Weight%
C	88.24	86.02
N	8.0	9.09
O	3.7	4.8

Figure 3 shows the elemental mapping of Py PBM800. The nitrogen content was found to be uniform throughout the sample. The atomic percentage (Table 2) of carbon was found to be 88.24% corresponding to a weight percentage of 86.02 and a nitrogen content of 8.0% corresponding to a weight percent of 9.09%. Further, 3.7 atom percentage of oxygen was detected due to the adsorbed CO<sub>2</sub> on the sample corresponding to a weight percentage of 4.8%.

#### 4.4.2 X-ray photo electron spectroscopy

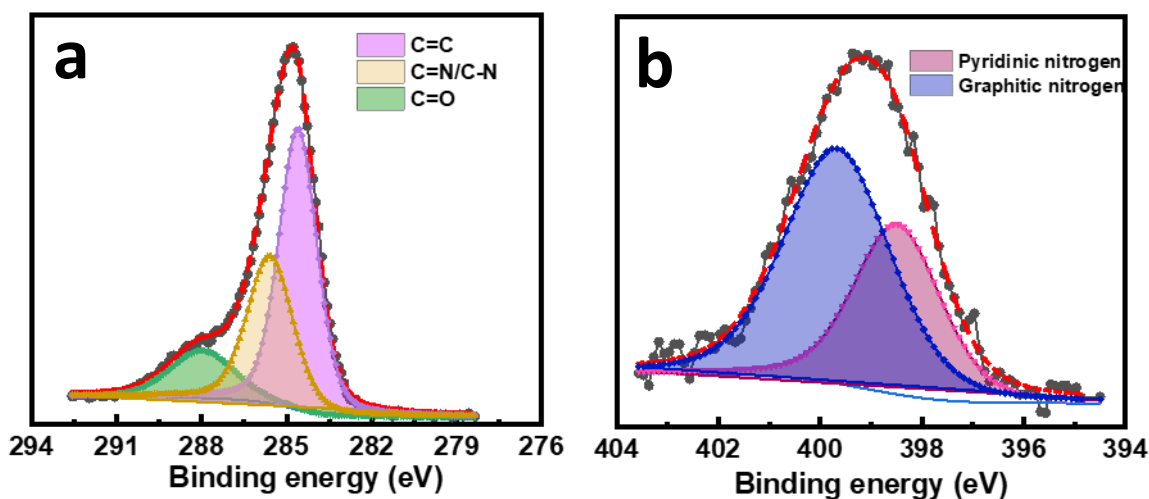


Figure 4-a) C1s XPS spectra of PyPBM600 b) N1s spectra of PyPBM600

The deconvoluted C1s XPS spectra (shown in Figure 4a) of PyPBM600 shows peaks at 284.6 eV, 285.59 eV, 287.98 eV corresponding to C=C, C=N/C-N and C=O groups respectively. The deconvoluted N1s spectra (shown in Figure 4b) shows two peaks at 398.48 eV and 399.68 eV corresponding to pyridinic and graphitic nitrogen respectively. Further, the following formula<sup>7</sup> was used for calculating the atomic percentage,

$$\text{Atomic percentage} = \frac{\frac{\text{area of the peak}}{\text{sensitivity factor}}}{\sum \frac{\text{area}}{\text{sensitivity factor}}} \times 100 \dots\dots\dots (1)$$

From the above formula, the atomic percentage of nitrogen was found to be 14 %. This is similar with the observation made in EDX spectra. Among the nitrogen content present, 63% is in the form of graphitic nitrogen and 37% is in the form of pyridinic nitrogen. The relatively high amount of nitrogen in the sample suggests a better electrochemical performance as discussed earlier.

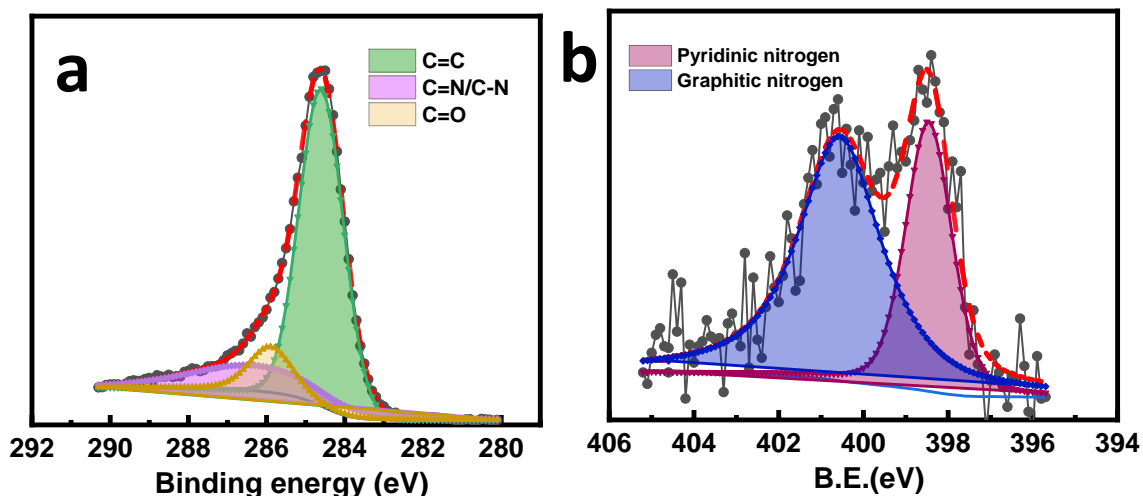


Figure 5- a) C1s XPS spectra of PyPBM600 b) N1s spectra of PyPBM800

The deconvoluted C1s XPS spectra (Figure 5a) of PyPBM800 shows peaks at 284.6 eV, 286.3 eV, 286.9 eV corresponding to C=C, C=N/C-N and C=O groups respectively<sup>17</sup>. The deconvoluted N1s spectra (Figure 5b) shows two peaks at 398.46 eV and 400.5 eV corresponding to pyridinic and graphitic nitrogen respectively<sup>18</sup>. Further, using equation (1), the atomic percentage of nitrogen was found to be 10 %. This is similar with the observation made in EDX spectra. Among the nitrogen content present, 67% is in the form of graphitic nitrogen and 33% is in the form of pyridinic nitrogen. The effect of lower nitrogen content will be demonstrated later in the light of electrochemical studies.

#### 4.4.3 Thermogravimetric analysis

Figure 6 a and b show TGA traces of Py PBM600 and py PBM800 in air, both the materials show 4 to 5% loss till 90°C corresponding to adsorbed gases or moisture, after which decomposition is observed corresponding to the oxidation of N-doped carbon material till 425°C. At 580°C the material is completely oxidized as understood by the sharp transition. The DTA curve of both materials show endothermic peaks beginning from 425°C after which a sharp peak indicating rapid oxidation was observed till 580°C. The area under the curve of the DTA peaks of both materials was observed to be similar indicating that the enthalpy of oxidation is similar for the materials.



Thus, Py PBM600 and Py PBM800 show a similar thermal property irrespective of the difference in composition, which implies that the slight variation in the nitrogen content doesn't have any significant effect on the thermal properties.

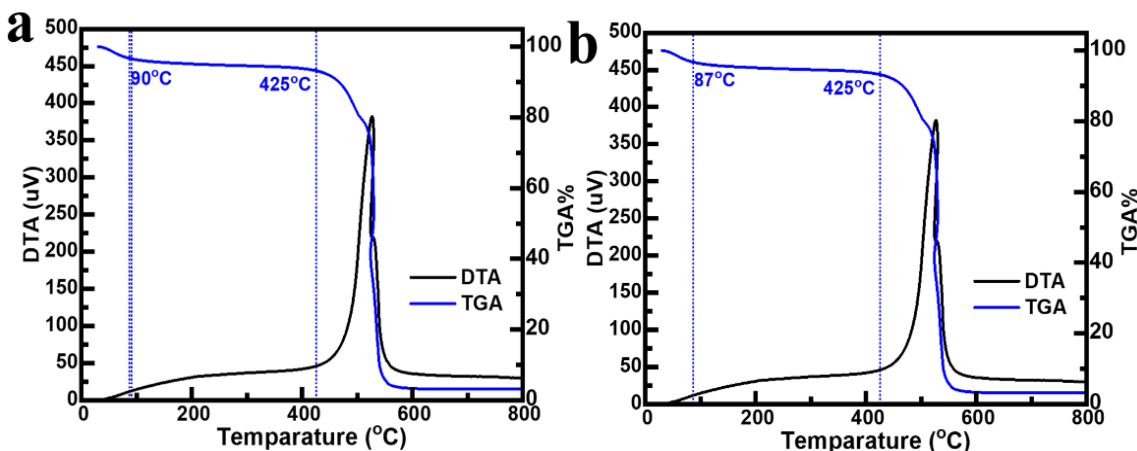


Figure 6-a) TGA and DTA of Py PBM600 b) TGA and DTA of Py PBM800

#### 4.4.4 X-ray diffraction

Figure 7 a and b show the X-ray diffractograms of Py PBM600 and Py PBM800 respectively. Py PBM600 show a relatively less intense and broad peak at  $25.7^\circ$  corresponding to an interlayer spacing of 0.35 nm. Py PBM800 shows a relatively intense and less broad peak at  $26.2^\circ$  corresponding to an interlayer spacing of 0.34 nm and a minor peak at  $12.5^\circ$ . The broad peaks observed in both the cases indicate that the arrangement of the layers of Py PBM600 and Py PBM800 is turbostratic in nature. It is important to note that Py PBM600 and Py PBM800 have exhibited similar thermal behavior irrespective of the slight variation in crystal structure thus

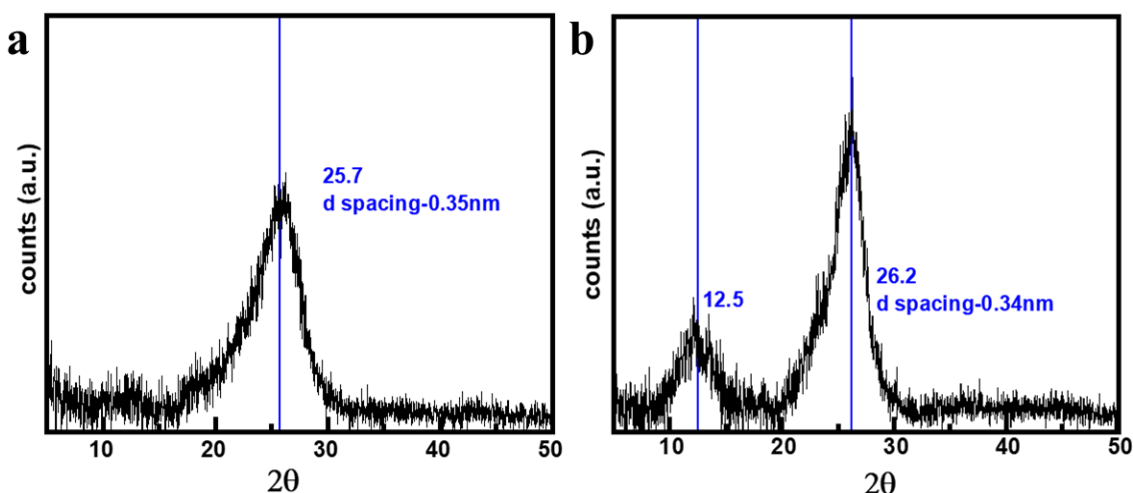


Figure 7-a) XRD pattern of Py PBM600 b) XRD pattern of Py PBM800

indicating that differences in micro crystallinity that were created due to the difference in synthesis temperature did not affect extrinsic property of the material.

#### 4.4.5 TEM images

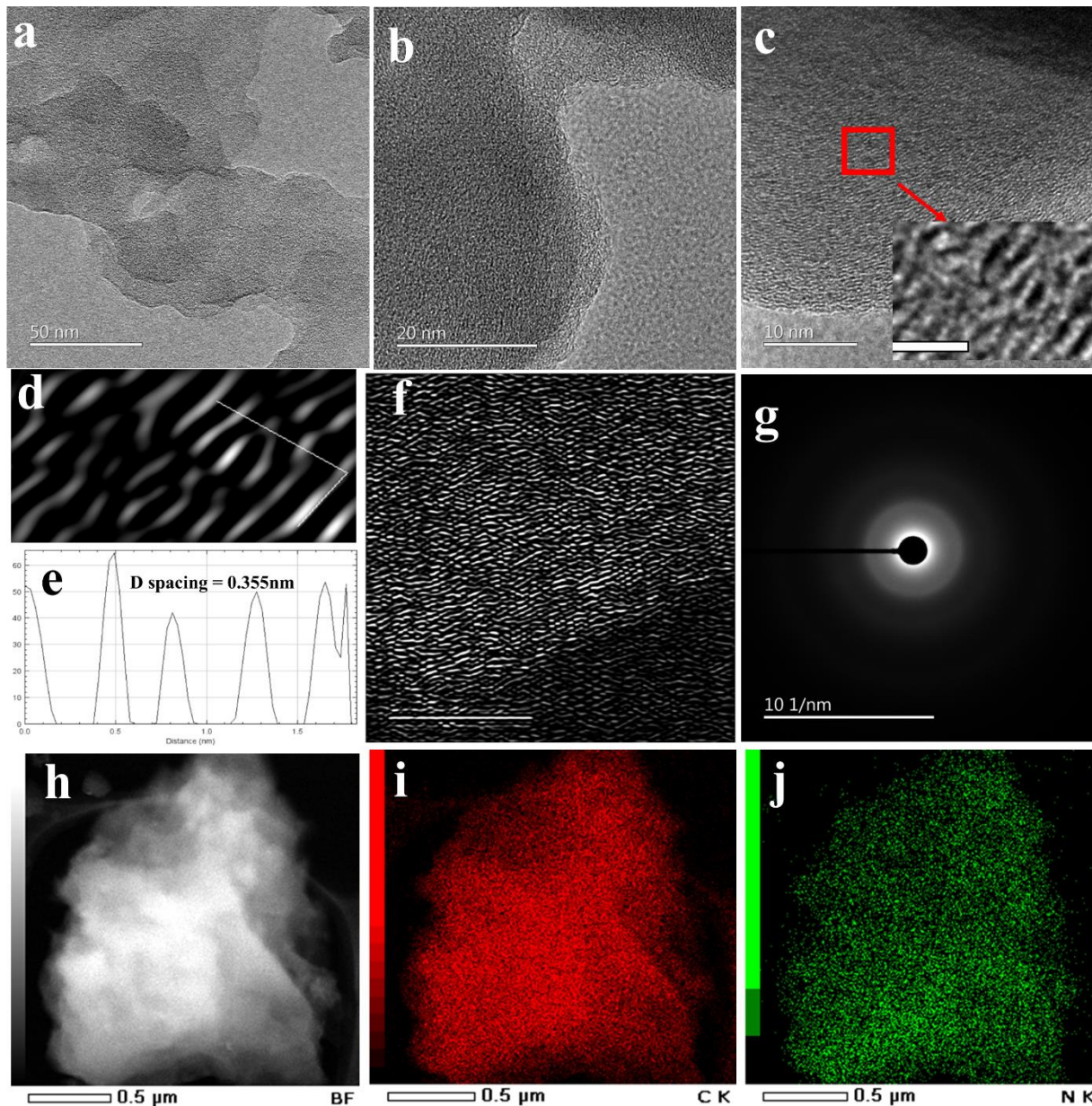


Figure 8-a) TEM image(50 nm) indicating layered nature of Py PBM600 b) TEM image(20 nm) indicating layered nature of Py PBM600 c) TEM image showing lattice fringes d) inverse Fourier transform of image d e) plot profile for d-spacing f) inverse Fourier transform of image c g) SAED pattern of Py PBM600 h) Bright field image of Py PBM600 at 0.5  $\mu\text{m}$  i) EDX image indicating the distribution of carbon j) EDX image indicating the distribution of nitrogen.

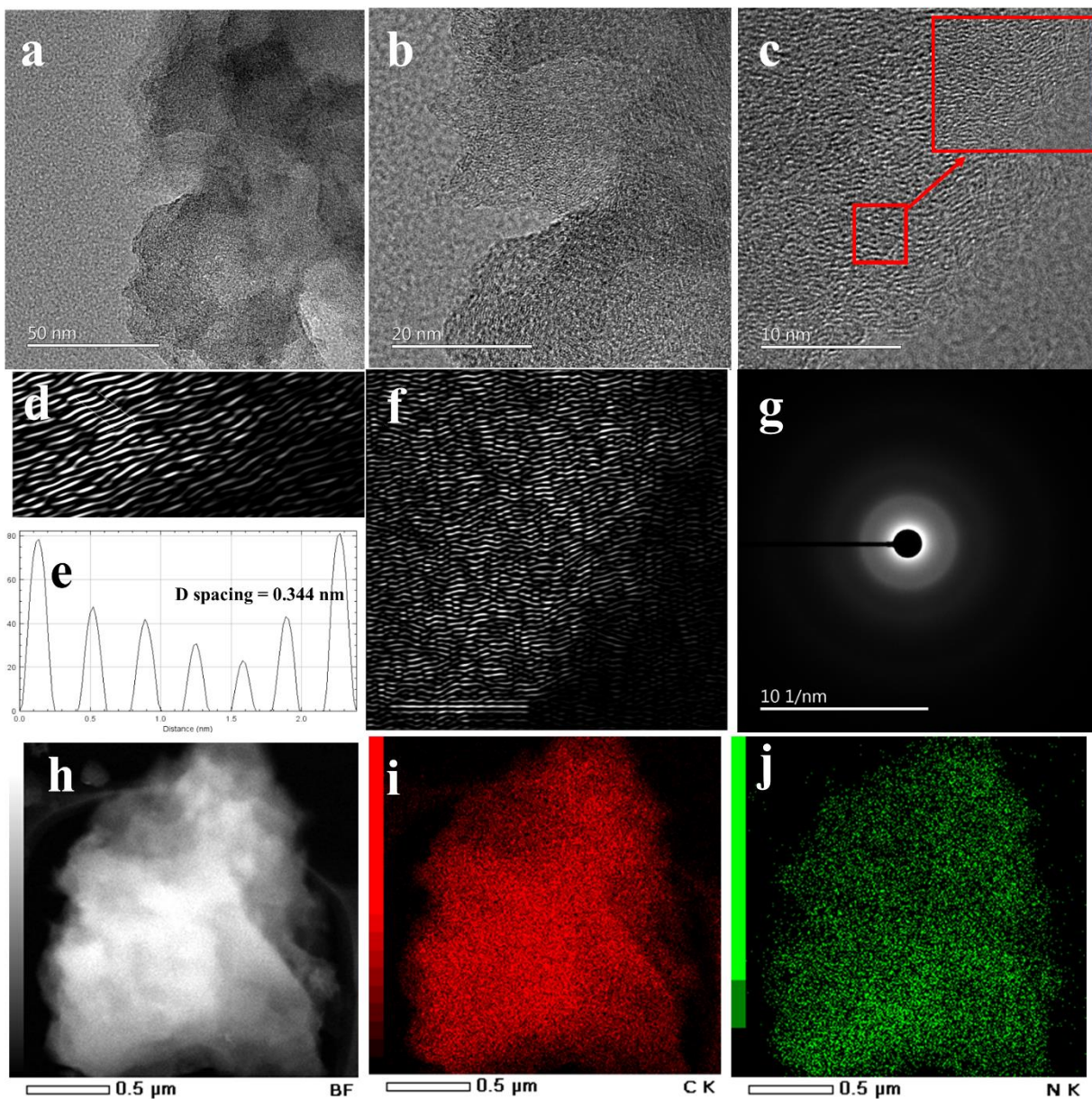


Figure 9- a) TEM image(50 nm) indicating layered nature of Py PBM800 b) TEM image(20 nm) indicating layered nature of Py PBM800 c) TEM image showing lattice fringes d) inverse Fourier transform of image c e) plot profile for d-spacing f) inverse Fourier transform of image c g) SAED pattern of Py PBM800 h) Bright field image of Py PBM600 at 0.5 μm i) EDX image indicating the distribution of carbon j) EDX image indicating the distribution of nitrogen.

Figures 8 and 9 show the TEM micrographs of PY PBM600 and Py PBM800. Figures 8a, 8b and 9a, 9b show the layered morphologies of Py PBM600 and Py PBM800. From Figures 8a and 9a, it can also be observed that the layer dimensions are not uniform unlike ordered materials like graphite. Figure 8c and 9c show the lattice fringes of Py PBM600 and Py PBM800. The

arrangement of both the materials was found to be turbostratic in nature<sup>19</sup>. To understand the d spacing of PY PBM600 and Py PBM800 inverse fourier transform was conducted (Figures 8d and 9d). The d-spacing was calculated to be 0.355 nm and 0.344 nm which is in close agreement with the d-spacing observed in XRD. However, it is important to note that the d-spacing calculated was for a short range and such extended layered nature was observed at fewer regions. Figures 8f and 9f show the inverse fourier transform images of Figure 8a and 9a respectively, which indicate a better micro crystallinity in case of Py PBM800 than in Py PBM600. Figures 8g and 9g show SAED pattern of Py PBM600 and Py PBM800 respectively. Both the patterns show diffusive and broad rings due to the amorphous nature of materials. Figures 8h and 9h show the bright field image of Py PBM600 and Py PBM800. EDX was conducted at the spot indicated in Figure 8h and 9h, to understand the elemental distribution. It was observed that the nitrogen distribution is uniform with the distribution of carbon (Figures 8i, 8j and 9i, 9j).

#### 4.4.6 RAMAN spectroscopy

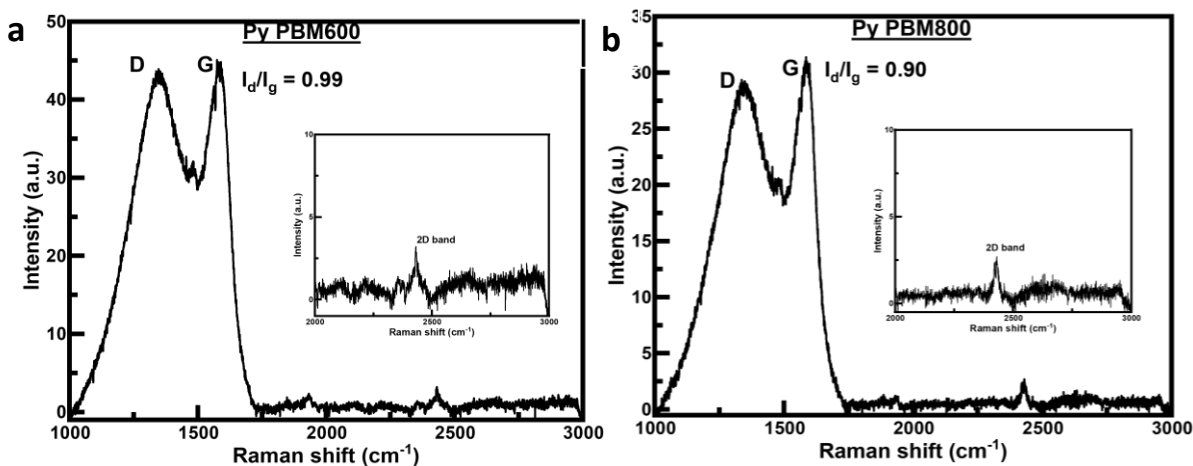


Figure 10-a) RAMAN spectra of PyPBM600 b) RAMAN spectra of PyPBM800

The Raman spectra of Py PBM600 (Figure 10a) exhibit two peaks at Raman shifts of  $\sim 1350\text{ cm}^{-1}$  and  $\sim 1570\text{ cm}^{-1}$ , which correspond to the D-band (defect-induced mode) and G-band ( $E_{2g}$  mode of graphite), respectively. The intensity ratio  $I_d/I_g$  is calculated to be 0.99 in Py PBM600 indicating the high degree of induced defects. A minor band at  $\sim 2450\text{ cm}^{-1}$  was observed corresponding to the 2D band of Py PBM600. The weak intensity of the 2D band suggests low stacking of the layers of Py PBM600. Further, the Raman spectra of Py PBM800 (Figure 10b) exhibit two peaks at similar Raman shifts of  $\sim 1350\text{ cm}^{-1}$  and  $\sim 1570\text{ cm}^{-1}$ , corresponding to D-band and

G-band respectively. The  $I_d/I_g$  ratio is calculated to be 0.91 in Py PBM800. The relatively lower intensity ratio indicate the relatively more arranged nature of Py PBM800. The relatively higher intensity of 2D band in Py PBM800 than Py PBM600 indicates better layered arrangement in Py PBM800.

## 4.5 Electrochemical characterization

### 4.5.1 Cyclic voltammetry

Figure 11a and 11b show cyclic voltammograms of anodic half-cells with Py PBM600 and Py PBM800 as active materials at 0.1 mV/s. The cyclic voltammogram of both the anodic half-cells with Py PBM600 anode and Py PBM800 anodes show reduction peaks at 0.65 V corresponding to the irreversible reduction of electrolyte. In the CV of Py PBM800 anodic half-cell, the reduction peak was observed to be less intense at 0.65 V but the lithiation peak observed in the first cycle was too broad suggesting that the formation of SEI<sup>20</sup> occurs at a range of potential.

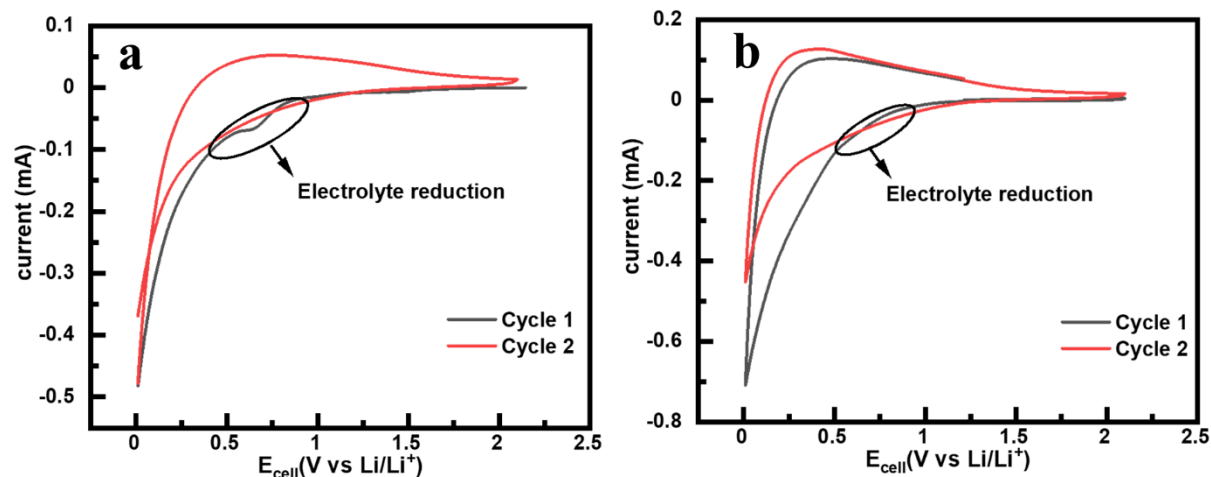


Figure 11-a) Cyclic voltammogram of anodic half-cell with Py PBM600 as anode at 0.1 mV/s  
 b) Cyclic voltammogram of anodic half-cell with Py PBM800 as anode at 0.1 mV/s

### 4.5.2 Potentiostatic impedance spectroscopy

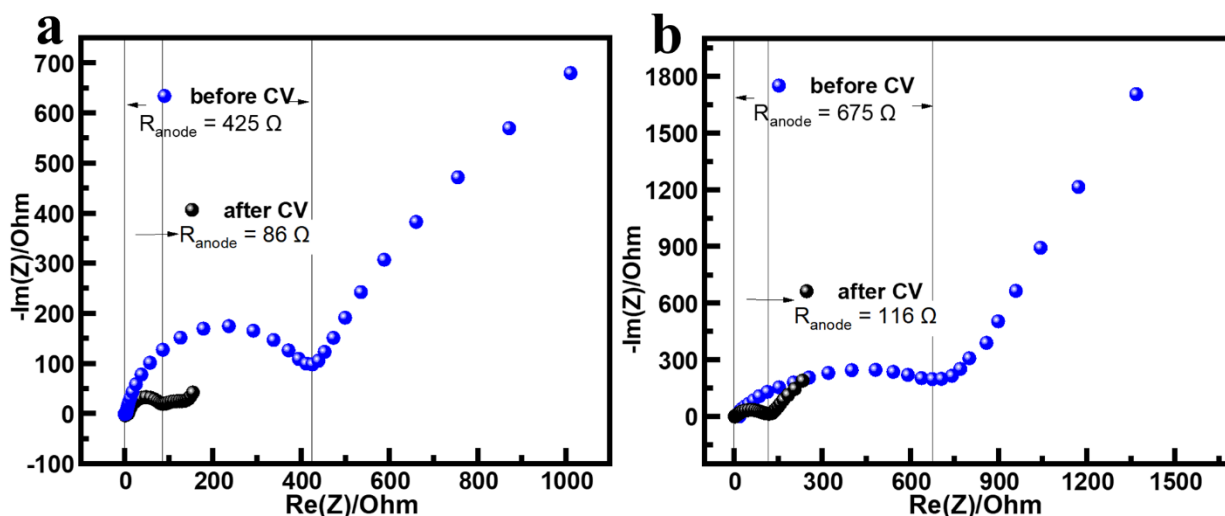


Figure 12-a) PEIS of anodic half-cell with Py PBM600 anode b) PEIS of anodic half-cell with Py PBM800 as anode

Figure 12 shows PEIS of Py PBM600 and Py PBM800 anodic half-cells. The resistance of anode<sup>21</sup> was found to be 425 ohms in case of Py PBM600 before cyclic voltammetry. After cyclic voltammetry, the anode resistance decreases due to the formation of SEI and was found to be 86 ohms. In the case of, Py PBM800 the resistance of anode<sup>22</sup> was found to be 675 ohms and after cyclic voltammetry, the anode resistance decreased and was found to be 116 ohms. The anode resistance was found to be slightly higher in case of Py PBM800 which can be due to the difference in the crystallinity of the material.

### 4.5.3 Galvanostatic charge-discharge studies

Galvanostatic charge-discharge studies were conducted on anodic half-cells with Py PBM600 anode. Figure 13a shows the rate studies of the anodic half-cell with Py PBM600 anode. Reversible capacities of 425 mAh/g, 280 mAh/g, 235 mAh/g, 191 mAh/g, 172 mAh/g, 110 mAh/g, 52 mAh/g were observed at 50 mA/g, 200 mA/g, 400 mA/g, 750 mA/g, 1000 mA/g, 2000 mA/g and 4000 mA/g respectively. Figure 13b shows the long cycling studies of Py PBM600 anodic half-cell, reversible capacities of 250 mAh/g, 140 mAh/g, 120 mAh/g were observed for 2000, 1500 and 1000 cycles respectively at 1000 mA/g, 2000 mA/g and 4000 mA/g current densities respectively. The coulombic efficiency was found to be 100% for all three cells. The capacity retention was found to be 90% for 2000 cycles, 82% for 1500 cycles and 79% for 1000 cycles at 1000 mA/g, 2000 mA/g and 4000 mA/g respectively. Figure 13c shows the potential vs capacity curves of anodic half-cell with Py PBM600 anode at 1000 mA/g current density. The plots of each cycle

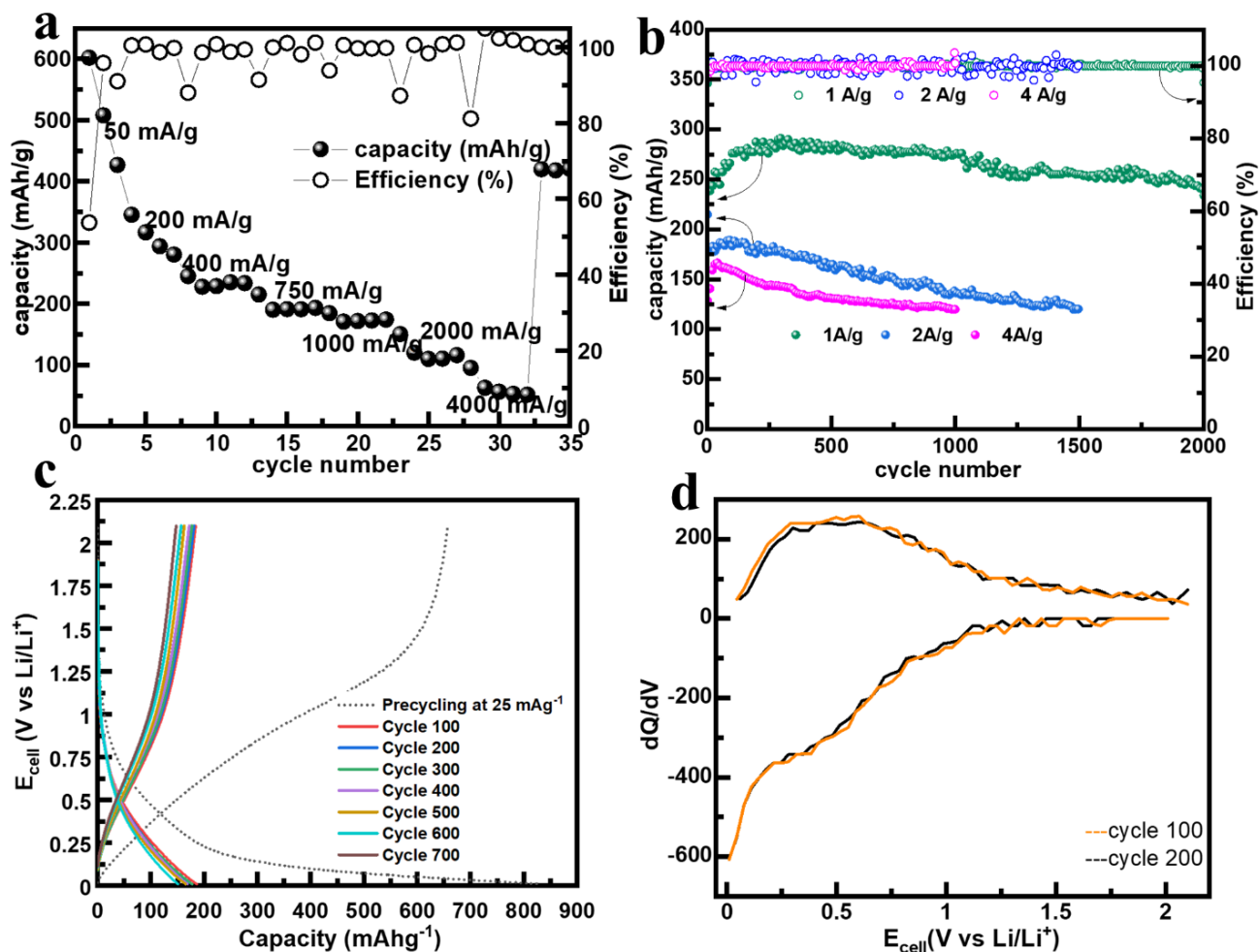


Figure 13-a) Rate studies of anodic half-cell with Py PBM600 anode b) Long cycling studies of anodic half-cell with Py PBM600 anode c) potential vs capacity curve at 1A/g d)  $dQ/dV$  plots of anodic half-cell with Py PBM600 anode at 1 A/g

show a minor reduction in capacity compared to the initial cycle. This indicates the better capacity retention of the active material. Further the data presented in Figure 13c was used to construct  $dQ/dV$  plots shown in Figure 13d. The capacity contribution was observed majorly from the potential region of 10 mV to 1.0 V wherein a broad curve was observed indicating no specific redox potential, which is a characteristic feature of capacitive materials<sup>23</sup>. The  $dQ/dV$  plot was observed to become narrower compared to the region till 1 V suggesting a relatively lower but substantial capacity contribution<sup>24</sup>.

Figure 14a shows the rate studies of the anodic half-cell with Py PBM800 anode. Reversible capacities of 440 mAh/g, 365 mAh/g, 252 mAh/g, 200 mAh/g, 177 mAh/g, 122 mAh/g, 65 mAh/g were observed at 50 mA/g, 200 mA/g, 400 mA/g, 750 mA/g, 1000 mA/g, 2000 mA/g and 4000 mA/g respectively. Figure 14b shows the long cycling studies of Py PBM800 anodic half-cell in

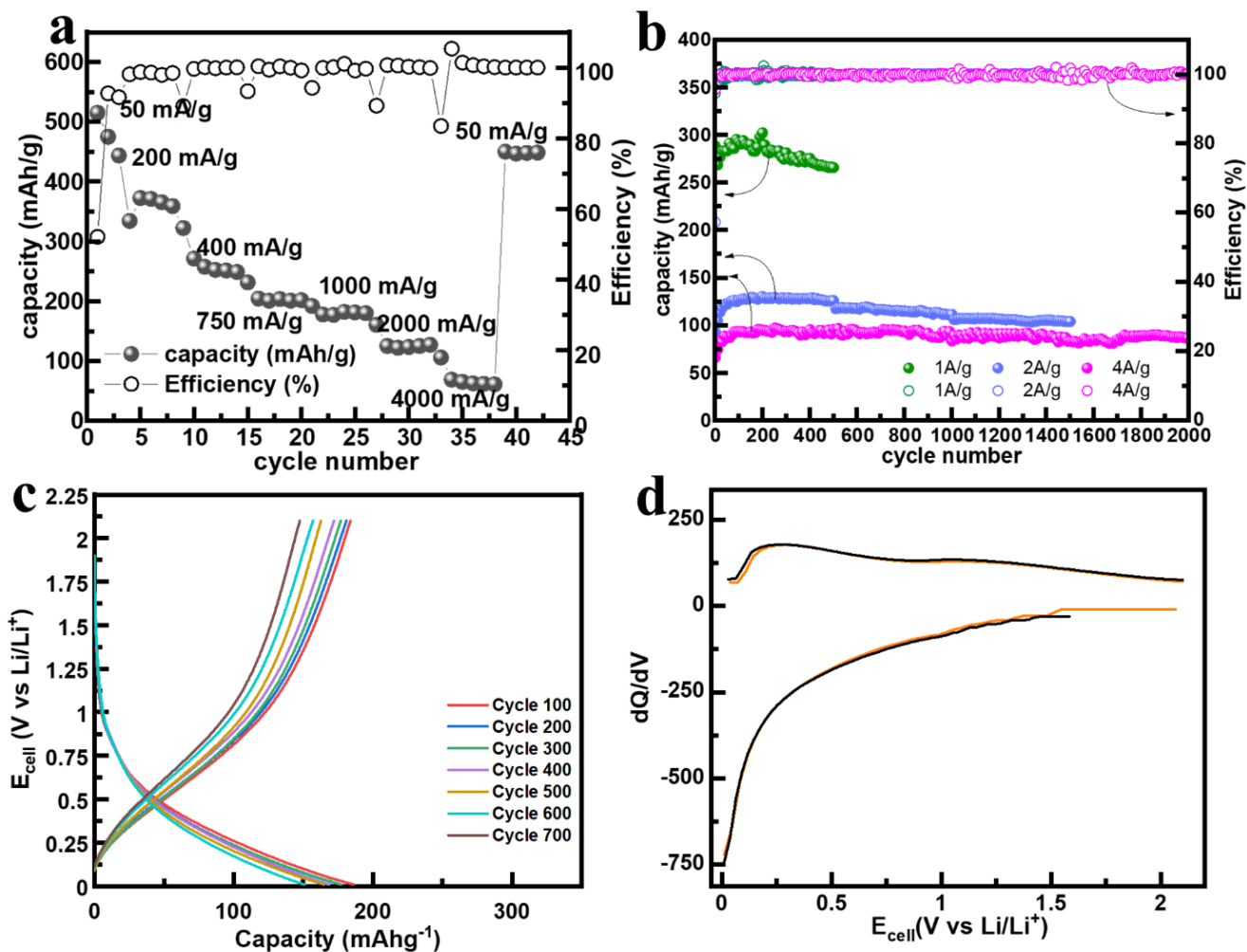


Figure 14-a) Rate studies of anodic half-cell with Py PBM800 anode b) Long cycling studies of anodic half-cell with Py PBM800 anode c) potential vs capacity curve at 1A/g d)  $dQ/dV$  plots of anodic half-cell with Py PBM800 anode at 1 A/g

which, reversible capacities of 260 mAh/g, 105 mAh/g, 86 mAh/g were observed for 500, 1500 and 2000 cycles respectively at 1000 mA/g, 2000 mA/g and 4000 mA/g current densities respectively. The coulombic efficiency was found to be 100% for all three cells. The capacity retention was found to be 91% for 500 cycles, 92% for 1500 cycles and 99% for 2000 cycles at 1000 mA/g, 2000 mA/g and 4000 mA/g respectively. Figure 14c shows the potential vs capacity curves of anodic half-cell with Py PBM800 anode at 1000 mA/g current density. The plots of each cycle show a minor reduction in capacity compared to the initial cycle. This indicates the better capacity retention of the active material. Further the data presented in Figure 14c was used to construct  $dQ/dV$  plots shown in Figure 14d. The capacity contribution was observed majorly from the potential region of 10 mV to 1.0 V wherein a broad curve was observed indicating no specific redox potential, which is a characteristic feature of capacitive materials. The  $dQ/dV$  plot was



observed to become narrower compared to the region till 1 V suggesting a relatively lower but substantial capacity contribution. However, unlike the  $dQ/dV$  plots of Py PBM600 anodic half-cell, decrease after 1.0 V is not so rapid. Even after 1.0 V the curve remain significantly broad suggesting that the material is more active for lithium storage between 1.0 V to 2.1 V compared to the Py PBM600 counterpart. Also, the reversible capacity exhibited by Py PBM600 anodic half-cell is slightly higher than that of Py PBM800 anodic half-cell. However, low-capacity retention in case of Py PBM600 half-cell offsets the benefit of better capacity. The capacity retention is relatively much higher in case of Py PBM800 anodic half-cell at higher currents. This suggests that at higher currents, like 4000 mA/g where in the time of charge is 80 seconds, Py PBM800 anode seems to be better suited.

#### 4.5.4 DEIS

Figures 16 and 17 show the DEIS and the variation of charge transfer and SEI resistances of anodic half-cells with Py PBM600 and Py PBM800 as anodic active materials respectively. The Nyquist plots at each potential step during lithiation and delithiation are shown in Figures 16a, b and 15a, b. The Nyquist plot profiles indicate that decrease in Warburg type diffusion resistance with the decrease in potential. As observed in the  $dQ/dV$  plots shown in Figures 12d and 13d, maximum lithiation of both the anodes takes place after 1 V which indicates that lithium storage (intercalation) is more favorable below 1 V and the decrease in Warburg type resistance after 1 V in DEIS profiles support the hypothesis that after 1 V the lithium storage in the anode is more favorable. Further, the semi-circle region corresponding to the internal resistance of the anode was observed to decrease with potential in both the cases. The following circuit (Figure 15) was employed to understand the physical elements contributing to the impedance:

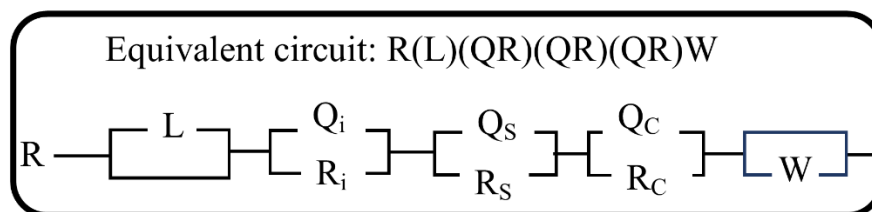


Figure 15-Equivalent circuit used to fit the impedance data

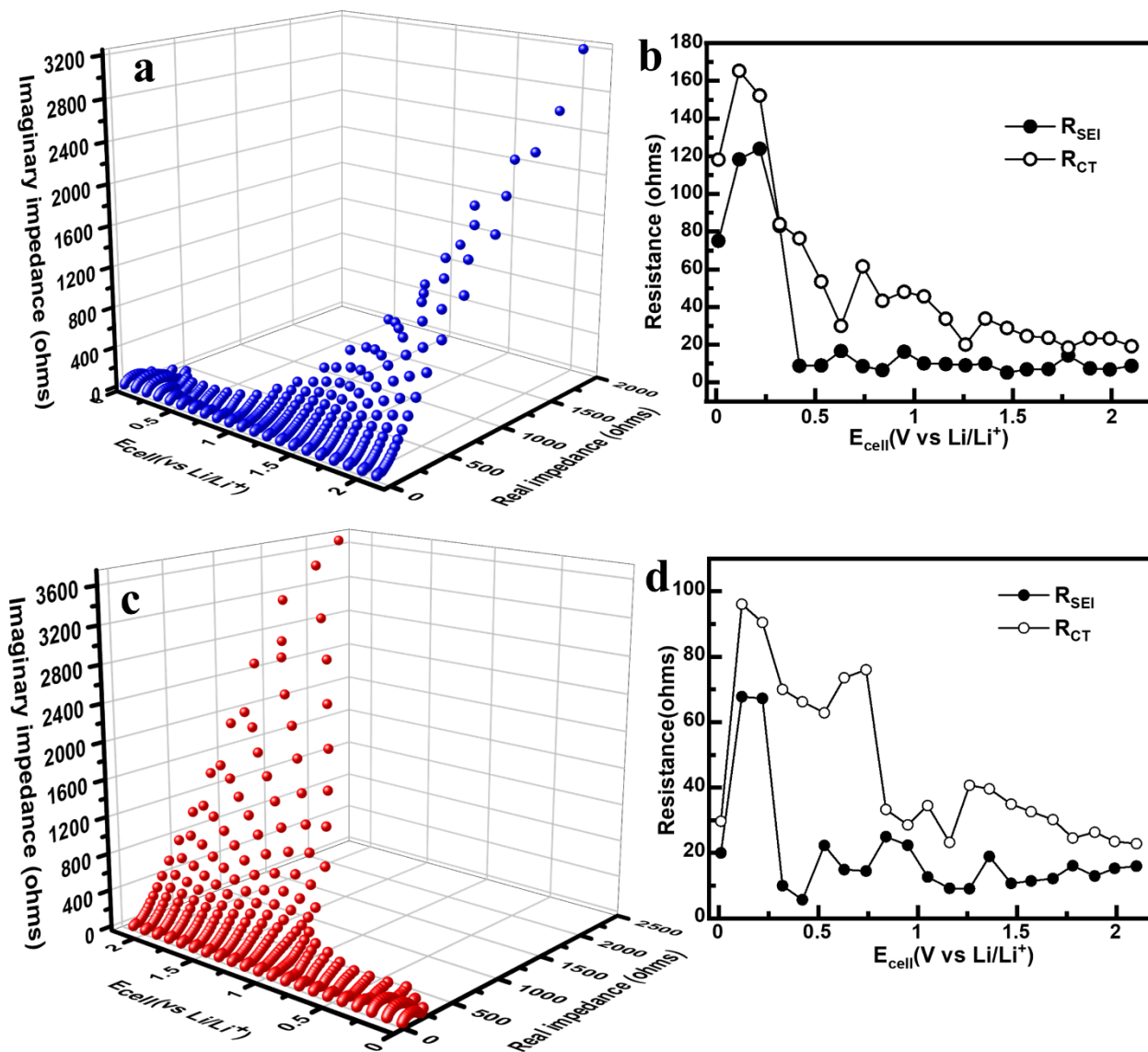


Figure 16-a) DEIS in the lithiation of anodic half-cell with Py PBM600 as anodic material b) SEI and charge transfer resistances in the lithiation of anodic half-cell with Py PBM600 as anodic material c) DEIS in the delithiation of anodic half-cell with Py PBM600 as anodic material d) SEI and charge transfer resistances in the delithiation of anodic half-cell with Py PBM600 as anodic material.

As seen in Figures 16 b and d the  $R_{SEI}$  of the anodic half-cell with Py PBM600 anode was observed to be in the range of 12-20 ohms and the  $R_{CT}$  of the anodic half-cell with Py PBM600 anode was observed to be in the range of 20-100 ohms. The charge transfer resistance was observed to decrease with potential. The charge transfer resistance from 10 mV to 1 V was observed to be higher in case of lithiation than in delithiation which can be due to the difference in activation energies required for lithiation and delithiation. The SEI resistance was also observed to be lower

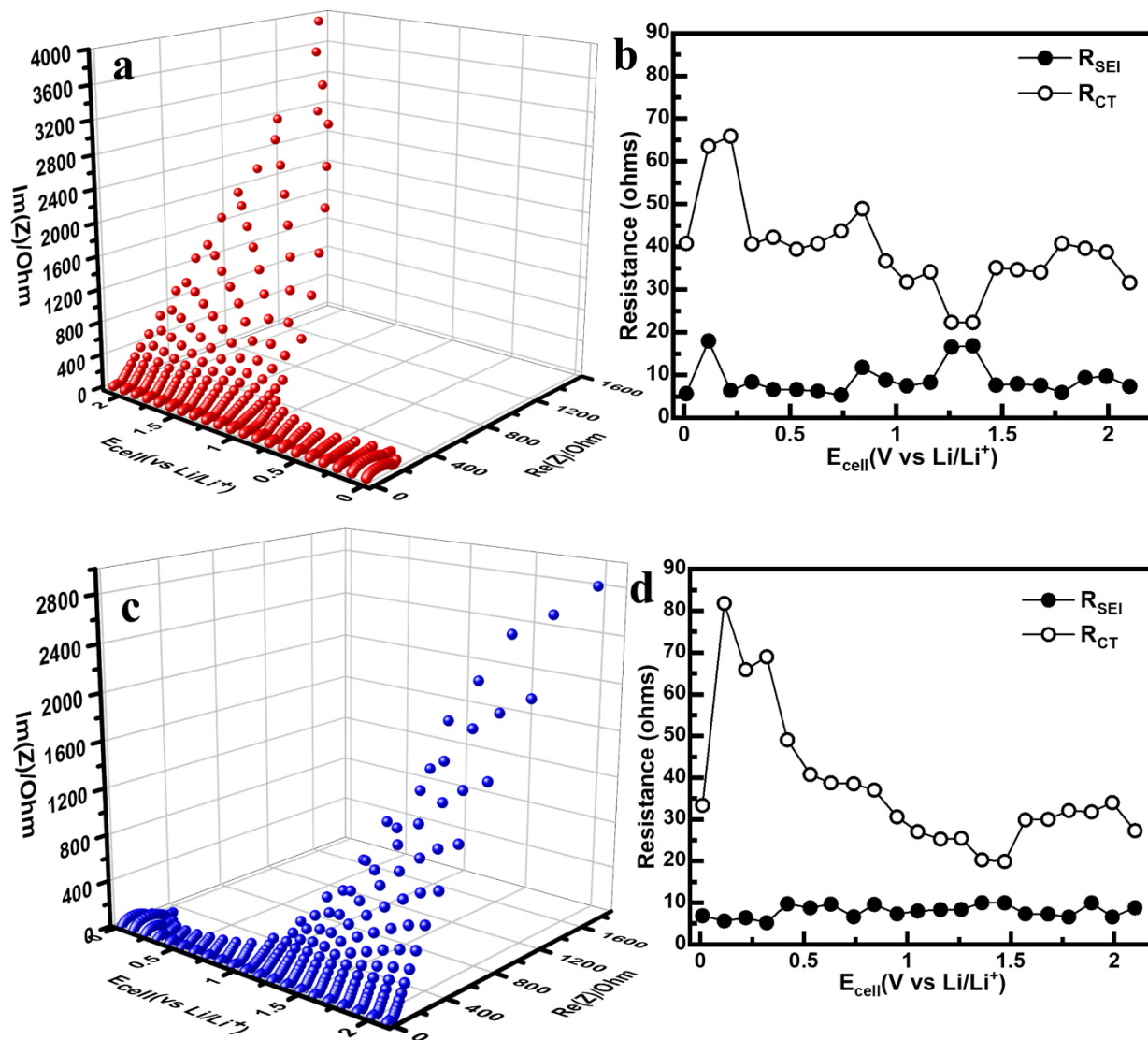


Figure 17-a) DEIS in the lithiation of anodic half-cell with Py PBM800 as anodic material b) SEI and charge transfer resistances in the lithiation of anodic half-cell with Py PBM800 as anodic material c) DEIS in the delithiation of anodic half-cell with Py PBM800 as anodic material d) SEI and charge transfer resistances in the delithiation of anodic half-cell with Py PBM800 as anodic material

in both the cases of lithiation and delithiation. Figures 17 a and c show DEIS profiles of anodic half-cell with Py PBM800 anode in the lithiation and delithiation halves respectively. The Warburg type diffusion resistance was observed to decrease with potential as observed in the Py PBM600 anodic half-cell. The charge transfer resistance and SEI resistance (shown in Figures 17 b and d) was evaluated using the circuit demonstrated in Figure 15. Both  $R_{\text{CT}}$  and  $R_{\text{SEI}}$  were observed to decrease with potential. Unlike the observation made in the case of Py PBM600, the charge transfer resistance during lithiation and delithiation were observed to be comparable. This suggests the

formation of better diffusion pathways in Py PBM800 and thereby reducing charge transfer resistance.

#### 4.5.5 Kinetic studies

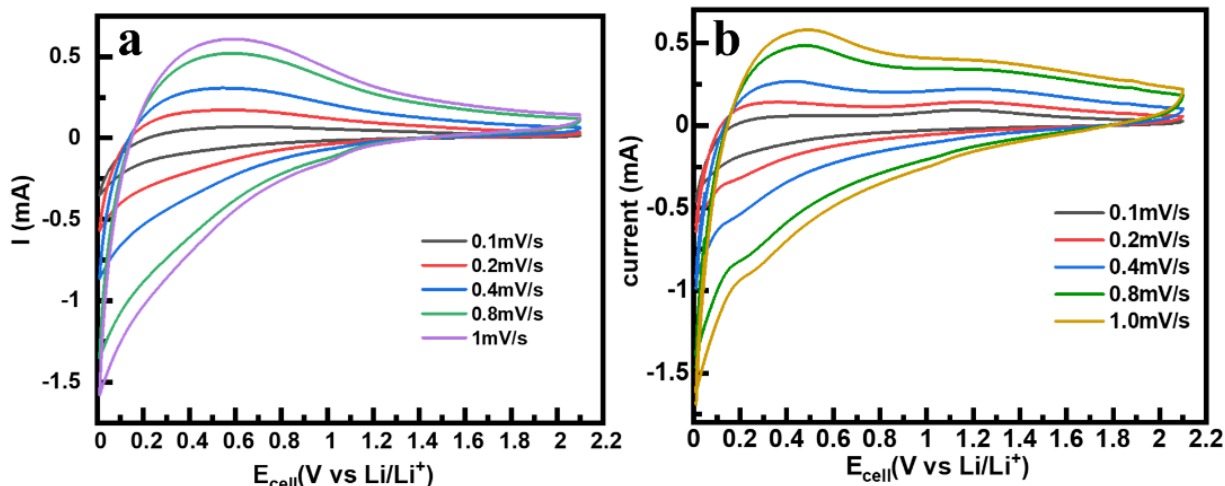


Figure 18-a) Cyclic voltammograms of anodic half-cell with Py PBM600 anode at various scan rates b) Cyclic voltammograms of anodic half-cell with Py PBM800 anode at various scan

Figures 18 a and b show cyclic voltammograms of Py PBM600 based anodic half-cell and Py PBM800 based anodic half-cell at various scan rates. The anodic half-cell with Py PBM600 anode shows higher over potential compared to the anodic half-cell with Py PBM800 anode. This observation is in line with the relatively better capacity retention of Py PBM800 anode than Py PBM600 anode. Further, randles-sevik equation<sup>15</sup>:

$$i = 2.69 * 10^5 n^{1.5} D^{0.5} A C \nu^{0.5} \dots\dots\dots (2)$$

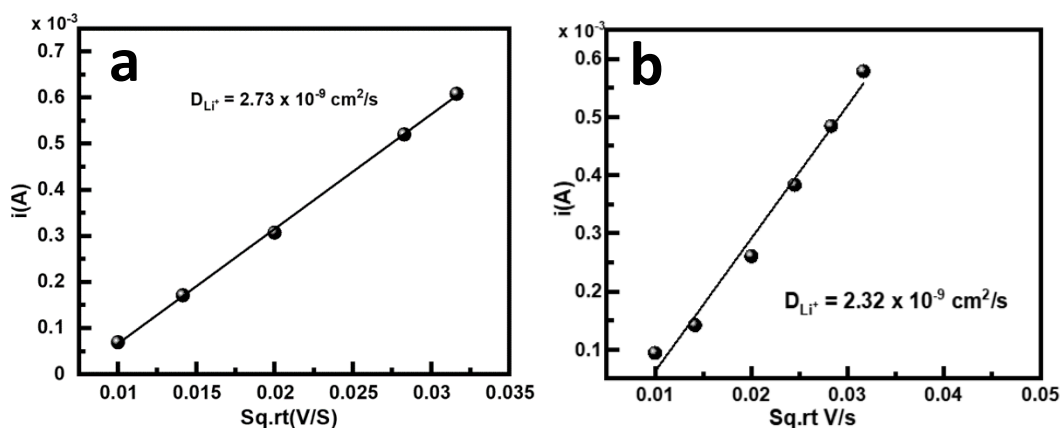


Figure 19-a) Linear fit of  $\nu^{0.5}$  vs peak current in Py PBM600 based anodic half-cell b) Linear fit of  $\nu^{0.5}$  vs peak current in Py PBM800 based anodic half-cell

Where,  $i$  is peak current,  $n$  is number of electrons or ions transferred,  $D$  is diffusion coefficient,  $A$  is area of the electrode,  $C$  is concentration of electrolyte and  $\vartheta$  is scan rate, was employed to evaluate the diffusion coefficient of the anodes. The data obtained from the cyclic voltammograms at various scan rates, was used to plot linear fits (Figure 19 a and b) from which the diffusion coefficient was evaluated to be  $2.73 \times 10^{-9} \text{ cm}^2/\text{s}$  and  $2.32 \times 10^{-9} \text{ cm}^2/\text{s}$  for Py PBM600 and Py PBM800 respectively.

The following equation as used to evaluate the contribution of capacitive and diffusive behaviors<sup>25</sup>:

$$i = i_{cap} + i_{diff} \dots \dots \dots \textcircled{3}$$

Where  $i_{cap}$  and  $i_{diff}$  are capacitive and diffusive currents.

$$i = k_{cap}\vartheta + k_{diff}\vartheta^{0.5} \dots \dots \dots \textcircled{4}$$

Where  $k_{cap}$  and  $k_{diff}$  are proportionality constant for capacitance and diffusion respectively.

Rearranging equation 4, we obtain:

$$\frac{i}{\vartheta^{0.5}} = k_{diff} + k_{cap}\vartheta^{0.5} \dots \dots \dots \textcircled{5}$$

Equation 5 was used to calculate the contribution of capacitive and diffusive behaviors by plotting linear fit of  $i/\vartheta^{0.5}$  vs  $\vartheta^{0.5}$  (Figure 20 a and b). The slope and intercept values obtained were used to calculate capacitive and diffusive behaviors as shown in equation 4. Figures 20 c and d show the contribution of capacitance and diffusive contributions in Py PBM600 and Py PBM800 anodic half-cells. Py PBM600 based anodic half-cell predominantly exhibits a capacitive behavior whereas Py PBM800 based anodic half-cell shows a substantial contribution of diffusive behavior along with a high capacitive behavior.

As seen in equations 3 and 4, the peak current and scan rate relation can be generalized into a power law<sup>26</sup>:

$$i = k\vartheta^b \dots \dots \dots \textcircled{6}$$

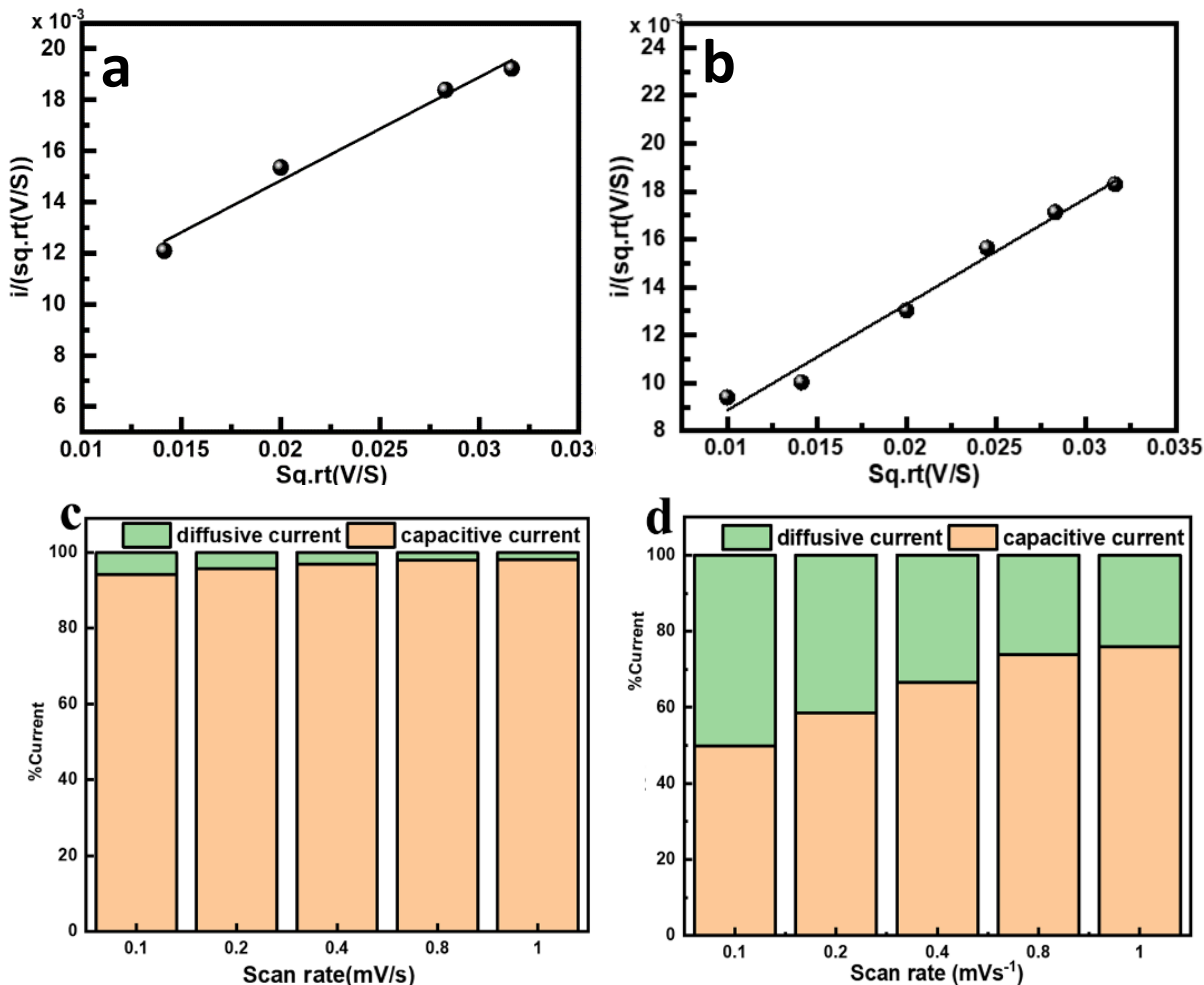


Figure 20-a) Linear fit of  $\vartheta^{0.5}$  vs  $i/\vartheta^{0.5}$  in Py PBM600 based anodic half-cell b) Linear fit of  $\vartheta^{0.5}$  vs  $i/\vartheta^{0.5}$  in Py PBM800 based anodic half-cell rates c) % current contribution from capacitive and diffusive behaviours in Py PBM600 anode d) % current contribution from capacitive and diffusive behaviours in Py PBM800 anode

Where  $i$  is peak current,  $\vartheta$  is scan rate and  $b$  is exponent of scan rate. The current response obtained from a cell during cyclic voltammetry is largely dependent on the scan rate applied and the mechanism of charge storage. If the charge storage is bulk controlled, the increase in scan rate does not directly correlate to increase in current. In bulk controlled materials, it is observed that the  $b$  value is 0.5. In surface-controlled charge storage, the increase in scan rate directly correlated to the increase in current. Hence, the  $b$  value was observed to be 1.0. Equation 6 was employed to determine the  $b$  value by plotting linear fit between  $\log i$  and  $\log \vartheta$  (Figure 21 a and b). The slope obtained i.e.,  $b$  (exponent) value was found to be 0.91 and 0.81 in case of Py PBM600 based anodic half-cell and Py PBM800 based anodic half-cell respectively. This suggests that Py PBM600 is

tending towards a capacitive behavior while Py PBM800 displays a balanced alliance between capacitance and diffusion.

The results from kinetic studies suggest that Py PBM600 is largely capacitive material whereas Py PBM800 apart from being capacitive in nature, also exhibits diffusive behavior. This can be due to the shorter interlayer spacing compared to Py PBM600. Py PBM800 also exhibited superior capacity retention while Py PBM600 showed slightly better capacity but lower capacity retention.

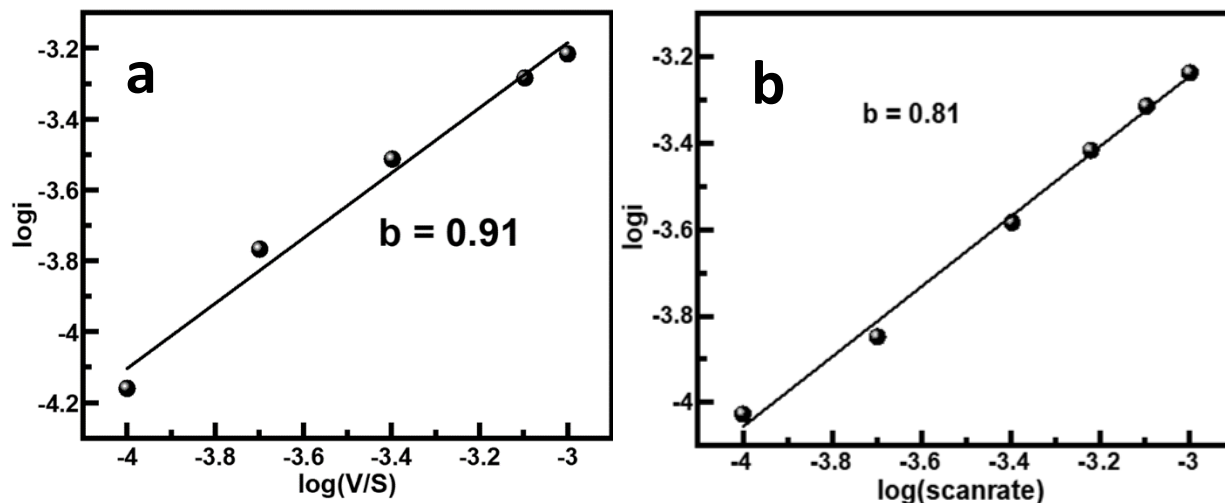


Figure 21-a) Linear fit of  $\log i$  vs  $\log \eta$  for the anodic half-cell with Py PBM600 anode b) a) linear fit of  $\log i$  vs  $\log \eta$  for the anodic half-cell with Py PBM800 anode

#### 4.5.6 Full-cell studies

To understand the competence of these materials in practical applications, full cells have been fabricated using LiNCAO ( $\text{LiNi}_{0.80}\text{Co}_{0.15}\text{Al}_{0.05}\text{O}_2$ ) material as cathode. To fabricate the full cells initially, anodic half-cells were prepared using Py PBM600 and Py PBM800 electrodes with  $8.5 \text{ mg/cm}^2$  mass loading. The anodic half-cells and cathodic half-cells with LiNCAO active material were then precycled at  $0.25 \text{ mA/cm}^2$  current. Figure 22 shows the charge-discharge studies of full-cells with Py PBM600 anode and Py PBM800 anodes at  $0.5 \text{ mA/cm}^2$ . The full cell with Py PBM600 anode delivered a reversible capacity of  $1.01 \text{ mAh}$  after 50 cycles and the full cell with Py PBM800 anode delivered a reversible capacity of  $1.65 \text{ mAh}$  after 50 cycles. In full cell

configuration, Py PBM800 is observed to be performing better than Py PBM600 in terms of stability which is also observed in case of half-cells.

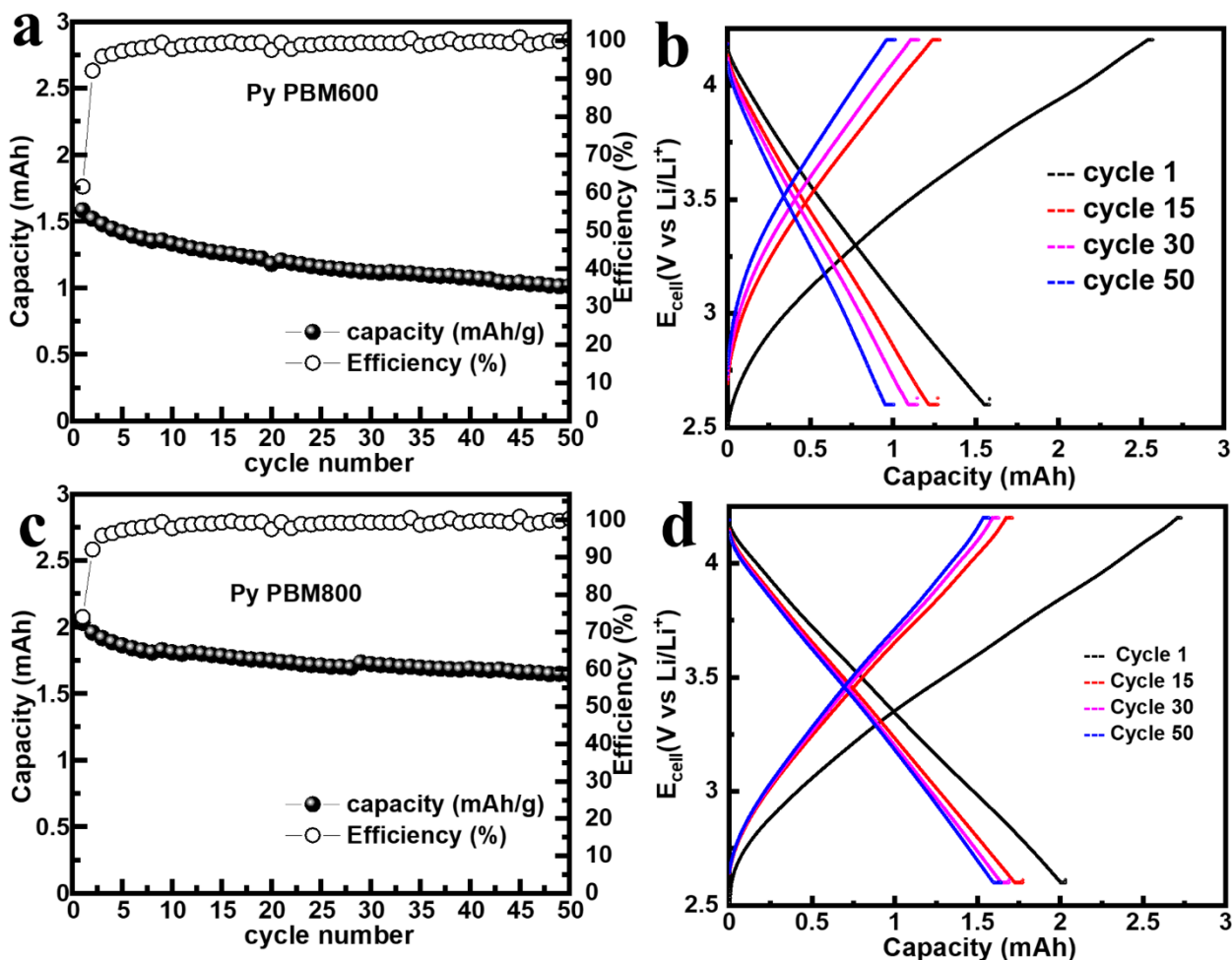


Figure 22-a) Charge-discharge plot of full cell with Py PBM600 anode and LiNCAO cathode b) Potential vs capacity plot of Py PBM600 at 0.5 mA/cm<sup>2</sup> c) Charge-discharge plot of full cell with Py PBM800 anode and LiNCAO cathode d) Potential vs capacity plot of Py PBM800 at 0.5 mA/cm<sup>2</sup>

#### 4.5 XPS after cycling

The half-cells cycled for 1500 cycles and 2000 cycles in case of Py PBM600 and Py PBM800 anodes respectively at 4000 mA/g were deprimed in Ar filed glove box (<0.5ppm H<sub>2</sub>O and <0.5 ppm O<sub>2</sub>). XPS analysis was conducted on the anodes obtained after depriming. Figure 23 shows the C1s, N1s and O 1s XPS spectra of cycled Py PBM600 anode and Figures 24 shows the C 1s and N1s spectra of cycled Py PBM800 anode. The penetration depth of X-rays in XPS is ~5 nm. The fact that nitrogen is detected in XPS indicates that the thickness of SEI formed is <5 nm.



The C 1s spectra of cycled Py PBM600 anode shows peaks at 283.8 eV, 284.6 eV, 285.3 eV, 286.1 eV, 287 eV and 289.4 eV corresponding to C-Li, C=C, C=N/C-N, C=O, C-O-C and  $\text{Li}_2\text{CO}_3$  respectively. The N 1s spectra of cycled Py PBM600 anode shows peaks at 397.8 eV and 399.8 eV corresponding to N-Li and C=N respectively<sup>27</sup>. The O 1s spectra of cycled Py PBM600 anode

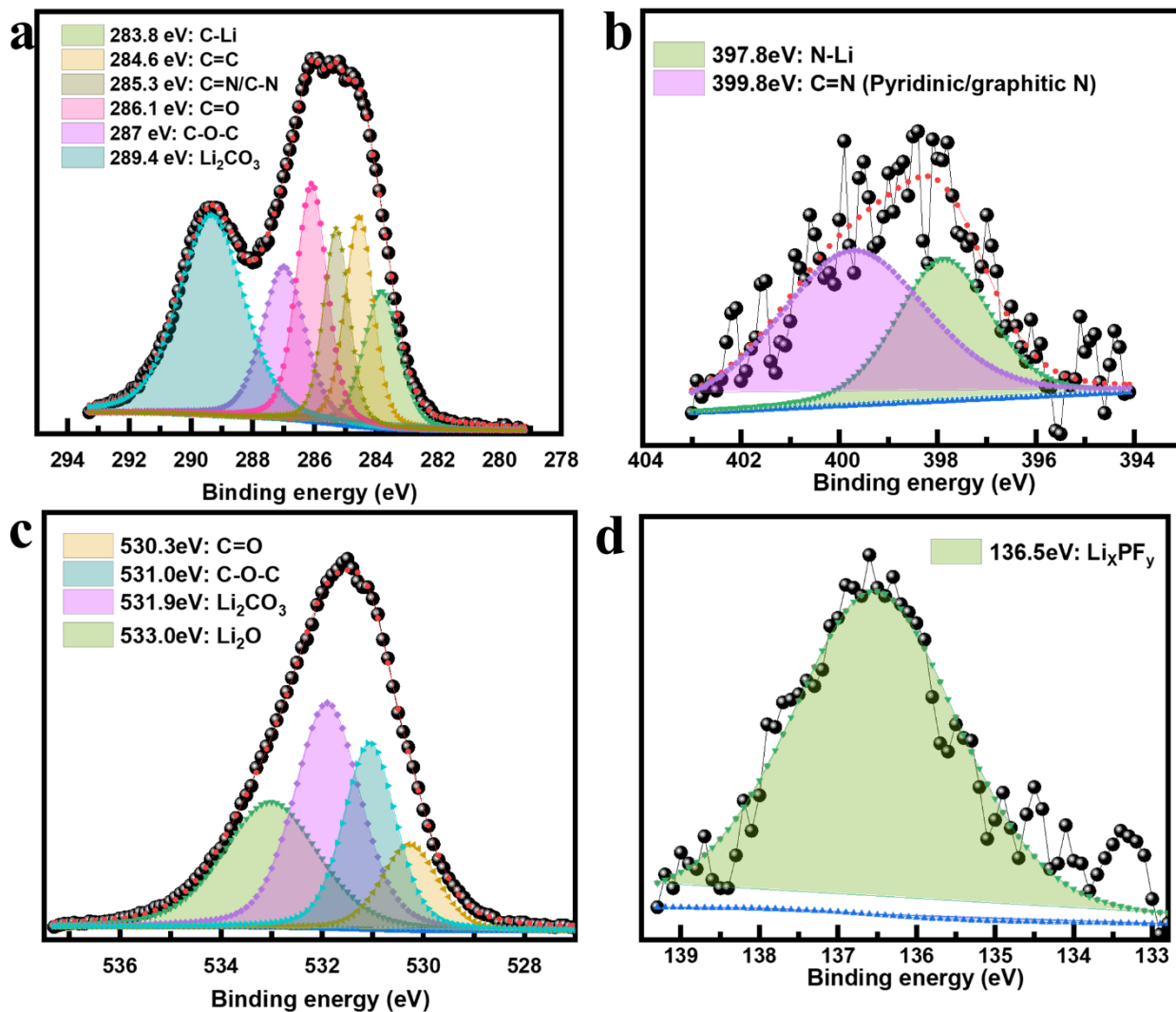


Figure 23-a) C 1s XPS spectra of Py PBM600 cycled electrode after 1500 cycles at 4A/g b) N 1s XPS spectra of Py PBM600 cycled electrode after 1500 cycles at 4A/g c) O 1s XPS spectra of Py PBM600 cycled electrode after 1500 cycles at 4A/g d) P 1s spectra of Py PBM600 anode after 1500 cycles at 4 A/g.

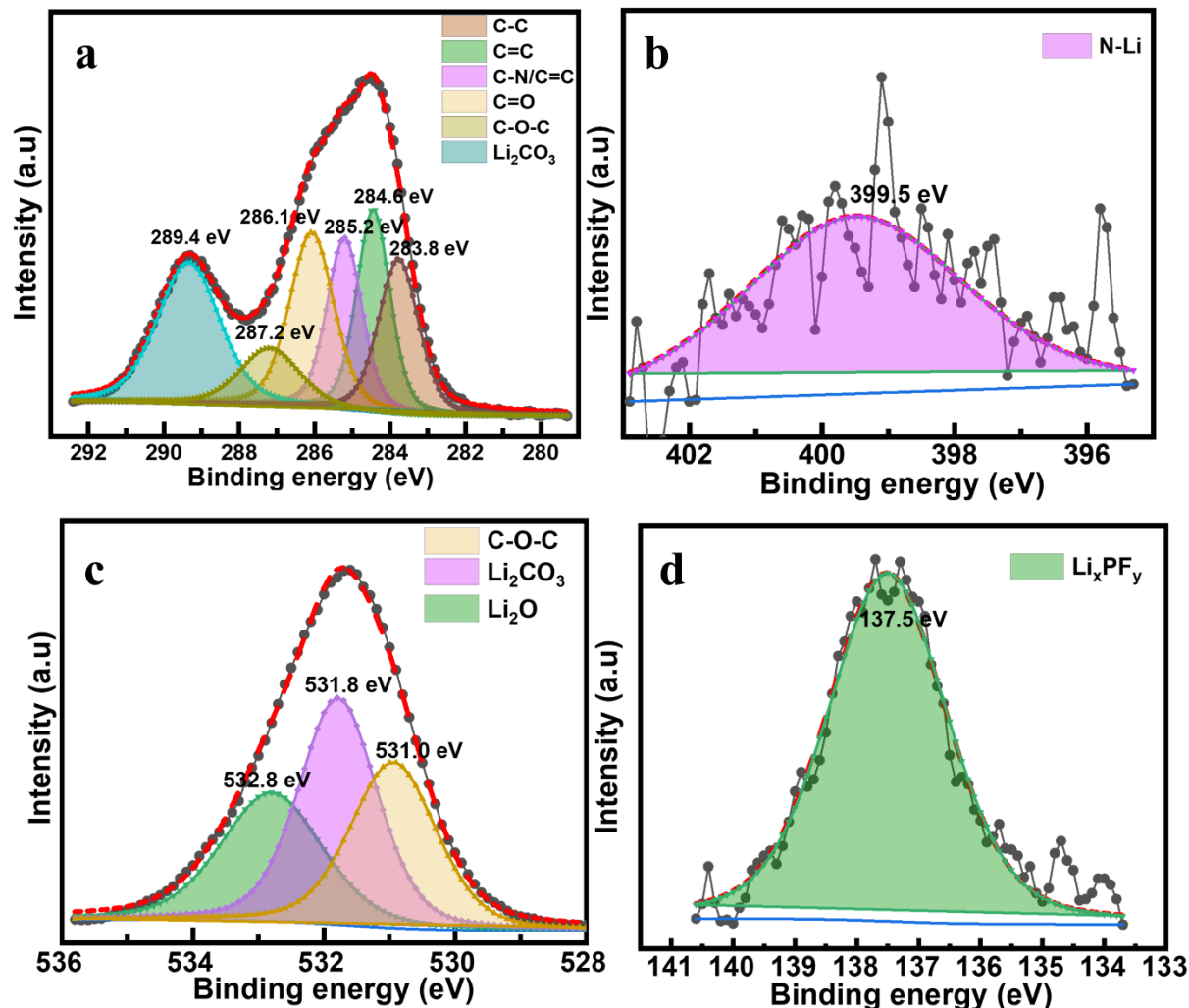


Figure 24- a) C 1s XPS spectra of Py PBM800 cycled electrode after 2000 cycles at 4A/g b) N 1s XPS spectra of Py PBM800 cycled electrode after 1500 cycles at 4A/g c) O 1s XPS spectra of Py PBM800 cycled electrode after 1500 cycles at 4A/g d) P 1s spectra of Py PBM800 anode after 1500 cycles at 4 A/g.

shows peaks at 530.3 eV, 531.0 eV, 531.9 eV and 533.0 eV corresponding to C=O, C-O-C, Li<sub>2</sub>CO<sub>3</sub> and Li<sub>2</sub>O<sup>28</sup>. The P 1s spectra of cycled Py PBM600 shows a peak at 136.5 eV corresponding to Li<sub>x</sub>PF<sub>y</sub><sup>29</sup>. The XPS results suggest that Li<sub>2</sub>CO<sub>3</sub>, Li<sub>2</sub>O and Li<sub>x</sub>PF<sub>y</sub> are the components of SEI in case of cycled Py PBM600 electrode<sup>30</sup>. The C 1s spectra of cycled Py PBM800 anode shows peaks at 283.8 eV, 284.6 eV, 285.2 eV, 286.1 eV, 287.2 eV and 289.4 eV corresponding to C-Li, C=C, C=N/C-N, C=O, C-O-C and Li<sub>2</sub>CO<sub>3</sub> respectively. The N 1s spectra of cycled Py PBM800 anode shows a single peak at 399.5 eV corresponding to N-Li<sup>27</sup>. The O 1s spectra of cycled Py PBM800 anode shows peaks at 531.0 eV, 531.8 eV and 532.8 eV corresponding to C-O-C, Li<sub>2</sub>CO<sub>3</sub> and Li<sub>2</sub>O<sup>28</sup>. The P 1s spectra of cycled Py PBM800 shows a peak at 137.5 eV corresponding to

$\text{Li}_x\text{PF}_y$ <sup>29</sup>. As observed in case of Py PBM600, the components of SEI in the case of cycled Py PBM800 electrode were found to be  $\text{Li}_2\text{CO}_3$ ,  $\text{Li}_2\text{O}$  and  $\text{Li}_x\text{PF}_y$ <sup>30</sup>.

## 4.6 Conclusion

BIAN-melamine based organic polymer was used as single source of carbon and nitrogen to synthesize nitrogen doped carbon. The synthesis was carried out at two different temperatures i.e., 600°C and 800°C yielding carbon with different nitrogen content. At 800°C the nitrogen content was found to be 9% which is lesser than 14 atomic percentage nitrogen observed when the synthesis temperature was 600°C. Py PBM800 was observed to have better micro crystallinity than Py PBM600 (as seen in TEM micrographs). Correspondingly, Py PBM800 anodic half-cell exhibited a higher fraction of diffusion-based charge storage than Py PBM600 anodic half-cell. By the virtue of higher capacitance contribution and higher nitrogen content, Py PBM600 anodic half-cell exhibited better specific capacity compared to Py PBM800 anodic half-cells. However, the capacity retention of the material was observed to be better in Py PBM800. Hence, the minor difference in terms of specific capacity is out balanced by better retention in Py PBM800 as observed in the full cell studies too. Hence 800°C was found to be an optimal condition to synthesize nitrogen doped carbon for lithium-ion battery applications in the case of BIAN-melamine based organic polymer<sup>31,32</sup>.

## References

- 1 H. Yamamoto, S. Muratsubaki, K. Kubota, M. Fukunishi, H. Watanabe, J. Kim and S. Komaba, *J. Mater. Chem. A*, 2018, **6**, 16844–16848.
- 2 T. Hosaka, K. Kubota, A. S. Hameed and S. Komaba, *Chem. Rev.*, 2020, **120**, 6358–6466.
- 3 T. Sun, J. Xie, W. Guo, D. S. Li and Q. Zhang, *Adv. Energy Mater.*, 2020, **10**, 1–23.
- 4 A. Gupta, R. Badam, A. Nag, T. Kaneko and N. Matsumi, *ACS Appl. Energy Mater.*, 2021, **4**, 2231–2240.
- 5 S. G. Patnaik, R. Vedarajan and N. Matsumi, *J. Mater. Chem. A*, 2017, **5**, 17909–17919.
- 6 E. Kazyak, K. H. Chen, Y. Chen, T. H. Cho and N. P. Dasgupta, *Adv. Energy Mater.*, 2022, **12**, 1–12.
- 7 K. S. Patnaik, R. Badam, Y. Peng, K. Higashimine, T. Kaneko and N. Matsumi, *Chem.*

- Commun.*, 2021, **57**, 13704–13707.
- 8 J. Kim, S. M. Nithya Jeghan and G. Lee, *Microporous Mesoporous Mater.*, 2020, **305**, 110325.
  - 9 D. Chakraborty, S. Nandi, R. Illathvalappil, D. Mullangi, R. Maity, S. K. Singh, S. Haldar, C. P. Vinod, S. Kurungot and R. Vaidhyanathan, *ACS Omega*, 2019, **4**, 13465–13473.
  - 10 P. Meister, H. Jia, J. Li, R. Kloepsch, M. Winter and T. Placke, *Chem. Mater.*, 2016, **28**, 7203–7217.
  - 11 J. Li, X. Jing, Q. Li, S. Li, X. Gao, X. Feng and B. Wang, *Chem. Soc. Rev.*, 2020, **49**, 3565–3604.
  - 12 C. Synthesis, N.-D. Graphene, T. Annealing, G. Oxide and I. E. Electrocatalysis, 2011, 4350–4358.
  - 13 L. Sun, L. Wang, C. Tian, T. Tan, Y. Xie, K. Shi, M. Li and H. Fu, 2012, 4498–4506.
  - 14 S. Huang, Z. Li, B. Wang, J. Zhang, Z. Peng, R. Qi, J. Wang and Y. Zhao, *Adv. Funct. Mater.*, 2018, **28**, 1–10.
  - 15 J. Asenbauer, T. Eisenmann, M. Kuenzel, A. Kazzazi, Z. Chen and D. Bresser, *Sustain. Energy Fuels*, 2020, **4**, 5387–5416.
  - 16 D. Yan, Y. Wu, R. Kitaura and K. Awaga, *J. Mater. Chem. A*, 2019, **7**, 26829–26837.
  - 17 S. G. Patnaik, R. Vedarajan and N. Matsumi, *ACS Appl. Energy Mater.*, 2018, **1**, 1183–1190.
  - 18 P. Lazar, R. Mach and M. Otyepka, *J. Phys. Chem. C*, 2019, **123**, 10695–10702.
  - 19 L. Fu, K. Tang, K. Song, P. A. Van Aken, Y. Yu and J. Maier, *Nanoscale*, 2014, **6**, 1384–1389.
  - 20 M. B. Pinson and M. Z. Bazant, *J. Electrochem. Soc.*, 2013, **160**, A243–A250.
  - 21 M. Gaberšček, *Nat. Commun.*, 2021, **12**, 19–22.
  - 22 F. Linsenmann, D. Pritzl and H. A. Gasteiger, *J. Electrochem. Soc.*, 2021, **168**, 010506.

- 
- 23 Y. Jiang and J. Liu, *Energy Environ. Mater.*, 2019, **2**, 30–37.
  - 24 I. Bloom, A. N. Jansen, D. P. Abraham, J. Knuth, S. A. Jones, V. S. Battaglia and G. L. Henriksen, *J. Power Sources*, 2005, **139**, 295–303.
  - 25 V. Augustyn, P. Simon and B. Dunn, *Energy Environ. Sci.*, 2014, **7**, 1597–1614.
  - 26 X. Liu, J. Zhang, S. Guo and N. Pinna, *J. Mater. Chem. A*, 2016, **4**, 1423–1431.
  - 27 Z. Chen, A. Jaworski, J. Chen, T. M. Budnyak, I. Szewczyk, A. Rokicińska, R. Dronskowski, N. Hedin, P. Kuśtrowski and A. Slabon, *Dalt. Trans.*, 2021, **50**, 6857–6866.
  - 28 N. L. Hamidah, F. M. Wang and G. Nugroho, *Surf. Interface Anal.*, 2019, **51**, 345–352.
  - 29 A. Gomez-martin, J. Martinez-fernandez, M. Rutttert, M. Winter, T. Placke and J. Ramirez-rico, *Carbon N. Y.*, 2020, **164**, 261–271.
  - 30 E. Peled and S. Menkin, *J. Electrochem. Soc.*, 2017, **164**, A1703–A1719.
  - 31 B. S. Mantripragada, R. Badam and N. Matsumi, *ACS Appl. Energy Mater.*, 2022, **5**, 6903–3912.
  - 32 B. S. Mantripragada, R. Badam and N. Matsumi, *ECS Meet. Abstr.*, 2021, **MA2021-01**, 104–104.

## 5. Conclusion

### Chapter 1

In chapter 1, a general introduction to the various energy sources that are currently under use is provided. The demerits of fossil fuel-based energy resources and the need to divert our energy quest towards sustainable energy resources was discussed in detail. Though a variety of sustainable energy resources are available and can provide abundant energy, the lack of consistency, portability and hence leading to the need of effective energy storage systems was presented. In this context electrochemical energy storage devices offer both portability and effective energy storage. Electrochemical energy storage devices are devices that can convert electrical energy to chemical energy and chemical energy to electrical energy. Based on the operating principles electrochemical energy storage devices can be broadly categorized as batteries, fuel cells and supercapacitors. The working principles and a brief discussion on various components involved in these devices was presented. Among the various electrochemical energy storage devices, lithium-ion batteries offer high power density, the possibility of fast charging as required in electric vehicles and the relatively safe usage make them very crucial from the perspective of future energy requirements. Hence, the working mechanism, various components involved in lithium-ion battery were discussed. Evolution of cathode materials from the noble prize winning  $\text{LiCoO}_2$  to the current status of cathodes, various types of electrolytes, different types of anodes and their working principles were discussed in detail. Also, the principles of various electrochemical techniques used in this thesis were discussed briefly. Further, the design principles of lithium-ion batteries were presented to understand the contribution of individual components of lithium-ion battery. In a lithium-ion battery, anode plays a crucial role. Currently, cathodic materials supporting faster kinetics are well established. However, the anodes supporting faster kinetics are very few. The draw backs of commercially used graphite anode in terms of faster kinetics and low specific capacity is presented. This calls for the development of anodes supporting faster kinetics and higher specific capacity. In this regard, the design strategy employed in this thesis is to optimize the morphology of the anodic active material to support faster kinetics and deliver higher specific capacity. The chapter is concluded with the discussion on objective and scope of the thesis i.e., to study the effect of including porosity and heteroatoms in the anodic framework with BIAN based materials and their derivatives as illustrative examples.

## Chapter 2

Chapter 2 presents the design and applications of BIAN-Bismarck brown based organic polymer (BBP). The importance and applications of organic anodic materials was discussed. The synthesis of BBP using 1,4,4'-(m-Phenylenebisazo) bis-m-phenylenediamine (Bismarck brown) as crosslinking moiety was presented. The characterization of BBP using various techniques like IR, XPS, XRD was presented in characterization section. Electrochemical studies were conducted by preparing anodic-half cells with BBP as anodic active material. The rate capability and charge-discharge studies are presented in detail. The charge storage mechanism was investigated using power law. The predominant capacitive behavior of BBP anode was demonstrated. Dynamic electrochemical impedance spectroscopy results were presented and the SEI, charge transfer resistances were compared. XPS results of cycled BBP electrode revealed the composition of SEI, the relevant details were presented in the post-mortem studies. The chapter is concluded with summary of the morphological characteristics and electrochemical properties of BBP.

## Chapter 3

In chapter 3, a brief introduction to organic materials was presented. The importance of porosity in the framework of anode and the polarity induced by the inclusion of heteroatoms is discussed in the context of BIAN-Melamine based organic polymer (PBM) with high nitrogen content as an organic anode in lithium-ion battery. The synthesis of the polymer and the characterization using techniques like IR, XPS, XRD, TEM, BET was demonstrated. The experimentally obtained data was found to be matching the data obtained theoretically using  $dmol^3$  module of material studio. Followed by synthesis and characterization, electrochemical studies were conducted. The anodic half-cells prepared with PBM were found to deliver high specific capacities even at higher currents. The charge storage mechanism was found to be a combination of diffusive and capacitive mechanisms. Theoretical studies were conducted to understand the chemical reactions during charge-storage, and the relevant data was presented. Furthermore, the postmortem XPS studies revealed the SEI components to be  $LiF$ ,  $Li_2CO_3$ ,  $Li_xPF_y$ . The morphological changes that led to the gradual activation of the anode was also demonstrated. The chapter was concluded by comparing the performance of PBM anode with previously reported materials in which it was found that PBM outperforms many of the earlier reported works.

## Chapter 4

In chapter 4, the author presented another application of PBM i.e., the synthesis of N-doped carbon with PBM as single source of carbon and nitrogen. PBM was pyrolyzed at 600°C and 800°C yielding N-doped carbon with different morphologies (labeled as Py PBM600 and Py PBM800). The differences in the morphologies of both the materials was investigated by XPS, XRD and TEM studies. Py PBM800 was observed to be having better micro-crystallinity than Py PBM600. The effect of morphology on electrochemical properties was demonstrated by various electrochemical techniques. In comparison, though Py PBM600 delivered relatively more specific capacity, better retention was observed in Py PBM800 with very small difference in specific capacity. The detailed charge-discharge study and the redox characteristics of anodic half-cells was presented. Full cells were prepared using Py PBM600 and Py PBM800. The better performance of Py PBM800 was demonstrated by the charge-discharge studies of full-cells. Further the post cycling details like the composition of SEI was also presented. The chapter is concluded by the summary of the morphology and electrochemical properties of Py PBM600 and Py PBM800.

## Future scope

The applications of BIAN based materials in lithium storage applications as demonstrated in this thesis is an effort towards understanding the wide scope of applications that are possible with BIAN based materials and in general with organic molecules. The flexibility of organic anodes can offer a possible alternative to the inorganic anodes. In addition to being a possible anode materials, BIAN based organic molecules can also be used as precursors for the synthesis of materials like heteroatom doped carbon, surface modified silicon etc., Also the composites of these materials with high-capacity anodes like silicon, MoS<sub>2</sub> etc., might help in negotiating the demerits of these anodes. The high density of active sites in BIAN based polymers and the N-doped carbon from BIAN materials can be exploited for various catalytic reactions like oxygen reduction which is a crucial reaction in metal-air batteries and fuel cells. Further, due to the high capacitive behavior of these materials, they can be used as electrode materials in super-capacitors with high power density. Besides this, as lithium resources are less abundant than metals like sodium, potassium, aluminum, iron, magnesium etc., The larger ionic radius of these metal ions than lithium ion pose a challenge in designing suitable electrode materials. The versatility of organic reactions can be



utilized to synthesize suitable electrodes and electrolytes for other metal-ion batteries too. With this background the author believes that BIAN based organic materials have wide range of applications in the perspective of energy storage and the enticing properties of these materials in various fields are to be explored in the future.

## **Publications and Conferences**

1. **Bharat Srimitra Mantripragada, Rajashekar Badam and Noriyoshi Matsumi**, “BIAN based porous organic polymer as high performing anode for lithium-ion batteries”, ACS Appl. Energy Mater., 2022, 5, 6903-6912.

### **Under Review**

1. Rajashekar Badam, Masanori Hara, Hsin-Hui Huang, **Bharat Srimitra Mantripragada**, Noriyoshi Matsumi, Masamichi Yoshimura. “Functionalized Acetylene-black Substrate to Stabilize Ultra-small IrO<sub>2</sub> Nanoparticles for Oxygen Evolution Reaction in Acidic Medium.”

### **Under preparation**

1. **Bharat Srimitra Mantripragada, Rajashekar Badam and Noriyoshi Matsumi**, “Pyrolyzed BIAN-Melamine based porous organic polymer as fast charging anode material in lithium-ion battery”.

2. Krishna Prasad Gannavarapu, **Bharat Srimitra Mantripragada**, Rajashekar Badam, and Noriyoshi Matsumi, “Creation of a stable solid electrolyte interface using pyridyl substituted poly(borosiloxane) type self-healing polymer for stabilization of Si-anode in LIB”.

3. **Bharat Srimitra Mantripragada, Rajashekar Badam and Noriyoshi Matsumi**, “BIAN-Bismarck brown based porous organic polymer and derivatives as efficient anode materials for lithium-ion batteries”

### **Conference presentations**

1. **Bharat Srimitra Mantripragada, Rajashekar Badam, and Noriyoshi Matsumi**, Nitrogen Rich BIAN-Melamine Covalent Organic Framework as High-Capacity Anode in Lithium-Ion Batteries. 62<sup>nd</sup> Battery Symposium, November 30-December 2, 2021. **Oral**.

2. **Bharat Srimitra Mantripragada, Rajashekar Badam, and Noriyoshi Matsumi**, Bis-Imino-Acenaphthenequinone Based Covalent Organic Framework for Lithium-Ion Battery Applications. 3<sup>rd</sup> Symposium on Industrial Science and Technology, August 24-26, 2021. **Oral**.

3. **Bharat Srimitra Mantripragada, Rajashekar Badam, and Noriyoshi Matsumi**, Bis-Imino-Acenaphthenequinone Based Covalent Organic Framework for Lithium-Ion Battery Applications. 239<sup>th</sup> ECS Meeting with the 18<sup>th</sup> International Meeting on Chemical Sensors, May 30-June 26, 2021. **Oral.**
4. **Bharat Srimitra Mantripragada, Rajashekar Badam, and Noriyoshi Matsumi**, Nitrogen Rich BIAN-Melamine Porous Organic Polymer as High-Capacity Anodic Active Material in Lithium-Ion Batteries. International Meeting on Lithium Batteries, June 26-July 1, 2022. **Poster.**
5. **Bharat Srimitra Mantripragada, Rajashekar Badam, and Noriyoshi Matsumi**, Bis-Imino-Acenaphthenequinone Based Covalent Organic Framework for Lithium-Ion Battery Applications, 70<sup>th</sup> SPSJ Annual Meeting Fall, September 7, 2021. **Oral.**
6. **Bharat Srimitra Mantripragada, Rajashekar Badam, and Noriyoshi Matsumi**, BIAN Based Covalent Organic Framework as Anodic Active Material in Lithium-Ion Battery, 70<sup>th</sup> SPSJ Annual Meeting Spring, May 28, 2021. **Poster.**
7. **Bharat Srimitra Mantripragada, Rajashekar Badam, and Noriyoshi Matsumi**, BIAN Based Covalent Organic Framework for Lithium-Ion Battery Applications, 101<sup>st</sup> CSJ Annual Meeting, March 20, 2021. **Poster.**
8. **Bharat Srimitra Mantripragada, Rajashekar Badam, and Noriyoshi Matsumi**, BIAN Based Covalent Organic Framework as Anodic Active Material in Lithium-Ion Battery, CSJ Festa 2021, October 21, 2021. **Poster.**
9. **Bharat Srimitra Mantripragada, Rajashekar Badam, and Noriyoshi Matsumi**, BIAN Based Covalent Organic Framework for Lithium-Ion Battery Applications, CSJ 2021 Hokuriku Area Lecture and Research Presentation, November 21, 2021. **Poster.**
10. **Bharat Srimitra Mantripragada, Rajashekar Badam, and Noriyoshi Matsumi**, Poly(1,2-diphenyldiazine) as Binder for Hard Carbon Anode in Sodium-ion Battery, Elements Strategy Initiative for Catalysis and Batteries Meeting, February 14, 2022. **Poster.**

## **Curriculum Vitae**

### **Personal data**

Name: Mantripragada Bharat Srimitra

Date of Birth: August-18,1997

Nationality: Indian

### **Education:**

10/2019-Present: Doctoral student in Graduate School of Advanced Science and Technology, Japan Advanced Institute of Science and Technology, Ishikawa, Japan (Under MEXT scholarship).

06/2017-04/2019: Master of science in chemistry, Sri Sathya Sai Institute of Higher Learning, Andhra Pradesh, India (CGPA: 8.0/10.0).

06/2014-04/2017: Bachelor of science, chemistry honors, Sri Sathya Sai Institute of Higher Learning, Andhra Pradesh, India (CGPA: 7.1/10.0).